Spectroscopy and Dynamics of High Orbital Angular Momentum Rydberg States

by

Timothy J. Barnum

B.A., Drew University (2013)

Submitted to the Department of Chemistry
in partial fulfillment of the requirements for the degree of

Doctor of Philosophy in Chemistry

at the

MASSACHUSETTS INSTITUTE OF TECHNOLOGY

February 2020

Author .....
Department of Chemistry
January 6, 2020

Certified by .....
Robert W. Field
Haslam and Dewey Professor of Chemistry
Thesis Supervisor

Accepted by .....
Robert W. Field
Haslam and Dewey Professor of Chemistry
Chair, Department Committee on Graduate Students

Spectroscopy and Dynamics of High Orbital Angular Momentum Rydberg States

by

Timothy J. Barnum

Submitted to the Department of Chemistry
on January 6, 2020, in partial fulfillment of the
requirements for the degree of
Doctor of Philosophy in Chemistry

Abstract

Rydberg states of molecules with high orbital angular momentum ($\ell \gtrsim 3$) are a unique class of electronic states. These high-ℓ Rydberg states escape the rapid non-radiative decay by predissociation, which is typical of the intensively studied low-ℓ Rydberg states. Access to high-ℓ Rydberg states is challenging due to the $\Delta\ell = \pm 1$ transition propensity rule in combination with the short lifetimes of the optically accessible, low-ℓ Rydberg states. To address these dual challenges, we implement optical-millimeter-wave stimulated Raman adiabatic passage (optical-mmW STIRAP), which enables efficient population transfer from a low-lying electronic state to a high-ℓ Rydberg state without directly populating a lossy, low-ℓ Rydberg state. Our demonstration of optical-mmW STIRAP on an atomic system includes examination of the experimental and theoretical details of every step of this coherent process and demonstrates its promise for molecular applications. We explore the physics of the Rydberg electron↔ion-core system through investigation of the spectroscopy and dynamics of high-ℓ Rydberg states of NO. We populate ng Rydberg states of NO by a three-color triple-resonance excitation scheme and probe Rydberg-Rydberg transitions by chirped-pulse millimeter-wave (CPmmW) spectroscopy. The precision of the experimental data obtained and the breadth of the state space examined by CPmmW spectroscopy provides challenges to the existing theory of the structure of high-ℓ Rydberg states. We apply a long-range electrostatic model to disentangle and describe the physical mechanisms that contribute to the autoionization dynamics of NO Rydberg states. Our model accounts for the decay rates of vibrationally excited ng Rydberg states. We explain the previously measured NO^+ ion rotational state population distributions produced by autoionization of NO nf states and propose methods to generate single quantum state-selected NO^+ ions by selective population of specific ng Rydberg states.

Thesis Supervisor: Robert W. Field
Title: Haslam and Dewey Professor of Chemistry

Acknowledgments

Although the experiments described in this thesis happen in a vacuum, my Ph.D. experience did not. An enormous number of people have contributed to my journey through graduate school, and I will merely attempt to thank everyone in these acknowledgments.

First, I want to thank my thesis advisor, Bob. His unrelenting enthusiasm for science, student-centered approach to research, and fierce support for his students' personal and professional development create a unique space in which to grow and learn. Bob's approach to research embodies Einstein's maxim that "everything should be made as simple as possible, but no simpler."[a] Rather than lengthy linelists and abstruse molecular constants, simple models of complex phenomena are the key to new insight and deeper scientific truth. I am excited to take Bob's ethos and apply it in all of my future endeavors.

In the Field group, I have learned from and collaborated with an extraordinary group of colleagues. David Grimes and Yan Zhou inducted me into the "Rydberg project" and served as dependable sources of constructive feedback and new ideas, long after they each left the lab. Jun Jiang joined the Rydberg side of the lab about halfway through my Ph.D. and immediately began teaching me new things about Rydberg states; his ability to probe deeply into a seemingly simple question amazed me and brought incredible intellectual rigor to everything we worked on. Steve Coy and John Muenter have contributed to every project in this thesis, from experimental designs to lessons on electric properties of molecules; I want to thank them both for always asking questions that challenged my assumptions about how things work. Outside of the Rydberg project, I learned a staggering amount from other lab members: Barratt Park, Liz Foreman, Carrie Womack, Alex Hull, and Trevor Erickson. In particular, Trevor and I have been sitting back-to-back in the office for nearly my entire Ph.D. and he has been a constant and much appreciated

[a] This aphorism first appeared in the article, Sessions, R. *New York Times*, Section Arts & Leisure, p. 89, (8 January 1950), and appears to be a paraphrase of a similar quote that is correctly attributed to Einstein.

source of humor, quantum mechanics knowledge, and Dr. Pepper.

I had the opportunity to work with several talented undergraduate and visiting students during my time at MIT, including Ben Arenas, Mariyam Fatima, Alice Green, Catherine Saladrigas, and Clare Keenan. I want to especially acknowledge Ethan Klein, a precocious UROP who has become a good friend and colleague; Holger Herburger, who did extraordinary work on the STIRAP experiment; and Gloria Clausen, a gifted undergraduate who performed beautiful laser spectroscopy on NO.

Outside of MIT, I have benefited tremendously from collaborations and interactions with several researchers. During his sabbatical in 2015, Ed Eyler gave us the courage and resources to revisit NO, a molecule that has been intensively studied for decades. Ed's earlier work on NO, specifically, and Rydberg states of molecules, generally, underpins many, if not all, of our new insights into the Rydberg states of NO. In addition, Philip Martin has been a wonderful collaborator on our NO work and I look forward to continuing our investigation of his high-resolution laser spectra. Discussions with Klaas Bergmann on our STIRAP work have greatly improved our understanding of this experiment, and generated a flurry of new ideas about how to build a vastly improved, second generation STIRAP experiment. My work on vibrational autoionization was initially prompted by our collaboration with Heather Lewandowski to find a method for state-selected ion generation. This evolved into one of the most exciting projects of my Ph.D. and allowed me to explore the world of cold chemistry. Heather has been an incredibly generous collaborator, and much of the work in this thesis would not have been possible without her support. I want to also acknowledge her lab members, especially James Greenberg, for their warm welcome on several trips to Boulder.

Away from the lab, I have met some truly extraordinary people during my time in Cambridge. I want to acknowledge my "first friend" and long-time housemate, Jessica Carr, for baking birthday cakes each year with enterprising new designs, trudging through snow to work every winter, and being the biggest fan of the Old South Ringers. Wesley Transue was my always reliable partner at the Muddy Charles, and our conversations over a pitcher — scientific or otherwise — make up some of my

warmest memories of graduate school. Thank you to Daniel Franke, the Muddy chair-extraordinaire who brightened many of my low days with his infectious good mood; Kathleen White, my flea market companion and undisputed Loopin' Louie champion; Hendrik Utzat, an evergreen source of entertaining conversations about science, fitness, and Jacques Cousteau; and Maciej Korzynski, my yogi-capoeirista-bodypumper buddy who also enjoys Dominoes and High Life. Thank you to the Bawendi group for being my lab away from lab, especially Michel, Lea, and Matthias, and to the many other friends who made the last several years special in ways both large and small.

I would like to thank the members of the Chemistry Student Seminar team, Kathleen White, Anna Wuttig, Mike Geeson, and Soyoung Kim, for becoming good friends and contributing to one of my favorite parts of our department. Thank you to the members of the Old South Ringers for the warm fellowship and all of the great music that we have made together.

I want to acknowledge the incredible teachers over the years that helped me reach MIT in the first place, especially Michael Amendola, Mary-Ann Pearsall, and Ryan Hinrichs.

Finally, I want to express my deepest gratitude to my family for their continuous support on my path to a Ph.D. Anne has been a source of constant encouragement and sometimes commiseration during this time. More importantly, I could never have imagined finding such an incredible partner during my time in graduate school. Thanks to my parents and siblings for never getting tired of asking "how's it going in lab," and always believing in my goals. Without all of your support throughout the years, this Ph.D. thesis would not have been possible.

This doctoral thesis has been examined by a Committee of the Department of Chemistry as follows:

Professor Adam P. Willard .....
Chairman, Thesis Committee
Associate Professor of Chemistry

Professor Robert W. Field .....
Thesis Supervisor
Haslam and Dewey Professor of Chemistry

Professor Sylvia T. Ceyer .....
Member, Thesis Committee
John C. Sheehan Professor of Chemistry

Contents

List of Figures

List of Tables

Chapter 1

Introduction

The focus of this thesis is the spectroscopy and dynamics of Rydberg states of atoms and molecules with high electron orbital angular momentum, ℓ. The following chapters describe in detail a new method to populate these states, as well as new physical insights gained through spectroscopic and dynamical investigations. In this introductory chapter, we review some basic physics of Rydberg states and highlight current research areas of relevance to this work. Next, a review of Hund's angular momentum coupling cases is presented, which is critical to the theory developed in Chapters 4 and 5. An outline of this thesis appears in the final section, which summarizes the primary results of each project.

1.1 Rydberg states

Rydberg states of atoms and molecules are electronic states in which the outer electron is placed in a highly excited state. These states take their name from Johannes Rydberg, who developed his eponymous formula that reproduced the spectral lines observed in the emission of the hydrogen atom.[132] In the limit of a nucleus with infinite mass, this formula is written as:

$$E_n = -\frac{R_\infty}{n^2} \tag{1.1}$$

where n is the principal quantum number, and R_∞ is the Rydberg constant in the infinite mass limit. This Rydberg constant can be written in terms of fundamental constants:

$$R_\infty = \frac{m_e e^4}{8\epsilon_0^2 h^3 c} \tag{1.2}$$

where m_e is the electron mass, e is the fundamental unit of charge, ϵ_0 is the permittivity of free space, h is Planck's constant, and c is the speed of light. Using the reduced mass of the system, the constant, R_∞, can be related to the Rydberg constant of an atom or molecule with finite mass, $m_A = m_{\text{core}} + m_e$, where m_{core} is the mass of all particles except the Rydberg electron (the "ion-core"):

$$\begin{aligned} R_A &= R_\infty \cdot \frac{\mu_e}{m_e} && (1.3)\\ &= R_\infty \cdot \frac{1}{m_e}\left(\frac{m_e m_{\text{core}}}{m_e + m_{\text{core}}}\right) && (1.4)\\ &= R_\infty \cdot \left(\frac{m_A - m_e}{m_A}\right) && (1.5)\\ &= R_\infty \cdot \left(1 - \frac{m_e}{m_A}\right) && (1.6) \end{aligned}$$

Any state with sufficiently high n, such that the energy level spacing approximately obeys the Rydberg formula, may rightly be considered a Rydberg state.

Beyond the difference in the value of the Rydberg constant, atoms other than hydrogen possess core structure. The core has a finite size and the nuclear charge is incompletely shielded by the core electrons. This results in deviations from a purely Coulombic potential at short distances from the core, as shown schematically in Figure 1-1. Outside of some critical distance from the core, the potential again resembles that of a hydrogenic system. This short-range, non-Coulombic interaction results in an overall phase shift of the Rydberg wavefunction and modification of Equation 1.1 by a so-called quantum defect:

$$E_{n,\ell} = -\frac{R_\infty}{(n - \delta_\ell)^2} \tag{1.7}$$

where δ_ℓ is the quantum defect for the Rydberg series with orbital angular momentum,

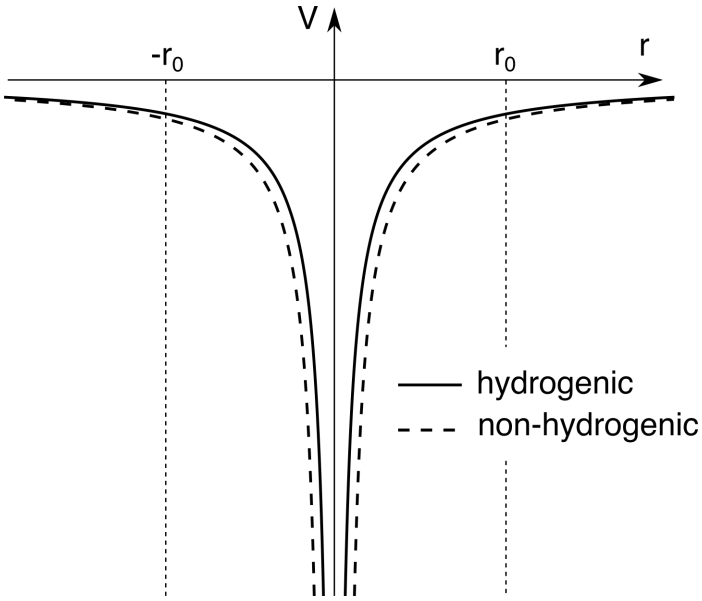

Figure 1-1: For the hydrogen atom, the interaction potential is purely Coulombic. For non-hydrogenic atoms and molecules, the finite size of the core and incomplete nuclear shielding distort the potential. Beyond some critical radius, r_0, the non-hydrogenic potential closely matches the hydrogenic potential.

ℓ. In fact, this quantum defect depends on all properties of the ion-core, including the hyperfine, electronic, and spin-orbit state. In molecules, the rotational and vibrational states must also be considered, as well as the projection quantum numbers of the orbital and spin angular momenta of the Rydberg electron. Nevertheless, the quantum defects generally depend most significantly on the orbital angular momentum, ℓ. For low-ℓ states, the quantum defects are very large because the Rydberg electron closely approaches the core and experiences complicated, non-Coulombic interactions. As ℓ increases, the quantum defects approach zero because the centrifugal barrier results in a very low probability for the Rydberg electron to be found in the core region. The centrifugal potential is defined by:

$$V_{\text{cent}} = \frac{\boldsymbol{\ell}^2}{2r^2} = \frac{\ell(\ell+1)}{2r^2} \tag{1.8}$$

For two Rydberg states with radial wavefunction, $R(r)$, and $\ell = 1$ (red) or $\ell = 5$ (blue), the quantity r^2R^2 is plotted as a function of r in Figure 1-2. This represents the probability distribution function of the Rydberg electron and highlights the enormous

difference between low-ℓ and high-ℓ states at short distances.

The distinction between these low-ℓ, *core-penetrating*, and high-ℓ, *core-nonpenetrating* Rydberg states is particularly important for Rydberg states of molecules. Unlike atoms, molecular Rydberg states generally suffer from non-radiative decay. The non-radiative decay pathways include autoionization, the transition from a bound Rydberg state with energy above the first ionization limit to a free ion and electron, and predissociation, the transition from a bound Rydberg state to a dissociative continuum state at the same energy, which leads to fragmentation into constituent atoms. Predissociation is particularly insidious because, at the high internal energies characteristic of Rydberg states, many possible dissociation pathways exist, which often leads to complex multi-state interactions that are not easily disentangled. The dissociative states responsible for fragmentation are generally valence electronic states. All valence states possess large wavefunction amplitude in the core region. As a result, core-nonpenetrating Rydberg states are relatively immune to predissociation and possess much longer lifetimes than core-penetrating states.

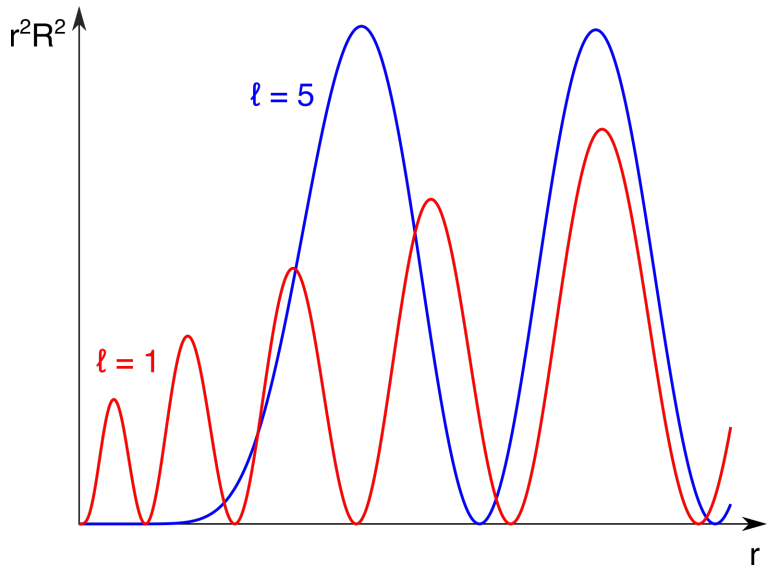

Figure 1-2: Radial probabilities for $\ell = 1$ (red) and $\ell = 5$ Rydberg wavefunctions. The centrifugal barrier in the high-ℓ state results in negligible probability of finding the Rydberg electron at short r values.

Rydberg states play a key role in modern physics experiments due to their simplified energy level structure and exaggerated atomic properties. A Rydberg state with

$n = 50$ has a radius of over 100 nm and a radiative lifetime of nearly 100 μs.[53] These properties are best explored by considering the hydrogen wavefunction as the model for the Rydberg wavefunction and examining how its properties scale with n. For example, consider the transition dipole moment between a Rydberg state and the ground state. As $n \to \infty$, the transition frequency between the ground state and the Rydberg state approaches a constant since the binding energy is given by Equation 1.1. Thus, the transition amplitude is due entirely to the integral, $\langle \text{valence}|r|\text{Rydberg}\rangle$, between the valence state wavefunction and Rydberg wavefunction. The intensity of this integral accumulates near a point of stationary phase in the ion-core region.[91] As n increases, the inner-lobe of a hydrogenic wavefunction does not change shape, but the amplitude decreases as $n^{-3/2}$. This means the transition dipole moment between a Rydberg state and the ground state (or indeed any low-lying electronic state) scales as $n^{-3/2}$, and the radiative lifetime must scale as n^3. This scaling of the radiative lifetime means atomic Rydberg states are spectacularly stable in spite of their huge amount of internal energy. Several other properties of interest and their n-scaling are presented in Table 1.1.

Taking advantage of these exaggerated properties and their simple scaling rules has enabled the development of many exciting areas of active research. One prominent example is the use of electric fields for Rydberg state-enabled spatial manipulation of atoms and molecules. The ability to control the spatial degrees of freedom of atoms and molecules is the hallmark of modern atomic physics. Since all atoms and molecules possess Rydberg states, techniques relying upon Rydberg state physics to achieve this control open up a wide range of atoms and molecules for study.

It was recognized nearly forty years ago that the very large electric dipole moments of Rydberg states, which scale as n^2, result in a very strong interaction between a dipolar Rydberg state and an externally applied electric field gradient.[18,162] A number of manipulations have since been demonstrated including deflection,[147] deceleration,[155] and reflection[154] of atomic beams, and even trapping[68,166] of Rydberg states on timescales limited only by their fluorescence lifetime. While the majority of these experiments were performed on atomic Rydberg states, one seminal study

Table 1.1: Principal quantum number (n) scaling of several Rydberg state properties.[53] These n-scaling rules are derived from the hydrogen radial wavefunctions and assume a small value of ℓ. For very high ℓ values, the "circular" state limit, $\ell = n-1$, is approached, and some properties exhibit different n-scaling. For example, the transition dipole moment between the Rydberg state and the ground state goes to zero for all n, and the radiative lifetime scales as n^5.

Property	Scaling
Binding energy	n^{-2}
Energy level spacing	n^{-3}
Mean radius	n^2
Transition dipole moment: Rydberg to ground state	$n^{-3/2}$
Radiative lifetime	n^3
Transition dipole moment: Rydberg-Rydberg	n^2
Dipole-dipole interaction	n^4
Polarizability	n^7
van der Waals interaction	n^{11}

by the Merkt group demonstrated the ability to both decelerate and three dimensionally trap nf Rydberg states of H_2.[69] These spatial manipulations with electric fields are not possible unless the Rydberg states exist for long enough, typically 10s of microseconds, to alter their trajectories and localize them in traps. Core-penetrating Rydberg states of molecules predissociate too quickly. In the study by Merkt and co-workers on trapping H_2 Rydberg states,[69] a triple-resonance scheme was used to populate a high-ℓ state that did not significantly interact with the ion-core. The authors explicitly mention that "essential for the success of these experiments was the excitation of core-nonpenetrating Rydberg-Stark states."[69]

Another area of intense research into Rydberg atoms and molecules is microwave spectroscopy of Rydberg-Rydberg transitions. Since the energy spacing between Rydberg levels scales as n^{-3}, the frequencies of many Rydberg-Rydberg transitions fall in the microwave spectral region: $\Delta n = \pm 1$ transitions with $25 \lesssim n \lesssim 100$ have frequencies of $400 \gtrsim \nu \gtrsim 6$ GHz. These transitions have enormous transition dipole moments due to their n^2 scaling. At $n = 50$, $\mu \approx 10$ kiloDebye (kD). This allows very

weak microwave sources to be used for excitation and has also enabled coherent spectroscopy in the form of chirped-pulse Fourier transform millimeter-wave (CPmmW) spectroscopy.[126,169]

These high-resolution spectroscopic investigations have allowed for determination of difficult-to-measure electric properties of the ion-core,[6,74] precision measurements of the energy levels in few-electron systems to challenge *ab initio* theory,[63,137] and new insights into many-body Rydberg physics.[61,105] Rapid decay by predissociation limits the achievable resolution of microwave experiments, and thereby, the physical insights that can be attained. In addition, CPmmW spectroscopy necessitates sufficiently long lifetimes to accomplish both polarization of the Rydberg-Rydberg transition and time-domain detection of the coherent emission.

Finally, an application that has been proposed in recent years exploits excitation of an autoionizing Rydberg state to generate molecular ions in selected quantum states. The first experimental demonstration of this idea was in the electron electric dipole moment (eEDM) search at JILA.[92] The investigators found 30% of all HfF^+ ions were produced in one rotational state following autoionization of a vibrationally excited HfF Rydberg state. Although the efficiency of this state-selected ion generation is promising, the mechanism is not clearly established. The latest generation of the eEDM experiment proposes a similar approach to generate ThF^+ ions.[170] Beyond this particular precision measurement application, there is significant interest in producing quantum state-selected molecular ions for chemical reactivity studies in cold ion traps.[134,146]

Both low-ℓ and high-ℓ Rydberg states decay by autoionization. However, the electron in a high-ℓ, core-nonpenetrating Rydberg state does not experience the complex, many-electron dynamics in the core region. This typically leads to autoionization into only a few rotational channels. Moreover, the physics of the autoionization process is enormously simplified for high-ℓ states, allowing for detailed theoretical analysis and predictive power.

In all of these applications, a requirement, or at least, a significant advantage, is the use of high-ℓ, core-nonpenetrating Rydberg states. This class of electronic

states represents a unique platform for study and control. These core-nonpenetrating states behave both like atomic Rydberg states, characterized by simplified physics and exaggerated properties, and molecules, characterized by non-radiative internal dynamics and many degrees of freedom. The unifying theme of this thesis is access to and exploitation of these special high-ℓ, core-nonpenetrating Rydberg states of molecules.

1.2 Hund's Angular Momentum Coupling Cases

When it is possible to resolve the rotational structure of a molecular transition, it is necessary to consider the interaction between the molecular rotation and the electronic motion in order to explain the spectrum. In the theory of the structure and dynamics of diatomic molecules, an extremely useful tool for understanding the angular momentum coupling in a particular electronic state is the recognition of the dominant Hund's coupling case. Each Hund's case corresponds to a complete set of basis states with which the details of the spectrum can be calculated. The choice of one coupling case over another can dramatically simplify this calculation by placing the most important matrix elements of the molecular Hamiltonian along the diagonal. Moreover, the approximately good quantum numbers, that is, the angular momentum operators that commute with the zeroth-order Hamiltonian, $\mathbf{H}^0$, and typically serve as the spectroscopic "assignment," are immediately specified by the choice of a Hund's case. Although there are six traditional cases (a)–(e) and (e'), and a multitude of more complex Rydberg-specific cases (a^+e, b^+d, etc.),[160] we will only consider in detail cases (a), (b), and (d), which are most relevant to and extensively used in this work.

The vector model of angular momentum will be used throughout. In this model, the total angular momentum $\boldsymbol{J}$ is the vector sum of the angular momenta: $\boldsymbol{R}$, $\boldsymbol{L}$, and $\boldsymbol{S}$. These correspond to the rotational angular momentum of the molecular frame, the electron orbital angular momentum, and the electron spin angular momentum, respectively. The upper case angular momentum vectors, for instance, $\boldsymbol{L}$ or $\boldsymbol{S}$, refer

Table 1.2: Hund's angular momentum coupling cases. The relative strengths of different parts of the molecular Hamiltonian determine the most appropriate Hund's case to use in calculations for a given electronic state.

Hund's Case	$\boldsymbol{H}_{el}$	$\boldsymbol{H}_{so}$	$\boldsymbol{H}_{rot}$
(a)	strong	intermediate	weak
(b)	strong	weak	intermediate
(c)	intermediate	strong	weak
(d)	intermediate	weak	strong
(e)	weak	intermediate	strong
(e')	weak	strong	intermediate

to the total angular momentum summed over all electrons with angular momentum $\boldsymbol{\ell}_i$ or $\boldsymbol{s}_i$. In other words, $\boldsymbol{L} = \sum_i \boldsymbol{\ell}_i$ and $\boldsymbol{S} = \sum_i \boldsymbol{s}_i$. This situation will break down when handling Rydberg states, in which the angular momenta of the Rydberg electron will be (almost) completely decoupled from the rest of the molecule. A shift in notation to the single-electron angular momenta will be detailed in Section 1.2.3 on Hund's case (d).

An intuitively appealing way to distinguish among the different Hund's cases is to consider the relative strength of different parts of the total molecular Hamiltonian, $\boldsymbol{H}$.[91] In particular, we will examine the pure electronic Hamiltonian, $\boldsymbol{H}_{el}$, the spin-orbit Hamiltonian, $\boldsymbol{H}_{so}$, and the rotational Hamiltonian, $\boldsymbol{H}_{rot}$. The nonspherical part of $\boldsymbol{H}_{el}$ destroys the quantum number L, lifting the degeneracy of states with different values of Λ, the projection of $\boldsymbol{L}$ on the internuclear axis. $\boldsymbol{H}_{so}$ destroys both L and S quantum numbers, causing energy splitting between states with different values of $\Omega = \Lambda + \Sigma$, where Σ is the projection of $\boldsymbol{S}$ on the internuclear axis. Finally, $\boldsymbol{H}_{rot}$ destroys the Λ and Σ quantum numbers, resulting in states separated predominantly by rotational intervals rather than electronic influences. By ranking the order of importance of these different contributions, an initial decision about the correct basis set can be made according to Table 1.2.

1.2.1 Case (a)

In Hund's case (a), represented schematically in Figure 1-3, the orbital and spin angular momenta are strongly coupled to the internuclear axis, z. Of course, since the potential of a diatomic molecule is cylindrically rather than spherically symmetric, $\boldsymbol{L}$ *cannot* be a rigorously good quantum number. However, the projection of $\boldsymbol{L}$ (and $\boldsymbol{S}$) on the internuclear axis are well-defined and labeled Λ (and Σ). The values of Λ are integers 0, 1, 2, ..., and are represented symbolically as Σ, Π, Δ, ... The two orbital and spin projection quantum numbers are summed to obtain the projection of the total electron angular momentum on the internuclear axis,

$$\Omega = \Lambda + \Sigma \tag{1.9}$$

The total angular momentum $\boldsymbol{J}$ is then formed by addition of Ω and the rotational angular momentum $\boldsymbol{R}$. Since $\boldsymbol{R}$ is, by definition, perpendicular to the internuclear axis, Ω also represents the projection of the total angular momentum on the internuclear axis. In addition, the projection of $\boldsymbol{J}$ on the space-fixed, or laboratory frame axis Z is also well-defined and denoted by M. The total wave function in case (a) is written as the product of an electronic orbital part, $|n\Lambda\rangle$, an electronic spin part, $|S\Sigma\rangle$, a vibrational part, $|v\rangle$, and a rotational part, $|J\Omega M\rangle$, where n represents all remaining state labels (e.g., electronic configuration). The electronic character of a case (a) state is compactly summarized by the symbol ${}^{2S+1}\Lambda_{\Omega}$. The approximately good angular momentum quantum numbers in case (a) are J, S, Ω, Λ, and Σ.

The real advantage of case (a) basis states is that many operators of interest are diagonal in this basis, or in other words, they commute with the rotational Hamiltonian,

$$\boldsymbol{H}_{rot} = B\boldsymbol{R}^2 \tag{1.10}$$

From our vector model, we know $\boldsymbol{J} = \boldsymbol{R} + \boldsymbol{L} + \boldsymbol{S}$, so we can evaluate the matrix elements of this Hamiltonian in case (a) by,

$$\boldsymbol{H}_{rot} = B(\boldsymbol{J} - \boldsymbol{L} - \boldsymbol{S})^2 \tag{1.11}$$

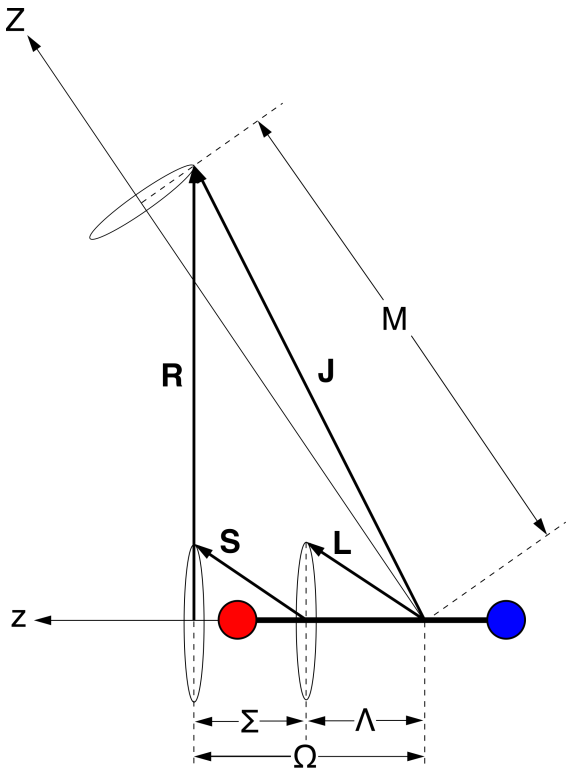

Figure 1-3: Schematic representation of Hund's case (a). $\boldsymbol{L}$ is not defined because the potential of a diatomic molecules is cylindrically, rather than spherically symmetric. $\boldsymbol{L}$ and the well-defined $\boldsymbol{S}$ are strongly coupled to the internuclear axis, and make the projections Λ and Σ. Since $\boldsymbol{R}$ is, by definition, perpendicular to the internuclear axis, the total angular momentum $\boldsymbol{J}$ makes the projection $\Omega = \Lambda + \Sigma$ on the internuclear axis. Simultaneously, the projection of $\boldsymbol{J}$ on the space-fixed Z-axis is specified by the quantum number M.

$$= B\left[\boldsymbol{J}^2 + \boldsymbol{S}^2 + \boldsymbol{L}^2 - 2\boldsymbol{J}\cdot\boldsymbol{S} - 2\boldsymbol{J}\cdot\boldsymbol{L} + 2\boldsymbol{S}\cdot\boldsymbol{L}\right] \tag{1.12}$$

$$\begin{aligned} = B\left[\boldsymbol{J}^2 + \boldsymbol{S}^2 - 2J_zL_z - 2J_zS_z + 2S_zL_z + L_z^2\right] \\ - B\left[J_+S_- + J_-S_+\right] \\ - B\left[J_+L_- + J_-L_+\right] \\ + \left[S_+L_- + S_-L_+\right] \\ + \frac{1}{2}B\left[L_+L_- + L_-L_+\right] \end{aligned} \tag{1.13}$$

In Equation 1.13, we recognize that the terms on the first line are diagonal in this basis. The term on the second line decreases Ω and Σ by one; it is called the "$\boldsymbol{S}$-uncoupling" operator and operates within a case (a) $^{2S+1}\Lambda$ multiplet. The term on the third line decreases Λ and Ω by one, and is called the "$\boldsymbol{L}$-uncoupling" operator. The term on the fourth line connects states with the same Ω, differing in Λ and Σ by one. These terms from the third and fourth lines are the off-diagonal elements responsible for "perturbations" between electronic states. The last line of Equation 1.13 can be re-written as:

$$\frac{1}{2}B\left[L_+L_- + L_-L_+\right] = B\left[L_x^2 + L_y^2\right] \tag{1.14}$$

$$= B\left[\boldsymbol{L}^2 - L_z^2\right] \tag{1.15}$$

$$= BL_\perp^2 \tag{1.16}$$

This $L_\perp^2$ term, which has no dependence on J, contributes an unknown, constant energy shift, and is typically incorporated into the electronic part of the Hamiltonian.[91] Neglecting this term, and re-writing Equation 1.13 using the relationship $J_z = L_z + S_z$, we find the case (a) rotational Hamiltonian has the form:

$$\begin{aligned} \boldsymbol{H}_{rot} = B\left[\boldsymbol{J}^2 - J_z^2 + \boldsymbol{S}^2 - S_z^2\right] \\ - B\left[J_+S_- + J_-S_+\right] - B\left[J_+L_- + J_-L_+\right] + B\left[S_+L_- + S_-L_+\right] \end{aligned} \tag{1.17}$$

From Equation 1.17, the eigenvalues of the basis states are given by $E_{rot} =$

$B\left[J(J+1)-\Omega^2+S(S+1)-\Sigma^2\right]$. This result is obtained from the well known angular momentum operators in the case (a) basis, which are summarized below in atomic units.

$$\langle J\Omega M|\boldsymbol{J}^2|J\Omega M\rangle = J(J+1) \tag{1.18}$$

$$\langle J\Omega M|J_z|J\Omega M\rangle = \Omega \tag{1.19}$$

$$\langle J\Omega M|J_Z|J\Omega M\rangle = M \tag{1.20}$$

$$\langle J\Omega \mp 1M|J_\pm|J\Omega M\rangle = \left[J(J+1)-\Omega(\Omega \mp 1)\right]^{1/2} \tag{1.21}$$

$$\langle S\Sigma|\boldsymbol{S}^2|S\Sigma\rangle = S(S+1) \tag{1.22}$$

$$\langle S\Sigma|S_z|S\Sigma\rangle = \Sigma \tag{1.23}$$

$$\langle S\Sigma \pm 1|S_\pm|S\Sigma\rangle = \left[S(S+1)-\Sigma(\Sigma \pm 1)\right]^{1/2} \tag{1.24}$$

$$\langle \Lambda|L_z|\Lambda\rangle = \Lambda \tag{1.25}$$

The subscripted operators O_z and O_Z give projections onto the molecule-fixed z-axis and the space-fixed Z-axis, respectively, and the projections onto the two additional axes are not simultaneously specified. This indeterminacy is represented in the vector model as precession of the angular momentum vector about an axis; for instance, $\boldsymbol{J}$ precesses about the Z-axis because we can only construct states that are simultaneous eigenfunctions of $\boldsymbol{J}^2$ and any one component of $\boldsymbol{J}$, traditionally, $J_Z = M$. The operators $O_\pm = O_x \pm iO_y$ are ladder operators, which connect states with the same value of angular momentum, but different projections. Note the phase convention that gives different forms for $J_\pm$ and $S_\pm$. This can be traced back to the anomalous commutation relations of the molecule-fixed projection operators $J_{x,y,z}$:

$$[J_x, J_y] = -iJ_z \tag{1.26}$$

This feature (or flaw) arises as a result of our simultaneous specification of the eigenvalues of both J_z and J_Z for the rotational wave function.[163]

1.2.2 Case (b)

When dealing with ${}^{2S+1}\Sigma^{+/-}$ states, in which there is no orbital angular momentum, a case (a) treatment is unnecessary and the much simpler case (b) rotational Hamiltonian can be used. The vector coupling model for case (b) is shown in Figure 1-4. In this case, the spin of the electron is no longer coupled to the internuclear axis. Thus, the projection of $\boldsymbol{L}$ on the internuclear axis, $\Lambda\hat{z}$, couples to the molecular frame rotation, $\boldsymbol{R}$, to form the angular momentum $\boldsymbol{N}$, which is the total angular momentum neglecting spin. Since $\boldsymbol{R}$ is perpendicular to the internuclear axis, the projection of $\boldsymbol{N}$ on the internuclear axis is Λ. The electronic spin is coupled next to form the total angular momentum $\boldsymbol{J} = \boldsymbol{N} + \boldsymbol{S}$. Note that as a result of this secondary coupling, the projection of J_z is not diagonal in the case (b) basis and Ω is not specified. The approximately good angular momentum quantum numbers in case (b) are J, S, N, and Λ.

We can evaluate the rotational Hamiltonian in case (b) exactly as before,

$$\begin{aligned}
\boldsymbol{H}_{rot} &= B\boldsymbol{R}^2 && (1.27)\\
&= B(\boldsymbol{N} - \boldsymbol{L})^2 && (1.28)\\
&= B\left[\boldsymbol{N}^2 + \boldsymbol{L}^2 - 2\boldsymbol{N}\cdot\boldsymbol{L}\right] && (1.29)\\
&= B\left[\boldsymbol{N}^2 - 2N_zL_z + L_z^2\right] \\
&\quad - B\left[N_+L_- + N_-L_+\right] \\
&\quad + \frac{1}{2}B\left[L_+L_- + L_-L_+\right] && (1.30)\\
&= \left[\boldsymbol{N}^2 - N_z^2\right] - B\left[N_+L_- + N_-L_+\right] && (1.31)
\end{aligned}$$

We recognize the third line of Equation 1.30 as the constant term, $L_\perp^2$, defined in Equation 1.16, and neglect it in the rotational Hamiltonian. In the last step, we use the fact that $N_z = L_z = \Lambda$. The first term of Equation 1.31 is diagonal in the case (b) basis and allows us to find the zeroth-order rotational energy, $E_{rot} = B\left[N(N+1) - \Lambda^2\right]$. Note as well that Equation 1.31 has no $\boldsymbol{S}$ dependence and so, to zeroth order, every rotational state in case (b) is $2S+1$ degenerate. In fact, this

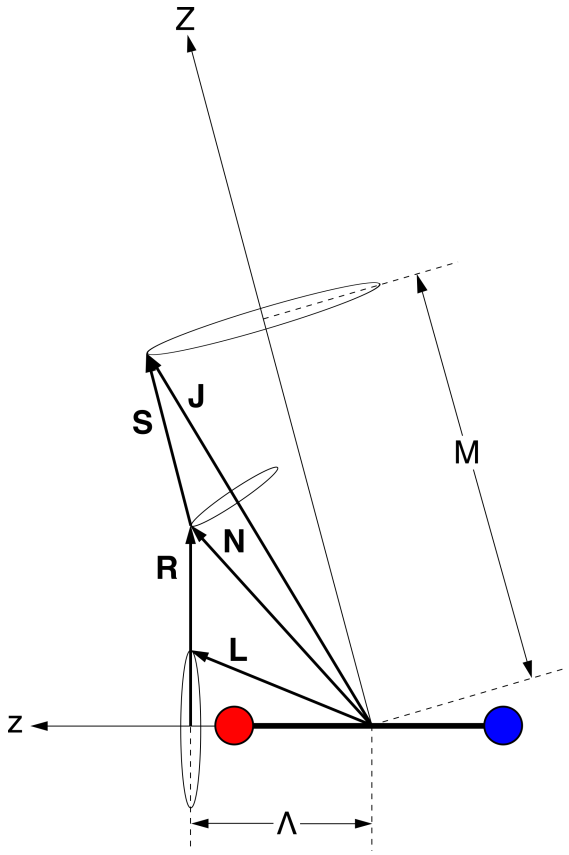

Figure 1-4: Schematic representation of Hund's case (b). Again, $\boldsymbol{L}$ is not well-defined because the molecular potential is not spherically symmetric, but $\boldsymbol{L}$ precesses rapidly around the internuclear axis, making the projection Λ. The total angular momentum neglecting spin, $\boldsymbol{N}$, is defined by the coupling of $\Lambda\hat{z}$ and the molecular frame rotation, $\boldsymbol{R}$. Lastly, the spin, $\boldsymbol{S}$, couples with $\boldsymbol{N}$ to form the total angular momentum, $\boldsymbol{J}$. The nutation of $\boldsymbol{N}$ and $\boldsymbol{S}$ about $\boldsymbol{J}$ averages out the direction of these component vectors so that only $\boldsymbol{J}$ makes a well-defined projection on the space-fixed axis, $J_Z = M$.

degeneracy is often lifted by terms in the molecular Hamiltonian other than $\boldsymbol{H}_{rot}$, such as spin-rotation coupling. This will be dealt with in a following chapter on the A $^2\Sigma^+$ state of NO. The cost for the simplicity of the rotational Hamiltonian in Hund's case (b) is the loss of S_z as a diagonal operator.

1.2.3 Case (d)

Hund's case (d) is perhaps the most important of the angular momentum coupling cases for the work presented in this thesis. The reason for this is simply that it is an excellent basis set with which to calculate properties of Rydberg states. When an electron is excited to some high-n, high-ℓ Rydberg level, it does not closely approach the ion-core and so it experiences an approximately spherical potential. In other words, $\boldsymbol{H}_{el}$ is weak, while the rotation of the ion-core strongly affects the level structure. The vector coupling scheme is shown in Figure 1-5. Since, the electron does not strongly "feel" the cylindrical symmetry of the ion-core, the orbital angular momentum is coupled instead to the axis of rotation. Similar to case (b), we first form the total angular momentum neglecting spin, $\boldsymbol{N} = \boldsymbol{R} + \boldsymbol{L}$. The total angular momentum $\boldsymbol{J}$ is then formed by coupling $\boldsymbol{S}$ to $\boldsymbol{N}$. It should be pointed out that, in general, one should choose an appropriate Hund's coupling case to describe the ion-core as well as the state of the Rydberg electron. There may be electronic spin and orbital angular momentum, $\boldsymbol{S}^+$ and $\boldsymbol{L}^+$, associated with the ion-core that require explicit treatment. Considering the goal of describing Rydberg states of NO, we restrict the discussion to ion-cores with $^1\Sigma^+$ ground states, in which $\boldsymbol{J}^+ = \boldsymbol{R}$. This means we will discuss only the simplest form of Hund's case (d), which has approximately good quantum numbers J, S, N, R, and L. In the limit of high rotation, L_R also becomes a good quantum number, specifying the projection of $\boldsymbol{L}$ on $\boldsymbol{R}$. At all times, however, L_R can be used as a state index that exactly specifies the value $L_R = N - R$.[91] As promised, it is useful at this point to slightly modify our notation for the orbital angular momentum. Our discussion of case (d) has focused almost exclusively on Rydberg states, where a single electron is excited to a high energy orbital. As such, we should switch from the multi-electron $\boldsymbol{S}$, $\boldsymbol{L}$, and L_R to the single-electron $\boldsymbol{s}$, $\boldsymbol{\ell}$, and ℓ_R. This is the

notation that will be used throughout the remainder of this thesis.

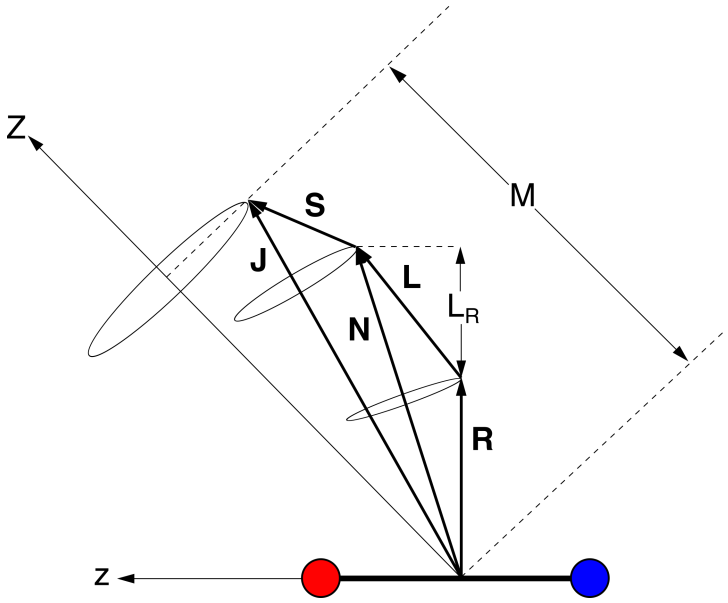

Figure 1-5: Schematic representation of Hund's case (d). Unlike case (a) and case (b), the weak interaction between the Rydberg electron and the ion-core leads to the coupling of $\boldsymbol{L}$ with the ion-core rotation, $\boldsymbol{R}$, to form $\boldsymbol{N}$. This re-coupling means the projection of $\boldsymbol{L}$ on the internuclear axis, Λ, is no longer defined. The projection of $\boldsymbol{L}$ on $\boldsymbol{R}$, called L_R, is only well-defined in the limit of high rotation. The spin, $\boldsymbol{S}$, is lastly coupled with $\boldsymbol{N}$ to give the total angular momentum, $\boldsymbol{J}$, with space-fixed projection, $J_Z = M$. The vector nutation indicated by circles results in an averaging out of the direction of the angular momentum vectors relative to the internuclear axis so that no body-fixed projection quantum numbers are defined.

The rotational Hamiltonian in case (d) is trivial to evaluate:

$$\boldsymbol{H}_{rot} = B^{+}\boldsymbol{R}^2 \tag{1.32}$$

where B^+ is the rotational constant of the ion-core rather than the neutral molecule. This expression immediately gives the zeroth-order rotational energy, $E_{rot} = B^{+}R(R+1)$. If we can specify $\ell_R = N - R$, then we can re-write the rotational energy as

$$E_{rot} = B^{+}\left[N(N+1) - 2N\ell_R - \ell_R + \ell_R^2\right] \tag{1.33}$$

This expression is practically useful because rotational combination differences, the energy difference of two spectroscopic lines originating or terminating on the same

energy level, rigorously determine N rather than R. When placed on a reduced term value plot,[a] the assigned levels fall along a line with slope $-2\ell_R$, thus allowing the assignment of R as well.

For Rydberg states that obey Hund's case (d) coupling, we use a compact notation to uniquely label every state: $n\ell R_N$. In this Rydberg "term symbol," n is the principal quantum number, ℓ is the orbital angular momentum of the Rydberg electron, R is the rotational quantum number of the ion-core, and N is the spinless total angular momentum. This notation exactly specifies one Rydberg state (neglecting spin), which, for $^1\Sigma^+$ ion-cores, has parity $p = R + \ell$, and allowed values of N given by:

$$|R - \ell| \leq N \leq R + \ell \tag{1.34}$$

1.2.4 Transforming between Hund's cases

Having chosen one Hund's case for the description of a particular electronic state, we are not doomed to live in that basis set forever. The coupling cases can be inter-related to one another by a unitary transformation of the particular basis. The transformation from a coupling case (β) to a coupling case (α) is written as

$$\boldsymbol{U}^{\alpha}_{\beta} = \langle \alpha | \beta \rangle \tag{1.35}$$

where the braket represents the projection of the initial basis function $|\alpha\rangle$ in coupling case (α) on the final basis function $|\beta\rangle$ in the coupling case (β). For two coupling cases, which differ by the coupling of only two angular momentum vectors, such as (a)→(b) or (b)→(d), this projection is naively given by a Clebsch-Gordan (C-G) coefficient $\langle j_1 m_1 j_2 m_2 | j_3 m_3 \rangle$, as in atomic cases. Thus, it is straightforward to perform the transformation (a)→(d) in two steps by first converting to case (b).

[a] A reduced term value plot is generated by subtracting the zeroth-order rotational energy from the total energy of an observed level and plotting this value against a rigorously good quantum number. These plots are extremely useful for identifying the quantum numbers that are pattern-forming.

Case (a) to case (b)

The transformation between cases (a) and (b) is frequently encountered since the transition dipole matrix element for a molecule is most conveniently written in a case (a) basis. The important angular momenta in this transformation are $\boldsymbol{N}$, $\boldsymbol{S}$, and $\boldsymbol{J}$, which are related by

$$\boldsymbol{J} = \boldsymbol{N} + \boldsymbol{S} \tag{1.36}$$

We immediately encounter a problem in writing down the transformation matrix as a result, once again, of the anomalous commutation relations of $\boldsymbol{J}$ in the molecule-fixed frame. In fact, all operators that describe rotations of the molecule-fixed coordinate system relative to the lab frame (e.g., $\boldsymbol{R}$, $\boldsymbol{N}$, $\boldsymbol{J}$,...) obey anomalous commutation rules. Thus, our problem is with $\boldsymbol{S}$. Following Van Vleck's procedure, we can find a consistent coupling scheme by writing the relationship as

$$\boldsymbol{J} - \boldsymbol{S} = \boldsymbol{N} \tag{1.37}$$

$$\boldsymbol{J} + \tilde{\boldsymbol{S}} = \boldsymbol{N} \tag{1.38}$$

where $\tilde{\boldsymbol{S}} = -\boldsymbol{S}$ is the reversed spin angular momentum with projection $-\Sigma$. This corrects the inconsistency because $\tilde{\boldsymbol{S}}$ now obeys the same anomalous commutation rules,

$$\left[\tilde{S}_i, \tilde{S}_j\right] = [-S_i, -S_j] \tag{1.39}$$

$$= (-S_i)(-S_j) - (-S_j)(-S_i) \tag{1.40}$$

$$= S_i S_j - S_j S_i \tag{1.41}$$

$$= iS_k \tag{1.42}$$

$$= -i\tilde{S}_k \tag{1.43}$$

Now we can write out the transformation matrix as previously described.

$$\boldsymbol{U}^N_{\Omega\Sigma} = \langle N|\Omega\Sigma\rangle \tag{1.44}$$

$$= \langle J\Omega \tilde{S} - \Sigma | N\Lambda \rangle \tag{1.45}$$

$$= (-1)^{J-S+\Lambda} \left[2N+1\right]^{1/2} \begin{pmatrix} J & S & N \\ \Omega & -\Sigma & -\Lambda \end{pmatrix} \tag{1.46}$$

In the second step, we have re-expressed the C-G coefficient in terms of the more convenient 3j symbol.

This procedure represents just one approach in addressing the anomalous commutation of molecule-fixed operators, which act on the rotational degree of freedom of the molecule. Another approach, championed by Brown and Howard,[22] is to evaluate all operators in a space-fixed frame. The magnitude of the transformation matrix elements will end up essentially identical, except for a phase factor.[b] We start this procedure by writing out the case (b) wavefunction in the decoupled space-fixed representation.

$$|N\Lambda SJM\rangle = \sum_{M_N, M_S} (-1)^{N-S+M} \left[2J+1\right]^{1/2} \begin{pmatrix} N & S & J \\ M_N & M_S & -M \end{pmatrix} |NM_N\Lambda\rangle \, |SM_S\rangle \tag{1.47}$$

where M_P is the space-fixed projection (Z-axis) of the operator $\boldsymbol{P}$. The lab frame spin wavefunction $|SM_S\rangle$ can be related to the body frame wavefunction $|S\Sigma\rangle$ by

$$|SM_S\rangle = \sum_{\Sigma} \left[\mathcal{D}^{(S)}_{M_S\Sigma}\right]^* |S\Sigma\rangle \tag{1.48}$$

where $\mathcal{D}^J_{M'M}(\phi, \theta, \chi)$ is the general symbol for a Wigner rotation matrix. The Euler angles will be supressed throughout the remainder of the derivation. Now, our task is to find the coupling element $\langle SM_S| \langle N\Lambda M_N | J\Omega M\rangle |S\Sigma\rangle$. Each rotational wavefunc-

[b] The following may seem like a lot of work for "just" a phase convention, since the phase is essentially arbitrary anyway. Zare cutely points out that a daily encounter with phase conventions is the decision to drive on the right or left side of the road. "As long as you and everyone else are consistent in this choice, it certainly does not matter, but inconsistency can be detrimental to your health!"[163] By being rigorous in our initial choice of phase, the results presented here can more easily be applied to other situations and compared with the literature.

tion can also be written in terms of a Wigner rotation matrix:

$$|JKM\rangle = \left[\frac{2J+1}{8\pi^2}\right]^{1/2} \left[\mathcal{D}^{(J)}_{MK}\right]^* = (-1)^{M-K} \left[\frac{2J+1}{8\pi^2}\right]^{1/2} \mathcal{D}^{(J)}_{-M-K} \tag{1.49}$$

where the angular momentum $\boldsymbol{J}$ makes the projections M and K on the lab frame Z-axis and body frame z-axis, respectively. The coupling element is then written as

$$\begin{aligned}
&\langle SM_S| \langle N\Lambda M_N|J\Omega M\rangle |S\Sigma\rangle \\
&= \frac{\sqrt{(2N+1)(2J+1)}}{8\pi^2} \int \mathcal{D}^{(S)}_{M_S\Sigma} \mathcal{D}^{(N)}_{M_N\Lambda} \left[\mathcal{D}^{(J)}_{M\Omega}\right]^* \mathrm{d}(\phi,\theta,\chi) && (1.50)\\
&= (-1)^{M-\Omega} \frac{\sqrt{(2N+1)(2J+1)}}{8\pi^2} \int \mathcal{D}^{(S)}_{M_S\Sigma} \mathcal{D}^{(N)}_{M_N\Lambda} \mathcal{D}^{(J)}_{-M-\Omega} \mathrm{d}(\phi,\theta,\chi) && (1.51)\\
&= (-1)^{M-\Omega} \sqrt{(2N+1)(2J+1)} \begin{pmatrix} S & N & J \\ M_S & M_N & -M \end{pmatrix} \begin{pmatrix} S & N & J \\ \Sigma & \Lambda & -\Omega \end{pmatrix} && (1.52)
\end{aligned}$$

Now that we have determined the projection of the space-fixed case (b) wavefunction on the molecule-fixed case (a) wavefunction, we can use this coupling element to determine the projection of the molecule-fixed case (b) wavefunction on the molecule-fixed case (a) wavefunction:

$$\begin{aligned}
\langle N|\Omega\Sigma\rangle &= \sum_{M_S,M_N} (-1)^{N-S+M+M-\Omega} \sqrt{2N+1}(2J+1) \begin{pmatrix} N & S & J \\ M_N & M_S & -M \end{pmatrix} \\
&\qquad \times (-1)^{N+S+J} \begin{pmatrix} N & S & J \\ M_N & M_S & -M \end{pmatrix} (-1)^{N+S+J} \begin{pmatrix} N & S & J \\ \Lambda & \Sigma & -\Omega \end{pmatrix} && (1.53)\\
&= (-1)^{N+S-\Omega} \left[2N+1\right]^{1/2} \begin{pmatrix} J & S & N \\ \Omega & -\Sigma & -\Lambda \end{pmatrix} \\
&\qquad \times \sum_{M_S,M_N} (2J+1) \begin{pmatrix} N & S & J \\ M_N & M_S & -M \end{pmatrix} \begin{pmatrix} N & S & J \\ M_N & M_S & -M \end{pmatrix} && (1.54)\\
&= (-1)^{N-S+\Omega} \left[2N+1\right]^{1/2} \begin{pmatrix} J & S & N \\ \Omega & -\Sigma & -\Lambda \end{pmatrix} && (1.55)\\
&= (-1)^{N-J+\Sigma} \langle J\Omega S-\Sigma|N\Lambda\rangle && (1.56)
\end{aligned}$$

where, in the second-to-last step, we have used the orthonormality of 3j symbols to simplify the result. In the final step, the coupling element is written in terms of a C-G coefficient and it becomes obvious that this result is identical to our previous result in Equation 1.45, obtained by the reversed angular momentum method, with the exception of the phase factor.

Case (b) to case (d)

We encounter the same difficulty in this basis set transformation as dealt with in the previous section. The relevant angular momentum vectors are given by $\boldsymbol{N} = \boldsymbol{R}+\boldsymbol{\ell}$, and we are faced with the ambiguity of the anomalous commutation of $\boldsymbol{N}$ and $\boldsymbol{R}$ in the molecule-fixed frame. Van Vleck's reversed angular momentum method could be applied again:

$$\boldsymbol{N} - \boldsymbol{\ell} = \boldsymbol{R} \tag{1.57}$$

$$\boldsymbol{N} + \tilde{\boldsymbol{\ell}} = \boldsymbol{R} \tag{1.58}$$

where $\tilde{\boldsymbol{\ell}}$ is the reversed orbital angular momentum with projection quantum number $-\Lambda$. The transformation matrix element is then just the C-G coefficient $\langle N\Lambda\tilde{\ell} - \Lambda|R0\rangle$. Instead, we take the more rigorous approach outlined above by explicitly evaluating the matrix element in the lab frame where all operators obey normal commutation rules. The decoupled space-fixed case (d) wavefunction is written as

$$|R\ell NM\rangle = \sum_{M_\ell, M_R} (-1)^{\ell - R + M} \left[2N+1\right]^{1/2} \begin{pmatrix} \ell & R & N \\ M_\ell & M_R & -M \end{pmatrix} |R0M_R\rangle \, |\ell M_\ell\rangle \tag{1.59}$$

Again, we can connect the lab frame electronic wavefunction $|\ell M_\ell\rangle$ to the body frame wavefunction $|\ell\Lambda\rangle$ by

$$|\ell M_\ell\rangle = \sum_{\Lambda} \left[\mathcal{D}^{(\ell)}_{M_\ell\Lambda}\right]^* |\ell\Lambda\rangle \tag{1.60}$$

Now, we can evaluate a matrix element similar to the case(a)-case(b) transformation:

$$\begin{aligned}
&\langle \ell M_\ell | \langle R0 M_R | N \Lambda M \rangle | \ell \Lambda \rangle \\
&= \frac{\sqrt{(2R+1)(2N+1)}}{8\pi^2} \int \mathcal{D}^{(\ell)}_{M_\ell \Lambda} \mathcal{D}^{(R)}_{M_R 0} \left[\mathcal{D}^{(N)}_{M\Lambda} \right]^* \mathrm{d}(\phi, \theta, \chi) && (1.61) \\
&= (-1)^{M-\Lambda} \frac{\sqrt{(2R+1)(2N+1)}}{8\pi^2} \int \mathcal{D}^{(\ell)}_{M_\ell \Lambda} \mathcal{D}^{(R)}_{M_R 0} \mathcal{D}^{(N)}_{-M-\Lambda} \mathrm{d}(\phi, \theta, \chi) && (1.62) \\
&= (-1)^{M-\Lambda} \sqrt{(2R+1)(2N+1)} \begin{pmatrix} \ell & R & N \\ M_\ell & M_R & -M \end{pmatrix} \begin{pmatrix} \ell & R & N \\ \Lambda & 0 & -\Lambda \end{pmatrix} && (1.63)
\end{aligned}$$

This coupling element can now be used to evaluate the projection of the molecule-fixed case (d) wavefunction on the molecule-fixed case (b) wavefunction:

$$\begin{aligned}
\langle R|\Lambda\rangle &= \sum_{M_\ell, M_R} (-1)^{\ell - R + M + M - \Lambda} \sqrt{2R+1} (2N+1) \begin{pmatrix} \ell & R & N \\ M_\ell & M_R & -M \end{pmatrix} \\
&\quad \times \begin{pmatrix} \ell & R & N \\ M_\ell & M_R & -M \end{pmatrix} \begin{pmatrix} \ell & R & N \\ \Lambda & 0 & -\Lambda \end{pmatrix} && (1.64) \\
&= (-1)^{\ell - R - \Lambda} \left[2R+1\right]^{1/2} (-1)^{\ell + R + N} \begin{pmatrix} R & \ell & N \\ 0 & \Lambda & -\Lambda \end{pmatrix} \\
&\quad \times \sum_{M_\ell, M_R} (2N+1) \begin{pmatrix} \ell & R & N \\ M_\ell & M_R & -M \end{pmatrix} \begin{pmatrix} \ell & R & N \\ M_\ell & M_R & -M \end{pmatrix} && (1.65) \\
&= (-1)^{N-\Lambda} \left[2R+1\right]^{1/2} \begin{pmatrix} R & \ell & N \\ 0 & \Lambda & -\Lambda \end{pmatrix} && (1.66) \\
&= (-1)^{\ell+\Lambda} \langle N \Lambda \ell - \Lambda | R 0 \rangle && (1.67)
\end{aligned}$$

Again, we see that this result is only different by a phase factor from our naive expectation of the matrix element's value. Going one step further, we can take explicit consideration of the parity, to write this element as:

$$\langle R|\Lambda\rangle = (-1)^{N-\Lambda} \left[\frac{1 + (-1)^{p+R+\ell}}{2} \right] \left[\frac{2(2R+1)}{1+\delta_{\Lambda 0}} \right]^{1/2} \begin{pmatrix} R & \ell & N \\ 0 & \Lambda & -\Lambda \end{pmatrix} \quad (1.68)$$

where p is the parity and $\delta_{\Lambda 0}$ is a Kronecker delta.

1.2.5 Transition intensities

The transition intensity between two electronic states is easily evaluated using Hund's case (a) basis states. The transition dipole operator in the space-fixed frame is written in terms of the molecule-fixed components as:

$$\mu(1,r) = \sum_q \left[D^{(1)}_{rq}\right]^* \mu(1,q) \tag{1.69}$$

where the number 1 indicates a rank 1 tensor, r refers to the space-fixed component of interest and, in the experiments described here, corresponds to the polarization of the radiation. For two case (a) basis states, $|J\Omega M\Lambda v S\Sigma\rangle$, with vibronic part $|\Lambda v\rangle$ and rotational part $|J\Omega M\rangle$, we can now write the transition dipole matrix element, recognizing that the electromagnetic radiation does not act directly on the spin part of the wavefunction:

$$\begin{aligned}
&\langle J\Omega M\Lambda v S\Sigma|\mu(1,r)|J'\Omega' M'\Lambda' v' S'\Sigma'\rangle \\
&\quad = \left\langle J\Omega M\Lambda v S\Sigma \left| \sum_q \left[D^{(1)}_{rq}\right]^* \mu(1,q) \right| J'\Omega' M'\Lambda' v' S'\Sigma' \right\rangle && (1.70)\\
&\quad = \sum_q \left\langle J\Omega M \left| \left\langle \Lambda v \left| \left[D^{(1)}_{rq}\right]^* \mu(1,q) \right| J'\Omega' M' \right\rangle \right| \Lambda' v' \right\rangle && (1.71)\\
&\quad = \sum_q \left\langle J\Omega M \left| \left[D^{(1)}_{rq}\right]^* \right| J'\Omega' M' \right\rangle \langle \Lambda v|\mu(1,q)|\Lambda' v'\rangle && (1.72)\\
&\quad = \sum_q \frac{\left[(2J+1)(2J'+1)\right]^{1/2}}{8\pi^2} \int D^{(J)}_{M\Omega} \left[D^{(1)}_{rq}\right]^* \left[D^{(J')}_{M'\Omega'}\right]^* \mathrm{d}\boldsymbol{\Omega} \\
&\qquad \times \langle \Lambda|\mu(1,q)|\Lambda'\rangle \langle v|v'\rangle && (1.73)\\
&\quad = \sum_q \frac{\left[(2J+1)(2J'+1)\right]^{1/2}}{8\pi^2} (-1)^{M-\Omega} \left[\int D^{(J)}_{-M-\Omega} D^{(1)}_{rq} D^{(J')}_{M'\Omega'} \mathrm{d}\boldsymbol{\Omega}\right]^* \\
&\qquad \times \langle \Lambda|\mu(1,q)|\Lambda'\rangle \langle v|v'\rangle && (1.74)
\end{aligned}$$

$$= \sum_q (-1)^{M-\Omega} \left[(2J+1)(2J'+1)\right]^{1/2} \begin{pmatrix} J & 1 & J' \\ M & -r & -M' \end{pmatrix} \begin{pmatrix} J & 1 & J' \\ \Omega & -q & -\Omega' \end{pmatrix}$$
$$\times \langle \Lambda | \mu(1,q) | \Lambda' \rangle \langle v | v' \rangle \tag{1.75}$$

In Equation 1.73, we assumed a separation of the electronic and vibrational wavefunctions, where the square of the overlap integral is the Franck-Condon factor, $FC = \langle v|v' \rangle^2$. We will typically ignore this factor throughout since we are mainly considered with rotational line intensities within a single vibronic band. The relative polarization of the radiation fields determines r, the projection of the photon angular momentum on the laboratory Z-axis: $r = \pm 1$ for left- and right-handed circular polarization, respectively, and $r = 0$ for linear polarization along the Z-axis. The molecule-fixed component, q, is determined by $q = \Lambda - \Lambda'$, where $q = 0$ is a "parallel" transition and $q = \pm 1$ is a "perpendicular" transition. To calculate the total rotational line intensity, Equation 1.75 is squared and then summed over the relevant M values. Equation 1.75 will serve as the starting point for the calculation of all transition intensities in this work. While only the ground X $^2\Pi_{1/2}$ state of NO is a near case (a) state, the unpaired Rydberg electron in NO means there will be spin doublets to consider in every electronic state that we will encounter. As pointed out by Petrović and Field,[122] a rigorous treatment of the line intensities in a multiple resonance spectroscopic experiment requires explicit consideration of the spin doublets, even if they are unresolved in the experiment. Since the dye lasers used in most of the described experiments have only modest coherence properties, we assume that all unresolved spin doublets are excited incoherently. Thus, just as for magnetic sub-levels, the transition intensities for each spin component, given by the squares of Equation 1.75, are summed to obtain the total transition line intensity.

1.3 Outline

Chapter 2 presents the experimental tools used throughout this thesis. We describe the operation of our traditional pulsed dye lasers and the construction and

testing of a high-coherence laser source, based on pulsed amplification of a continuous-wave laser. We discuss the theory and technical details of chirped-pulse millimeter-wave spectroscopy, and its particular advantages in the study of Rydberg states. Finally, the physics of our atomic and molecular sources, supersonic jets and buffer-gas cooled beams, is reviewed.

In Chapter 3, we describe the development of a coherent population transfer technique, optical-millimeter-wave stimulated Raman adiabatic passage (optical-mmW STIRAP), to move population from a low-lying valence state to a high-ℓ Rydberg state *via* a potentially lossy intermediate state. This situation describes a typical molecule, in which optical access is usually available to predissociated, low-ℓ Rydberg states, and one additional unit of angular momentum is needed to gain access to a long-lived, core-nonpenetrating state. Our proof-of-principle demonstration is performed on an atomic beam of Ca, which allows for quantitative characterization of the mechanism and efficiency of population transfer. This result opens the door wide to systematic study and control of the Rydberg states of many molecular species.

In Chapter 4, we discuss our chirped-pulse millimeter-wave spectroscopy experiments on ng Rydberg states of nitric oxide, only the second molecule studied by this method. A three-color triple-resonance laser excitation *via* the low-lying $4f$ state is critical to populating these core-nonpenetrating states. The extreme electric field sensitivity of high-n, high-ℓ Rydberg states results in line broadening, observation of "forbidden" transitions, and superradiant emission. We explain that all of these observations arise due to the Stark effect. This chapter also describes a mechanistically explicit, long-range electrostatic model of Rydberg energy level structure and the ways in which our high-ℓ mmW spectra allow new insights into this model.

Autoionization of NO Rydberg states is the subject of Chapter 5. A long-range electrostatic model again serves as our theoretical framework. We demonstrate that ng states decay predominantly by autoionization consistent with our model predictions. We interpret previous work on nf states in light of our autoionization model and suggest that, in spite of the rapid predissociative decay of nf states, autoionization is controlled mainly by long-range forces. Finally, this chapter concludes by

prescribing specific schemes to generate state-selected molecular NO^+ ions.

A brief summary of these results and outlook for new developments appears in Chapter 6.

Chapter 2

Experimental methods

2.1 Laser sources

Rydberg states of atoms and molecules lie $1/2n^2$, in atomic units, below the ionization limit, which is typically several eV above the ground state. As a reference, most small organic molecules have ionization potentials of about 10 eV.[34] Classical spectroscopy of Rydberg states involved observing emission spectra from electric discharge sources[33] or absorption spectra from deep UV lamp sources.[79] To perform state-selective preparation of Rydberg states, narrowband laser radiation is required. Moreover, by using a multiple step laser excitation scheme, we can exert additional control over the choice of Rydberg state to investigate, for instance, by increasing the value of ℓ beyond what is accessible from the ground electronic state configuration. In this work, two types of tunable lasers are used: Nd:YAG-pumped pulsed dye lasers and pulse-amplified CW lasers.

2.1.1 Pulsed dye lasers

Pulsed dye lasers have been the workhorse of molecular electronic spectroscopy for decades. Using an organic dye as the lasing medium and a high-power pulsed laser as the pump, this type of laser allows for near continuous frequency coverage across the visible and near-infrared (NIR) spectrum, from approximately 400 to 900 nm,

with appropriate selection of the dye and pump wavelength. The high-energy, pulsed output of a dye laser is ideal for performing non-linear optical frequency conversion, which further extends the operating range of these lasers into the UV and infrared regions.

In all of our experiments, the pump laser radiation is provided by solid state Nd:YAG lasers with a 20 Hz repetition rate (Spectra Physics, GCR-290 and PRO-270). The second harmonic (532 nm) or third harmonic (355 nm) of the laser is used depending on the desired dye laser frequency. The 1064, 532, and 355 nm beams have pulse widths of approximately 10, 8, and 7 ns, respectively. In most cases, the Nd:YAG laser is injection-seeded, meaning a CW laser locked to the cavity length seeds the generation of the pulsed light. This process dramatically narrows the linewidth of the fundamental from ~ 1 cm^{-1} to ~ 0.003 cm^{-1} by selecting a single cavity mode for lasing. If an Nd:YAG wavelength is used in a later frequency conversion step, the ~ 1 cm^{-1} linewidth would reduce the efficiency of this process and lead to an unacceptably large bandwidth for our experiments. An additional effect of this process is to produce a smooth temporal profile for the pulsed output. When operating without injection seeding, many longitudinal modes of the cavity are amplified by laser operation and the beating between these slightly different frequencies produces intensity variation within the laser pulse. Since the temporal shape of the dye laser pulse closely matches the pump laser pulse, this intensity variation would be evident in the dye laser output as well.

Three types of dye lasers are used in this work: a Lambda Physik Scanmate 2E, a Sirah Cobra-Stretch, and a Continuum ND6000. The Sirah and Continuum lasers are dual grating systems. The use of two gratings as wavelength selectors reduces the effective bandwidth of the laser output to ~ 0.04 cm^{-1}, however two to three longitudinal cavity modes operate simultaneously. The Lambda Physik laser is a single grating laser with a pulsed output bandwidth of ~ 0.1 cm^{-1}. Although not used in the experiments described here, an intracavity etalon can be installed in this laser to reduce the bandwidth to ~ 0.03 cm^{-1}. Unlike the dual-grating systems, when operating with an intracavity etalon, each pulse of this laser typically occurs

in a single mode with linewidth ~ 0.008 cm^{-1}, though this frequency will drift and eventually mode hop within the specified bandwidth of ~ 0.03 cm^{-1}. Early coherent population transfer experiments in the Field group employed the Lambda Physik laser because of this unusual characteristic, though it was found that the coherence properties were still too poor to achieve the desired coherent population transfer.[60]

2.1.2 Pulse-amplified CW lasers

The development of a pulse-amplified CW laser system was motivated by the goal of optical-mmW STIRAP, discussed in Chapter 3. As mentioned above, pulsed dye lasers, even the nearly single-mode operation of the Lambda Physik laser lacked the necessary coherence properties. In order to generate near Fourier-transform limited, high-energy laser pulses, we turned to pulsed amplification. This technique uses a narrowband CW laser source to seed light amplification in dye cells pumped by a pulsed Nd:YAG laser, thus producing pulse energies similar to a simple dye laser, but with a linewidth close to the Fourier transform limit.

A schematic of the pulse amplification setup is shown in Figure 2-1. A tunable CW Ti:Sapphire laser (MSquared Solstis) produces the seed light from ~ 725 to ~ 975 nm. This laser light is launched into a polarization-maintaining optical fiber and approximately 100 mW of power is delivered to the amplifier. Optical isolators on each end of the fiber prevent feedback from the amplification stages to the laser. Such feedback could destabilize the single-mode operation of the laser or cause damage to the optics due to the high pulse energy. Significantly, the fiber improves the pointing stability of the seed laser relative to a path through free space, so realignment of the seed laser is rarely necessary.

The amplifier setup (Lioptec, custom) is composed of two rectangular dye cells and one Bethune (capillary) cell. Each cell is pumped in stages in the transverse direction by progressively more power from the second harmonic of a Nd:YAG laser (Spectra Physics, LAB-170, 10 Hz). After each of the first two cells, spatial filters serve to transmit the desired laser radiation, while reducing the amplified spontaneous emission (ASE), which propagates with slightly different wavevectors, from reaching

the next amplification stage. The ratio of lasing to ASE content in the pulsed output of each stage can be estimated by comparing, on a fast photodiode, the signal when the seed laser is unblocked and blocked. This is not an exact measurement since the presence of the seed radiation will certainly reduce the ASE content relative to what is observed without any seed radiation present. However, we have found this method useful in practice for improving the amplifier alignment.

In general, the alignment is improved when the overlap between the seed laser, the pump laser, and the dye stream is optimized. This requires matching the seed laser beam size to the width of the dye stream, while using cylindrical lenses to expand the pump laser along the direction of the seed laser propagation. In addition, it is necessary to focus the pump laser in the perpendicular direction in order to match the size of the seed laser beam. If the pump laser beam is larger than the seed laser beam, unseeded dye will undergo population inversion and produce exclusively ASE. If the pump laser beam is smaller than the seed laser beam, the nonuniform pumping intrinsic to the transversely pumped rectangular cell design is exacerbated. This effect produces a nonuniform spatial profile of the laser intensity as well as spatially nonuniform phase evolution of the laser frequency.[54] Overlap of the two laser beams is critical to operation of the pulsed amplifier. Small alignment drifts can have profound effects on the output power and spectral quality. Thus, regular re-alignment of the system is necessary.

The final amplification stage is a Bethune cell, which is a triangular prism with a dye capillary running through the center. This configuration allows the dye to be pumped from all sides by reflection of the pump laser off of the two angled faces. As a result, the critical overlap of seed and pump laser is almost trivial to obtain. In this cell it is important to adjust the beam diameter of the seed laser to be slightly smaller than the bore of the capillary in order to maximize overlap while avoiding diffraction rings. The dye concentration in the cell should also be chosen so that the absorption depth of the pump laser beam matches the bore diameter to maximize the gain in transit through the dye cell.

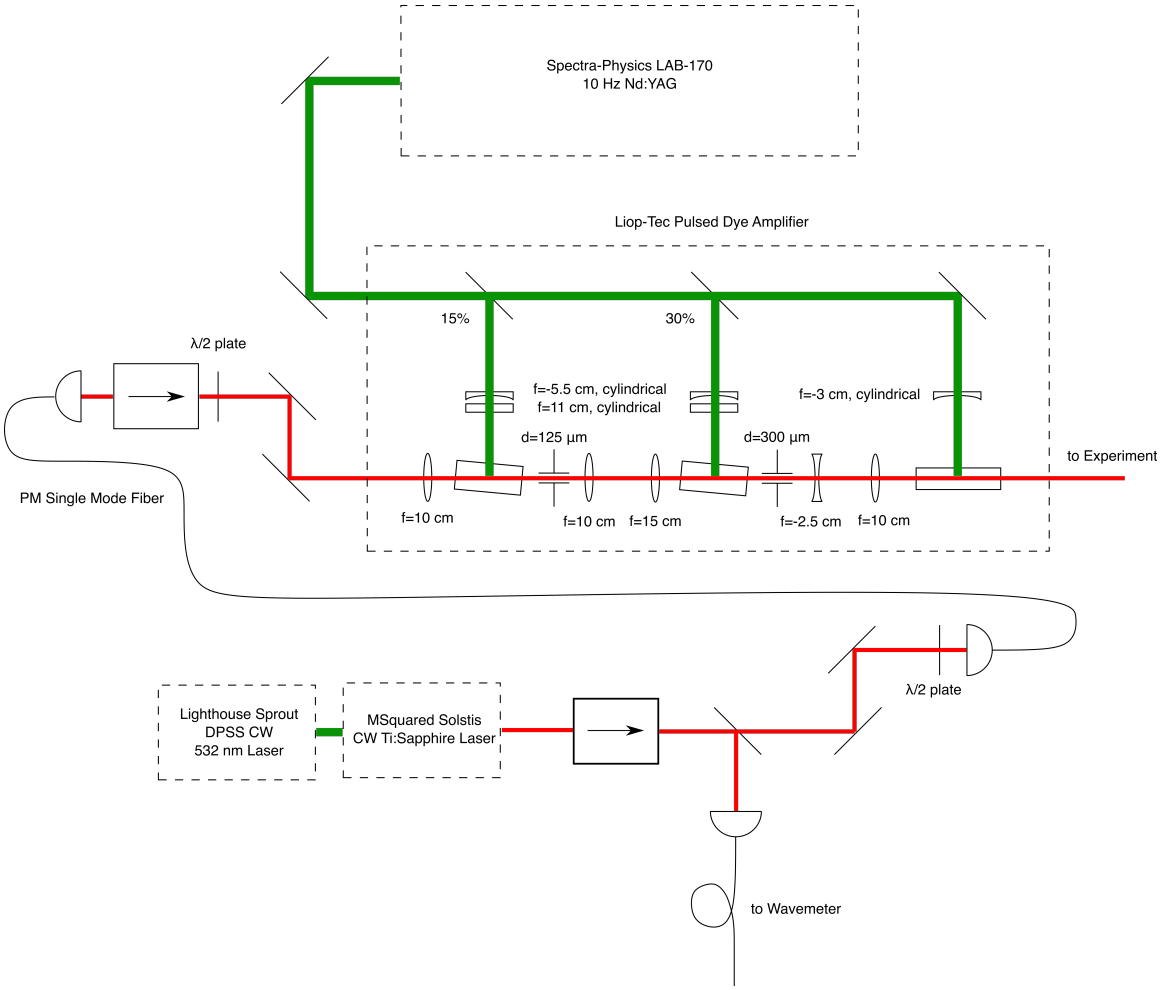

Figure 2-1: Schematic diagram of the pulse-amplified CW laser system. A CW laser, transmitted through a polarization-maintaining optical fiber, seeds the pulsed dye amplifier. Three dye cells are transversely pumped by the second harmonic of a Nd:YAG laser and produce up to 10 mJ per pulse of near-infrared radiation. Spatial filtering around each dye cell serves to reduce the ASE content in the pulsed laser output.

2.1.3 Frequency chirping in dye amplifiers

A well-known phenomenon associated with pulsed laser amplification in a dye solution is a broadening of the laser pulse frequency beyond the Fourier transform limit due to time-dependent frequency variation within the pulse. In addition, this frequency change need not be symmetric about the seed frequency, and can produce a frequency offset in addition to broadening. Often, the use of a pulsed amplification system is motivated by the desire to perform non-linear frequency conversion (e.g., second harmonic generation, four-wave mixing) and these additional steps cause further degradation of the frequency purity of the laser. Thus, the intra-pulse phase evolution of pulse amplified CW laser systems limits the precision and accuracy of high-resolution laser spectroscopy experiments.

This phenomenon was investigated in detail by the Eyler group,[54] who determined that the source of these frequency deviations is predominantly due to time-varying gain in the amplifier, rather than transient heating, which might produce a time-varying refractive index of the solvent. A simple model of this effect gives the evolution of the instantaneous frequency of the laser pulse at position L and time τ in the dye amplifier:

$$f_{\text{inst}}(L,\tau) = f_{\text{inst}}(0,\tau) - \frac{L}{2n(\omega)\lambda}\alpha'(\omega)\frac{\mathrm{d}}{\mathrm{d}t}N_1(\tau) \tag{2.1}$$

where $f_{\text{inst}}(0,\tau)$ is the instantaneous frequency at the input of the dye amplifier, n is the index of refraction of the solvent at frequency ω or wavelength λ, and $N_1(\tau)$ is the number density of dye molecules in the first excited state. The real part of the effective polarizability, $\alpha'(\omega)$, is defined as the real part of the electric susceptibility per dye molecule per unit volume: $\chi'(\omega,\tau) = \alpha'(\omega)N_1(\tau)$. Since the population in the first excited state, N_1, varies significantly over the short duration of the laser pulse, large excursions in frequency become possible.

We have experimentally characterized the typical phase behavior of our pulsed dye amplification system by the standard optical heterodyne technique.[54] To obtain the phase variation of a laser pulse at optical frequencies, we beat the pulsed output of the amplifier chain against the seed CW beam, shifted by a constant radio frequency

offset. The CW laser field can be described as

$$E_0 = E_{\mathrm{cw}} e^{-i(\omega_0 + \omega_{\mathrm{RF}})t} + \text{c.c.} \tag{2.2}$$

where E_{cw} is the amplitude of the CW laser, ω_0 is the optical frequency, ω_{RF} is the offset frequency and c.c. stands for the complex conjugate. We can write a similar expression for the pulsed laser field:

$$E_1 = E_{\mathrm{p}}(t) e^{-i(\omega_0 t + \phi(t))} + \text{c.c.} \tag{2.3}$$

where $E_{\mathrm{p}}(t)$ is the time-varying amplitude of the pulsed laser, and $\phi(t)$ is the (unknown) time-varying phase function. The photodiode is a power detector that sees the total signal:

$$V_{\mathrm{photodiode}} \propto |E_0 + E_1|^2 \tag{2.4}$$

$$= E_{\mathrm{cw}}^2 + E_{\mathrm{p}}^2(t) + E_{\mathrm{cw}} E_{\mathrm{p}}(t) \times \left(e^{i(\phi(t) - \omega_{\mathrm{RF}} t)} + e^{-i(\phi(t) - \omega_{\mathrm{RF}} t)} \right) \tag{2.5}$$

The first term in Equation 2.5 produces a DC offset and can be ignored. The second term results in amplitude variation, and the third term contains the significant information — the RF beat frequency modified by the phase fluctuations of the pulsed laser output. Extracting that term allows the instantaneous frequency of the laser pulse to be deduced by:

$$f_{\mathrm{inst}} = \frac{1}{2\pi} \frac{\mathrm{d}\phi}{\mathrm{d}t} \tag{2.6}$$

Most previous works have performed this phase extraction in the frequency domain by performing a Fourier transform of the photodiode signal, applying a filter to isolate the signal at ω_{RF} from the low frequency amplitude variation, then performing an inverse Fourier transform to recover the complex-valued electric field of the laser pulse, which contains the desired phase evolution.[5443] Our method works entirely in the time domain by taking advantage of the high-speed oscilloscopes available in our lab.

A schematic of the experimental setup appears in Figure 2-2. A fraction of the CW beam with frequency ω_0, which seeds the pulsed amplification chain, is split off and double-passed through an acousto-optic modulator (AOM) operating at frequency Ω. The first order diffracted beam is shifted by a small angle relative to the original beam so that a beam block can separate the two frequencies, ω_0 and $\omega_0 - \Omega$. A "cat's eye" retroreflector composed of a lens and mirror combination sends the frequency-shifted beam back through the AOM, while reducing the impact of any small misalignment. The first order diffracted beam traveling in the opposite direction, now with frequency $\omega_0 - 2\Omega$, is deflected back along the path of the original input beam. This defines the beat frequency defined above as $\omega_{\mathrm{RF}} = 2\Omega$. A Fresnel rhomb placed after the AOM rotates the polarization of the diffracted beam by $\lambda/2$ after two passes and the frequency-shifted beam is then separated from the input beam by a polarizing beam splitter. This frequency shifted CW radiation is combined with a portion of the pulsed output from the amplification chain at a non-polarizing beamsplitter. The combined radiation passes through a single mode fiber, in order to overlap the wavefronts of the two fields, and is then detected on a fast photodiode. The output signal from the photodiode is high-pass filtered to remove the low frequency amplitude variation and digitized on a 12.5 GHz oscilloscope at 25 GS/s.

A typical chirp measurement signal, using LDS 798 dye at 800 nm and a 750 MHz RF frequency, appears as the data points (red circles) in the top panel of Figure 2-3. The 10 ns sample shown represents the signal between the $\sim$10% intensity limits of the laser pulse. This data is fit directly in the time domain by a nonlinear least squares algorithm with a sinusoidal function that includes a constant frequency term, as well as a phase term with time dependence up to third order. The fit is shown as a black line in the top panel of Figure 2-3. Applying Equation 2.6 to the fitted phase gives the measured instantaneous frequency of the laser pulse, shown in the bottom panel of Figure 2-3. We find an obvious negative frequency chirp in this pulse, spanning at least 50 MHz and centered at $\sim$ 100 MHz. The negative chirp direction indicates that the electric susceptibility of the dye at this wavelength is negative. This is typical since most dyes are used at wavelengths red of their fluorescence maximum in order

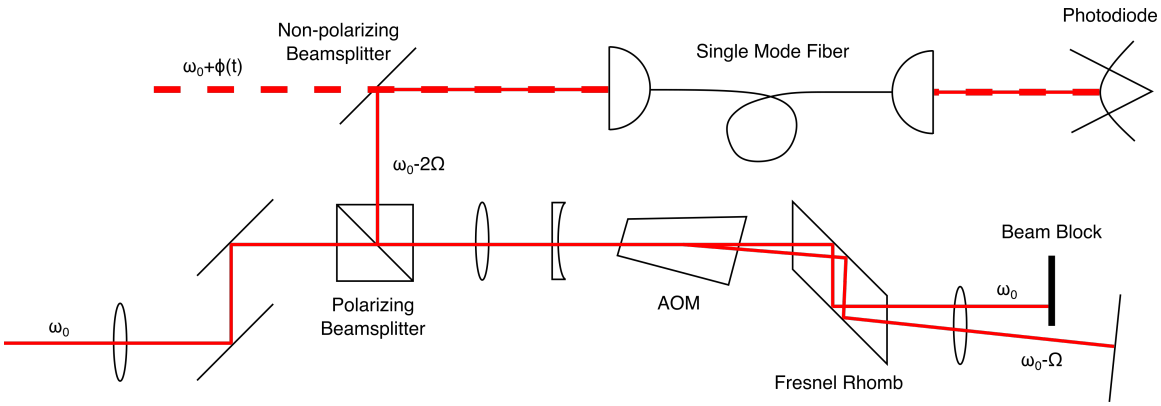

Figure 2-2: Experimental setup for measurement of the frequency offset and chirp in a pulsed dye amplifier. The same CW beam that seeds the amplifier with frequency ω_0 is double-passed through an AOM operating at frequency Ω. This shifted beam is combined with the pulsed output of the amplifier chain with frequency $\omega_0 + \phi(t)$ where $\phi(t)$ is the unknown phase function produced in the dye amplifiers. The two beams are passed through a single mode fiber to overlap their wavefronts and then detected on a fast photodiode.

to avoid overlap with the absorption band of the dye. This single measurement is representative of the phase behavior in our amplification system, but every pulse is far from identical. We observe the center frequency and chirp width to vary by several tens of MHz in either direction.

This significant shot-to-shot variation in the phase evolution is explained by the findings of Eyler and co-workers and is a result of the rectangular dye cells used in our setup.[54] They found that rectangular cells, as a result of the required tight focusing of the pump beam, are extraordinarily sensitive to the alignment of the system. Small deviations of the pump or seed laser beams result in dramatic changes in the time-varying gain of the system and thus produce large changes in the phase evolution of the laser pulses. In addition, the tight pump beam focus produces significant variation of the pump intensity across the dye cell, which results in both amplitude and phase variation in the transverse profile of the amplifier chain output. It is entirely possible that the pointing instability in the beam path could result in sampling slightly different portions of the output beam in the chirp measurement shot-to-shot. This would further add to the observed variation in phase evolution.

Eyler and co-workers found that capillary-type cells did not suffer from the same

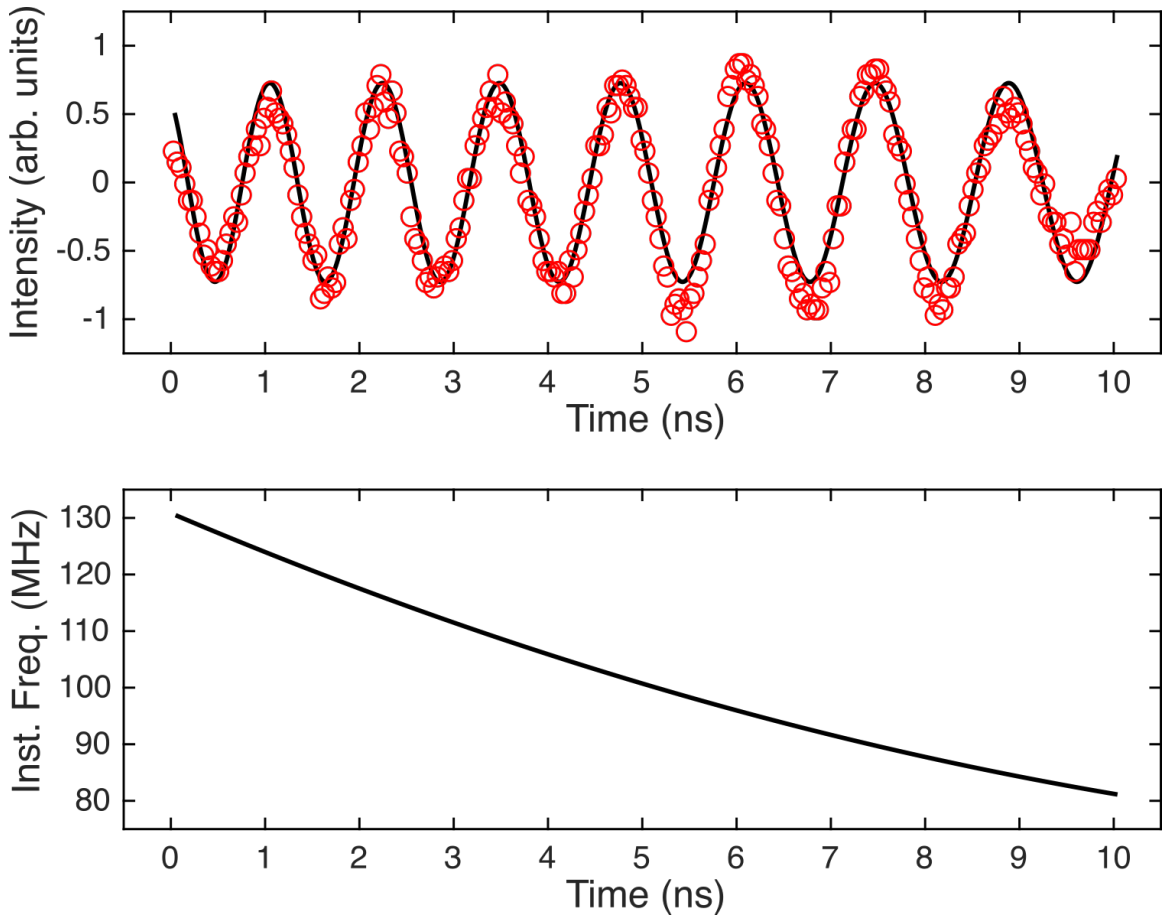

Figure 2-3: A typical measurement of the frequency chirp in the output of the pulsed dye amplification chain. The top panel shows data points (red circles) measured with a high-speed photodiode and digitized on an oscilloscope at 25 GS/s. The black line is a fit to the data, including a constant frequency term, as well as a phase term with time dependence up to third order. The instantaneous frequency of the pulse appears in the lower panel, which shows a chirp of about 50 MHz within the 10% intensity limits of the pulse and with a constant offset of about 100 MHz.

extreme sensitivity to alignment as rectangular cells. This is unsurprising since the transverse pump beam is not tightly focused on such cells and the entire dye volume is illuminated, reducing the spatial variation in gain. Eikema and co-workers used longitudinally pumped dye cells,[37] which should similarly reduce fluctuations in the phase evolution since excellent overlap of the dye stream, pump laser, and seed laser, can be achieved without tight focusing. In our setup, the use of a single capillary cell in the last stage does not significantly improve the intensity variation in the output laser pulse, and likely has limited impact on spatial phase variation as well.

The very large offset frequency is somewhat unusual and is a result of the phase of the emission not returning to the same value as at the beginning of the pulse. This type of behavior was observed by Eikema and co-workers who suggested that this is a result of some remaining excited state population at the end of the laser pulse.[37] They attributed this residual population to re-absorption of the dye laser frequency that occurs at later points in the dye cell. This interpretation was supported by the observation that the offset increased as the amplification wavelength was tuned blue toward the absorption band center of the dye. We have no further experimental observations to challenge this hypothesis and a similar mechanism may be operative here.

There are several methods that have been explored for controlling or reducing the chirping effect in dye amplifiers. Eikema and co-workers have employed an active compensation scheme, which uses an electro-optic modulator (EOM) on the seed beam to compensate for measured phase fluctuations in an active feedback loop.[37] This method produced a larger frequency offset, but significantly reduced the pulsed laser bandwidth. Another technique pursued by Eyler and co-workers allowed for passive compensation of frequency chirps around a small wavelength range.[42] The authors noted that Equation 2.1 will only result in zero frequency chirp if the real part of the effective polarizability is itself equal to zero. For a particular dye, this will only occur at one wavelength in the fluorescence band. However, by mixing two dyes with opposite signs for the real part of the electric susceptibility and no overlap of their respective absorption and emission bands, zero susceptibility at chosen

wavelengths could be achieved. Their method was demonstrated using a 10:1 mixture of Rhodamine 610 and DCM, which produced a near-Fourier transform limited laser pulse at 606 nm. This is a straightforward improvement that will be incorporated in future work. At the time of writing, we have not obtained truly Fourier transform-limited laser pulses with our pulsed amplification system. However, the measured phase evolution is incorporated into the simulations presented in Chapter 3.

2.1.4 Frequency calibration

In general, high-resolution *laser* spectroscopy has not been the focus of this thesis and so careful absolute frequency calibration has not been undertaken. Throughout, a wavemeter (High Finesse, Ångstrom WS/7) has been used to monitor and set the frequency of all lasers. This wavemeter is regularly calibrated using a frequency-stabilized HeNe laser (Spectra Physics, 117A) and is specified to have an absolute accuracy of 60 MHz.[67] All pulsed dye lasers are measured by sending a small fraction of the pulsed laser output directly to the wavemeter.

The pulsed dye amplification system takes further advantage of the wavemeter. A portion of the CW seed laser is sent to the wavemeter for measurement. A Labview program controls the frequency of the CW laser via an ethernet network, using the wavemeter measurement in an active feedback loop. This method allowed the pulsed amplification system to be set at a desired frequency for many hours despite the slow (typically temperature-induced) frequency drift intrinsic to the CW laser. In addition, this allowed for a simple method of scanning the laser by changing the desired frequency in discrete steps and allowing the continuously operating wavemeter lock to drag the CW laser frequency.

When absolute frequency calibration is required, it is advisable to use an additional frequency reference, such as a frequency comb or molecular spectrum. In the near-infrared range where the Ti:Sapphire system operates, the standard reference is a high-temperature (ca. 500°C) iodine cell.

2.2 Chirped-pulse millimeter-wave spectroscopy

Chirped-pulse millimeter-wave (CPmmW) spectroscopy was first demonstrated in the Field Lab in 2011,[116] and is an extension of the chirped-pulse Fourier transform microwave (CP-FTMW) technique pioneered in the lab of Brooks Pate.[19,20] As in traditional Fourier transform microwave spectroscopy, the CP-FTMW technique uses pulsed radiation to polarize (typically rotational) transitions in the microwave region of the spectrum. The polarization of all emitters in the sample interferes constructively to produce a macroscopic polarization, which emits radiation at the natural frequency of the transition. This detected field, called free induction decay (FID), gradually diminishes in amplitude as dephasing of the ensemble occurs due to motional (Doppler broadening) and collisional (pressure broadening) effects. The FID is detected by an antenna in the apparatus and phase-coherently averaged in the time domain. Following data collection, the FID signal, averaged over many pulses, is Fourier transformed to obtain a frequency domain spectrum of the excited transitions. In a traditional FTMW instrument, a cavity is placed around the sample to reduce the required input power and enhance the resultant FID signal. This limits the detection bandwidth in a single experiment, typically to ~ 1 MHz, and requires simultaneous tuning of the cavity length and excitation frequency to obtain a ~ 10 GHz broadband spectrum.

In contrast to the cavity-based technique, chirped-pulse methods are truly broadband. The first key change is to remove the cavity from the experiment and simply place the sample between the excitation and detection antennae. Without a cavity, the excitation pulse can cover the entire frequency range of interest, ~ 10 GHz, in a single pulse experiment. To generate an excitation pulse with a very wide bandwidth, one might use a pulse with a very short time duration, as is typical in optical spectroscopy. For a Gaussian shaped pulse, the time-bandwidth product is given by:

$$\Delta\nu\Delta\tau \approx 0.44 \tag{2.7}$$

Thus, to cover several GHz of spectra in a single-shot, a pulse with a 100 ps duration

will have a FWHM in the frequency domain of about 4.4 GHz. The problem with this strategy is that the power delivered to a single transition with a typical < 1 MHz linewidth will be extremely small.

The alternative, made possible by the development of high-speed arbitrary waveform generators (AWG), is to stretch the bandwidth over a much longer duration pulse by chirping the frequency, thereby delivering much more power per unit bandwidth. Chirped pulses are typically ~ 1 μs in duration because they must be shorter than the dephasing time of the sample, typically ~ 10 μs at 10 GHz due to Doppler broadening. On the detection side of the experiment, a broadband, high-speed digitizer is the critical piece of technology required to perform averaging in the time domain for all signals within the bandwidth of the excitation pulse. Finally, all frequency sources must be phase-locked to a common reference in order to perform the averaging phase-coherently. If the phase of the excitation pulse were to drift from shot to shot, the sample FID would also exhibit a shot-to-shot phase shift. Since the detection circuit begins sampling at the same time for each experiment, the random phases of the individual FIDs would interfere destructively and all signal would be lost.

The main advantage of the chirped-pulse method is the time required to collect a broadband spectrum relative to a cavity FTMW instrument. Since the cavity instrument must be finely scanned over the entire spectrum, a large fraction of the collection time is consumed in moving the mirrors rather than collecting data. To obtain a spectrum with a similar signal-to-noise ratio (SNR), the Pate group reports a typical cavity experiment time of ~ 15 hours and a typical chirped-pulse experiment time of ~ 15 minutes.[20] Beyond this extraordinary speed up in data acquisition, since the chirped-pulse method collects a broadband spectrum in a single acquisition, the experiment time and hence SNR, can be chosen independently of the bandwidth of the desired spectrum.

One of the main disadvantages to the chirped-pulse technique is the greater power requirement. In a cavity instrument, the power build-up due to the cavity, with a typical Q of 10^4, allows the use of pulses with peak power on the order of 10 μW.[20]

In the chirped-pulse case, the absence of a cavity implies $Q = 1$ and a factor of 10^4 more power is required. Moreover, the ~ 1 MHz bandwidth of the cavity instrument relative to the $\sim$ 10 GHz bandwidth of a chirped pulse setup results in another factor of approximately 10^4 in power required. Thus, most CP-FTMW instruments employ high-power traveling wave tube amplifiers to reach $\sim$1 kW peak excitation powers. This has additional technical implications. For example, a protection switch is required after the receiving antenna to protect the sensitive detection circuit from being destroyed by this enormous power input.

The physics of both pulsed excitation and chirped excitation are determined by the time evolution of a density matrix, ρ, which describes the quantum states of interest under the influence of a Hamiltonian, H, that describes the light-matter interaction. This evolution is governed by the Liouville-von Neumann equation:

$$i\hbar\frac{\mathrm{d}\rho}{\mathrm{d}t} = [H, \rho] \tag{2.8}$$

The purpose of a density matrix approach is that the effects of decoherence can be handled easily by including additional evolution terms in Equation 2.8. This is the starting point for the derivation of the well-known Bloch equations used in NMR. McGurk and co-workers have presented several analytical results that are specifically relevant to microwave experiments.[100] If we consider a chirped pulse with a linear frequency sweep, the E-field is written as

$$E = E_{max}e^{i\left(\omega_0 t + \frac{1}{2}\alpha t^2\right)} \tag{2.9}$$

where E_{max} is the peak electric field, ω_0 is the initial frequency, and α is the sweep rate. The instantaneous frequency of the chirped pulse is give by

$$\omega_{\mathrm{inst}} = \frac{\mathrm{d}}{\mathrm{d}t}\left(\omega_0 t + \frac{1}{2}\alpha t^2\right) = \omega_0 + \alpha t \tag{2.10}$$

For a linear chirped pulse in the weak field limit, McGurk et al. showed that the

signal scales as[100]

$$P \propto \frac{\mu^2 E_{max} \Delta N}{\sqrt{\alpha}} \tag{2.11}$$

where μ is the transition dipole moment and ΔN is the population difference between the two levels. This result highlights the favorable scaling with bandwidth for a chirped pulse relative to a Fourier transform limited pulse, which we previously discussed qualitatively. The signal for a chirped pulse with fixed duration scales inversely as the square root of the bandwidth. The signal for a single-frequency pulse scales inversely with the bandwidth because the bandwidth and pulse duration are inversely proportional.

Relative to microwave frequencies, spectrometers in the millimeter-wave region face a number of additional technical and fundamental challenges. The first technical challenge is that CPmmW experiments are nearly always power-limited. The high-power amplifiers typically used in CP-FTMW experiments are not readily available above frequencies of ∼50 GHz. In the spectrometers used in this work, maximum powers of 10 to 30 mW are typical. For a typical rotational transition with a dipole moment of 1 Debye, this is well below the power required for optimal polarization. Although the current state-of-the-art cannot compete with more mature microwave technology, the millimeter-wave and terahertz regions are currently undergoing rapid development due to applications in communications, imaging, and radio-astronomy.[104] Already, Virginia Diodes is producing millimeter-wave broadcast systems that can generate >100 mW within select bands.[151] Further technological advances, for example, fast protection switches, may be on the horizon.

Second, CPmmW spectrometers typically generate the required high frequency signals by multiplication of a low frequency signal by a large factor, which can be anywhere from ×8 to ×24 or more. This renders the technique more sensitive to phase instability in the setup since a small phase jitter at low frequency can become very large after several multiplication steps. As mentioned, phase coherence is essential to performing averaging in the time domain. This problem reduces the effectiveness of averaging to improve the SNR, which ideally scales as the square root of the number

of averages. While phase jitter can arise from several sources including electrical fluctuations, temperature fluctuations, and mechanical vibrations, there are two main types of jitter: t-jitter and ϕ-jitter.[116] These are illustrated by Equations 2.12 and 2.13, respectively.

$$E \propto \sin\left[\omega_0(t+\Delta t) + \frac{1}{2}\alpha(t+\Delta t)^2 + \phi\right] \tag{2.12}$$

$$E \propto \sin\left[\omega_0 t + \frac{1}{2}\alpha t^2 + (\phi + \Delta\phi(\omega))\right] \tag{2.13}$$

In some cases, the effect of phase jitter can be minimized by collecting many FIDs with few averages, post-processing the data, and then averaging these results. For example, a slow drift in Δt could be corrected by shifting each FID in the time domain to realign their phases. Park et al. observed jitter in $\Delta\phi$ that was independent of frequency.[116] This allowed development of a method in which the phase of the Fourier transform of each collection was rotated to maximize the phase coherence and hence the signal amplitude.

The final difference between the millimeter-wave and microwave experiments that will be discussed here is fundamental. In most rotational spectroscopy experiments, the dephasing is dominated by Doppler broadening, both in molecular beams and in static cells. Since the Doppler effect is proportional to the frequency of the transition, dephasing is significantly faster in the millimeter-wave range. For example, Pate et al. observe 10 μs Doppler-limited FID lifetimes below 20 GHz in a supersonic expansion,[20] while Park et al. observe 2 μs lifetimes around 90 GHz.[116] This has two major effects. First, the excitation must be performed in a shorter pulse than the dephasing time scale in order to observe FID. This further exacerbates the problem of limited excitation power. It also makes observation of coherent phenomena, like Rabi flopping, more challenging. Second, it limits the resolution of the spectrometer. Around 90 GHz, linewidths of several hundred kHz are typical in a supersonic jet. Although Doppler broadening is a fundamental challenge, it can be reduced by careful experimental choices. The beam type (effusive vs. supersonic), temperature, geometry (axial vs. transverse), and choice of carrier gas will all affect the timescale for Doppler

dephasing.

2.2.1 Spectrometer design

In this work, millimeter-wave spectrometers in the 75-110 GHz (W band) and 220-330 GHz (high-frequency band) regions of the millimeter-wave spectrum are used. The millimeter-wave region is generally defined as light with frequencies of 30-300 GHz or wavelengths of 10-1 mm. Microwaves occupy the lower frequency range of 3-30 GHz (100-10 mm) and are sometimes defined as broadly as 300 MHz - 300 GHz (1 m - 1 mm). Above the millimeter-wave region is the sub-millimeter-wave or terahertz band, which is defined to be in the range of 300 GHz - 3 THz (1 - 0.1 mm), but often refers to frequencies as high as 30 THz in the far-infrared, and as low as 0.1 THz in the millimeter-wave region.[104] Our millimeter-wave spectrometers rely on the same solid-state diode technology as modern microwave sources, rather than the optical techniques used to generate far-infrared and high-frequency terahertz light. In the millimeter-wave spectrum, light is resonant with high-frequency rotations, either low-J transitions of small molecules or high-J transitions of large molecules, and more rarely, some very low frequency vibrations. In this work, however, millimeter-wave radiation will polarize "pure electronic" transitions between Rydberg states of atoms and molecules. In general, the high-frequency band will cover $\Delta n = \pm 1$ transitions with principal quantum numbers of $27 < n < 31$, $\Delta n = \pm 2$ transitions with $34 < n < 40$, and $\Delta n = \pm 3$ transitions with $38 < n < 46$, etc. The W band will cover $\Delta n = \pm 1$ transitions with $39 < n < 45$, and larger Δn transitions at higher principal quantum number values.

A schematic diagram of the W band CPmmW spectrometer is shown in Figure 2-4. A 10 MHz Rubidium frequency standard (i) provides a reference frequency to the fast oscilloscope (xxx) and the 9.375 GHz phase-locked oscillator (ii). This 9.375 GHz source serves as the primary frequency source for the spectrometer; it clocks the arbitrary waveform generator and is mixed with the two output channels of the AWG to produce the excitation pulse and the down-conversion signal. We found that this arrangement significantly reduced phase noise in the spectrometer. It is possible

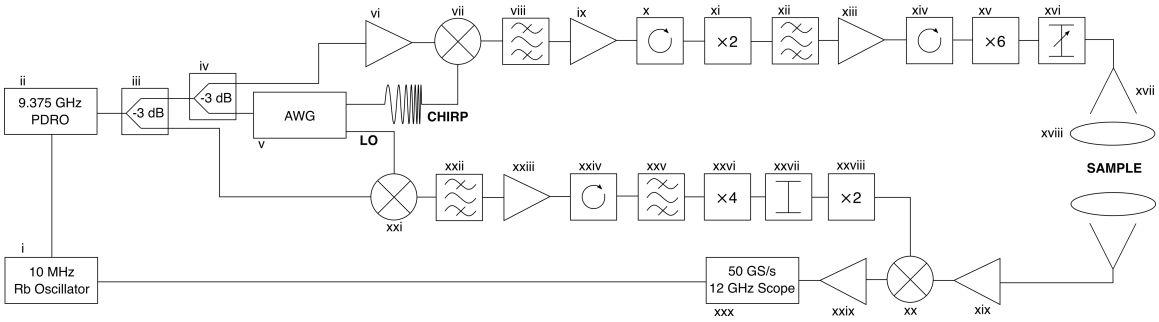

Figure 2-4: Schematic diagram of the W band millimeter-wave spectrometer. Parts labeled by roman numerals are described in the text.

that further improvement in the phase stability could be achieved by using the same multiplication factor on both the broadcast and receiver arms of the microwave circuit. One channel of the AWG outputs a chirped or single frequency pulse, or a train of pulses, which is then mixed with the 9.375 GHz oscillator. The lower sideband from this mixing step is selected and undergoes amplification and multiplication by a total factor of 12 to produce W band frequencies. The filter used in this step (viii) with a pass band from approximately 6.3 to 8.3 GHz, sets the W band frequency limits from approximately 75.6 to 99.6 GHz. A wider bandpass filter would allow access to higher W band frequencies, up to $12 \times 9.17 = 110$ GHz, although a notch filter may be required to further suppress the nearby 9.375 GHz signal. A rotary attenuator (xvi) located before the broadcast horn (xvii) allows for attenuation of the excitation pulse to produce optimal polarization of the Rydberg-Rydberg transitions. The excitation pulse is approximately collimated by a Teflon lens (xviii) and intersects the sample transverse to the direction of the molecular beam propagation.

The FID signal is focused by a second teflon lens onto an identical receiver horn. The rectangular horn antennae preserve the polarization of the microwave field, allowing for polarization-sensitive diagnostics of the investigated transitions. The FID signal is then amplified in a W band low-noise amplifier (LNA) (xix) and down-converted in a harmonic mixer (xx). The local oscillator frequency for this step is generated by mixing the 9.375 GHz source with a constant frequency output from the second channel of the AWG. The upper sideband of this mixing step is selected, then amplified and multiplied by a factor of 8. The intermediate frequency (IF) output of

the harmonic mixer is amplified by a LNA (xxix) and then digitized on a 50 GS/s oscilloscope. The spectrometer design follows each passive frequency conversion step with filtering, amplification, and isolation steps. Due to the large multiplication factors involved, it is important to maintain the highest frequency purity possible for all signals. Filtering steps remove unwanted sidebands, harmonics, and spurious signals, while isolation steps reduce the likelihood of spurious signals generated by backward propagating reflections through the amplifier-multiplier chain. All components of the spectrometer are specified in detail in the list below and roman numerals correspond to the labels in Figure 2-4.

i) 10 MHz Rubidium frequency standard (Stanford Research Systems, FS725)

ii) 9.375 GHz phase-locked dielectric resonator oscillator (Miteq, DLCRO 010-09375-3-15P)

iii) Power Divider, -3 dB, 2-18 GHz (Anaren, 41130)

iv) Power Divider, -3 dB, 2-18 GHz (Norsal Ind., 8121)

v) Arbitrary Waveform Generator, 12 GS/s (Agilent, M8190A)

vi) Low Noise Amplifier, 6-18 GHz (Pasternack, PE1523)

vii) Triple-Balanced Mixer, 2-18 GHz, 10 dB loss (Macom, M93)

viii) Bandpass Filter, 20 dB suppression, 6.3-8.3 GHz (Spectrum Microwave, 311-307246-001)

ix) Amplifier, 24 dB gain, +14 dBm min., 6-12 GHz (Avantek, AFT-12633-10F)

x) Isolator, 4-12 GHz (Innowave, 1090IR-549)

xi) Passive Frequency Doubler, 9.5-19 GHz, 10 dB loss (Marki, D95190)

xii) Bandpass Filter, 12-18 GHz (unknown, 0955-0553-1)

xiii) Amplifier, 20 dB gain, +13 dBm min., 6-18 GHz (ALC Microwave, ALS03-0283)

xiv) Isolator, 15 dB, 6-18 GHz (TRW Microwave, AMF 6483)

xv) ×6 Active Multiplier Chain, 75-110 GHz (Millitech, AMC-10-RFHB0)

xvi) Rotary Attenuator, 0-50 dB, 75-110 GHz (Hitachi, W0519)

xvii) Standard gain horn, 24 dBi, WR10 (TRG Control Data, W890)

xviii) 3" Teflon Lens, $f = 150$ mm at 500 GHz (Thorlabs, LAT150)

xix) Low Noise Amplifier, 20 dB gain, 75-110 GHz (Millitech, LNA-10-02150)

xx) Balanced Mixer, 75-110 GHz, 10 dB loss (Millitech, MXP-10-RFSSL)

xxi) Triple-Balanced Mixer, 4-16 GHz, 7 dB loss (Miteq, DM0416LW2)

xxii) Bandpass Filter (Reactel, AG1233-1)

xxiii) Amplifier, 30 dB gain, 7-12 GHz (Phase One Microwave, SG12-2515)

xxiv) Isolator, 15 dB, 6-18 GHz (Ditom, DM16018)

xxv) Bandpass Filter, 7-12 GHz (Time, BXF334)

xxvi) ×4 Active Frequency Multiplier, 33-50 GHz (Phase One, SX50-416)

xxvii) Fixed Attenuator, WR22, 10 dB loss (Millitech, FXA-22-R10GN)

xxviii) ×2 Active Multiplier Chain, 60-90 GHz (Millitech, AMC-12-110546)

xxix) Low Noise Amplifier, 25 dB gain, 0.1-18 GHz (Miteq, AMF-7D-00101800-24-10P)

xxx) 50 GS/s, 12 GHz Digital Oscilloscope (Tektronix, DPO71254B)

Essentially the same spectrometer allows access to the high frequency (220-330 GHz) band as well. The schematic diagram of the high frequency configuration is shown in Figure 2-5. All components of the broadcast arm are identical and a passive frequency tripler (I) is added between the attenuator and the broadcast horn. This

device has a typical efficiency of only 3%, resulting in approximately 1 mW output power across the frequency range 226.8 to 298.8 GHz, limited by the bandpass filter (viii) as discussed above. While this extreme power loss would be unacceptable for most rotational spectroscopy experiments, the large transition dipole moments of Rydberg-Rydberg transitions make this low power setup still useful. In the W band experiments at high n, we typically attenuate the broadcast by 15-20 dB to obtain optimal polarization. For the high frequency experiments performed on $\Delta n > 1$ transitions at high n or $\Delta n = 1$ transitions at lower n, the weaker transition moments and lower broadcast power make attenuation rarely necessary. On the detection side of the spectrometer, the multiplication chain (xxvi-xxviii), W band LNA (xix), and harmonic mixer (xx) are replaced by the Virginia Diodes integrated detection module MixAMC156 (II and III). All other components are the same as in the W band spectrometer. On both the broadcast and detection arms, WR10 rectangular horn antennae are attached via a waveguide transition to the WR3.4 ports of the high frequency devices. The use of a larger waveguide size results in an overmoded waveguide, meaning propagation modes other than the fundamental (TE10) are present. This is generally not a problem for our spectroscopic experiments, and the use of larger horn antennae simplifies the horn-to-horn alignment of the spectrometer. This low power, high frequency design was adopted in order to access a wider high frequency range than allowed by the Virginia Diodes AMC291 module and to simplify conversion between W band and high frequency band experiments.

I) Passive Frequency Tripler, 220-330 GHz, 3% typical efficiency (Virginia Diodes, WR3.4X3)

II) Subharmonic Mixer, 220-330 GHz (Virginia Diodes, component of MixAMC156)

III) $\times$12 Active Multiplication Chain, 110-175 GHz (Virginia Diodes, component of MixAMC156)

A schematic diagram of the high power, high frequency CPmmW spectrometer appears in Figure 2-6. The design of this spectrometer is similar to the W band

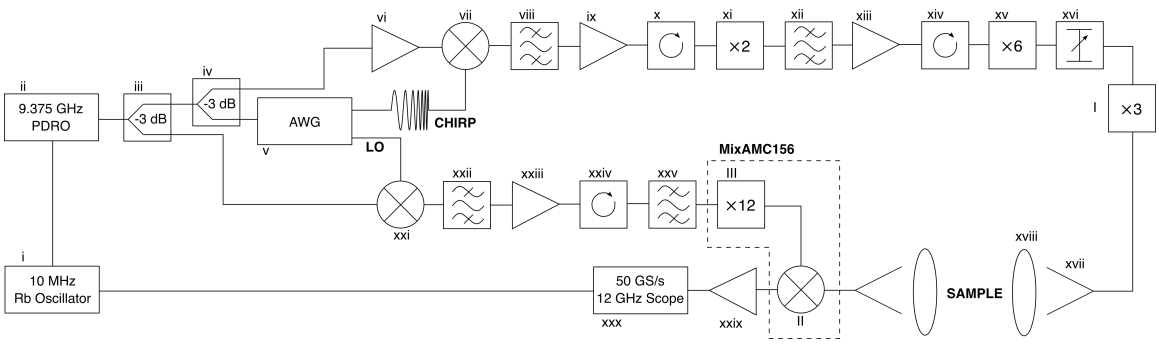

Figure 2-5: Schematic diagram of the low power, high frequency millimeter-wave spectrometer. By replacing only a few components of the W band spectrometer, the same setup allows access to the high frequency band. Parts labeled by lower case roman numerals are identical to those in the W band spectrometer. The additional components, labeled by upper case roman numerals, are described in the text.

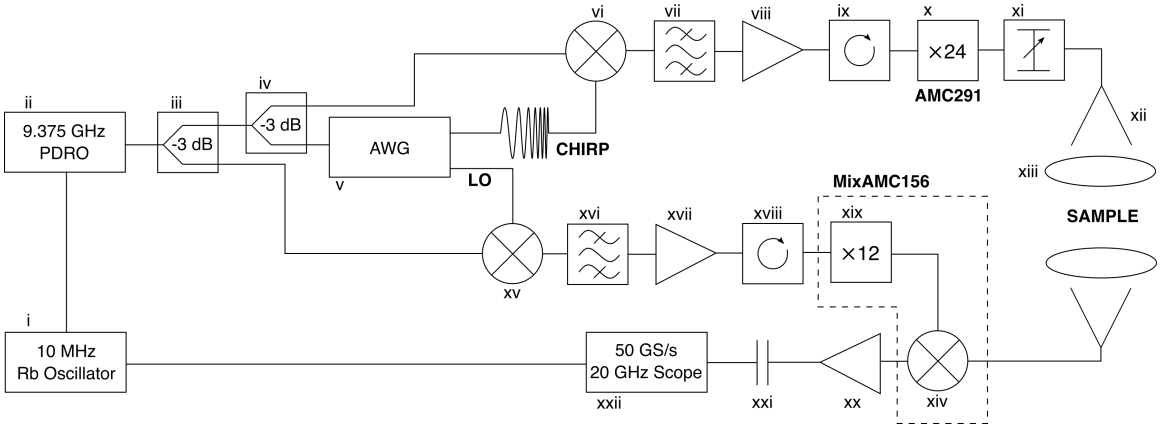

Figure 2-6: Schematic diagram of the high frequency millimeter-wave spectrometer. Parts labeled by roman numerals are described in the text.

spectrometer and its high frequency configuration. The biggest difference is the use of the AMC291 integrated broadcast unit (x) and the MixAMC156 integrated receiver unit (xiv and xix). These two units involve frequency multiplication, amplification, filtering, and isolating steps just as in the home-built W-band system. The AMC291 unit has an operating range of approximately 260-300 GHz, and produces up to 30 mW of output power, substantially more than is obtained by passive frequency tripling. The MixAMC156 unit uses a subharmonic mixer (xiv) rather than a harmonic unit so the required LO frequency is half the RF frequency. In all experiments with this spectrometer, a larger bandwidth (20 GHz) Agilent oscilloscope (xxii) was used in order to simultaneously monitor transitions with large frequency differences. Again, WR3.4 to WR10 waveguide transitions and WR10 rectangular standard gain horns are used on the broadcast and receiver arms. All parts of this spectrometer are listed below and roman numerals correspond to the labels in Figure 2-6.

i) 10 MHz Rubidium frequency standard (Stanford Research Systems, FS725)

ii) 9.375 GHz phase-locked dielectric resonator oscillator (Miteq, DLCRO 010-09375-3-15P)

iii) Power Divider, -3 dB, 2-18 GHz (Anaren, 41130)

iv) Power Divider, -3 dB, 2-18 GHz (Norsal Ind., 8121)

v) Arbitrary Waveform Generator, 12 GS/s (Agilent, M8190A)

vi) Triple-Balanced Mixer, 4-16 GHz, 7 dB loss (Miteq, DM0416LW2)

vii) Bandpass Filter, 10.9-12.7 GHz (Spectrum Microwave, C11800-1951-1355)

viii) Amplifier, 7-12 GHz, 25-35 dB gain (Phase One Microwave, SG12-2515)

ix) Isolator, 15 dB, 6-18 GHz (Ditom, DM16018)

x) $\times$24 Active Multiplier Chain (Virginia Diodes, AMC291)

xi) Micrometer Driven Variable Attenuator, WR3.4, 0-25 dB attenuation (Virginia Diodes)

xii) Standard gain horn, 24 dBi, WR10 (TRG Control Data, W890)

xiii) 3" Teflon Lens, $f = 150$ mm at 500 GHz (Thorlabs, LAT150)

xiv) Subharmonic Mixer, 220-330 GHz (Virginia Diodes, component of MixAMC156)

xv) Triple-Balanced Mixer, 4-16 GHz, 7 dB loss (Miteq, DM0416LW2)

xvi) Bandpass Filter, 9.9-12.9 GHz (Lorch, 13EZ5-11450/A1700-S)

xvii) Amplifier, 6-18 GHz, 30-40 dB gain (Wright Technologies, ASG-183020)

xviii) Isolator, 15 dB, 6-18 GHz (Ditom, DM16018)

xix) $\times$12 Active Multiplication Chain, 110-175 GHz (Virginia Diodes, component of MixAMC156)

xx) Low Noise Amplifier, 25 dB gain, 0.1-18 GHz (Miteq, AMF-7D-00101800-24-10P)

xxi) DC Block, 0.01-18 GHz (Mini-Circuits, MCL 15542 BLK-18-S+)

xxii) 50 GS/s, 20 GHz Digital Oscilloscope (Tektronix, DPO72004)

In all of our spectrometer setups, we find that the use of flexible coaxial cable is detrimental to the amplitude and phase stability of the down-converted FID signal. For this reason, mostly rigid connectors are used on the receiver arm of the spectrometers and the flexible cable length was minimized by placing the oscilloscope as close as possible to the detection unit. All active microwave components are cooled by clamping water-cooled brass blocks to the devices. Temperature regulation to approximately 20 °C is required to prevent damage from overheating and to improve phase stability.

One challenge in our CPmmW experiments on Rydberg states is the need to overlap the mmW field with one or more lasers in the interaction volume. Previous experiments in the Field lab have used either a flat metal plate[30126] or an off-axis

parabolic mirror[60 61 169] with a small hole drilled through the center as a beam combiner. The necessary lasers were overlapped upstream of the beam combiner then focused through the drill hole. The laser radiation then expanded across the molecular beam to produce a large, but non-uniform excitation volume. The millimeter-wave field was reflected by the metal plate or parabolic mirror and propagated in the same direction as the laser beams. Although the hole in the beam combiner is much smaller than the diameter of the mmW beam, it has dimensions similar to the mmW wavelength. Thus, diffraction from the beam combiner slightly perturbs the mmW field propagation.

In order to address the issue of mmW diffraction and non-uniform laser excitation volume, we have employed a different method for combining the laser and mmW beams. For laser wavelengths in the visible and near-infrared, we use indium tin oxide (ITO) coated glass plates to combine the laser and mmW beams. ITO is a conductive coating transparent in the visible and near-infrared that is often used as an electrode when optical access is required, for instance, in solar cells. Due to its conductivity, ITO also acts as a mirror for low frequency radiation from the far-infrared to the microwave region.[11] Thus, ITO-coated glass plates are very effective shortpass dichroics for visible and mmW radiation. Below $\sim$400 nm, ITO begins to absorb significantly,[47] preventing its use as a beam combiner for UV radiation. Instead, we use large diameter optics with a dielectric coating that reflects the UV wavelength of interest. Dielectric coatings are extremely thin and non-conductive so they are transparent to mmW radiation, and the large optic size prevents diffractive losses of the large diameter mmW beam. Thus, dielectric mirrors are useful as longpass dichroics for UV and mmW radiation. Using these two types of optics we are able to collimate the laser beams to a desired size and avoid mmW diffraction from small diameter drill holes. Both of these changes give us greater control over the Rydberg sample that we prepare and interrogate.

2.3 Cryogenic Buffer Gas-Cooled Beams

Essential to the success of the optical-mmW STIRAP experiment described in Chapter 3, as well as several recent experiments in the Field lab,[60,61,169] is the use of a cryogenic buffer gas-cooled beam as the source of our cold atoms. The following section discusses the physics behind the cryogenic buffer gas beam (CBGB) technique, as well as the more traditional effusive and supersonic beam sources, which are also employed in the experiments described in this thesis. In large part, this discussion is adapted from the excellent review article by Hutzler et al.,[72] supplemented with results and insights from the many groups now working with CBGBs. I have made estimates of some of the important parameters of our own buffer gas system, using the details of our initial work[169] in this area on BaF in 20 K Ne buffer gas. Many of the technical details of our buffer gas system appear in the theses of Yan Zhou[168] and David Grimes[59] and will not be repeated here. Creation of a buffer gas beam involves four main steps: 1) A cold cell is filled with a buffer gas. 2) Hot atoms/molecules of interest are introduced and thermalize with the buffer gas. 3) The atoms/molecules diffuse through the cell and freeze on the cold walls or escape through the aperture. 4) Formation of a beam occurs at the aperture of the buffer gas cell with properties determined by the conditions inside the cell. Each step is discussed in detail in the following sections.

2.3.1 Flow rate and stagnation pressure

A schematic of a typical buffer gas cell is shown in Figure 2-7. The important geometric parameters to consider are the cell length L_{cell}, the cell diameter, d_{cell}, the cross-sectional cell area, $A_{\text{cell}} \approx d_{\text{cell}}^2$, the cell volume, $V_{\text{cell}} = A_{\text{cell}} \times L_{\text{cell}}$, the aperture diameter, d_{aperture}, and the aperture area, $A_{\text{aperture}} \approx d_{\text{aperture}}^2$. We assume that the cell is held at a constant temperature, T_0, which in our case is 20 K. Buffer gas is typically introduced into the cell via a mass flow controller, which indicates flow rate in units of standard cubic centimeters per minute (SCCM). For reference, 1 SCCM $= 4.42 \times 10^{17}$ s^{-1}.

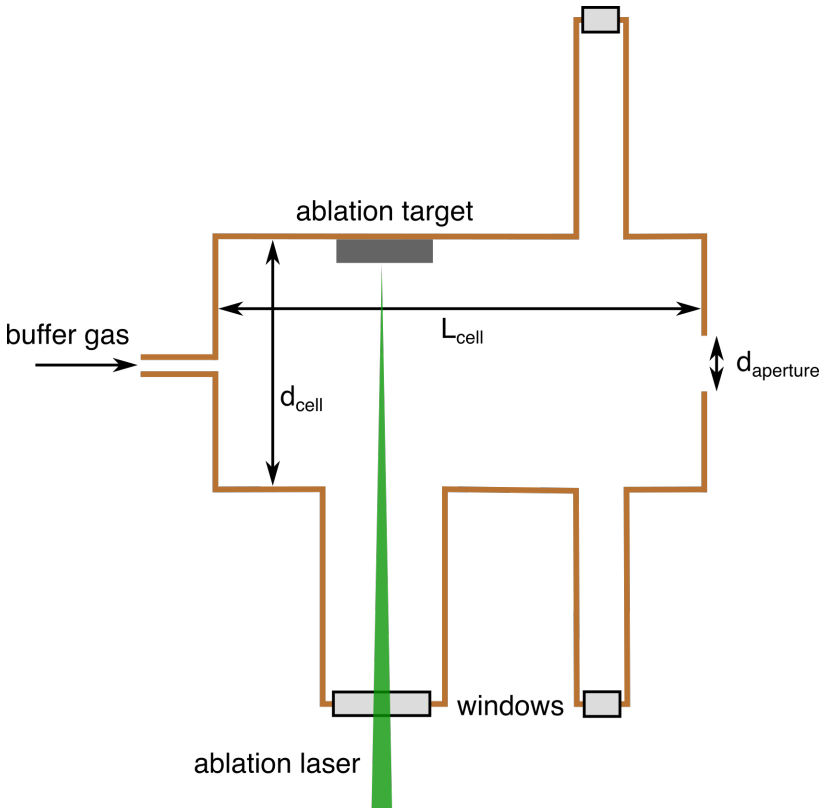

Figure 2-7: Schematic diagram of a buffer gas cell in which atoms/molecules are loaded by laser ablation of a solid target. Windows are typically mounted on the cell far from the ablation target to slow the collection of ablated dust. The important geometrical parameters of the buffer gas cell are labeled.

The flow rate out of the cell, f_{out} is given by a standard result from gas kinetic theory for the conductance of an aperture.

$$f_{\text{out}} = \frac{1}{4} n_{0,b} \bar{v}_{0,b} A_{\text{aperture}} \tag{2.14}$$

In this expression, $n_{0,b}$ refers to the number density of buffer gas ("b") under stagnation or steady-state conditions ("0"). The mean velocity of the buffer gas is also a standard result, and is equal to 145 m/s for both Ne at 20 K and He at 4 K,

$$\bar{v} = \sqrt{\frac{8 k_B T}{\pi m}} \tag{2.15}$$

At steady state, the flow rate of the buffer gas into the cell must be equivalent to the flow rate out, $f_{0,b} = f_{\text{out}}$, so the buffer gas number density can be determined as a function of the flow rate, controlled by the experimenter,

$$n_{0,b} = \frac{4 f_{0,b}}{A_{\text{aperture}} \bar{v}_{0,b}} \tag{2.16}$$

According to Hutzler et al.,[72] typical flow rates are $f_{0,b} = 1 - 100$ SCCM, which, for typical cell dimensions, give a stagnation density of $10^{15} - 10^{17}$ cm^{-3}. For our buffer gas cell, we estimate a stagnation density of 3.4×10^{16} cm^{-3} at a flow rate of 20 SCCM. This corresponds to a pressure of 70 mtorr at 20 K, as calculated from the ideal gas law:

$$P = \frac{N}{V} \frac{R}{N_A} T = n_{0,b} k_B T \tag{2.17}$$

where N is the number of particles, R is the gas constant, N_A is Avogadro's number, and k_B is Boltzmann's constant. It should be noted that these estimates rest on the initial assumption that the flow out of the cell aperture is free-molecular, rather than fluid-like (hydrodynamic), as one might expect at high number density. The maximum flow rate in the hydrodynamic regime is given by[121]

$$f_{\text{out}} = n_{0,b} \bar{v}_{0,b} \frac{\sqrt{\pi}}{2} \left(\frac{\gamma}{\gamma + 1} \right)^{1/2} \left(\frac{2}{\gamma + 1} \right)^{1/(\gamma+1)} \tag{2.18}$$

Here, γ is the specific heat ratio and $\gamma = 5/3$ for a monatomic gas like helium. With this value of γ, the maximum hydrodynamic flow rate is 1.8 times the effusive flow rate discussed above. Considering this relatively small difference in the two limits, we will continue to use the effusive limit result to estimate the cell parameters throughout. In fact, the flow rate approaches the effusive rate at low buffer gas loading rates and approaches the hydrodynamic rate at higher buffer gas loading rates. The details of this transition have been investigated in numerical simulations by the Imperial College group.[24, 136]

2.3.2 Thermalization

This section begins with the derivation of a simple thermalization model, originally presented by Kim.[83] We consider thermalization of species atoms/molecules at initial temperature T_i, which reach a temperature T_N after N collisions with the buffer gas at temperature T_b. We start by examining the effect of a single collision on the temperature. Assume that the buffer gas and the species are point particles of mass m and M, respectively, with velocities v_i and V_i before the collision and velocities v_f and V_f after the collision. We switch to the center of mass frame where $V_{cm} = \dfrac{MV_i + mv_i}{M+m}$. Let $\tilde{v}_i$, $\tilde{V}_i$, $\tilde{v}_f$, and $\tilde{V}_f$ be the aforementioned velocities in the center of mass frame. In this frame, the laws for conservation of momentum and energy are given by:

$$P^{\text{tot}} = 0 = M\tilde{V}_i + m\tilde{v}_i = M\tilde{V}_f + m\tilde{v}_f \tag{2.19}$$

$$E^{\text{tot}} = \frac{M}{2}\tilde{V}_i^2 + \frac{m}{2}\tilde{v}_i^2 = \frac{M}{2}\tilde{V}_f^2 + \frac{m}{2}\tilde{v}_f^2 \tag{2.20}$$

After some rearrangement of the conservation laws, and averaging over statistical distributions, we find

$$\langle \tilde{V}_f^2 \rangle = \langle \tilde{V}_i^2 \rangle \tag{2.21}$$

$$= \langle V_i^2 + V_{cm}^2 - 2V_i \cdot V_{cm} \rangle \tag{2.22}$$

$$= \langle V_i^2 \rangle + \langle V_{cm}^2 \rangle - \frac{2M}{M+m}\langle V_i^2 \rangle - \frac{2m}{M+m}\langle V_i \cdot v_i \rangle \tag{2.23}$$

$$= \left(1 - \frac{2M}{M+m}\right) \langle V_i^2 \rangle + \langle V_{cm}^2 \rangle \tag{2.24}$$

$$\langle V_f^2 \rangle = \left\langle \left(\tilde{V}_f + V_{cm}\right)^2 \right\rangle \tag{2.25}$$

$$= \langle \tilde{V}_f^2 \rangle + \langle V_{cm}^2 \rangle + 2\langle \tilde{V}_f \cdot V_{cm} \rangle \tag{2.26}$$

$$= \left(1 - \frac{2M}{M+m}\right) \langle V_i^2 \rangle + 2\langle V_{cm}^2 \rangle \tag{2.27}$$

$$= \left(1 - \frac{2M}{M+m}\right) \langle V_i^2 \rangle + \frac{2}{(M+m)^2} \left(M^2 \langle V_i^2 \rangle + m^2 \langle v_i^2 \rangle\right) \tag{2.28}$$

$$= \frac{M^2+m^2}{(M+m)^2} \langle V_i^2 \rangle + \frac{2m^2}{(M+m)^2} \langle v_i^2 \rangle \tag{2.29}$$

$$\langle V_f^2 - V_i^2 \rangle = \frac{M^2+m^2}{(M+m)^2} \langle V_i^2 \rangle + \frac{2m^2}{(M+m)^2} \langle v_i^2 \rangle - \langle V_i^2 \rangle \tag{2.30}$$

$$= -\frac{2Mm}{(M+m)^2} \langle V_i^2 \rangle + \frac{2m^2}{(M+m)^2} \langle v_i^2 \rangle \tag{2.31}$$

$$= -\frac{2m}{(M+m)^2} \left(M \langle V_i^2 \rangle - m \langle v_i^2 \rangle\right) \tag{2.32}$$

Note in the above derivation that the cross terms $\langle V_i \cdot v_i \rangle$ and $\langle \tilde{V}_f \cdot V_{cm} \rangle$ must be zero by symmetry. Finally, we recognize the definition of temperature $T = \frac{1}{2} m \langle v^2 \rangle$ in the above equation to arrive at the change in temperature from a single collision,

$$T_f - T_i = -\frac{1}{\kappa} \left(T_i - T_b\right) \tag{2.33}$$

where $\kappa \equiv \dfrac{(M+M)^2}{2Mm}$. The temperature difference between the N^{th} and $(N-1)^{\text{th}}$ collision can be written as

$$T_N - T_{N-1} = -\frac{T_{N-1} - T_b}{\kappa} \tag{2.34}$$

where T_N is the temperature of the species molecule after N collisons with the buffer gas. We generalize this discrete equation to a differential equation and solve.

$$\frac{\mathrm{d}T}{\mathrm{d}N} = -\frac{T - T_b}{\kappa} \tag{2.35}$$

$$T(N) = (T_i - T_b) e^{-N/\kappa} + T_b \tag{2.36}$$

Now, we recognize κ as a characteristic (i.e., $1/e$) number of collisions for thermalization. Perhaps more significant is the number of collisions required for a species molecule to be within 10% of the buffer gas temperature. This typically occurs in around 50 collisions. As a specific example, consider thermalization of $^{138}Ba^{19}F$, initially at 1000 K after laser ablation of a solid BaF_2 target, in 20 K ^{20}Ne. For these parameters, the characteristic constant is 5 collisions, while the temperature of the BaF molecules would reach within 2 K of the Ne buffer gas temperature after 31 collisions.

Of more practical significance than the number of collisions required for thermalization, we would like to estimate both the time and cell size required for thermalization. We begin by considering the mean free path of the species molecule in a buffer gas, which is defined by

$$\lambda_{b,s,0} = \frac{(n_{0,b}\sigma_{b,s})^{-1}}{\sqrt{1 + m_s/m_b}} \tag{2.37}$$

where the subscript "b, s" refers to a property in which the buffer gas and species molecule are collision partners. For a buffer gas number density of 3.4×10^{16} cm^{-3} and an approximate collisional cross-section, $\sigma_{b,s}$, of 1×10^{-14} cm^2, the mean free path of $^{138}Ba^{19}F$ in Ne is about 0.01 mm. Molecules produced by ablation, like BaF, are much more massive than the buffer gas and are at elevated translational temperatures (typically, 1000 K). Transport through the buffer gas can be assumed to be ballistic, giving a thermalization length of $N \times \lambda_{b,s,0}$ rather than $\sqrt{N} \times \lambda_{b,s,0}$ as one might expect for a random walk model of diffusion through the buffer gas,[a] where N is the number of collisions. Our earlier estimate established that thermalization occurs in <

[a] A cute, non-rigorous argument for the $\sqrt{N}$ dependence goes something like this: Consider a one-dimensional discrete random walk. By symmetry, the expected position after n steps must be the same as after $n-1$ steps, since a random walk is unbiased and motion in each direction is equally likely.

$$\langle x_n \rangle = \langle x_{n-1} \rangle$$

Therefore, $\langle x \rangle$, the first moment of position, is invariant. The expected position cannot change. Now consider the second moment of position, $\langle x^2 \rangle$. Suppose after several steps the particle is at position 7, i.e., $x = 7$ and $\langle x^2 \rangle = 7^2 = 49$. After the next step, it must be at either $x = 6$ or $x = 8$. Then,

$$\langle x^2 \rangle = \frac{1}{2}\left(6^2 + 8^2\right) = 50$$

The expected squared position increased by 1. Consider another example. If the particle is at $x =$

50 collisions, so the thermalization length for BaF in Ne is $< 50 \times 0.01$ mm $= 0.5$ mm. This length establishes a minimum size for the buffer gas cooling cell in order to ensure that thermalization occurs before the molecules freeze to the walls. The time required for this to happen is $\tau_{\text{therm}} = N \times \lambda_{b,s,0} \times \bar{v}_{0,b}^{-1}$, where $\bar{v}_{0,b}$ is the mean velocity of the buffer gas. Here, we assumed that the velocity of the buffer gas is the only important parameter because the number density of buffer gas is usually orders of magnitude larger than that of the species molecule. Plugging 145 m/s into this equation yields the thermalization time, $\tau_{\text{therm}} \approx 3$ μs with a mean time between collisions, $\tau_{b,s,0} \approx 70$ ns. For lower buffer gas densities, larger cells are required for effective thermalization.

For ablation-loaded buffer gas beams, it has been noted that the time for thermalization is typically a few milliseconds, significantly longer than what is predicted from the above simple model for thermalization. This is believed to be due to heating of the buffer gas itself, which must then re-thermalize with the walls of the cold cell. The Imperial College group has performed detailed experimental studies of this phenomenon in ablation-loaded cells of Yb atoms and YbF molecules.[24,136] Their observations suggest that translational (and rotational) thermalization occurs on a time scale shorter than the time resolution of their experiment ($\lesssim 100$ μs), and the observed temperature evolution can be attributed entirely to the temperature evolution of the He buffer gas. They consider a thermal diffusion model similar to matter diffusion inside the cell.

For a cell with characteristic length a, the lowest-order thermal diffusion mode has

---

10, then $\langle x^2 \rangle = 100$ and, after one more step,

$$\langle x^2 \rangle = \frac{1}{2}\left(9^2 + 11^2\right) = 101$$

An increase of 1 again! Thus, we conclude that

$$\langle x_{n+1}^2 \rangle = \langle x_n^2 \rangle + 1$$

which is the same as saying

$$\langle x_n^2 \rangle = n$$

Perhaps surprisingly, this result holds in three dimensions as well. If each step is the same distance, l, then the distance traveled after n steps is

$$\Delta x_n \sim l \times \sqrt{\langle x_n^2 \rangle} = \sqrt{n} l$$

a time constant $\tau_D = a^2/(3\pi^2\alpha)$ where α is the thermal diffusivity given by $\alpha = k/c_p n$. In this expression, k is the thermal conductivity, c_p is the heat capacity at constant pressure, and n is the number density. This calculated time constant agrees well with that obtained by a single exponential decay fit to the data, $T(t) = T_f + (T_i - T_f)e^{-t/\tau_D}$. In this fit, T_i and T_f are the initial and final temperature of the buffer gas. The initial temperature can be in the range of 10 - 50 K due to rapid heating of the buffer gas during the ablation pulse, and generally increases with higher flow rates. The Imperial group has also observed more complicated thermalization dynamics, in which the temperature evolution exhibited a clear double exponential decay. The slower time constant was consistent with the lowest-order thermal diffusion time, while the faster decay time constant was approximately an order of magnitude smaller. This fast time constant was attributed to a sum of higher-order diffusion modes that rapidly conduct heat away, leaving only the small amplitude lowest-order mode operative at long times. This model is analogous to the double exponential decay that the authors fit to the diffusion behavior of the atoms in this experiment, further supporting their interpretation.

Rotational cooling

Rotational relaxation cross sections for molecules in a buffer gas are typically $\sigma_{rot} \approx 10^{-15} - 10^{-16}$ cm^2, which are only one to two orders of magnitude smaller than typical elastic collision cross sections. This implies a rotational "quench" occurs once every 10 to 100 elastic collisions. Since this is similar to the number of elastic collisions required to thermalize the translational temperature, one expects very similar translational and rotational temperatures in a buffer gas cell. The physical intuition behind this result is that rotational quenching is controlled by the angular anisotropy of the interaction between the rotating molecule and the buffer gas atom, and the timescale for a cold collision is similar to a rotational period.[25]

Vibrational cooling

Collision-induced quenching of vibrations is generally much less efficient than for rotations. The relaxation is driven by the dependence of the buffer gas-species molecule interaction on the internuclear distance of the molecule. The vibrational motion of nuclei, which is characterized by large energy gaps, is much faster than a cold atom collision.[25]

The vibrational relaxation dynamics of a small number of molecules have been investigated under buffer gas cooling conditions. These species are listed in Table 2.1 and the data are plotted in Figure 2-8. The dimensionless parameter ζ is defined as the ratio of the buffer gas-species molecule momentum transfer collision cross section to the vibrational relaxation cross section, $\sigma_{b,s}/\sigma_{\mathrm{vib}}$. Under the conditions listed in Table 2.1, all species undergo many-partial wave collisions with the buffer gas and so it is worthwhile to attempt to draw some general conclusions. I have fit an exponential function to the data in Figure 2-8, where the experimental value of ζ is plotted as a function of vibrational frequency. The data point for NH has been excluded because its frequency is much higher than the other species considered, and the experimentally determined lower bound was limited by radiative decay of the vibrationally excited NH molecules.[26] The data point for TiO was excluded due to the large uncertainty of the value reported by the authors.[161] Neglecting these specific cases, the demonstrated strong dependence of ζ on vibrational frequency agrees generally with our intuition. Lower frequency vibrations have energy gaps closer to the energy of a cold atom-molecule collision and thus translational-vibrational energy transfer is more efficient.

Further details of vibrational relaxation may be explored in polyatomic species, where modes can be distinguished not only by frequency, but also by vibrational motion, e.g., bend vs. stretch. Indeed, Piskorski points out that the fluorobenzene mode 18b is an in-plane C-F bend, while the other two studied modes of fluorobenzene are out-of-plane deformations of the ring.[123] Fluorobenzene(18b) has the smallest vibrational relaxation cross section (largest ζ) among these three vibrations, and clearly appears above the fit line. In contrast, benzonitrile(21), an out-of-plane C-

Table 2.1: Vibrational relaxation parameters for several molecule-buffer gas systems, listed in the first column. For polyatomic molecules, the particular vibrational mode is indicated in parentheses. The dimensionless parameter, ζ, appears in the second column and is defined as the ratio of the buffer gas-molecule momentum transfer collision cross section to the vibrational relaxation cross section. The third column lists the energy (cm^{-1}) of the vibration, and the fourth column lists the temperature of the buffer gas in the experiment. All experiments operate at temperatures high enough that the molecules undergo many-partial wave collisions with the buffer gas.

System	ζ	ω (cm^{-1})	T (K)	Ref.
CaH-^{3}He	$> 9 \times 10^5$	1258	0.5	[161]
NH-^{3}He	$> 5 \times 10^4$	3093	0.6	[26]
ThO-^{3}He	2×10^4	896	1.2	[8]
TiO-^{4}He	130	1000	5	[94]
SrOH(100)-^{4}He	700	527	2.2	[87]
SrOH(010)-^{4}He	< 100	364	2.2	[87]
Benzonitrile(21)-^{4}He	8.33	372	6	[123]
Benzonitrile(22)-^{4}He	6.25	141	6	[123]
Fluorobenzene(18b)-^{4}He	280	400	6	[120,123]
Fluorobenzene(16a)-^{4}He	70	414	6	[120,123]
Fluorobenzene(11)-^{4}He	9.33	249	6	[120,123]

C-N deformation, has a smaller ζ value than might be expected from the fit line, and is similar to the ζ value of the much lower frequency benzonitrile(22) in-plane C-N bending mode. It is therefore tempting to speculate that out-of-plane modes of substituted benzene rings may generally have larger vibrational relaxation cross sections than in-plane modes, since, classically, the cross section of a ring face is larger than the cross section of a ring edge. Further investigation of these complex dynamics is certainly warranted, and buffer gas cells are an ideal experimental tool.

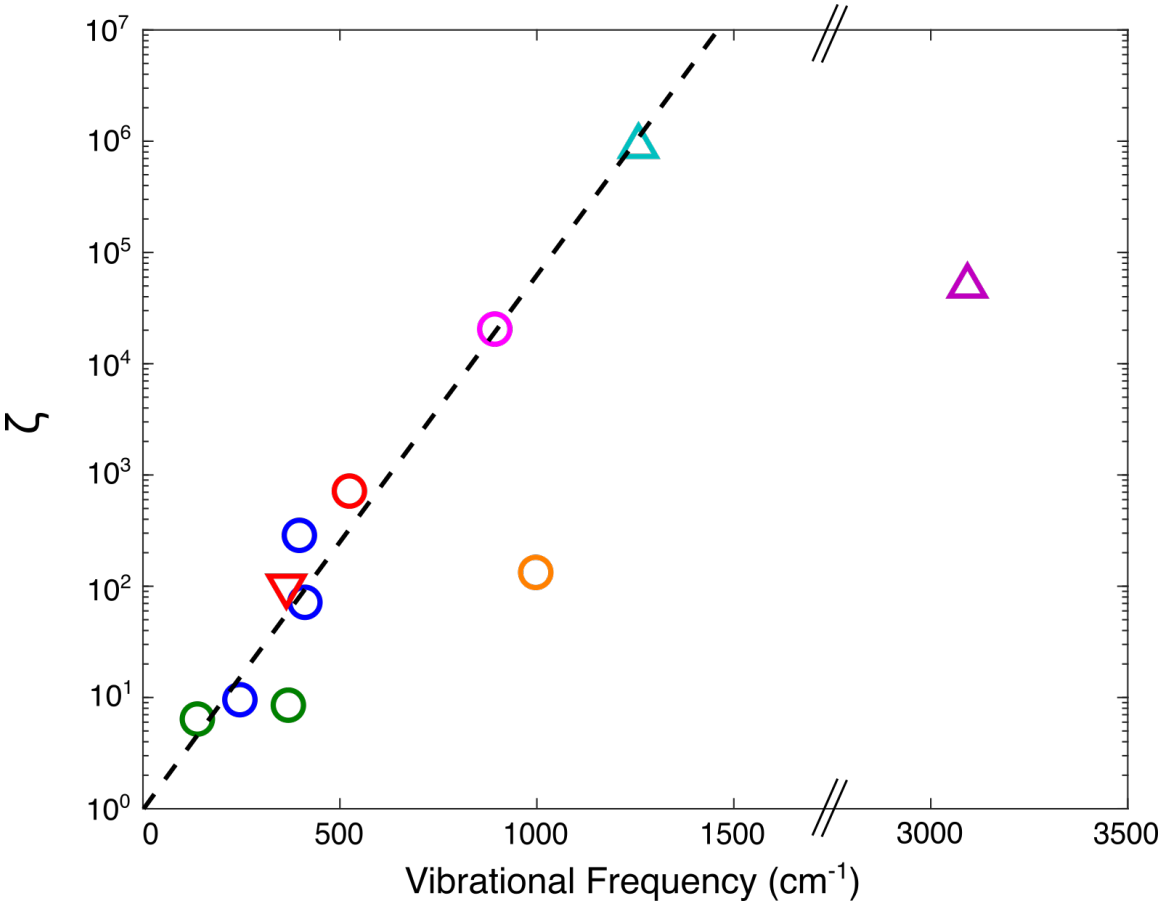

Figure 2-8: Experimentally determined ratio of translational to vibrational cross sections (ζ) for one or more vibrational modes of the molecules: benzonitrile (green), fluorobenzene (blue), SrOH (red), ThO (magenta), CaH (cyan), TiO (orange), and NH (purple), under experimental conditions listed in Table 2.1. The upward- and downward-pointing triangles indicate lower and upper bounds, respectively. The dashed line is a fit to the data, excluding the TiO and NH data points. These results suggest an exponential relationship between vibrational relaxation cross section and the frequency of vibration.

2.3.3 Diffusion and extraction

To make some estimates of the diffusion behavior in the cell, we take just the first term in a series approximation for the diffusion coefficient,

$$D = \frac{3}{16(n_{0,s} + n_{0,b})\sigma_{b,s}}\sqrt{\frac{2\pi k_B T}{\mu}} \tag{2.38}$$

where $n_{0,s}$ is the stagnation number density of the species ("s") of interest, $\sigma_{b,s}$ is the buffer gas-species molecule collisional cross section, and $\mu = \dfrac{m_s m_b}{m_s + m_b}$ is the reduced mass. If we make the approximations $n_{0,s} \ll n_{0,b}$ and $m_s \gg m_b$, then the diffusion constant equation simplifies to

$$D = \frac{3}{16 n_{0,b}\sigma_{b,s}}\sqrt{\frac{2\pi k_B T}{m_b}} = \frac{3\pi}{32}\frac{\bar{v}_{0,b}}{n_{0,b}\sigma_{b,s}} \tag{2.39}$$

The second step follows by inserting the expression for the mean velocity from Equation 2.15. After a time, t, a species molecule will have a mean-squared displacement from its starting point:

$$\langle \Delta x^2 \rangle(t) = 6Dt = \frac{9\pi}{16}\frac{\bar{v}_{0,b}}{n_{0,b}\sigma_{b,s}} \tag{2.40}$$

The diffusion time scale, τ_{diff}, is determined by the characteristic length of the cell, which is the cross-sectional length d_{cell}. Then, we can equate $\langle \Delta x^2 \rangle(\tau_{\text{diff}}) = d_{\text{cell}}^2 \approx A_{\text{cell}}$ or, after rearrangement,

$$\tau_{\text{diff}} = \frac{16}{9\pi}\frac{A_{\text{cell}} n_{0,b}\sigma_{b,s}}{\bar{v}_{0,b}} \tag{2.41}$$

Hutzler et al. note that typical diffusion times are in the range of 1-10 ms.[72] In order to estimate the diffusion time in our setup, it is necessary to estimate the collisional cross-section $\sigma_{b,s}$. To make some rough estimates, we assume $\sigma_{b,s} \approx \sigma_{He,He} = 1.05 \times 10^{-14}$ cm^2. This is a common assumption with some experimental justification. Barry et al. make this approximation for the quantity $\sigma_{SrF,He}$ and obtain reasonable estimates of their cell parameters.[10] Skoff et al. calculated values of 7.1×10^{-15} cm^2 and 8.0×10^{-15} cm^2 for $\sigma_{Li,He}$ and $\sigma_{YbF,He}$, respectively, and measured a value for

$\sigma_{YbF,He}$ of 2.0×10^{-14} cm^2.[136]

Making this approximation, the diffusion time of our system is $\tau_{\text{diff}} = 130$ ms, somewhat longer than the "typical" values described by Hutzler et al.[72] From the expression for τ_{diff} it is clear that this value can be tuned by changing the geometry (building a cell with a larger or smaller cross-sectional area) or the experimental conditions (increasing or decreasing the input flow rate and thus the stagnation number density).

It is worth noting here some details from the results of Skoff et al.[136] By collecting absorption images of ablated Li atoms and YbF molecules in their buffer gas cell, they obtained an experimental measurement of the diffusion constant for these species. At low He densities ($\lesssim 3\times10^{15}$ cm^3), they observed the linear dependence on density that would be predicted from Equation 2.41. Above that density, however, the diffusion lifetime generally plateaued or increased more slowly. They interpreted these results to mean higher-order diffusion modes, not considered in this simple model, become increasingly important. These results also suggest that this model likely overestimates the diffusion time in our own system.

To estimate the pump-out time for the cell, we simply re-examine the expression for the flow rate out of the cell, f_{out}, recognizing that f_{out} is the number of buffer gas atoms leaving the cell per unit time.

$$f_{\text{out}} = \frac{1}{4} n_{0,b} \bar{v}_{0,b} A_{\text{aperture}} \tag{2.42}$$

$$\frac{\mathrm{d}N_b}{\mathrm{d}t} = \frac{1}{4} N_b \bar{v}_{0,b} \frac{A_{\text{aperture}}}{V_{\text{cell}}} \tag{2.43}$$

By integrating both sides of Equation 2.43, we obtain an expression for the number of buffer gas atoms that is a simple exponential decay as a function of time. The time constant for this process, τ_{pump}, is given by

$$\tau_{\text{pump}} = \frac{4V_{\text{cell}}}{\bar{v}_{0,b} A_{\text{aperture}}} \tag{2.44}$$

Again, Hutzler et al. note that a typical pump-out time is 1-10 ms, similar to the

diffusion time scale.[72] Again, we calculate a longer time of $\tau_{\text{pump}} = 105$ ms for our buffer gas system. For pulsed introduction of species molecules, as in laser ablation, this time should be roughly consistent with the pulse duration of the beam if the buffer gas density is high enough that the ablated molecules follow the flow of the buffer gas. To characterize the cell extraction, we can examine the dimensionless parameter:

$$\gamma_{\text{cell}} \equiv \frac{\tau_{\text{diff}}}{\tau_{\text{pump}}} \tag{2.45}$$

There are now two regimes to consider. For $\gamma_{\text{cell}} \lesssim 1$, diffusion to the walls is faster than extraction from the cell and only a small fraction of the species molecules will be present in the beam. By increasing the flow rate, the extraction efficiency can be improved, although this efficiency does not have an easily guessed dependence on γ_{cell}.

For $\gamma_{\text{cell}} \gtrsim 1$, many molecules are extracted from the cell into the beam before freezing on the cell walls. The extraction efficiency typically plateaus as the flow rate is further increased. Maximum extraction efficiencies of $> 40\%$ have been observed,[10] although 10% is more typical.

2.3.4 Beam formation

Throughout this discussion on beam formation in buffer gas-cooled and other sources, we will make use of the Reynolds number to characterize the flow. This concept, first introduced by George Stokes,[139] is defined as the ratio of inertial forces to viscous forces in a fluid,

$$Re = \frac{\rho w d}{\mu} \tag{2.46}$$

where ρ is the density of the fluid, w is the flow velocity, μ is the dynamic viscosity of the fluid, and d is a characteristic length scale, which in the case of atomic/molecular beams will refer to the aperture diameter of the source. The Reynolds number can be related to two other dimensionless parameters common in fluid dynamics by the approximate relation:

$$Ma \approx \frac{1}{2} KnRe \tag{2.47}$$

In the above equation, Kn is the Knudsen number defined by λ/d, where λ is the mean free path as defined in Equation 2.37. Ma is the Mach number, defined by w/c, where c is the speed of sound in a gas and is given by,

$$c = \sqrt{\frac{\gamma k_B T}{m}} \tag{2.48}$$

for a gas with specific heat ratio, γ, equal to 5/3 for a monatomic gas. Near the aperture of a reservoir, gas atoms travel near the mean thermal velocity, $\bar{v} = \sqrt{8k_B T/\pi m}$. For a monatomic gas, $c \approx 0.8\bar{v}$, so that near the aperture, $Ma \approx 1$, and $KnRe \approx 2$. When referring to the Reynolds number throughout the following discussion, Re has the meaning that this relationship holds near the aperture. In this way, we can relate Re directly to the collisional environment of the beam source.

$$Re \approx \frac{2}{Kn} = \frac{2d}{\lambda} \tag{2.49}$$

The Reynolds number is proportional to twice the number of collisions within one aperture diameter of the aperture.

In the following, we will use the Reynolds number so specify three regimes, which roughly correspond with the three common types of atomic/molecular beams. When $Re \lesssim 1$, no collisions occur near the aperture, so the beam samples the thermal distribution of the cell. This corresponds to an *effusive* regime. At the opposite extreme, when $Re \gtrsim 100$, many collisions occur at the aperture and the gas behaves like a fluid rather than a rarefied gas. This describes *supersonic* beams. Lastly, in the *intermediate* regime, $1 \lesssim Re \lesssim 100$, there are enough collisions at the aperture to significantly modify the properties of the beam relative to the cell, but it is not appropriate to treat the flow as "fluid-like." This regime will best typify the behavior of cryogenic buffer-gas cooled beams, although CBGBs have been demonstrated to operate in all three regimes.

Effusive beams

Effusive beams are characterized by $Kn > 1$, meaning that the mean free path of the gas is greater than the aperture diameter so no collisions occur in the vicinity of the aperture or in the effusing flow. If the aperture area is small relative to the total wall area of the source (as we will generally assume), the thermal equilibrium of the source is not affected by the effusing particles. The combination of thermal equilibrium and no collisions implies that the effusive beam will also have an equilibrium distribution of internal states. The effusive beam extracts a representative sample of the source reservoir. Since kinetic theory describes the source accurately, we can also predict several beam properties in a straightforward manner. The number density from a differential aperture area, $\mathrm{d}A$, is given by

$$n_{\mathrm{eff}}(R, v, \theta) = n(R, \theta) f(v) \tag{2.50}$$

$$n(R, \theta) = \frac{n_0 \cos\theta}{4\pi R^2} \mathrm{d}A \tag{2.51}$$

$$f(v) = \frac{32}{\pi^2 \bar{v}^3} v^2 e^{-4v^2/\pi\bar{v}^2} \tag{2.52}$$

where R is the distance from the aperture, θ is the angle from the aperture normal, n_0 is the cell density, $n(R, \theta)$ is the total number density distribution integrated over velocity, and $f(v)$ is the normalized (Maxwellian) velocity distribution in the cell. Per unit time, $\mathrm{d}t$, all particles having a speed and direction with length of motion $v\mathrm{d}t$ will contribute to the particle flux through the aperture. Thus, the velocity distribution of the beam picks up an additional factor of v:

$$f_{\mathrm{beam}}(v) = \frac{v}{\bar{v}} f(v) = \frac{32}{\pi^2 \bar{v}^4} v^3 e^{-4v^2/\pi\bar{v}^2} \tag{2.53}$$

We can now calculate the expectation value of the velocity in order to determine the mean forward velocity of an effusive beam:

$$\bar{v}_{\parallel} = \int_0^\infty v f_{\mathrm{beam}}(v) dv = \frac{3\pi}{8} \bar{v} \approx 1.2\bar{v} \tag{2.54}$$

Next, we might wish to determine the full width at half maximum (FWHM) of the angular spread, $\Delta\theta$, by considering the velocity integrated number density function. The distribution has a cosine functional dependence as seen from Equation 2.51. Using the definition of FWHM, we find:

$$n(R, \Delta\theta/2) = \frac{1}{2} n(R, 0) \tag{2.55}$$

$$\Delta\theta = \frac{2\pi}{3} = 120^\circ \tag{2.56}$$

The FWHM solid angle is related to the angular spread, $\Delta\theta$, by

$$\Delta\Omega = 2\pi \left(1 - \cos\frac{\Delta\theta}{2}\right) = \pi \tag{2.57}$$

The angular spread can be determined spectroscopically through knowledge of the beam's forward velocity, $v_\parallel$, and its transverse velocity spread, $\Delta v_\perp$. The former is determined by measuring the longitudinal Doppler shift of a transition, and the latter by measuring the transverse Doppler broadening.

$$\Delta\theta = 2\tan^{-1}\left(\frac{\Delta v_\perp/2}{v_\parallel}\right) \tag{2.58}$$

Supersonic beams

Supersonic beams represent the opposite limiting behavior from that of effusive beams. Many collisions occur near the aperture and $Kn \ll 1$. Kinetic gas theory no longer applies and the gas flow must be treated as a fluid. Usually, supersonic beams are composed of a small fraction, $\sim 1\%$, of the molecule of interest seeded in a carrier gas, like He or Ar. Thus, the temperature and flow lines of the carrier gas expansion are considered representative of the molecule of interest. We start by reviewing some fundamentals of thermodynamics in order to understand the important features of supersonic beams.

We start by writing the first law of thermodynamics, using the unit volume, $1/n$,

as

$$\mathrm{d}q = \mathrm{d}u + P\mathrm{d}(1/n) \tag{2.59}$$

Similarly, the enthalpy, h, can be written as

$$h = u + PV = u + \frac{P}{n} = u + k_B T \tag{2.60}$$

Since the internal energy of an ideal gas depends only on temperature, the enthalpy is determined entirely by the temperature of the gas. Inserting this expression for the enthalpy into the first law yields

$$\mathrm{d}q = \mathrm{d}h - \frac{1}{n}\mathrm{d}P \tag{2.61}$$

The constant-volume and constant-pressure specific heats, c_V and c_P, are defined by:

$$c_V = \left(\frac{\mathrm{d}u}{\mathrm{d}T}\right)_V \tag{2.62}$$

$$c_P = \left(\frac{\mathrm{d}h}{\mathrm{d}T}\right)_P \tag{2.63}$$

By differentiating Equation 2.60 with respect to temperature and using the specific heat definitions, we find

$$c_P = c_V + k_B \tag{2.64}$$

The specific heat ratio, $\gamma = c_P/c_V$, has been referred to previously and can be used to re-write Equations 2.62 and 2.63 as

$$c_V = \frac{1}{\gamma - 1} k_B \tag{2.65}$$

$$c_P = \frac{\gamma}{\gamma - 1} k_B \tag{2.66}$$

By the equipartition theorem, the constant-volume specific heat of a monatomic gas is equal to $1.5 k_B T$, where $0.5 k_B T$ comes from each degree of translational freedom for a gas in thermal equilibrium. Thus, the constant-pressure specific heat is equal

to $2.5k_BT$ and we obtain the ratio $\gamma = 5/3$. Although the specific heats do vary with temperature, we will make the assumption that they are constant for the temperature range of interest. In other words, our ideal gases are also calorically ideal gases.

To continue the examination of supersonic beams, we will neglect the viscosity of the gas, which is equivalent to neglecting friction and assuming a reversible process. In addition, we will neglect all heat conduction and assume adiabaticity, that is to say, no heat is exchanged between the gas and the surroundings ($\mathrm{d}q = 0$). For this reversible and adiabatic, or *isentropic* process, we can write

$$\mathrm{d}u + P\mathrm{d}\left(\frac{1}{n}\right) = 0 \tag{2.67}$$

$$\mathrm{d}h + \frac{1}{n}\mathrm{d}P = 0 \tag{2.68}$$

Plugging in the specific heat expressions (Equations 2.62 and 2.63) and the equation of state (Equation 2.17), we can rewrite these equations as

$$\frac{1}{\gamma - 1}\frac{\mathrm{d}T}{T} - \frac{\mathrm{d}n}{n} = 0 \tag{2.69}$$

$$\frac{\gamma}{\gamma - 1}\frac{\mathrm{d}T}{T} - \frac{\mathrm{d}P}{P} = 0 \tag{2.70}$$

$$\gamma\frac{\mathrm{d}n}{n} - \frac{\mathrm{d}P}{P} = 0 \tag{2.71}$$

where the last relation is obtained by combining the first two equations. Finally, we obtain the results for an isentropic expansion for constant γ by integrating the above three equations with initial and final conditions, (n_1, P_1, T_1) and (n_2, P_2, T_2).

$$\frac{P_2}{P_1} = \left(\frac{T_2}{T_1}\right)^{\gamma/(\gamma-1)} \tag{2.72}$$

$$\frac{n_2}{n_1} = \left(\frac{T_2}{T_1}\right)^{1/(\gamma-1)} \tag{2.73}$$

$$\frac{P_2}{P_1} = \left(\frac{n_2}{n_1}\right)^{\gamma} \tag{2.74}$$

In the far field, several aperture diameters away from the aperture, the density de-

creases as a point source, $n(R) \propto R^{-2}$, so according to Equation 2.73, the temperature also decreases as the gas expands.

$$T(R) \propto R^{-4/3} \tag{2.75}$$

We have walked through the thermodynamic argument for cooling of a supersonic beam, but there is an equally appealing intuitive argument. Near the aperture, gas atoms receive collisions mostly in the forward direction. As a result, the forward velocity, $v_{\parallel}$, increases as the gas expands into vacuum. Since there is no heat exchange with the environment, the increase in $v_{\parallel}$ must come at the expense of random thermal energy (temperature) in order to conserve energy. Thus, the beam cools as it expands and accelerates. This cooling continues in the beam until the density becomes too low and the atoms fly ballistically. This "freezing" or "quitting" occurs when the mean number of collisions is fewer than the number required to achieve thermalization. As discussed in Section 2.3.2, the collision number required for thermalization is $\lesssim 1$ for translational degrees of freedom and > 1 for internal degrees of freedom . As a result, the internal degrees of freedom of a molecule will fall out of equilibrium before the translational temperature reaches its final minimum value. Since vibrational relaxation cross sections are so much smaller than cross sections for rotational relaxation and momentum transfer, the vibrational temperature of supersonic beams is often significantly higher than the rotational or translational temperatures, which are typically quite similar. Quantitative predictions of the vibrational temperature are challenging and require numerical modeling of the expansion to fully characterize the number and energy of collisions throughout the expansion.

One can also see from Equation 2.72 that we can increase the cooling in the supersonic beam by increasing the pressure behind the aperture. In practice, increasing the backing pressure comes at the expense of producing clusters via three-body collisions in the beam, which can substantially reduce the concentration of the species of interest. Special pulsed nozzle designs, like the Evan-Lavie valve, have been developed to address this limitation.[38]

Beyond the "quitting surface," where the number of collisions approaches zero, the molecules continue to flow nearly collision-free. This region of the expansion is called the "zone of silence," since the local speed of sound is nearly zero, and is typically of greatest interest to the experimentalist because the molecules have reached their coldest temperatures and no collisional broadening of spectral lines occurs. In this region, the temperature parallel to the flow direction has reached a minimum since there are no additional collisions to change the velocity distribution. The perpendicular temperature, however, continues to decrease because molecules with large velocity components perpendicular to the flow continue to leave the expansion region as the flow moves downstream. This is a purely geometric effect that produces lower perpendicular temperatures further downstream.[121]

The "sudden freeze" model, which we qualitatively discussed above, has been quantitatively investigated by several authors.[7,121] In this model, the supersonic expansion is divided by the quitting surface into two regions: a region of isentropic fluid-like flow and a region of collision-less molecular flow. According to this model, which will not be re-derived here in detail, the number density in the far-field region decreases as a point source, with the explicit functional form:[121]

$$n(R) = 0.154 n_0 \left(\frac{R}{d}\right)^{-2} \tag{2.76}$$

where R is the distance from the nozzle, d is the aperture diameter, and n_0 is the source number density. Similarly, the temperature as a function of distance is found to be[121]

$$T(R) = 0.287 T_0 \left(\frac{R}{d}\right)^{-4/3} \tag{2.77}$$

The important feature of this model is that, beyond a certain distance from the nozzle, the properties of the beam become "frozen" because there are too few collisions to maintain thermal equilibrium. In other words, the quitting surface is located at the point where the collision rate is reduced to 1, the approximate collision number required for translational equilibrium to be maintained. Assuming a hard sphere

model for collisons, it can be shown that the quitting surface is located at[121]

$$R_q \approx d \times (0.1\sigma n_0 d)^{3/5} \tag{2.78}$$

where σ is the collisional cross section. This sudden freeze model will be useful in the discussion of cryogenic buffer-gas cooled beams to follow.

We can further use our thermodynamic results to analyze the maximum forward velocity of a supersonic beam. First, we will employ conservation of energy for a flowing gas. Any change in the kinetic energy of the flow must be compensated for by a commensurate change in enthalpy. For 1-D flow, this can be written in differential form as[121]

$$mw\mathrm{d}w + \mathrm{d}h = 0 \tag{2.79}$$

where w is the flow velocity and m is the mass of the gas particles. Integrating between two points in the flow, for example, at the source and a point far downstream, we obtain

$$\frac{1}{2}m\left(w_2^2 - w_1^2\right) = h_1 - h2 = \int_{T_2}^{T_1} c_P \mathrm{d}T \tag{2.80}$$

where the last step is a result of assuming isentropic flow. We can now perform the integration and substitute pressure for temperature by Equation 2.72.

$$w_2^2 - w_1^2 = \frac{2c_P T_1}{m}\left(1 - \frac{T_2}{T_1}\right) \tag{2.81}$$

$$= \frac{2c_P T_1}{m}\left[1 - \left(\frac{P_2}{P_1}\right)^{(\gamma-1)/\gamma}\right] \tag{2.82}$$

The initial point is inside the source, where the flow velocity is negligible, $w_1 \approx 0$. We recognize the flow velocity downstream, w_2, as the forward velocity of the beam, $v_\parallel$, and solve.

$$v_\parallel = \sqrt{\frac{2c_P T_1}{m}\left[1 - \left(\frac{P_2}{P_1}\right)^{(\gamma-1)/\gamma}\right]} \tag{2.83}$$

This equation is known as the St. Venant-Wantzel equation.[121] For a given source temperature, $T_1 = T$, the maximum forward velocity, $v_{\parallel,\max}$, is obtained when the

monatomic gas is expanded into a perfect vacuum, $P_2 = 0$.

$$v_{\parallel,\max} = \sqrt{\frac{5k_BT}{m}} = \bar{v}\sqrt{\frac{5\pi}{8}} \approx 1.4\bar{v} \tag{2.84}$$

The terminal velocities of rare gas supersonic beams are readily obtained in experiments and correspond to 1765 m/s for He, 786 m/s for Ne, 559 m/s for Ar, 386 m/s for Kr, and 308 m/s for Xe, all expanding from a 300 K source.

An analytic expression for the angular dependence of the density has been obtained by Ashkenas and Sherman:[7]

$$n(R,\theta) = n(R,0)\cos^2\left(\frac{\pi\theta}{2\phi}\right) \tag{2.85}$$

where ϕ is a parameter, independent of γ, that is equal to 1.365 for a monatomic gas. By equating $n(R,\Delta\theta/2) = 1/2n(R,0)$, we can obtain a prediction for the angular FWHM and the solid angle FWHM of the beam.

$$\Delta\theta = \phi = 1.365 \approx 78^\circ \tag{2.86}$$

$$\Delta\Omega \approx 1.4 \tag{2.87}$$

Finally, it is useful to revisit the meaning of the Mach number, Ma, in order to describe some further aspects of the supersonic expansion. Again, the Mach number is defined as $Ma = w/c$, where c is the speed of sound. The speed of sound (or acoustic speed or sonic speed) is the velocity of a sound wave, or small pressure disturbance, in a medium. In general, the speed of sound can be written for any medium as

$$c = \sqrt{\frac{\mathrm{d}P}{\mathrm{d}\rho}} \tag{2.88}$$

where ρ is the (mass) density of the medium. Recognizing that $\rho = mn$, where m is the particle mass, and using Equation 2.71, we can recover the expression for the speed of sound introduced in Equation 2.48.

Now, we will consider the meaning of c for subsonic ($w/c < 1$) and supersonic

($w/c > 1$) flows. In the frame of reference moving at the flow speed, w, the propagation speed of a pressure disturbance is identical to that in a medium at rest, c. In the space fixed frame, however, the propagation is at the relative velocity $\mathbf{c}+\mathbf{w}$, which is $c-w$ in the upstream direction and $c+w$ in the downstream direction. Consider a pressure disturbance occurring at some instant in time. The disturbance propagates at the speed of sound as a spherical wave, the center of which travels at the flow velocity, w. For subsonic flow, the sound wave will propagate in all directions, but at different velocities. For supersonic flow, the center moves faster than the propagation of the pressure disturbance, producing two important results: 1) All sound waves are confined within a cone about the propagation direction. Outside of the cone there are no pressure disturbances. This conical separating surface represents a wave front, called a Mach wave. The angle, α, between the Mach wave and the propagation direction is defined geometrically:

$$\sin\alpha = \frac{c}{w} = \frac{1}{Ma} \tag{2.89}$$

2) There is no propagation of sound in the backward (upstream) direction. This clearly follows from the definition of the relative speed, $c-w$, in the upstream direction, and has important implications for the "termination" of the supersonic expansion. We have so far considered the supersonic beam to be formed in some idealized environment with perfect vacuum and no walls. In reality, the expansion eventually terminates in both the transverse and longitudinal directions with the formation of shock waves. One way to understand the presence of shock waves is that some boundary conditions exist that the expansion must satisfy. Information about downstream boundary conditions can only travel at the speed of sound. Thus, the speed of the flow is faster than the speed of information transfer. A sudden discontinuity in pressure, in the form of a shock wave, is the only way that the flow can satisfy the boundary conditions. A more microscopic view of these shock waves is that the vacuum is not perfect and some background pressure exists in the chamber. The number density along the expansion will decrease until it approaches the number density of

the background gas. At that point, collisions between the atoms in the flow and atoms of the background gas result in randomization of the flow atoms' velocities and adjustment to the downstream boundary conditions. At the edges of the expansion, the "jet boundary," the collisions between atoms in the expansion and the background typically produce compression waves that are reflected from this boundary and act to re-compress the expansion, thereby forming the transverse shock region called the "barrel shock." At some distance downstream these compression waves intersect to form the "Mach disk," which is a shock wave normal to the propagation direction, and the expansion terminates. The location of the Mach disk has been determined empirically:[7]

$$x_{Ma} = 0.67\sqrt{\frac{P_0}{P_{bg}}} \tag{2.90}$$

where P_0 is the source pressure and P_{bg} is the background pressure in the chamber.

Cryogenic Buffer Gas Cooled Beams

Buffer gas beams have been demonstrated to operate over a wide range of flow conditions. We will revisit the results derived for both effusive and supersonic beams, while also addressing the physics of the intermediate flow regime that is unique to buffer gas beams.

Forward velocity For low flow, $Re \lesssim 1$, the forward velocity of the beam is identical to an effusive beam

$$v_{\parallel,s} = \frac{3\pi}{8}\bar{v}_{0,s} \tag{2.91}$$

Note that the low source temperatures of buffer gas cells (4-20 K) relative to oven sources ($>$ 1000 K) means that buffer gas cooled beams in the effusive regime have much slower forward velocities than traditional oven sources. Practically, operating buffer gas sources in the effusive regime can be challenging and often requires modification of the buffer gas cell to include additional slowing cells.[65]

As the flow is increased, $Re \gtrsim 1$, the species molecules will begin to experience collisions with buffer gas atoms near the aperture. The average velocity of buffer gas

atoms, $\bar{v}_{0,b}$, is typically larger than that of the more massive species molecules, $\bar{v}_{0,s}$, by the factor $\sqrt{m_s/m_b}$. The species molecules near the aperture will experience collisions primarily in the forward direction and be "boosted" to a larger forward velocity, as in a supersonic beam source. A simple model can be used to estimate the forward velocity $v_{\parallel}$ as a function of Re.[73] From Equation 2.49, we know that the number of collisions near the aperture is approximately $Re/2$. Each collision imparts the species molecule with momentum $m_b v_b$, giving a net velocity change of $v_b m_b Re/2m_s$. If there are relatively few collisions, the forward velocity of the buffer gas is approximately equal to the forward velocity of an effusive beam, $v_{\parallel,b} = \frac{3\pi}{8}\bar{v}_{0,b}$. Thus, over some range of small Re, the forward velocity of the species molecules is given by

$$v_{\parallel,s} = \frac{3\pi}{8}\bar{v}_{0,s} + \frac{3\pi}{16}\bar{v}_{0,b} Re \frac{m_b}{m_s} \tag{2.92}$$

This linear relationship between forward velocity and Re has been observed by several authors[73,99] for low values of Re. Of course, the maximum possible forward velocity is $\frac{5\pi}{8}\bar{v}_{0,b}$, as in a supersonic beam, therefore this linear model must break down as $v_{\parallel,s}$ approaches $\bar{v}_{0,b}$.

Hutzler et al.[73] used the sudden freeze model in order to describe the dynamics in this higher flow regime. We want to rewrite the St. Venant-Wantzel equation (Equation 2.83) in terms of the Reynolds number at the position of the quitting surface. This is accomplished by using the isentropic relation in Equation 2.74, and replacing the number density with the far-field functional form of Equation 2.76. Next, Equation 2.78 is substituted for the position of the quitting surface. Finally, from Equation 2.49 and the definition of the mean free path in Equation 2.37, we recognize that the Reynolds number near the aperture is given by $Re \approx 2\sqrt{2}\sigma n_0 d$. This procedure yields the desired relation between forward velocity and Reynolds number:

$$v_{\parallel,s} = \sqrt{\frac{5\pi}{8}}\bar{v}_{0,b}\sqrt{1 - \left(\frac{n(R_q)}{n_0}\right)^{2/3}} \tag{2.93}$$

$$\approx \sqrt{\frac{5\pi}{8}}\bar{v}_{0,b}\sqrt{1-0.3\left(\frac{R_q}{d}\right)^{-4/3}} \tag{2.94}$$

$$\approx \sqrt{\frac{5\pi}{8}}\bar{v}_{0,b}\sqrt{1-2\left(\sigma n_0 d\right)^{-4/5}} \tag{2.95}$$

$$\approx \sqrt{\frac{5\pi}{8}}\bar{v}_{0,b}\sqrt{1-4Re^{-4/5}} \tag{2.96}$$

By inspection of Equation 2.96, we can see that the sudden freeze model is only valid for $Re \gtrsim 10$, which corresponds with flow rates that produce collisions in the beam at downstream distances beyond about one aperture diameter.

In the limit of very high flow rate, or large Re, the beam is fully boosted to the terminal velocity of the buffer gas

$$v_{\parallel,s} \approx v_{\parallel,b} = \sqrt{\frac{5\pi}{8}}\bar{v}_{0,b} \tag{2.97}$$

This approximation is valid for $Re \gtrsim 100$, where, according to the sudden freeze model, $v_{\parallel,s} \approx 0.95 \times v_{\parallel,b}$. These four different regimes and their functional forms are summarized in Figure 2-9, where the calculated forward velocity of a buffer gas beam of ^{138}Ba^{19}F in ^{20}Ne (20 K cell temperature) is plotted on a semilog scale. Although the two functional forms in the intermediate regime do not overlap, note the similar slopes around the transition region, $Re \sim 10$. In our BaF buffer gas experiments, the forward velocity was measured by observing Doppler doublets of a Rydberg-Rydberg transition in a longitudinal CP mmW experiment.[169] The measured velocity of ~ 200 m/s suggests that our beam was operating in a regime of significant "hydrodynamic enhancement." This agrees with our additional observation that the BaF molecules have a rotational temperature, $T_{\text{rot}} \approx 3$ K, well below the cell temperature, $T_{\text{cell}} = 20$ K.

Velocity spread In the effusive regime, the longitudinal velocity spread is given by the FWHM of a 1-D Maxwell-Boltzmann velocity distribution:

$$\Delta v_{\parallel,s} = \sqrt{8\ln 2} \times \sqrt{\frac{k_B T_0}{m_s}} = \bar{v}_{0,s}\sqrt{\pi \ln 2} \approx 1.5\bar{v}_{0,s} \tag{2.98}$$

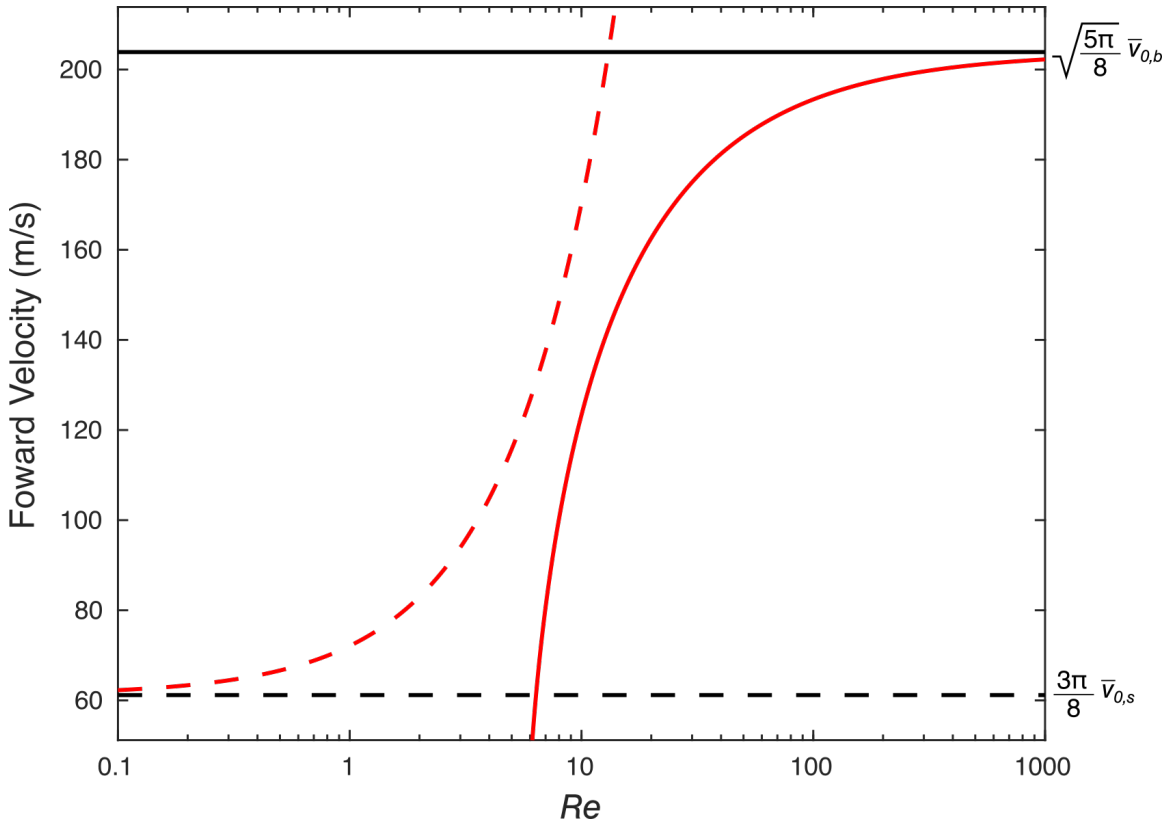

Figure 2-9: Theoretical forward velocity of a cryogenic buffer gas beam of BaF molecules in Ne with a 20 K source. The Reynolds number on the x-axis is scaled logarithmically to display the four flow regimes: effusive, $Re \lesssim 1$, dashed black; linear intermediate, $1 \lesssim Re \lesssim 10$, dashed red; "sudden freeze" intermediate, $10 \lesssim Re \lesssim 100$, solid red; fully hydrodynamic, $Re \gtrsim 100$, solid black. The four models for beam velocity are described in the text.

As the Reynolds number is increased, the forward velocity spread will decrease as the gas isentropically expands into vacuum. This is the same physics that produces a translationally cold supersonic beam. As a result, the beam can exhibit translational temperatures below the cell temperature.

The transverse velocity spread in the effusive regime is expected to be identical to the longitudinal velocity spread.

$$\Delta v_{\perp,s} \approx 1.5 \bar{v}_{0,s} \tag{2.99}$$

For low Re, collisions near the aperture result in an increase in the FWHM of the transverse velocity distribution. Hutzler et al.[73] developed a model that accounts for the increasing transverse velocity spread with increasing Re. As the flow increases, buffer gas-species molecule collisions, which are transverse to the forward beam direction at the aperture, increase the beam divergence. There will be a significant number of perpendicular collisions since the flow must be convergent due to the significant difference between d_{aperture} and d_{cell}. If the flow velocity at the aperture is approximated as $\bar{v}_{0,b}$, then the flow velocity in the cell should be reduced by approximately the ratio of cross sectional areas

$$v_{cell} \approx \bar{v}_{0,b} \frac{d_{\text{aperture}}^2}{d_{\text{cell}}^2} \tag{2.100}$$

Previously, we assumed that the in-cell dynamics are gas kinetic and there is no net flow inside the cell. The above equation gives a much smaller "flow" velocity inside the cell than at the aperture, in accord with this earlier intuition. Proceeding as before, we recall that there are around $Re/2$ collisions near the aperture, and that the relative velocities are scaled by m_b/m_s, to yield

$$\Delta v_{\perp,s} = \bar{v}_{0,s} \sqrt{\pi \ln 2} + \bar{v}_{0,b} \frac{Re}{2} \frac{d_{\text{aperture}}^2}{d_{\text{cell}}^2} \frac{m_b}{m_s} \tag{2.101}$$

Note that there is a typo in this formula in both the original paper[73] and the later review article,[72] but the numerical values are correct. This linear scaling of the

transverse velocity spread was observed near the aperture, while further downstream, linear scaling behavior was observed, but with a slightly different proportionality factor.[73] When Re is increased further, the transverse velocity spread will approach that of the buffer gas.

Note that different experiments have produced different results for the change in transverse velocity spread with Reynolds number. In some cases,[7399] there is a region of low Re where the transverse spread is relatively constant at $\sim 1.5\bar{v}_{0,s}$ before increasing linearly as described. Others have observed a constant increase in transverse velocity spread as a function of flow rate.[10] This discrepancy suggests that the transverse velocity spread is particularly sensitive to the geometry of the cell and the in-cell gas dynamics. Although there might be qualitatively similar features of the $\Delta v_\perp$ vs. Re relationship among different buffer gas set-ups, the quantitative relationship is unique to every set-up.

Divergence As a reminder, we found that for an effusive beam the angular spread is $\Delta\theta = 2\pi/3$ and the solid angle spread is $\Delta\Omega = \pi$, while for a supersonic beam, $\Delta\theta = \Delta\Omega \approx 1.4$. Consider first a buffer gas beam that displays a region of constant $\Delta v_{\perp,s} \approx 1.5\bar{v}_{0,s}$ as described above in the low Re range, $1 \lesssim Re \lesssim 10$. Over this same range, the forward velocity of the beam increases as described above. As a result of these two factors, over some range, the angular spread, or beam divergence, will decrease. If we make the gross simplification that the forward velocity of the species molecules approaches the mean velocity of the buffer gas in the cell, $v_{\parallel,s} \approx \bar{v}_{0,b}$, then the divergence will approach

$$\Delta\theta = 2\arctan\left(\frac{\Delta v_{\perp,s}/2}{v_{\parallel,s}}\right) \approx 2\sqrt{\frac{m_b}{m_s}} \tag{2.102}$$

where we assumed that $m_s \gg m_b$ in order to make the small angle approximation. Then, we can approximate the solid angle spread by

$$\Delta\Omega = 2\pi\left(1 - \cos\left(2\sqrt{m_b/m_s}\right)\right) \approx \pi\frac{m_b}{m_s} \tag{2.103}$$

where we have used the small angle approximation once again. It is significant that this solid angle spread can be much smaller than that of effusive or supersonic beams. For example, using the example of ^{138}Ba^{19}F in ^{20}Ne again, we find $\Delta\theta \approx 0.7$ and $\Delta\Omega \approx 0.4$. Although the regime of linearly decreasing divergence has only been observed in a few experimental setups, the reduced divergence of buffer gas beams is consistently noted in the literature.[10,73] This contributes to the typically enhanced "brightness" of buffer gas beams relative to more traditional sources, since more molecules will complete the transit from the source to the observation area of the apparatus, which is usually located many aperture diameters downstream.

Choice of buffer gas The final topic of relevance to our buffer gas beam apparatus is the choice of a species for the buffer gas. To maintain many of the important features of the buffer gas beam, this decision is a choice between helium and neon. By far, helium has been the first choice of experimentalists working with buffer gas cells. Helium has a very high vapor pressure at 4 K, a temperature which can be reached with standard refrigerators or even a simple liquid helium cryostat. Of course, helium continues to be an effective buffer gas at even lower temperatures. At lower temperatures, even slower and colder beams may be accessible. For this reason, experiments that are based on spectroscopy inside the buffer gas cell or the use of very slow beams will likely require the use of helium.

In contrast, neon can only be used as a buffer gas down to a temperature of $\sim$ 14 K, where the vapor pressure decreases substantially. Nevertheless, the beam properties with He and Ne sources can be quite comparable. Throughout this chapter the various characteristics of buffer gas beams have been referenced to the thermal buffer gas velocity in the cell, $\bar{v}_{0,b}$. For a cell of ^{20}Ne at 20 K or ^{4}He at 4 K, this velocity is about 145 m/s since the temperature to mass ratios are the same. Thus, many properties of these two beams will be similar, especially when the beams are boosted to a partially hydrodynamic regime. Indeed, Hutzler et al.[73] made a direct comparison of ThO in He and Ne buffer gas beams boosted to experience isentropic cooling. The molecules were found to have rotational temperatures of $\sim$ 2 K in both cases, despite

a 13 K difference in the two cell temperatures in that experiment. As a result, there is little difference in the choice of helium or neon when spectroscopy in the beam is the goal, particularly when operating beams with hydrodynamic enhancement.

The most significant difference between helium and neon set-ups is primarily technical. Any surface below $\sim$ 10 K will act as an effective and virtually unlimited capacity cryopump for neon. In our experiments, no additional pumping of the chamber is required while the refrigerator is running and the experiment can be run continuously for days. In contrast, one requires a large surface area adsorbent like activated charcoal at 4 K in order to efficiently cryopump helium. These charcoal sorbs have a limited capacity and require periodic warming up to release the stored helium in order to become effective again. Moreover, the pumping speed of sorbs slows down as they become full and the beam properties are affected even before the sorbs "crash" and completely stop adsorbing buffer gas. Perhaps related to this less effective pumping, experiments have found that ablation-loaded beams operating with helium display large variation in forward and transverse velocity profiles as a function of the time after ablation. Experiments with neon result in generally more reproducible beam characteristics.[73]

Chapter 3

Access to high-ℓ Rydberg states by Optical-mmW STIRAP

3.1 Introduction

The most significant limitation in the application of CPmmW spectroscopy to Rydberg states of molecules is the presence of fast non-radiative decay pathways. In particular, predissociation occurs due to the interaction of a quasibound excited state with one or more dissociation continua.[91] A form of electronic predissociation is illustrated schematically in Figure 3-1. A repulsive state interacts with an otherwise bound excited state, leading to dissociation of the molecule at an energy below the dissociation limit of the excited state curve. Our first demonstration of CPmmW spectroscopy on molecular Rydberg states[169] was performed on barium monofluoride, BaF, a rare molecule in which the first ionization potential lies below the lowest dissociation threshold. BaF and a few other lanthanide monofluorides[81] are the exception to the rule that all highly excited molecules suffer from predissociation. Despite this dire situation, the impact of predissociation can be reduced by excitation of particular Rydberg states. The rate of predissociation scales as n^{-3}, where n is the principal quantum number. This scaling occurs because the amplitude of the inner lobe of a hydrogenic wavefunction scales as $n^{-3/2}$, and the repulsive states responsible for predissociation are valence electronic states with wavefunction amplitude localized

near the ion-core. Increasing the orbital angular momentum, ℓ, of the Rydberg electron similarly limits the interaction with repulsive valence states. In a semi-classical picture, the point of closest approach of the Rydberg electron to the ion-core in a Keplerian orbit occurs at $r_{min} = n^2 - n\sqrt{n^2 - \ell(\ell+1)}$.[a] Thus, high-$\ell$ Rydberg states are more weakly perturbed by valence states and are therefore more weakly predissociated. The exact ℓ-scaling behavior for predissociation rates is not easily obtained by simple models. In general, states with $\ell \lesssim 3$ are all core-penetrating and, since the valence states also have low-ℓ characters, they all exhibit fast predissociation rates. Meanwhile, states with $\ell \gtrsim 3$ are all core-nonpenetrating and predissociation rates decrease rapidly with each increase of ℓ.

Access to high-angular momentum Rydberg states is challenging due to effective $\Delta\ell = \pm 1$ selection rules for dipole-allowed transitions and the short predissociation-limited lifetimes of low-ℓ Rydberg states. One technique particularly well-suited to population transfer in the presence of short-lived intermediate states is Stimu-

[a]The solutions of the Kepler problem in classical physics approximately describe the Rydberg electron's orbit. Keplerian orbits are elliptical, with inner and outer turning points given by the perihelion and aphelion of the ellipse:

$$r_{min} = a(1-e)$$
$$r_{max} = a(1+e)$$

where a is the semi-major axis, and e is the eccentricity. The eccentricity parameter can be related to the energy and angular momentum of the system by:

$$e = \sqrt{1 + 2EL^2}$$

where E is the energy and L is the angular momentum. Now, we can use the quantum mechanical values for the Rydberg energy, orbital angular momentum, and mean radius to derive the semi-classical results:

$$a = n^2$$
$$e = \sqrt{1 - \frac{\ell(\ell+1)}{n^2}}$$
$$r_{min} = n^2 - n\sqrt{n^2 - \ell(\ell+1)} = \frac{\ell(\ell+1)}{1+e}$$
$$r_{max} = n^2 + n\sqrt{n^2 - \ell(\ell+1)} = n^2(1+e)$$

Note that $|e| \leq 1$ for bound states. To a good approximation, the inner turning point is thus determined only by ℓ and the outer turning point is determined only by n. Since the inner turning point controls the strength of the Rydberg electron$\leftrightarrow$ion-core interaction, raising the value of ℓ is a more productive strategy to reduce predissociation than raising the value of n.

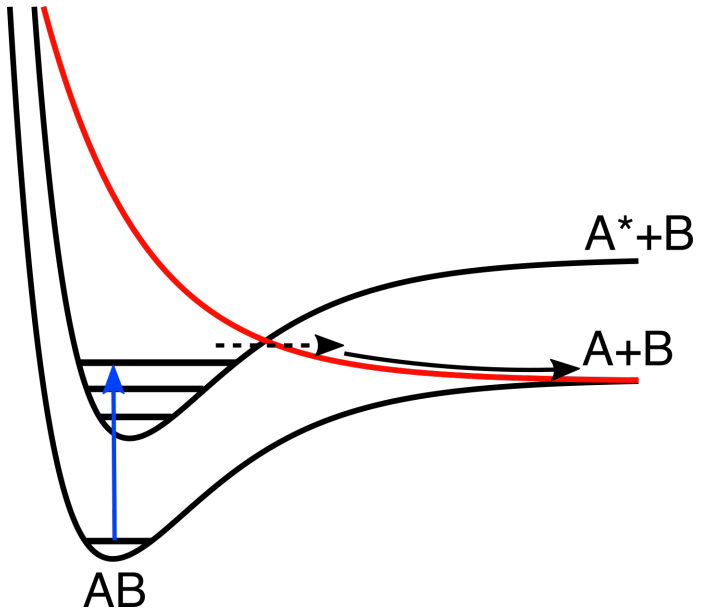

Figure 3-1: A repulsive curve (red) crosses a nominally bound excited state. When a level at an energy above the dissociation asymptote of the repulsive curve is excited, the population decays non-radiatively by tunneling through the barrier and dissociating along the repulsive curve.

lated Raman Adiabatic Passage (STIRAP). STIRAP has been extensively discussed in the literature and successfully applied to many systems in atomic and chemical physics.[12,64,89,110] In a three-level system, a "dark" population-trapping superposition of the initial and final states is prepared by two coherent time-varying fields. The amplitudes of the two coupling fields are smoothly changed in time to adiabatically evolve the dark state, transferring population from the field-free initial state to the final state.

We have demonstrated for the first time an implementation of optical-mmW STIRAP that relies on the combination of an optical Pump field and a millimeter-wave Stokes field. As a first test of this technique, we have coherently transferred $\gtrsim 50\%$ of the total population between the 4s5p and 4s28f states of atomic Ca. Our choice of an atomic system for this initial demonstration was motivated by the ability to quantitatively characterize the populations of the involved levels in the absence of non-radiative decay mechanisms. We discuss the particular challenges of STIRAP applied to our experiment and prospects for application to molecular systems.

3.2 Theoretical Background

The STIRAP technique is based on the physics of a three-level system. In this section, we will briefly review the theory underpinning population transfer by STIRAP, and discuss some of the characteristic features of STIRAP that will appear in our experimental observations.

Many authors have reviewed the STIRAP process[12,13,152]in the nearly 30 years since it was first introduced in the laboratory of Klaas Bergmann.[55] In many ways, it resembles the Stimulated Emission Pumping (SEP) technique developed in the Field lab a decade earlier.[85] In SEP, the goal is to populate some desired final state by using a carefully chosen intermediate state. One laser transfers population from the initial to the intermediate state and is followed by a second laser that transfers population from the intermediate to the final state. This technique has been most widely applied to access highly vibrationally excited states of a ground electronic state molecule via an excited electronic state with significant geometric distortion relative to the ground state. Since SEP is typically performed with pulsed dye lasers, which are only partially coherent, no more than 25% of the initial population can be transferred to the final state since each step saturates at 50% population transfer.

STIRAP improves on this limited population transfer by employing more highly coherent radiation sources and by switching to the "counter-intuitive" pulse sequence. In analogy to Raman processes, the initial-to-intermediate pulse is the "Pump" and the intermediate-to-final pulse is the "Stokes." By applying the Stokes pulse before the Pump pulse, with an appropriate time delay, near unity population transfer can be achieved. To illustrate how this process works, one can examine a generic time-dependent Hamiltonian for a three-level system. In the dressed state picture,[12] this Hamiltonian has the form

$$H = \frac{\hbar}{2}\begin{bmatrix} 0 & \Omega_P(t) & 0 \\ \Omega_P(t) & 2\Delta_P & \Omega_S(t) \\ 0 & \Omega_S(t) & 2\left(\Delta_P - \Delta_S\right) \end{bmatrix} \tag{3.1}$$

where $\Omega_P(t)$ and $\Omega_S(t)$ are the time-dependent Rabi frequencies of the Pump and Stokes transitions, respectively. The Rabi frequency is the key quantity for describing coherent radiation, and, in effect, parameterizes the interaction energy between the two involved levels,

$$\Omega(t) = \frac{\mu E(t)}{\hbar} \tag{3.2}$$

where $E(t)$ is the amplitude envelope function of the electric field and μ is the transition dipole moment. Δ_P and Δ_S are the "one-photon detunings" of the Pump and Stokes radiation, respectively, and are defined by: $\hbar\Delta_P = (E_2 - E_1) - \hbar\omega_P$ and $\hbar\Delta_S = (E_2 - E_3) - \hbar\omega_S$. The difference, $\Delta_P - \Delta_S$, represents the "two-photon detuning" of the system. It will become clear later that, although STIRAP is relatively insensitive to one-photon detuning, maintaining two-photon resonance is essential for efficient population transfer. This requirement, also called the "Raman resonance condition," can be expressed as $\Delta_P - \Delta_S = (E_3 - E_1) - \hbar(\omega_S - \omega_P) = 0$. The eigenstates of this Hamiltonian, $|a^+\rangle$, $|a^0\rangle$, $|a^-\rangle$, written in the basis of field-free states, $|1\rangle$, $|2\rangle$, and $|3\rangle$, are

$$|a^+\rangle = \sin\Theta \sin\Phi\,|1\rangle + \cos\Phi\,|2\rangle + \cos\Theta \sin\Phi]\,|3\rangle \tag{3.3}$$

$$|a^0\rangle = \cos\Theta\,|1\rangle - \sin\Theta\,|3\rangle \tag{3.4}$$

$$|a^-\rangle = \sin\Theta \cos\Phi\,|1\rangle - \sin\Phi\,|2\rangle + \cos\Theta \cos\Phi\,|3\rangle \tag{3.5}$$

where the mixing angle Θ is defined by

$$\tan\Theta = \frac{\Omega_P(t)}{\Omega_S(t)} \tag{3.6}$$

and the angle Φ is an explicit function of the Rabi frequencies and detunings, but is not important to the physics discussed here. The eigenvalues are similarly straightforward to obtain:

$$\omega^+ = \Delta_P + \sqrt{\Delta_P^2 + \Omega_P^2(t) + \Omega_S^2(t)} \tag{3.7}$$

$$\omega^0 = 0 \tag{3.8}$$

$$\omega^- = \Delta_P - \sqrt{\Delta_P^2 + \Omega_P^2(t) + \Omega_S^2(t)} \tag{3.9}$$

The special state $|a^0\rangle$ has a constant eigenvalue and contains no contribution from the basis state $|2\rangle$. This is the characteristic feature of a coherent population trapping state or "dark" state. It is referred to as "dark" because even if the two radiation fields are on continuously, any atoms in the dark state will remain in the dark state indefinitely without absorbing any photons. To demonstrate that this must be true, consider the absorption amplitude between the eigenstate $|a^0\rangle$ and the field-free state $|2\rangle$,

$$\langle a^0| \vec{\mu} \cdot \vec{E} |2\rangle = (\cos\Theta \langle 1| - \sin\Theta \langle 3|) \vec{\mu} \cdot \vec{E} |2\rangle \tag{3.10}$$

$$= (\cos\Theta)\Omega_P - (\sin\Theta)\Omega_S \tag{3.11}$$

$$= \frac{\Omega_S \Omega_P}{\sqrt{\Omega_P^2 + \Omega_S^2}} - \frac{\Omega_P \Omega_S}{\sqrt{\Omega_P^2 + \Omega_S^2}} \tag{3.12}$$

$$= 0 \tag{3.13}$$

Thus, no light is absorbed.

This derivation demonstrates that the state is dark at $t = 0$, but this does not guarantee that it will be dark at some later time, t. As time passes, the state acquires phase factors, $\exp(-iE_i t/\hbar)$, where E_i is the energy of the basis state $|i\rangle$, and the radiation field acquires phase factors, $\exp(-i\omega_i t)$, where ω_i is the laser frequency. We can set this modified absorption amplitude to zero:

$$\frac{\Omega_S e^{-iE_1 t/\hbar} \Omega_P e^{-i\omega_P t}}{\sqrt{\Omega_P^2 + \Omega_S^2}} - \frac{\Omega_P e^{-iE_3 t/\hbar} \Omega_S e^{-i\omega_S t}}{\sqrt{\Omega_P^2 + \Omega_S^2}} = 0 \tag{3.14}$$

Clearly, the absorption amplitude will vanish only if the phase factors are identical,

$$E_1/\hbar + \omega_P = E_3/\hbar + \omega_S \tag{3.15}$$

or, after rearrangement,

$$(E_3 - E_1) - \hbar(\omega_P - \omega_S) = 0 \tag{3.16}$$

This is exactly the Raman resonance condition. The dark state only remains dark as long as the two-photon detuning is zero. This is the first characteristic feature of the STIRAP process: the population transfer should be relatively insensitive to one-photon detuning as long as two-photon resonance is maintained.

Now, to examine how STIRAP is accomplished, we allow the Pump and Stokes Rabi frequencies to vary in time. One can see by examining the eigenstate $|a^0\rangle$ that before any radiation fields are turned on this eigenstate is identical to the field-free state $|1\rangle$. If the angle Θ can be tuned "slowly" from 0 to $\pi/2$, then the eigenstate $|a^0\rangle$ can be made to evolve from the pure basis state $|1\rangle$ to the pure basis state $|3\rangle$. This means that unity population transfer from the initial to final state is achieved without ever populating the intermediate state. By examining the functional form of Θ, the use of the "counter-intuitive" pulse sequence, where the Stokes pulse arrives before the Pump pulse becomes evident. When the Stokes Rabi frequency is large relative to the Pump Rabi frequency, the mixing angle is close to zero. By smoothly reducing the Stokes Rabi frequency and increasing the Pump Rabi frequency, this mixing angle increases until it approaches $\pi/2$. This is the second characteristic feature of the STIRAP process: enhanced population transfer must occur when the Stokes pulse occurs at a small negative delay relative to the Pump pulse. Figure 3-2 shows the time dependence of the Rabi frequencies, populations, and mixing angle over the course of a STIRAP process.

Alternatively, one can envision the Hilbert space for the STIRAP problem as shown in Figure 3-3, where the state vector, Ψ, is initially parallel to both the field-free state $|1\rangle$ and the eigenstate $|a^0\rangle$, while the other two basis states and eigenstates occupy the perpendicular $|2\rangle - |3\rangle$ plane. As the mixing angle Θ is changed from 0 to $\pi/2$ the angle between $|a^0\rangle$ and $|1\rangle$ is increased until $|a^0\rangle$ is finally anti-parallel to $|3\rangle$. This motion occurs in the $|1\rangle - |3\rangle$ plane, perpendicular to basis state $|2\rangle$.

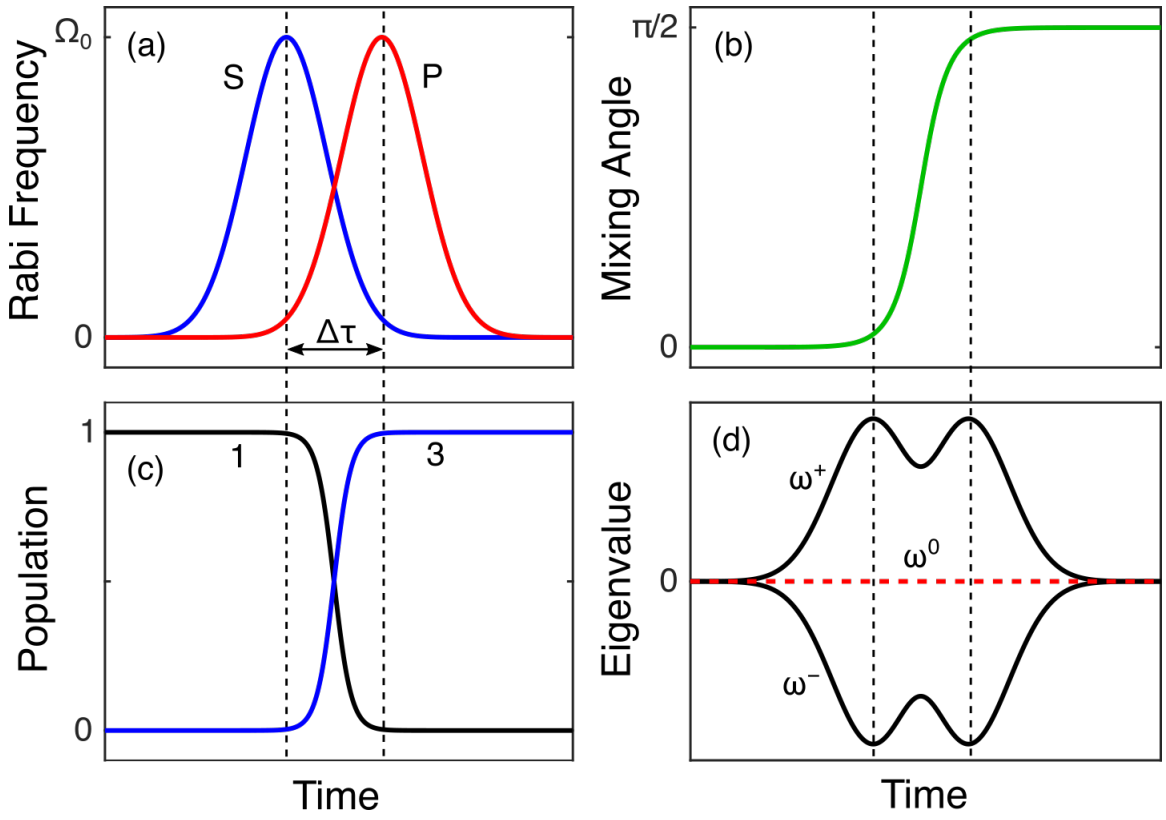

Figure 3-2: (a) Pump and Stokes Rabi frequencies as a function of time. The vertical dashed lines in all panels shows the timing of the peak Rabi frequency, Ω_0, and the approximate overlap period, $\Delta\tau$ between the two pulses. (b) The mixing angle Θ evolves smoothly from 0 to $\pi/2$. (c) The population of state $|1\rangle$ is moved entirely to state $|3\rangle$, while no population enter state $|2\rangle$ – note the sum of the $|1\rangle$ and $|3\rangle$ populations is 1 at all times. (d) Time dependence of the amplitudes of all three eigenvalues. The dark state eigenvalue, ω^0, is constant and equal to zero throughout the STIRAP process.

In order for the population transfer to be successful, the state vector must closely follow the eigenvector $|a^0\rangle$ during its evolution. If the coupling is too weak, meaning the Rabi frequencies are too small or the rate of change of $|a^0\rangle$ is too fast, the state vector will lag behind this motion, while precessing about $|a^0\rangle$. When the radiation fields are abruptly turned off, the time-evolving state vector will be projected onto all three basis states. In order to achieve efficient population transfer, the evolution of the state vector must be *adiabatic*.

The nonadiabatic coupling of the dark state $|a^0\rangle$ with either of the other eigenstates is expressed as $\langle a^{\pm}|\dot{a}^0\rangle$. Thus, the condition for adiabatic following is that this matrix element must be small relative to the splitting $|\omega^{\pm} - \omega^0|$ induced by the radiation fields.

$$|\langle a^{\pm}|\dot{a}^0\rangle| \ll |\omega^{\pm} - \omega^0| \tag{3.17}$$

Let's define this mean matrix element by the expression $|\langle a^{\pm}|\dot{a}^0\rangle|^2 = |\langle a^{+}|\dot{a}^0\rangle|^2 + |\langle a^{-}|\dot{a}^0\rangle|^2$ and use our previously derived expressions to calculate the value of the matrix element.

$$\begin{aligned}
&\langle a^{+}|\dot{a}^0\rangle \\
&= \big(\sin\Theta\sin\Phi\,\langle 1| + \cos\Phi\,\langle 2| + \cos\Theta\sin\Phi\,\langle 3|\,\big)\big(-\dot{\Theta}\sin\Theta\,|1\rangle - \dot{\Theta}\cos\Theta\,|3\rangle\,\big) && (3.18)\\
&= -\dot{\Theta}\sin^2\Theta\sin\Phi - \dot{\Theta}\cos^2\Theta\sin\Phi && (3.19)\\
&= -\dot{\Theta}\sin\Phi && (3.20)\\
&\langle a^{-}|\dot{a}^0\rangle \\
&= \big(\sin\Theta\cos\Phi\,\langle 1| + \cos\Phi\,\langle 2| + \cos\Theta\cos\Phi\,\langle 3|\,\big)\big(-\dot{\Theta}\sin\Theta\,|1\rangle - \dot{\Theta}\cos\Theta\,|3\rangle\,\big) && (3.21)\\
&= -\dot{\Theta}\sin^2\Theta\cos\Phi - \dot{\Theta}\cos^2\Theta\cos\Phi && (3.22)\\
&= -\dot{\Theta}\cos\Phi && (3.23)
\end{aligned}$$

$$\begin{aligned}
|\langle a^{\pm}|\dot{a}^0\rangle| &= \sqrt{\left|-\dot{\Theta}\sin\Phi\right|^2 + \left|-\dot{\Theta}\cos\Phi\right|^2} && (3.24)\\
&= \left|\dot{\Theta}\right|\sqrt{\sin^2\Phi + \cos^2\Phi} && (3.25)
\end{aligned}$$

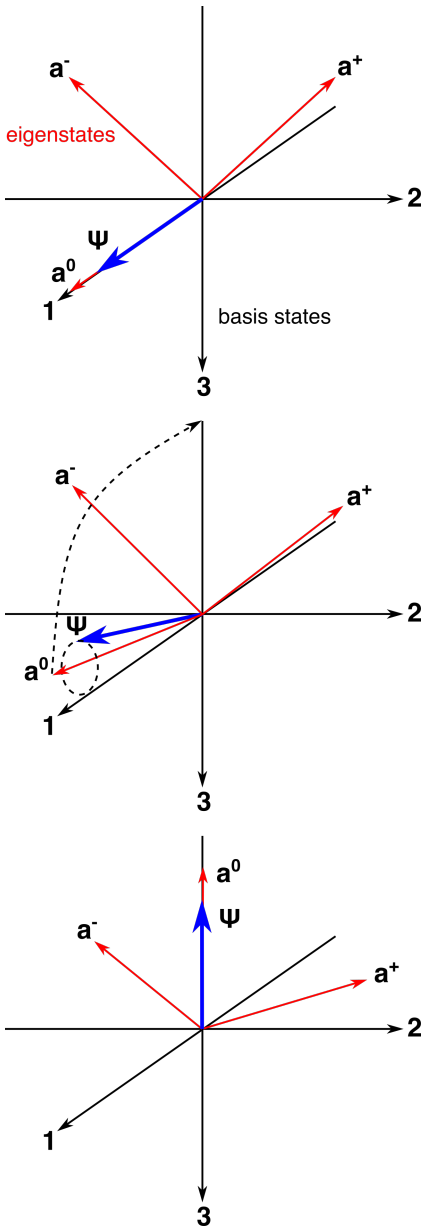

Figure 3-3: Hilbert space representation of the STIRAP process. (Left) Initially, when only the Stokes field is present, the state vector $|\Psi\rangle$ is identical to the basis state $|1\rangle$ and to the eigenstate $|a^0\rangle$. (Center) As the Stokes field turns off and the Pump field turns on, the eigenstates evolve in the space of the basis states. If the Rabi frequencies are high enough and the rate of change slow enough, the state vector will precess tightly about the eigenvector $|a^0\rangle$ during this change. If the adiabaticity criterion of Equation 3.31 is not satisfied, the state vector will lag behind the eigenvector $|a^0\rangle$ and end up in a superposition of all three basis states. (Right) At the end of a successful STIRAP process, when only the Pump field is present, the state vector has followed the eigenvector $|a^0\rangle$ through its entire evolution and is now identical to the basis state $|3\rangle$.

$$= \left|\dot{\Theta}\right| \tag{3.26}$$

In the last step, we have assumed that $\sin\Phi$ is of order unity to simplify the following results. The adiabaticity constraint is written as

$$|\dot{\Theta}| \ll |\omega^{\pm} - \omega^{0}| \tag{3.27}$$

From here, we recognize

$$\dot{\Theta} = \frac{\mathrm{d}}{\mathrm{d}t} \arctan\left(\frac{\Omega_P}{\Omega_S}\right) \tag{3.28}$$

$$= \frac{1}{1 + (\Omega_P/\Omega_S)^2} \frac{\dot{\Omega}_P\Omega_S - \Omega_P\dot{\Omega}_S}{\Omega_S^2} \tag{3.29}$$

$$= \frac{\dot{\Omega}_P\Omega_S - \Omega_P\dot{\Omega}_S}{\Omega_S^2 + \Omega_P^2} \tag{3.30}$$

Thus, we arrive at the requirement that

$$\left|\frac{\dot{\Omega}_P\Omega_S - \Omega_P\dot{\Omega}_S}{\Omega_S^2 + \Omega_P^2}\right| \ll |\omega^{\pm} - \omega^{0}| \tag{3.31}$$

which is considered the "local" adiabaticity criterion.[12] For any given time dependence of the radiation fields, this expression can be evaluated at any time t. This inequality must be satisfied at all times to ensure that the nonadiabatic coupling is "small enough."

If the radiation fields evolve smoothly in time, it is also useful to derive a "global" adiabaticity criterion, which will give approximate constraints on a STIRAP process without the need to specify the detailed time dependence of the Rabi frequencies. First, we take a time average of $\dot{\Theta}$, which, referring to Figure 3-2, is approximately given by $\langle\dot{\Theta}\rangle \approx \pi/(2\Delta\tau)$, where $\Delta\tau$ is the time period during which the pulses overlap. The other side of the inequality is approximated by

$$|\omega^{\pm} - \omega^{0}| \approx \sqrt{\Omega_P^2 + \Omega_S^2} = \Omega_{eff} \tag{3.32}$$

This effective Rabi frequency, Ω_{eff}, is simply the RMS Rabi frequency and the approximation is exact for zero one-photon detuning. This leads to the global adiabaticity criterion:

$$\Omega_{eff}\Delta\tau > 10 \tag{3.33}$$

where the value of 10, larger than the expected $\pi/2$, is a rule-of-thumb developed through numerical simulations and experimental evidence.[12] For pulsed lasers, it is often convenient to square this expression to yield

$$\Omega_{eff}^2\Delta\tau > \frac{100}{\Delta\tau} \tag{3.34}$$

where the left hand side of the equation is proportional to the mean pulse energy.

Now that we have established the counterintuitive ordering as the optimum STIRAP pulse sequence and defined the adiabaticity criterion, we can address the question of optimal pulse delay. This question can be qualitatively understood by considering the two limiting cases: perfectly overlapped pulses and very long pulse delay. When the pulses are overlapped, of course, $\dot{\Theta} = 0$ and the adiabaticity criterion is fulfilled in a trivial way. However, the initial state, $|1\rangle$, will end up with projections along all three eigenstates because the Pump pulse is present from the start of the experiment. In the long-pulse-delay experiment, the projection $|\langle 1|a^0\rangle|$ approaches 1 as desired. However, the mixing angle, Θ, will be changing when Ω_{eff} is less than its maximum, or in other words, the coupling of the state vector to $|a^0\rangle$ will be weak. This weak coupling is also undesirable for an adiabatic process. Thus, the optimum pulse delay should produce the maximum value of Ω_{eff} while the mixing angle is changing fastest, namely $\Theta \approx \pi/4$. For two identical Gaussian pulses, a pulse delay equal to the FWHM pulsewidth, results in a long period of high Ω_{eff} as Θ changes rapidly, and, in experiments, this typically maximizes the population transfer.[12]

Thus far, we have assumed coherent radiation, which for pulsed light means radiation with a Fourier transform-limited bandwidth, i.e.,

$$\Delta\nu\Delta t = \alpha \tag{3.35}$$

where $\Delta\nu$ is the FWHM (linear) frequency bandwidth, Δt is the pulse duration, and α is a pulse shape-dependent value. The minimum time-bandwidth product for a Gaussian pulse, for example, is $\alpha \approx 0.44$. However, pulsed laser sources, particularly dye lasers, frequently exhibit phase fluctuations that increase the bandwidth beyond the transform limit. Kuhn et al. studied the effects of phase fluctuations in detail[88] and derived a simple extension to the adiabaticity criterion:

$$\Omega_{eff}^2 \Delta\tau > \frac{100}{\Delta\tau}\left[1 + \frac{\Delta\omega}{\Delta\omega_{FT}}\right]\Gamma \tag{3.36}$$

where $\Delta\omega$ and $\Delta\omega_{FT}$ are the (angular) frequency bandwidths of the real pulse and a transform-limited pulse, respectively, and Γ is a factor depending on the pulse shape. Clearly, pulsed radiation with a bandwidth that is close to the Fourier transform limit is ideal for implementation of STIRAP. The study by Kuhn et al.,[88] as well as the work of David Grimes in the Field group,[60] included an explicit model for the phase noise, in which the Rabi frequency is modified by a time-dependent pseudo-random phase factor, which dramatically changes the population transfer efficiency from pulse to pulse. Similarly, pulsed lasers also exhibit pronounced intensity fluctuations, frequently as large as $\pm 15\%$. As a result, every laser pulse will result in slightly different population transfer for a given delay time. These two results demonstrate an important consideration for simulation of the STIRAP process. Any fluctuations in an experiment due to phase fluctuations, intensity fluctuations, Doppler shifts, beam profile effects, etc., must be explicitly simulated to obtain a realistic representation of the experiment. In other words, although the global adiabaticity requirement serves as a convenient rule of thumb, there is in fact no "average" STIRAP process in an ensemble measurement. The experimental measurement is the average population transfer experienced by all atoms that make up the sample. If STIRAP works for the atom that experiences the lowest Rabi frequency, it works for every atom. The average Rabi frequency experienced by the sample is meaningless because there is no "average" atom.

3.3 Experimental

An atomic Ca beam was generated in our ablation-loaded cryogenic buffer-gas cooled beam source. This apparatus has been described in detail previously[168] and we describe only the characteristics relevant to this experiment. Calcium atoms are produced by ablation of a calcium metal target by $\sim$ 10 mJ pulses of the 532 nm second harmonic of a nanosecond Nd:YAG laser (Spectra Physics, GCR-130), focused to a $\sim$ 1 mm^2 spot. The ablated Ca atoms thermalize in the 20 K neon buffer gas and undergo a mild hydrodynamic expansion through the output orifice of the cell. The laser and mmW radiation intersect the atomic beam transversely 30 cm downstream from the buffer gas cell. In the interaction region, the atomic beam exhibits a transverse velocity distribution with full width at half maximum (FWHM) of about 250 m/s. The density of Ca atoms is estimated to be $\sim 10^{10}$ cm^{-3} from laser induced fluorescence (LIF) measurements.[168] Figure 3-4 shows the relevant Ca energy levels and radiation sources for the experiment. The initial state in the STIRAP three-level system is populated by pumping the 4s5p$\leftarrow$4s^2 transition at 272 nm with a frequency-doubled dye laser (SIRAH Cobra Stretch), referred to as the "Prep" laser hereafter. No attempt is made to characterize the absolute number of atoms in this initial state.

The Pump photon couples the initial 4s5p and intermediate 4s30d states at 804 nm and is generated by pulsed amplification of a CW laser. The seed laser is a commercial Ti:Sapphire laser (M Squared SolsTiS) locked to a high-resolution wavemeter (Angstrom WS/7) which allows for reproducible tuning of the laser frequency during the course of an experiment. Approximately 100 mW of radiation is fiber coupled to the input of a three-stage dye amplifier pumped by the second harmonic of an injection-seeded, pulsed Nd:YAG laser (Spectra Physics, LAB-170). Spatial filtering after each amplification stage reduces the amplified spontaneous emission (ASE) in the output laser beam. We obtain 10 mJ, 7 ns FWHM pulses of near-infrared radiation.

A well-known problem in pulsed amplification in a dye solution is frequency chirp-

ing in the amplified laser pulse.[43,54] We characterize this phenomenon by the usual self-heterodyne measurement. A portion of the seed laser is frequency shifted by double-passing an acousto-optic modulator (Gooch and Housego, AOMO 3350-125) operating at 375 MHz. This frequency-shifted radiation, along with the output of the pulsed amplification chain, are coupled into a single mode fiber to effectively overlap the wavefronts of the two laser beams. The beat note between the two lasers is monitored on a fast photodiode and digitized on a high-speed oscilloscope. By using a large frequency offset of 750 MHz, we can fit the resultant beat pattern directly in the time-domain and extract the frequency chirp. We typically observe a chirp of approximately -50 MHz between the 10% intensity limits of the pulse, which broadens the pulsed output beyond the Fourier transform limit. This effect is directly included in our numerical simulations as a time-dependent one-photon detuning.

The intermediate 4s30d and final 4s28f states are coupled by a mmW field produced by a 260-300 GHz chirped-pulse spectrometer, which has been described in detail by the Pate group[138] and is briefly summarized here. The output of a 12.0 GS/s arbitrary waveform generator (AWG, Agilent M8150) is mixed with a phase-locked 9.375 GHz local oscillator (Miteq, DLCRO 0101-09375-3-15P), and filtered to select the upper sideband. This low frequency waveform is sent to an active multiplier chain (AMC, Virginia Diodes AMC291), which multiplies the frequency by 24 to produce the required mmW excitation pulses. The radiation is broadcast into the chamber by a standard gain horn antenna. The residual excitation pulses as well as the mmW FID from the sample are received on the opposite side of the sample volume by an identical horn antenna and down-converted. The local oscillator for down-conversion is generated by a second channel of the AWG that is mixed with the same phase-locked oscillator and multiplied by a factor of 12 in a second AMC (Virginia Diodes MixAMC156). Down-conversion is accomplished in a subharmonic mixer and the intermediate frequency (IF) signal is digitized directly on a 50 GS/s, 20 GHz digital oscilloscope (Tektronix DPO72004). The ability to create tailored sequences of mmW pulses with an AWG allows us to interrogate, on every experimental cycle, the populations of the intermediate and final states of our three-level

system by two linked "probe" transitions. Note that all pulses from the CPmmW spectrometer are constrained to have square temporal profiles. This non-ideal pulse shape is explicitly included in the numerical simulations and profoundly influences the population transfer.

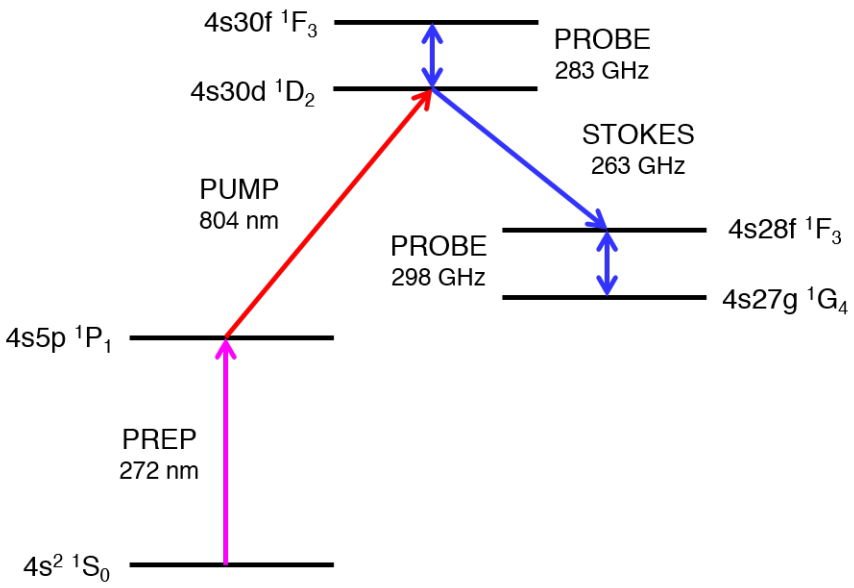

Figure 3-4: Level scheme in Ca for STIRAP demonstration. The three-level system for coherent population transfer is composed of the 4s5p, 4s30d, and 4s28f singlet states, which are the initial, intermediate, and final states, respectively.

The population transfer efficiency and the capability for numerical characterization of our STIRAP scheme require a sample volume in which the multiple radiation fields have a well-known spatial profile. The sample volume is defined by the Prep and Pump laser fields, which are collimated to $1/e^2$ beam diameters of approximately 7 and 10 mm, respectively, while the mmW radiation is approximately collimated by a Teflon lens to a cross-sectional area of 10 cm^2. The mmW radiation is first overlapped with the 804 nm laser beam at an ITO-coated glass plate, which acts as a mirror at mmW frequencies. These two radiation fields are then overlapped with the 272 nm laser beam by transmission through a large-diameter backside-polished mirror coated for reflectivity near 266 nm (CVI, Y4-3037-45-UNP).

3.4 Results

3.4.1 Doppler Broadening

The Doppler broadening present in the atomic sample is a critical parameter in the STIRAP experiment. A Doppler shift of the relevant transitions can create a two-photon detuning, which significantly reduces the population transfer efficiency. The geometry of the experiment can be chosen to reduce this effect. If the Pump and Stokes radiation fields have similar frequencies, the Doppler shift will be similar for a given velocity sub-group. For a Λ arrangement of energy levels, the Pump and Stokes pulses should co-propagate across the sample, while for a ladder arrangement, the two pulses should counter-propagate. The nearly equal Doppler shifts produce a simple one-photon detuning and permit maintenance of the all-important two-photon resonance. Unfortunately, as the frequency difference between the two photons increases, the cancellation of the Doppler shifts is reduced. In the case of optical-mmW STIRAP, the optical and mmW photons differ in frequency by approximately three orders of magnitude. As a result, there is negligible cancellation of the Doppler shifts for the two photons. Therefore, the Doppler shift of the Pump (near-infrared) photon across the sample represents a range of two-photon detunings. In this experiment, a cryogenic buffer-gas beam, with its typically small divergence, reduces the transverse Doppler broadening, while also allowing for the large interaction regions necessary for chirped pulse experiments on Rydberg states. Figure 3-5 shows the Doppler-broadened lineshape for the Pump 4s30d$\leftarrow$4s5p transition. This spectrum is collected by monitoring the CPmmW signal at the Stokes transition frequency while scanning the Pump laser frequency. The observed 310 MHz linewidth corresponds to a transverse velocity spread of 249 m/s FWHM. This velocity spread produces a Doppler width of appoximately 215 kHz for the Stokes transition at 263 GHz. For simulations of the STIRAP experiment, we will neglect this $<$1% cancellation between the 310 MHz and 215 kHz Doppler shifts.

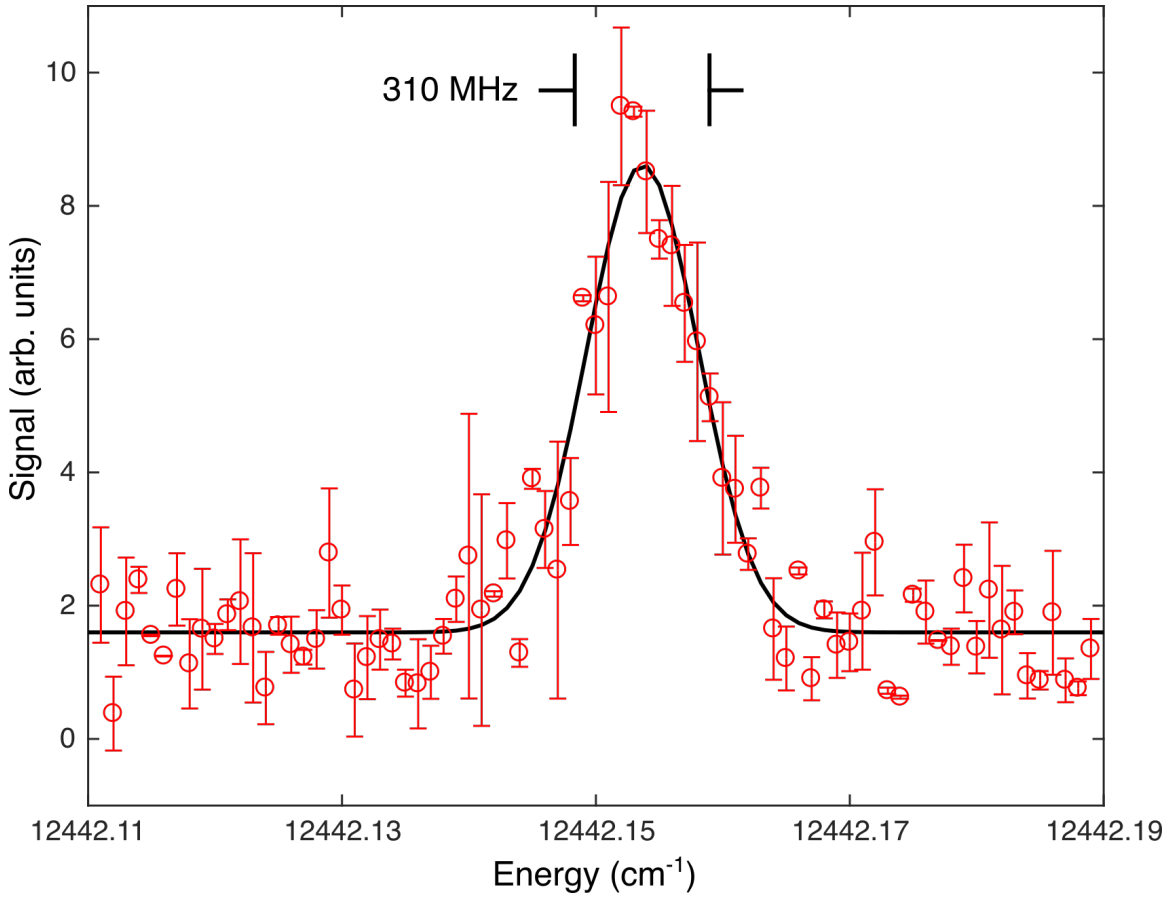

Figure 3-5: Spectrum of the 4s30d←4s5p transition, which is excited with the pulsed dye amplified CW laser. The signal is monitored by probing the 4s30d population with the 4s30d→4s28f mmW transition.

3.4.2 Population Calibration

In order to quantify the population distribution among the three STIRAP involved levels, we switch between the STIRAP experiment and a sequential, adiabatic rapid passage (ARP) excitation scheme. A schematic timing diagram of the two experimental sequences appears in Figure 3-6. For the calibration experiment, we have observed saturation of the 4s30d←4s5p transition as a function of Pump laser power (Figure 3-7). The pulse energy is monitored simultaneously with the signal from the 4s30d→4s28f mmW transition. The black solid line is a fit to the data by the saturation function:

$$\frac{S}{S_{\text{sat}}} = \frac{F/F_{\text{sat}}}{1 + F/F_{\text{sat}}} \tag{3.37}$$

where S is the signal, S_{sat} is the signal in the limit of saturation, F is the laser fluence, and F_{sat} is the characteristic saturation laser fluence. As a result of the large number of Rabi oscillations induced by the laser pulse and moderate pulse-to-pulse energy fluctuations, an average 50% population transfer between the two levels is achieved. Following laser excitation, we apply a mmW field with a cubic frequency chirp ($f_{\text{inst}} \propto t^3$) of 800 MHz over 300 ns centered at the Stokes transition frequency. This produces a complete population transfer ($\gtrsim 95\%$) to the final state. Probe pulses of identical power and duration are used in the ARP and STIRAP experiments, allowing for direct comparison of the signal from the intermediate and final state transitions. We switch between the calibration and experimental sequences after every choice of time delay for the STIRAP experiment. Thus, we have a 50% total population transfer signal with which to calibrate the STIRAP transfer. This calibration scheme additionally corrects for the slow fluctuations in the total signal due to ablation source and Prep laser fluctuations. This somewhat complicated calibration procedure was developed because of the challenge of being able to apply Probe pulses with well-defined pulse areas. The full output power of the mmW spectrometer is used to perform the STIRAP experiment, but this power is much greater than needed to perform a $\pi/2$ pulse on the Probe transitions within the Doppler dephasing time. As a result, each Probe pulse overdrives the Rydberg-Rydberg transition. We found it

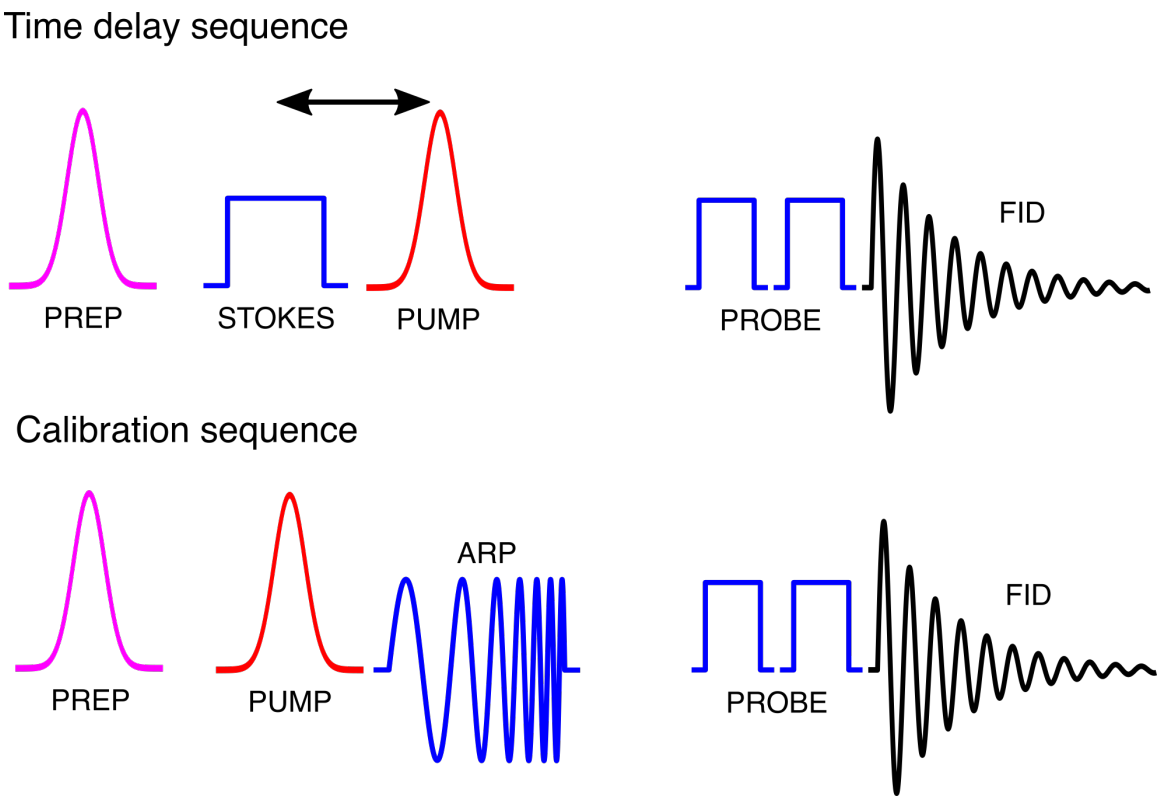

Figure 3-6: Schematic timing diagram for the time delay and calibration experiments as described in the text. Each timing sequence concludes with polarization of the two probe transitions and subsequent FID detection.

difficult to characterize the exact pulse area of these high-power probes because any inhomogeneity in polarization or power in the mmW field washes out the coherent Rabi oscillations, which must be observed in order to determine the pulse area. This challenge was the impetus for developing the described calibration procedure based instead on the more robust technique of adiabatic rapid passage.

3.4.3 Time Dependence

A typical STIRAP experiment involves scanning the time delay between the Pump pulse and Stokes pulse, while monitoring the populations of the intermediate and final levels. At large negative delay, the laser pulse arrives well after the mmW pulse, and thus only the intermediate level will be populated. At large positive delay the laser pulse arrives well before the mmW pulse and corresponds to the regime of sequential excitation of the three-level system. Between these limits, we anticipate enhanced

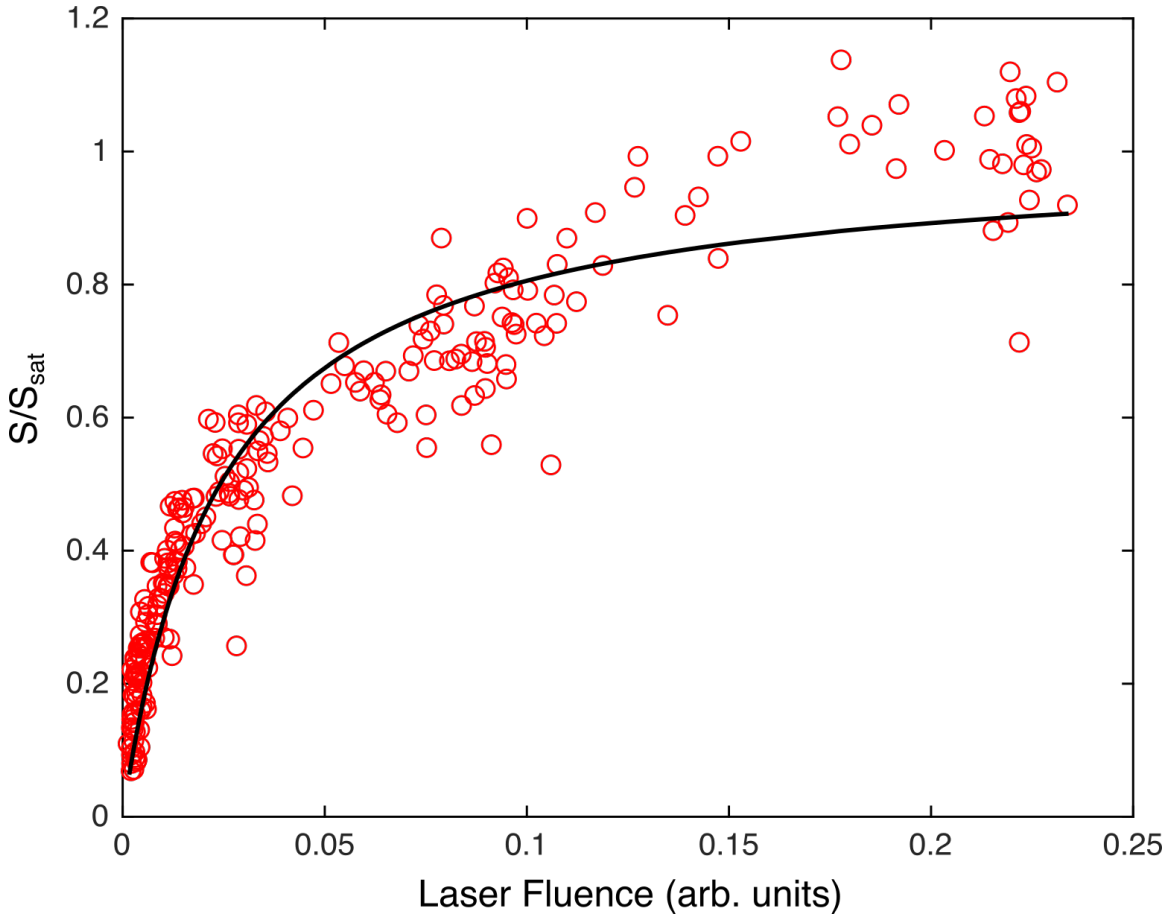

Figure 3-7: Saturation of the 4s30d←4s5p 804 nm transition signal as a function of laser fluence. For low laser fluence, a nearly linear signal dependence is observed, while at high laser fluence, the signal changes minimally with changes in the laser power.

population transfer to the final level at short negative delays, when the pulses are in the "counter-intuitive timing" that is a key requirement of the STIRAP process. The result of a typical such experiment is shown in Figure 3-8. At short negative delay we observe an enhanced population transfer to the final state of $\gtrsim$50%. Concurrently, the population in the intermediate state exhibits a pronounced dip. As the delay becomes positive but while the two pulses are still overlapped, the population transfer to both the final and intermediate levels show variation with pulse delay that is generally enhanced relative to the sequential excitation regime. The intermediate state population reaches a maximum at the point where the final state population dips, after which the final state population increases slightly as the intermediate state population begins decreasing. This type of population transfer has been observed in other systems[60,89,114] and we interpret this as further evidence for strong two-photon coupling.

3.4.4 Frequency Dependence

The other signature of STIRAP-mediated population transfer is insensitivity to one-photon detuning while two-photon resonance is maintained. This characteristic, which arises from the two-photon nature of the population transfer, produces a "STIRAP ridge" of enhanced population transfer at zero two-photon detuning as the Pump and Stokes detunings are varied.

Figure 3-9 shows the final state population transfer at the STIRAP timing as a function of Pump laser detuning for several fixed values of the Stokes microwave frequency. The spectra are obtained by scanning the Pump detuning at fixed values of the Stokes detuning. The right plot shows positive detunings from 600 MHz (dark blue) to 0 MHz (dark red) in steps of 50 MHz, and the right plot shows negative Stokes detunings from -600 MHz (dark blue) to 0 MHz (dark red) in 50 MHz steps. All spectra were scaled by the population transfer measured at the STIRAP timing in the time delay experiment.

The solid line for each spectrum is a fit to the data with a skew Gaussian function

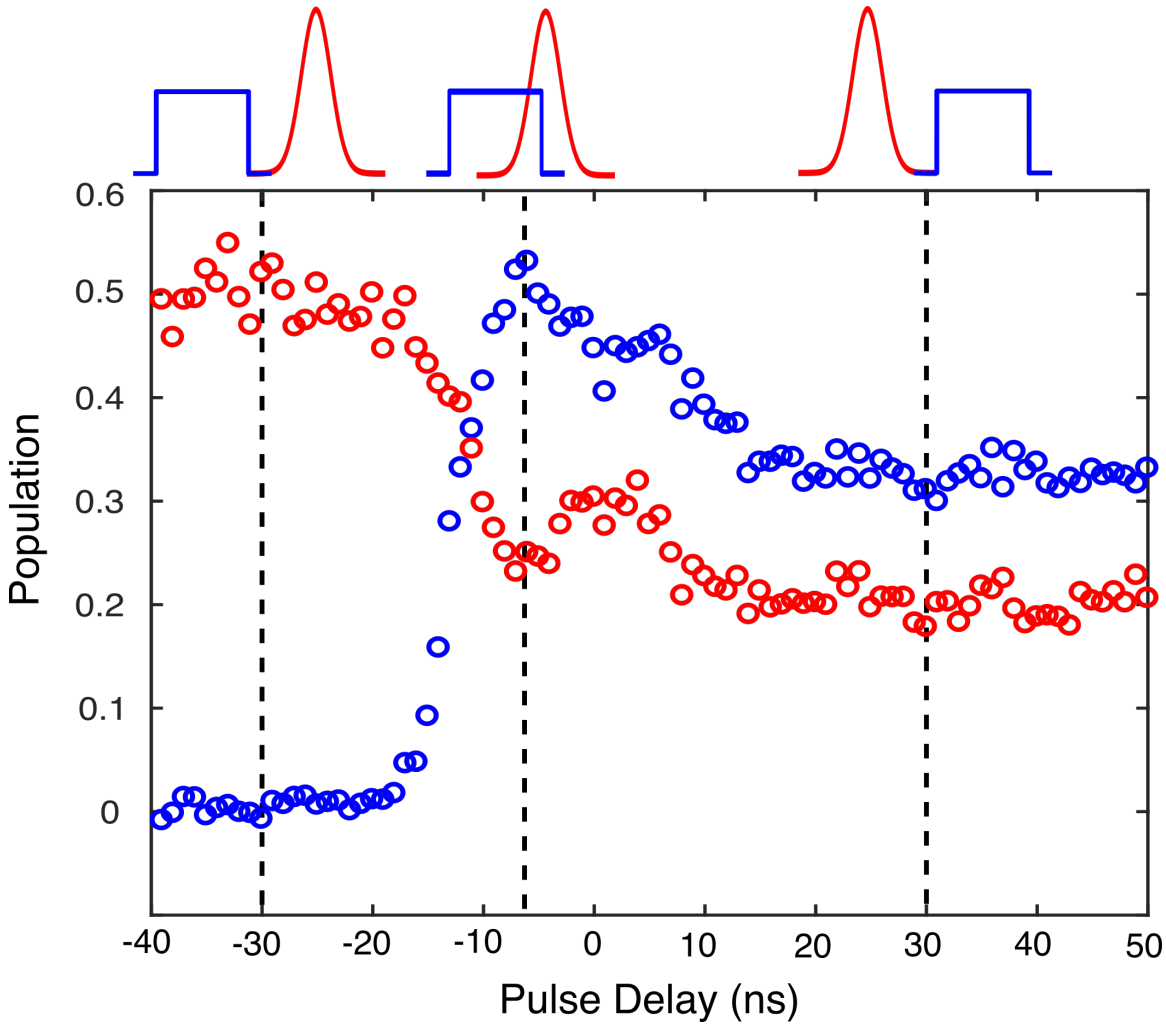

Figure 3-8: Population measured in the intermediate (red) and final (blue) states as a function of delay time between the Pump and Stokes pulses. At short negative delay times, enhanced population transfer to the final state is evident, while a dip in the population of the intermediate state occurs simultaneously. A schematic representation of the Pump and Stokes pulse timing appears above the main figure.

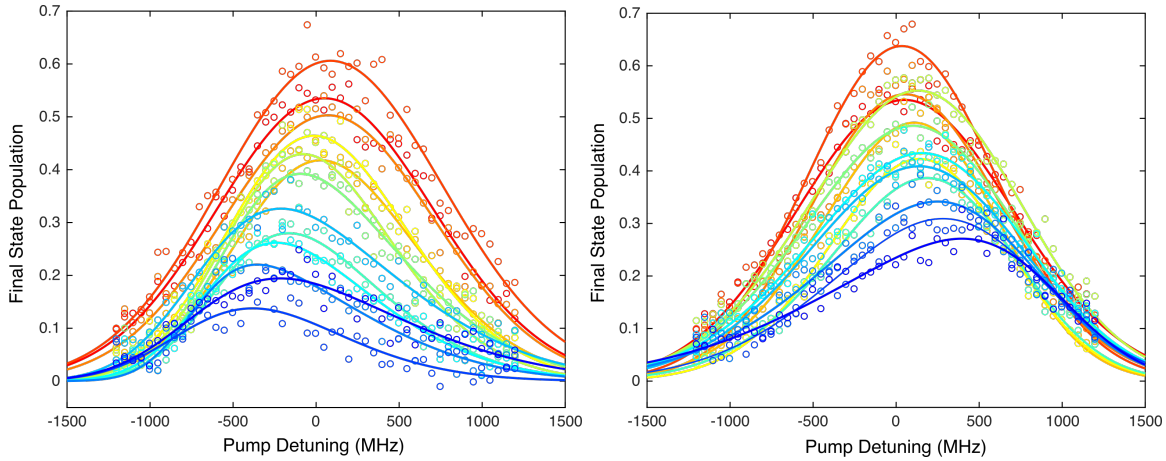

Figure 3-9: Detuning dependence of final state population. The left plot shows population transfer as a function of laser detuning for fixed microwave detunings from -600 MHz (dark blue) to 0 MHz (dark red) in steps of 50 MHz. The right plots correspond to microwave detunings from +600 MHz (dark blue) to 0 MHz (dark red). The solid lines are fits to the data with a skew Gaussian function. The STIRAP ridge appears as the peak population transfer along the approximate zero two-photon detuning line.

of the form:

$$f(\nu) = A\left[1 + \mathrm{erf}\left(\frac{\alpha(\nu-\mu)}{\sigma\sqrt{2}}\right)\right]\exp\left(-(\nu-\mu)^2/2\sigma^2\right) \tag{3.38}$$

where A is a scaling factor, μ is the center of the distribution, σ is the variance, and α is the skewness parameter. This choice of lineshape is not motivated by the physics of the system, but rather, it has a simple functional form that can represent the asymmetry, width, and shift of the observed lines. In fact, the physics that produces the observed population transfer profiles includes many contributions and likely will not have a simple analytical form for the particular experiment described here. More details of the lineshape are discussed in the next section.

In Figure 3-9, the Pump detuning that produces peak population transfer shifts as a function of the Stokes detuning. The shift is symmetric about zero detuning and approaches 400 MHz for Stokes detunings of 600 MHz, and -400 MHz for Stokes detunings of -600 MHz. The peak population transfer along this line of approximate zero two-photon detunings is the characteristic STIRAP ridge. In addition, the

linewidth for all detuning values is substantially larger than the 310 MHz Doppler width, which was measured in an experiment at low laser power and with sequential excitation. Lastly, as the microwave detuning is increased, the shape of the line becomes increasingly asymmetric, with the tail pointing toward zero Pump detuning. These characteristic features are interpreted and compared to the results of our numerical simulations in the next section.

3.4.5 Numerical Simulations

We have simulated the population transfer in this experiment by numerical integration of the Liouville equation using properties for the atomic ensemble and the two photons consistent with the experiment:

$$i\hbar\frac{\mathrm{d}\rho}{\mathrm{d}t} = [H, \rho] + \Gamma \tag{3.39}$$

where ρ is the density matrix for the three-level system, H is the total Hamiltonian for the atom-radiation system, which is given by Equation 3.1, written in a dressed state picture, with parameters as defined in Section 3.2. In Equation 3.39, the operator Γ is a phenomenological decay matrix, which, considering only predissociation of the intermediate level, has the form:

$$\Gamma = \begin{pmatrix} 0 & -\frac{\gamma}{2}\rho_{12} & 0 \\ -\frac{\gamma}{2}\rho_{21} & -\gamma\rho_{22} & -\frac{\gamma}{2}\rho_{23} \\ 0 & \frac{-\gamma}{2}\rho_{32} & 0 \end{pmatrix} \tag{3.40}$$

where γ is the predissociation rate of the intermediate state (State 2). By substituting the explicit forms of the total Hamiltonian (Equation 3.1) and decay operator (Equation 3.40) into Equation 3.39, we obtain a system of nine coupled differential equations. These equations describe all populations and coherences in the system. Noting that $\rho_{xy} = \rho_{yx}^*$, we obtain the following six Optical Bloch equations, which

completely describe the system of interest:

$$\dot{\rho}_{11} = \frac{i\Omega_P}{2}(\rho_{12} - \rho_{21}) \tag{3.41}$$

$$\dot{\rho}_{22} = \frac{i\Omega_P}{2}(\rho_{21} - \rho_{12}) + \frac{i\Omega_S}{2}(\rho_{23} - \rho_{32}) - \gamma\rho_{22} \tag{3.42}$$

$$\dot{\rho}_{33} = \frac{i\Omega_S}{2}(\rho_{32} - \rho_{23}) \tag{3.43}$$

$$\dot{\rho}_{12} = \frac{i\Omega_P}{2}(\rho_{11} - \rho_{22}) + \frac{i\Omega_S}{2}\rho_{13} + \left(-\frac{\gamma}{2} + i\Delta_P\right)\rho_{12} \tag{3.44}$$

$$\dot{\rho}_{13} = \frac{i\Omega_S}{2}\rho_{12} - \frac{i\Omega_P}{2}\rho_{23} + i\left(\Delta_P - \Delta_S\right)\rho_{13} \tag{3.45}$$

$$\dot{\rho}_{23} = \frac{i\Omega_S}{2}(\rho_{22} - \rho_{33}) - \frac{i\Omega_P}{2}\rho_{13} + \left(-\frac{\gamma}{2} - i\Delta_S\right)\rho_{23} \tag{3.46}$$

In our simulations we find that the relevant Rabi frequencies, $\Omega_P = 2\pi \times 115$ MHz, and $\Omega_S = 2\pi \times 68$ MHz, best reproduce the experimental observations. The population transfer is integrated over the observed Doppler width of the Pump laser transition of 310 MHz FWHM and the Gaussian variation of pump laser intensity across the laser beam profile. Both Gaussian-distributed fluctuations of the Pump laser intensity and fluctuations in the magnitude of the Pump laser chirp are included. We average 100 simulations in order to compare the simulated time and frequency dependence with the experimental results.

3.5 Discussion

3.5.1 Adiabaticity

We begin this discussion by noting that the Rabi frequencies used in our simulation should be considered *effective* Rabi frequencies. While a number of the experimental imperfections have been explicitly modeled in the simulations, all neglected imperfections will have the general effect of reducing the Rabi frequencies that describe the experiment. Based on our measurement of the pulse energies and durations, both the Stokes and Pump Rabi frequencies used in the simulations are about 40% smaller than our initial estimates. Simulations that use the initially estimated Rabi frequen-

cies show significantly worse agreement with all experimental data. In the following sections of this discussion, we will address in detail the experimental imperfections that could give rise to some of the discrepancies between the simulations and experiment. All such imperfections have the effect of additionally reducing the effective Rabi frequency below our initial estimate.

As discussed in Section 3.2, STIRAP requires an adiabatic evolution of the dark state in order to coherently move population from the initial to the final state. The global adiabaticity requirement in Equation 3.33 provides an approximate benchmark for determining the effectiveness of STIRAP. Our effective Rabi frequencies and pulse overlap time result in $\Omega_{eff}\Delta\tau \approx 5$. While the detailed pulse shape and other parameters will impact the final population transfer as well, this simple $\Omega_{eff}\Delta\tau$ metric indicates that our experiment is operating near to but not deeply in the adiabatic regime. This fact is primarily responsible for the less than perfect population transfer to the final state of approximately 50%.

The second major impediment to adiabatic following in our experiment is our use of a nearly square mmW pulse. The very sharp turn-off of the Stokes pulse is antithetical to the required slow, smooth change in Rabi frequencies. As a result, the peak population transfer occurs at a smaller negative pulse delay than might be expected from the naive picture presented in Figure 3-2, where the pulse delay was equal to the duration of the two identical, smooth Gaussian pulses. In other words, our pulse overlap time must be long in order to "make up for" the poor adiabatic following that results from the pulse shape. This is true in both the experimental data and the simulation results discussed in the next section. If one arbitrarily increases the Rabi frequencies in our simulation, the pulse delay timing for peak population transfer shifts to longer negative pulse delays as the adiabatic following improves.

3.5.2 Time Dependence

Our simulations qualitatively capture many of the features of the time delay experiment. In Figure 3-10, the experimental data are shown as points, the solid lines are the average of 100 simulations, and the shaded area represents the standard devi-

ation of the 100 simulations. As before, red denotes the intermediate state and blue denotes the final state. Population transfer of at least 50%, though not much larger, is observed in both experimental and simulation results. This enhanced population transfer to the final state is, as expected, accompanied by a pronounced decrease in the population transfer to the intermediate state. While the calculation yields near quantitative agreement with the final state population, the observed intermediate state population is about 10% larger than in the calculation. As the pulse delay increases beyond the STIRAP timing, the final state population transfer is reduced and a peak in the intermediate state population transfer appears. This is the point of most significant quantitative discrepancy. The simulation suggests that the intermediate state population should approach nearly the same value as the STIRAP transfer and the final state population should decrease dramatically. However, the experimental data show similar changes of less than 10% in both values of the absolute population transfer. A second dip in intermediate state population and peak in final state population occurs when the two radiation pulses partially overlap at short positive delays. This simulated final oscillation in the populations is even weaker than the preceding one in our experimental results. The population transfer at long delay times is quantitatively reproduced. At long negative delays, the simulation captures the $\sim$50% population transfer expected from our measurement of saturation of the 4s30d$\leftarrow$4s5p transition. At long positive delays, the Pump and Stokes pulses interact with the system sequentially, and the final and intermediate state populations are simply dependent on the ratio of Stokes and Pump Rabi frequencies.

We will turn next to some speculation regarding the poor agreement between the simulation and experiment during the overlap timing, but first we will discuss the significance of *why* the agreement is poor. This overlap period represents a time when the atoms simultaneously experience both laser and millimeter-wave fields. As a result, the atoms will undergo two-photon Rabi flopping among the initial, intermediate, and final levels. This is not an adiabatic process like STIRAP, but rather depends entirely on maintaining high coherence among the three levels for long times. If coherence is lost over time, the oscillations will be "washed out" and some sort of

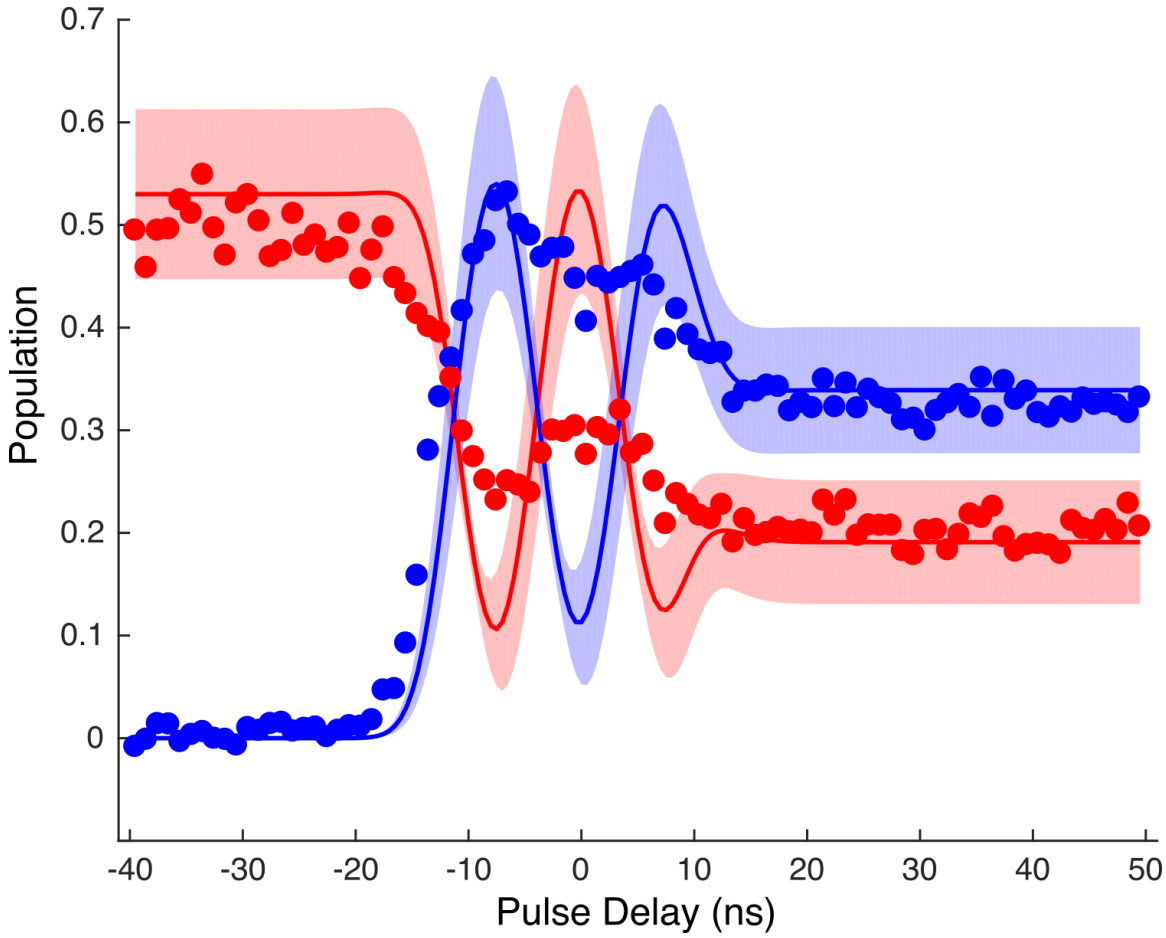

Figure 3-10: Simulation results for the intermediate (red) and final (blue) state population transfer as a function of pulse delay. The solid lines are the mean population and the standard deviation of the 100 simulations is shown as a shaded area. For comparison, the experimental data points appear as circle markers in matching colors.

average population will be measured in the three levels. This process is precisely the type of "delicate" population transfer that STIRAP aims to avoid, because exquisite experimental control is required. A host of experimental imperfections, which are not included in our simulations *because* they are difficult to control and/or quantify, will reduce the contrast of the two-photon Rabi oscillations, in agreement with what we observe in the experimental data.

The reduced contrast in the population transfer ratio during the pulse overlap could have several experimental explanations. Many of these explanations are linked to the very long beam path and, hence, to the large number of optics in our set-up required to direct the Pump laser into the experimental chamber. This can produce imperfections in the laser beam at the entrance to the chamber, which have not been accounted for in our simulation, including variations or fluctuations in phase, amplitude, and polarization. The importance of high coherence radiation and Fourier transform-limited pulses has already been discussed here and in our previous work,[60] where, in the presence of very large Pump pulse phase fluctuations, all coherent oscillations became averaged out. Amplitude variations in the form of uneven illumination or hot spots in the beam profile would also have significant impacts. Although STIRAP is relatively insensitive to power fluctuations, hot spots in the beam profile can enhance the local electric field by orders of magnitude, making this type of imperfection problematic. Lastly, polarization plays an important role that we have not yet addressed. These experiments were performed with all three radiation fields nominally having linear polarizations aligned in the same direction. The polarization arrangement matters because every state in the excitation scheme is $(2\ell + 1)$-fold degenerate due to the presence of magnetic sub-levels. The ground state of Ca is a non-degenerate $^1S_0$ state with one $m = 0$ sub-level. By using linear, parallel polarization for each step, only one magnetic sub-level is involved for every electronic state, even though the total number of magnetic sub-levels increases for every step along the STIRAP path. If the polarization is corrupted, then transitions to other m levels become allowed and the many possible excitation paths can produce interference effects in the population transfer. This effect has been previously investigated, and

both constructive and destructive interference are possible, depending on the chosen polarization arrangement.[84,89] At a more basic level, the transition dipole moment is m-dependent so the presence of more than one magnetic sub-level and more than one transition path produces several sets of alternate three-level systems each with a different effective Rabi frequency. The sum of these many contributions will significantly reduce the contrast of the two-photon Rabi flopping. The STIRAP process is much more robust with respect to variations in the Rabi frequencies as long as the Rabi frequencies are large enough, so the population transfer at the STIRAP timing is not significantly affected. This highlights the importance of controlling the polarization of the radiation field to produce the desired effect. Again, while we have attempted to clean up the polarization of the laser fields, corruption is possible and the beam combining optics are the leading suspect.

Regarding the magnetic sub-levels, it is also important to point out that the degeneracy of these levels can be lifted, producing transitions to additional m levels. The presence of a small magnetic field, due to nearby electrical equipment or the Earth, can produce m level splittings in the Rydberg states of interest. While passive shielding (for instance, with μ-metal) is the standard method for eliminating this effect,[63] this type of shielding is incompatible with our CPmmW experiments, because the experiments require optical access across a large volume for laser and microwave fields. Instead, we have pursued active compensation by placing Helmholtz coils around the apparatus in three dimensions.[168] When a magnetic field is present, we observe line splittings in the Rydberg-Rydberg mmW spectra. By tuning the currents in each pair of coils, we can compensate for the magnetic field and reduce these splittings. Importantly, we cannot claim to "eliminate" the Zeeman splitting, but we can only state that it is reduced below the largest line broadening, the Doppler width. Thus, transitions to additional m sub-levels may still be possible, though the energy splittings and transition amplitudes are reduced to the best of our ability.

An additional complication in the STIRAP experiment is the possibility of mmW reflections inside the chamber. The mmW radiation can experience significant reflections from the window surfaces and, especially, from the receiver horn, where the

impedance mismatch between the waveguide and free space is significant. While the intensities of these reflected beams would only be a small fraction of the intensity of the incident mmW radiation, additional population transfer after the STIRAP timing would be possible due to the large (∼kiloDebye) Rydberg-Rydberg transition dipole moments. This would lead to a loss of contrast in the Rabi flopping region since these weak pulses could only cause a reduction in the population difference between the two levels. In many CP-FTMW experiments, in which the low frequency microwaves are much less "beam-like," the interior of the experimental chamber is coated with microwave-absorbing foam or paint to reduce reflections. Such a modification may be beneficial for future mmW experiments as well.

3.5.3 Frequency Dependence

The simulation of the frequency detuning experiment, shown in the bottom panels of Figure 3-11, also captures many of the features observed in our experiment. For ease of comparison, the fit lines to the experimental data are presented in the top panels of Figure 3-11, and the dashed arrow is a guide to the eye, highlighting the frequency shift of the peak population transfer. In both experiment and simulation, as the Stokes detuning is increased, the Pump detuning spectra show a clear frequency shift in the peak population transfer along with a pronounced increase in lineshape asymmetry. In order to make a more quantitative comparison, Figure 3-12 shows the maximum of the fits to the experimental data (red circles) and the maximum of the simulated population transfer (black circles) as a function of Stokes detuning. The black dashed line is the naive expectation for a STIRAP process in which the peak population transfer occurs at exactly $\Delta_P = \Delta_S$. Both the experiment and simulation deviate from this naive expectation and the change in peak transfer is much flatter near resonance. As the detuning increases, the rate of change of the peak Pump detuning increases and the value of peak Pump detuning approaches the two-photon resonance line. The experimental results show a similar trend in the detuning dependence, although the magnitude of the observed shift, particularly at large detunings, is smaller than expected from the simulations.

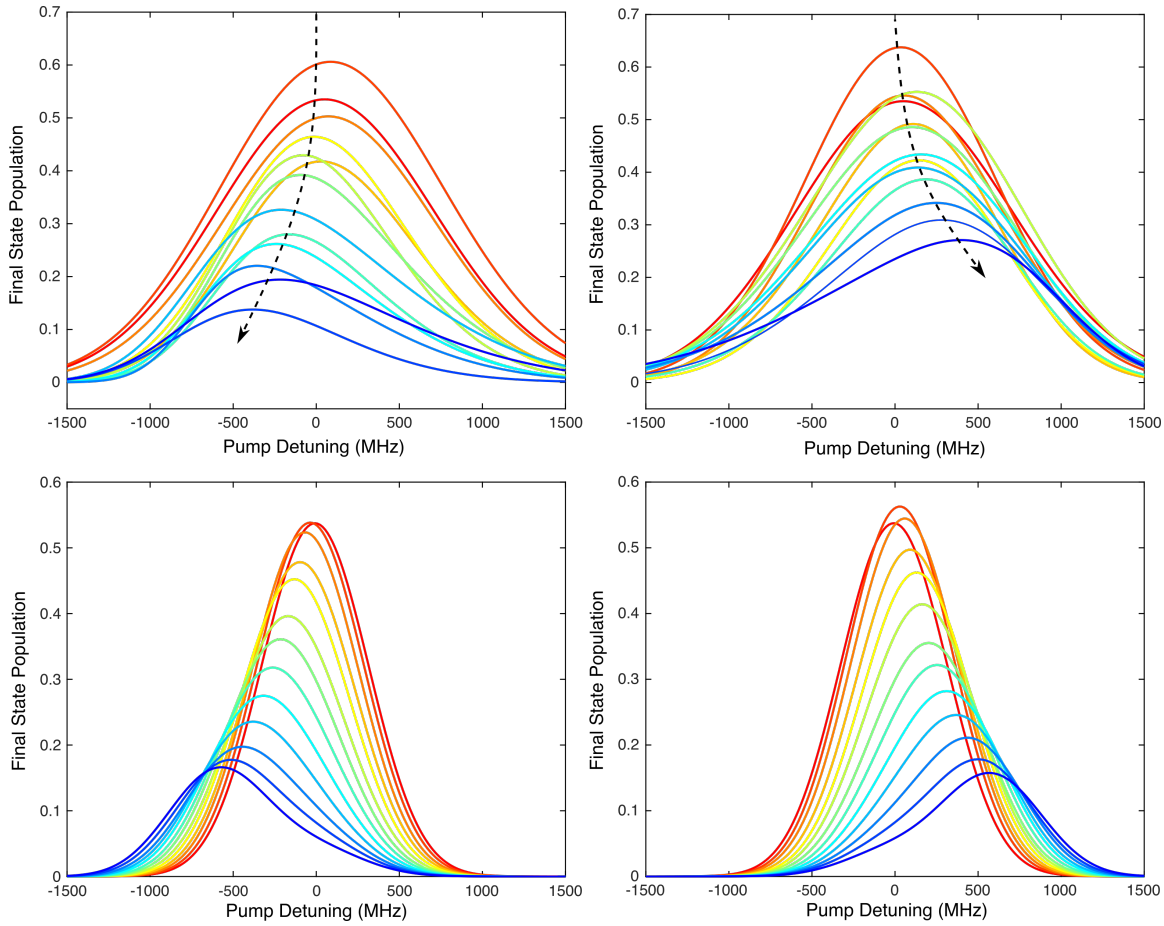

Figure 3-11: Top: Fitted skew Gaussian lineshapes to the experimental data presented in Figure 3-9. The dashed arrow is a guide to the eye, indicating the frequency shift in peak population transfer as the Stokes detuning is changed. Bottom: Simulation results for the population transfer as a function of Pump detuning for fixed values of the Stokes detuning. Left: -600 MHz (dark blue) to 0 MHz (dark red) in steps of 50 MHz. Right: 600 MHz (dark blue) to 0 MHz (dark red) in steps of -50 MHz.

Next, we turn to an examination of the lineshape. The simulation clearly shows that in the STIRAP timing, the linewidth of the two-photon process is broader than the one-photon Doppler linewidth of 310 MHz, which is explicitly included in the simulation. The large Rabi frequencies in the STIRAP experiment allow for enhanced population transfer even in the presence of a one-photon detuning. Clearly, the experimental broadening is significantly larger than the simulated broadening. As mentioned in the above discussion, the effective Rabi frequencies in our simulations are smaller than expected for the measured pulse energies and durations of the Pump and Stokes pulses. This suggested to us that fluctuations in phase or amplitude, or significant ASE in the Pump laser beam degrade the overall coherence. These imperfections can increase the observed linewidth by broadening the laser or mmW bandwidth, or increasing the effect of power broadening.[153]

Both the simulation and the experiment show lineshapes which grow increasingly asymmetric as the detuning is increased. We can quantitatively compare this asymmetry by examining the skewness and kurtosis of the fitted and simulated lines. Skewness is defined as the third standardized moment, given by the expression:

$$\tilde{\mu}_3 = \frac{\mu_3}{\sigma^3} = \frac{E\left[(X-\mu)^3\right]}{\left(E\left[(X-\mu)^2\right]\right)^{3/2}} \tag{3.47}$$

where μ_3 is the third moment about the mean defined by the expectation value $E\left[(X-\mu)^3\right]$, and σ is the standard deviation defined as the square root of the second moment about the mean, $\left(E\left[(X-\mu)^2\right]\right)^{1/2}$. This skewness is a valuable measure for comparing the shapes of two distributions because it is scale invariant. Even though two lineshapes may look quite different because the mean and/or standard deviation are different, the skewness of the two lineshapes can be quantitatively compared. Qualitatively, the skewness describes the asymmetry of a distribution and can be positive or negative depending on the direction of the tail. For comparison, a Gaussian distribution is perfectly symmetric and has a skewness of zero. Similarly, the kurtosis

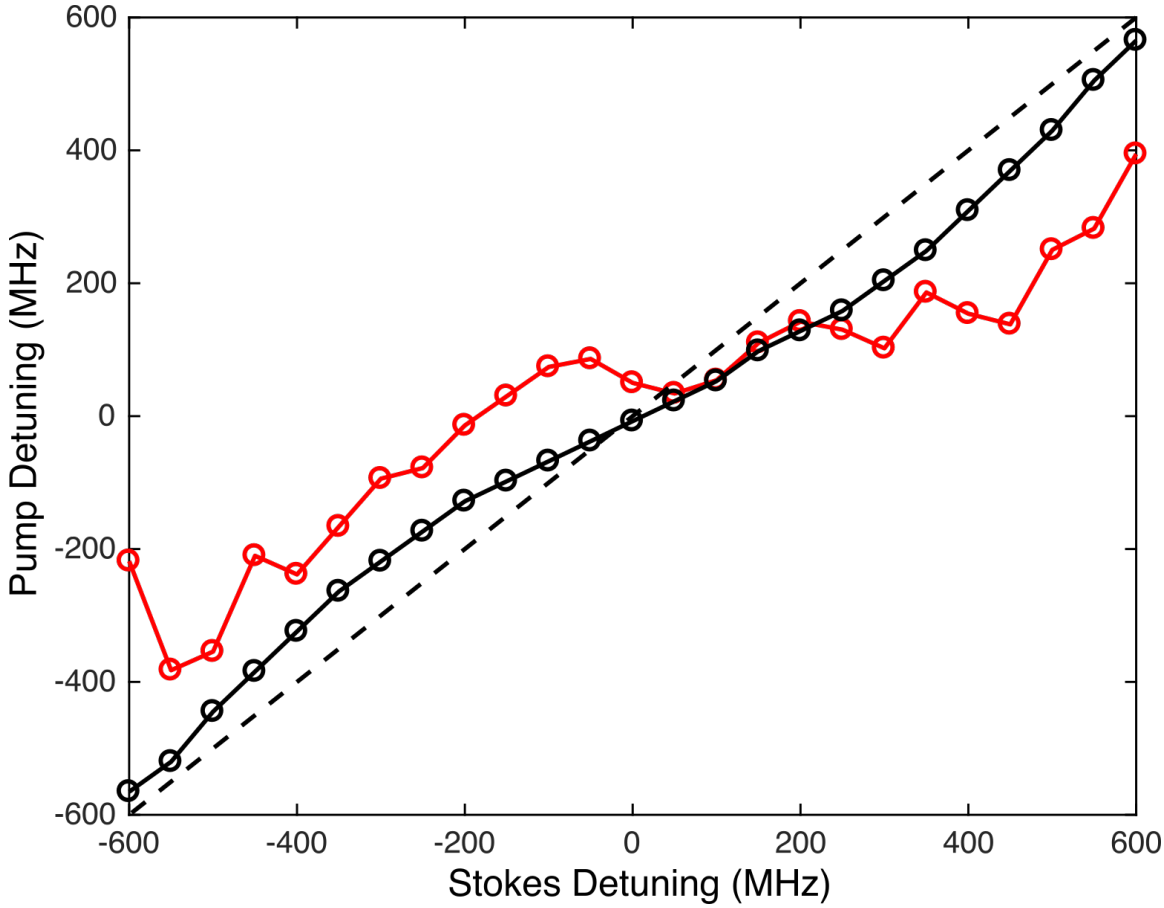

Figure 3-12: Pump detuning that produces the peak population transfer as a function of Stokes detuing. The experimental data is shown as red circles and the simulated data as black circles. The dashed black line is the two-photon resonance line, $\Delta_P = \Delta_S$. The experiment and simulation deviate from the two-photon resonance line in the same way.

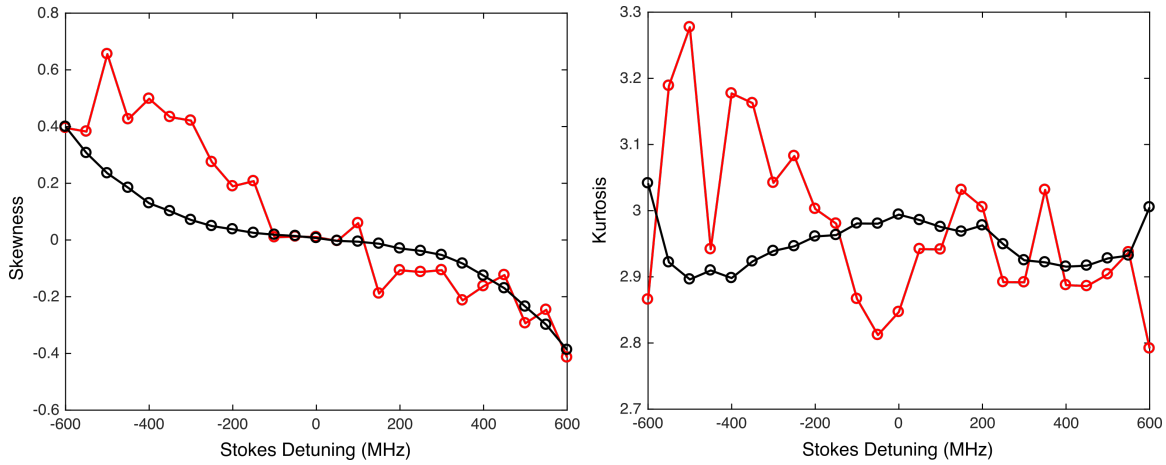

Figure 3-13: Skewness (left) and kurtosis (right) of the observed (red) and simulated (black) lineshapes for each value of the Stokes detuning.

is defined as the fourth standardized moment and given by,

$$\tilde{\mu}_4 = \frac{\mu_4}{\sigma^4} = \frac{E\left[(X-\mu)^4\right]}{\left(E\left[(X-\mu)^2\right]\right)^2} \tag{3.48}$$

This quantity is also scale invariant and describes the "tailedness" of a distribution, or, in other words, how much weight appears in both tails relative to the center of the distribution. For reference, values of the kurtosis for a Gaussian distribution, a hyperbolic secant distribution, and a uniform distribution are 3, 5, and 1.8, respectively. The skewness and kurtosis of the simulated (black) and fitted (red) lines are shown in the left and right panels of Figure 3-13, respectively. The calculated skewness quantitatively agrees for small negative and all positive Stokes detuned spectra. There is greater deviation for the negative Stokes detuned spectra, though the direction and order of magnitude are correct. The values of kurtosis for both the simulated and calculated lines are very close to the Gaussian value of 3. Again, there is better agreement for the positive Stokes detuned spectra than the negative Stokes spectra. The generally flat trend across the experimental data set agrees qualitatively with the simulation. We interpret the similar lineshapes between the simulation and experiment to mean that our simulation is likely capturing most of the physics, though estimates for the particular parameters (e.g., Rabi frequencies, frequency/amplitude fluctuations, etc.) may not be exactly correct.

The reason for the observed asymmetry in the population transfer is the presence of diabatic transitions from the initial to final state caused by the frequency fluctuations in the Pump field and the sharp turn-off of the Stokes field. As a result, there is enhanced population transfer as the Pump frequency is tuned toward one-photon resonance relative to away from one-photon resonance. This effect is enhanced by the presence of Doppler broadening in our sample because a Doppler subgroup with significant population will be one-photon resonant with the Pump transition even at detunings of several hundred MHz. At some specific values of the pulse overlap and detuning, we have observed simulated spectra that are double-peaked, with a second local maximum in the population transfer near zero Pump detuning. This suggests that the population transfer in the tail is due to diabatic transitions, or, in other words, step-wise transitions from the initial to intermediate to final state caused mainly by the sharp turn-on of the mmW pulse. This is in contrast to the STIRAP process, in which population is adiabatically transferred by the smooth change of Pump and Stokes Rabi frequencies. These step-wise, diabatic transitions are significantly more sensitive to one-photon detuning than STIRAP. Furthermore, we observe in simulations that when the Stokes detuning is increased beyond the ± 600 MHz region investigated experimentally, the intensity in the tail rapidly decreases and eventually the lineshape becomes symmetric again when only the adiabatic process contributes.

We have generally discussed that the result of diabatic transitions is to cause greater population transfer to the final state. However, this is not always true. If the excitation is partly incoherent or substantially modified by pulse-to-pulse intensity fluctuations, then saturation occurs, limiting the population transfer to maximally 50%. The STIRAP process has no such limitation and can transfer up to 100% of the population from the inital to final states. This means it is possible for diabatic transitions to actually reduce the total population transfer by moving population from the final state back to the intermediate state. In both the experimental data and simulations, there is a small dip in the population transfer when both Pump and Stokes fields are on one-photon resonance. At small detunings above and below one-

photon resonance, we observe slightly enhanced population transfer to the final state. This is expected behavior because the maximum adiabatic and diabatic population transfers occur near one-photon resonance, but the adiabatic transfer efficiency is much less sensitive to one-photon detuning. Thus, the balance of these diabatic and adiabatic mechanisms controls where the peak transfer occurs in the detuning space. In both experimental and simulation results, the difference in population transfer at small detunings is subtle and merits further investigation. However, previous STIRAP experiments have reported this effect, especially when fast intermediate state decay is involved, because diabatic transitions into the intermediate state lead to irreversible loss of that population.[114]

3.5.4 Lossy Intermediate State

It is informative to examine how our system behaves in the presence of a hypothetical lossy intermediate state. All simulation parameters are the same as previously described, but the intermediate state is assumed to have a 1 ns non-radiative lifetime. This represents a typical predissociation lifetime for a low-ℓ Rydberg state in a diatomic molecule. Figure 3-14 shows the population transfer to the intermediate (red) and final (blue) states as a function of pulse delay. In the presence of this rapid decay channel, significant population transfer to the final state only occurs at the STIRAP timing. At all other times, either through sequential excitation or two-photon Rabi flopping, population is moved into the intermediate state and immediately lost. The very modest population transfer of just over 10% is a reflection of the previously described experimental imperfections in our system.

Figure 3-15 shows the same simulated population transfer as a function of detuning as Figure 3-11 with a 1 ns intermediate state lifetime. As observed in the time delay simulation, the peak transfer on resonance is just over 10% for this hypothetical system. Unlike the simulations with no intermediate state decay, there is significant variation in the population transfer for different values of the pump detuning even at very large detunings. We believe this is an artifact of the fluctuating parameters in the simulation. Even with 100 simulations, the fluctuations are not averaged out

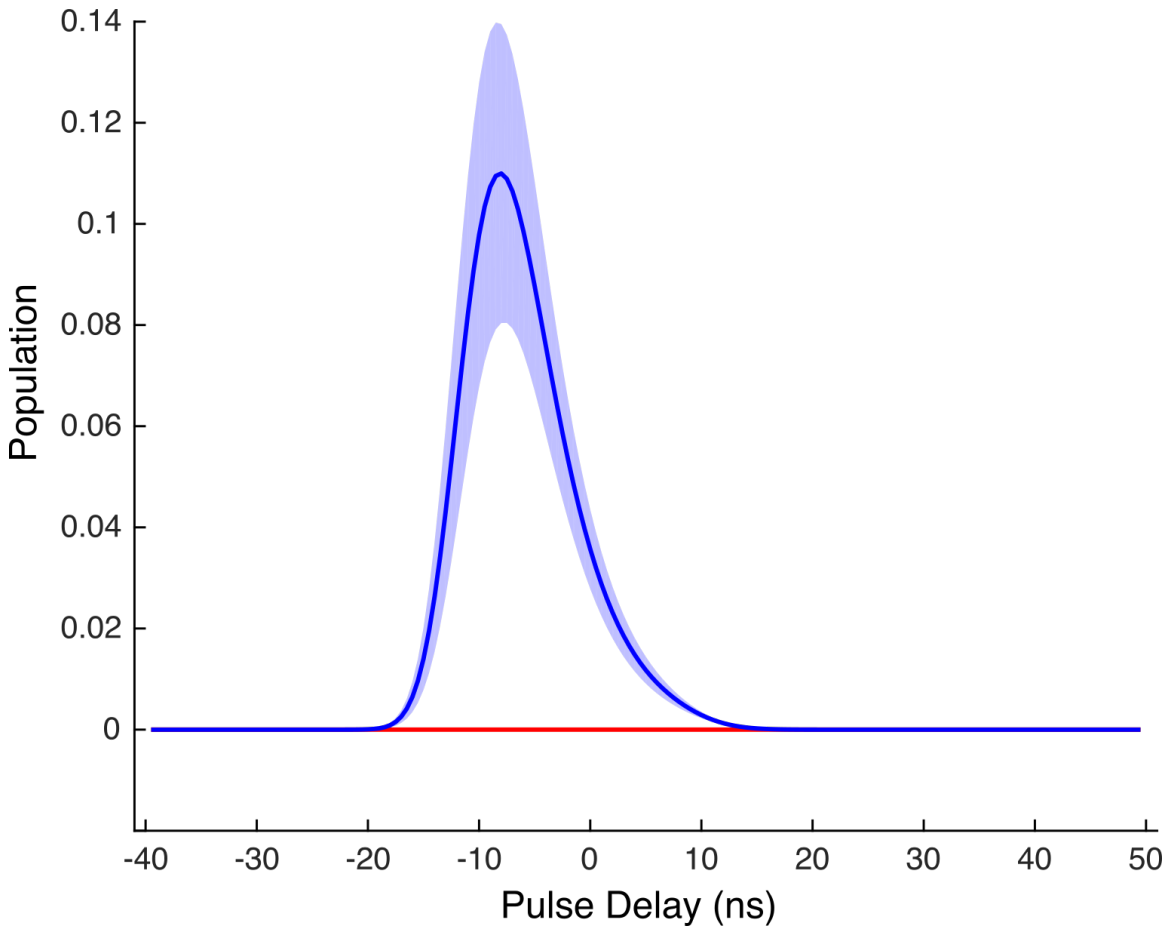

Figure 3-14: Simulation results for the intermediate (red) and final (blue) state population transfer as a function of pulse delay when the intermediate state has non-radiative lifetime of 1 ns. The solid lines are the mean population and the standard deviation of the 100 simulations is shown as a shaded area.

when zoomed in to this level. As a result, it is difficult to interpret the slightly lower population transfer observed when both fields are on one-photon resonance. It is likely that strong diabatic transitions on one-photon resonance increase the population loss relative to small one-photon detunings, as discussed in the case with no decay. This would also be consistent with previous investigations.[114] However, this difference is similar to the observed population differences due to fluctuations.

As the one-photon detuning is increased, the population transfer appears to be much more robust than in the case with no decay, varying from a peak of $\gtrsim$10% to about 7% at the largest detunings. This is about half the population transfer observed at the extreme detunings for the case of no decay, while the transfer on resonance is about five times lower. In addition, the lines are significantly more symmetric for the simulation with decay, and are missing the long tails in the direction of zero Pump detuning. Both of these observations point to the fact that only adiabatic population transfer can move significant population from the initial to the final state in the presence of a very lossy intermediate state. The lineshape is more symmetric because diabatic population transfer near zero Pump detuning is not operative. This is also why the population transfer is similar for all detunings. STIRAP is characteristically insensitive to the one-photon detuning and so the adiabatic population transfer does not decrease substantially across the detuning range. In contrast, for the case with no decay, the diabatic population transfer is strongly one-photon dependent and dramatically increases the population transfer only near zero Pump detuning.

In a sense, this hypothetical lossy state is the true test of STIRAP. The defining feature of STIRAP is that the intermediate state is not substantially populated en route to the final state. By simulating a fast intermediate state decay, the sequential excitation path is turned off and only STIRAP transfer can produce a signal. In our previous work, this test was the clear indication that STIRAP had *not* been achieved.[60] These positive simulation results further bolster our interpretation that optical-mmW STIRAP is operative, though not ideal, in our experiment, and that implementation of this technique in a molecule under similar conditions would be feasible.

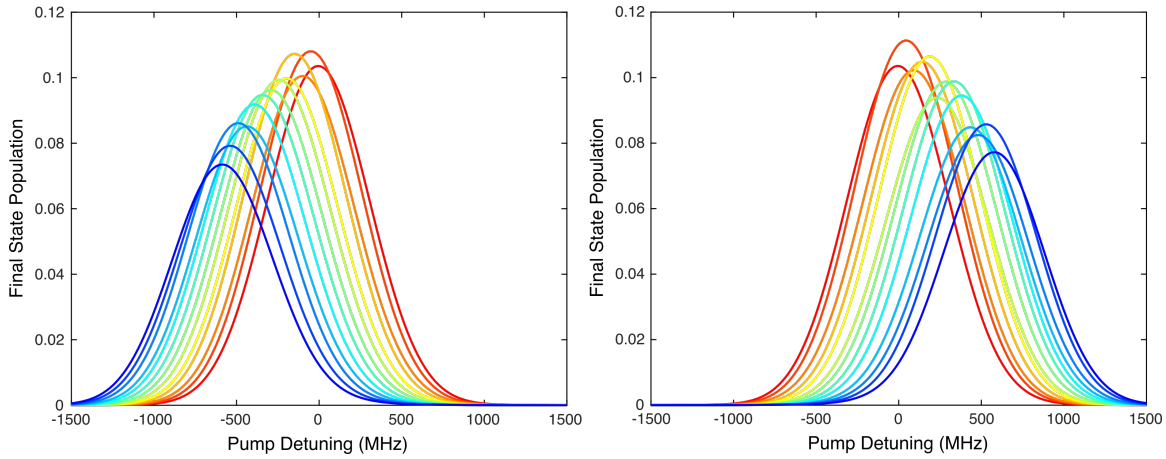

Figure 3-15: Simulation results for the population transfer as a function of Pump detuning for fixed values of the Stokes detuning for a system with a 1 ns intermediate state lifetime. Left: -600 MHz (dark blue) to 0 MHz (dark red) in steps of 50 MHz. Right: 600 MHz (dark blue) to 0 MHz (dark red) in steps of -50 MHz.

3.5.5 Future Improvements

Obviously, the final state population transfer of just over 50% for this proof-of-principle system is far below the near-unity population transfer typically associated with STIRAP. Beyond simply increasing the Rabi frequencies or eliminating the possible experimental imperfections discussed in Section 3.5.2, our simulations suggest a number of specific areas for improvement in experimental design.

First, the mmW pulse with a nearly square temporal profile immediately hinders the adiabatic following necessary for STIRAP. The sharp turn-on and turn-off produce non-adiabatic transitions between the intermediate and final states, corrupting the purity of the desired dark state. In the mmW frequency range, temporal pulse shaping on nanosecond time scales is technically inaccessible. In some spectral regions, electrically tuned variable attenuators exist, which can produce some pulse shaping although not in an arbitrary manner. Both David Grimes and Holger Herburger in the Field group have computationally explored some simplified pulse shapes that can be achieved with variable attenuators and demonstrated that population transfer efficiencies similar to smooth Gaussian pulses are possible.[59,60,66] Another strategy is to take advantage of the arbitrary pulse shapes available with an AWG and up-convert these shaped low-frequency pulses to the mmW range in a harmonic mixer.

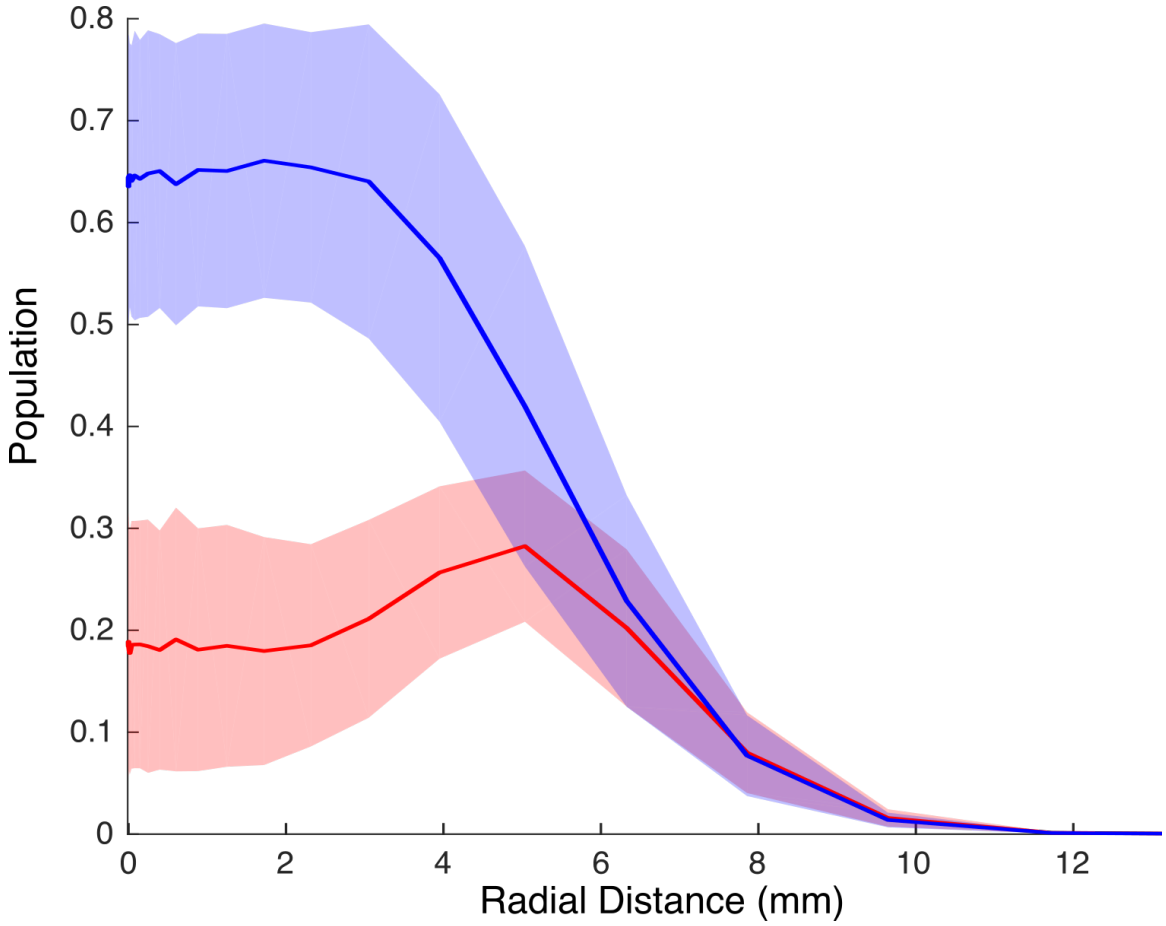

Figure 3-16: Simulated population transfer to the intermediate (red) and final (blue) state at the STIRAP timing as a function of the radial coordinate of the Pump laser. The Gaussian variation in the Pump laser intensity (HWHM 5 mm) gives rise to pronounced variation in the population transfer across the Pump beam profile.

We demonstrated the ability to generate a Gaussian-shaped, 10 ns, ∼90 GHz pulse, however, the pulse power following mixing and filtering of the undesired sideband was found to be too low for STIRAP experiments. With higher power mmW sources, this may be a fruitful strategy.

Figure 3-16 shows the simulated population transfer in the STIRAP timing as a function of the radial dimension of the Pump laser pulse. For this simulation, we have made the simplifying assumption that the Stokes Rabi frequency is constant due to the large beam profile of the mmW radiation. The Pump laser has a near-Gaussian transverse beam profile; as a result, the Rabi frequency varies dramatically as a function of the radial dimension of the laser spot. Near the center of the Pump

beam, where the laser intensity is greatest, the simulated transfer plateaus around 65% and the intermediate state population is just 20%. Moving out toward the edge of the beam profile, the population transfer efficiency decreases precipitously, while the intermediate state population actually increases. This indicates that the Pump laser does move significant population out of the initial state, but the Rabi frequency is too low to ensure adiabatic following. Eventually, the laser power decreases to zero and no population is transferred out of the initial state. This issue of radial variation in laser intensity has been identified in other STIRAP experiments.[32] By re-shaping the beam, for instance to a top-hat profile, it should be possible to achieve uniform population transfer efficiency across the width of the laser beam.

One of the most significant challenges in optical-mmW STIRAP relative to previous STIRAP implementations is the very large frequency difference that leads to negligible cancellation in Doppler shifts for the two photons. The use of a buffer gas cooled beam, with its relatively low beam divergence, certainly improved the population transfer efficiency relative to what would be possible with a high divergence supersonic jet. Figure 3-17 shows the simulated population transfer as a function of the Pump detuning. On this plot, the Doppler width would be represented by a Gaussian distribution centered at 0 MHz with HWHM of 155 MHz. The advantage of the narrow Doppler width from the buffer gas beam is evident. The majority of velocity sub-groups that contribute to the total population transfer have population transfer efficiencies of more than 50%. By skimming the beam, the transverse Doppler width could be further reduced at the expense of the total number of atoms/molecules. While this would make chirped-pulse experiments very challenging, a more sensitive detection technique like pulsed field ionization would be entirely compatible with this strategy. Moreover, the smaller molecular beam size would allow use of more tightly focused laser and microwave fields and thus a dramatic increase of the achievable Rabi frequencies.

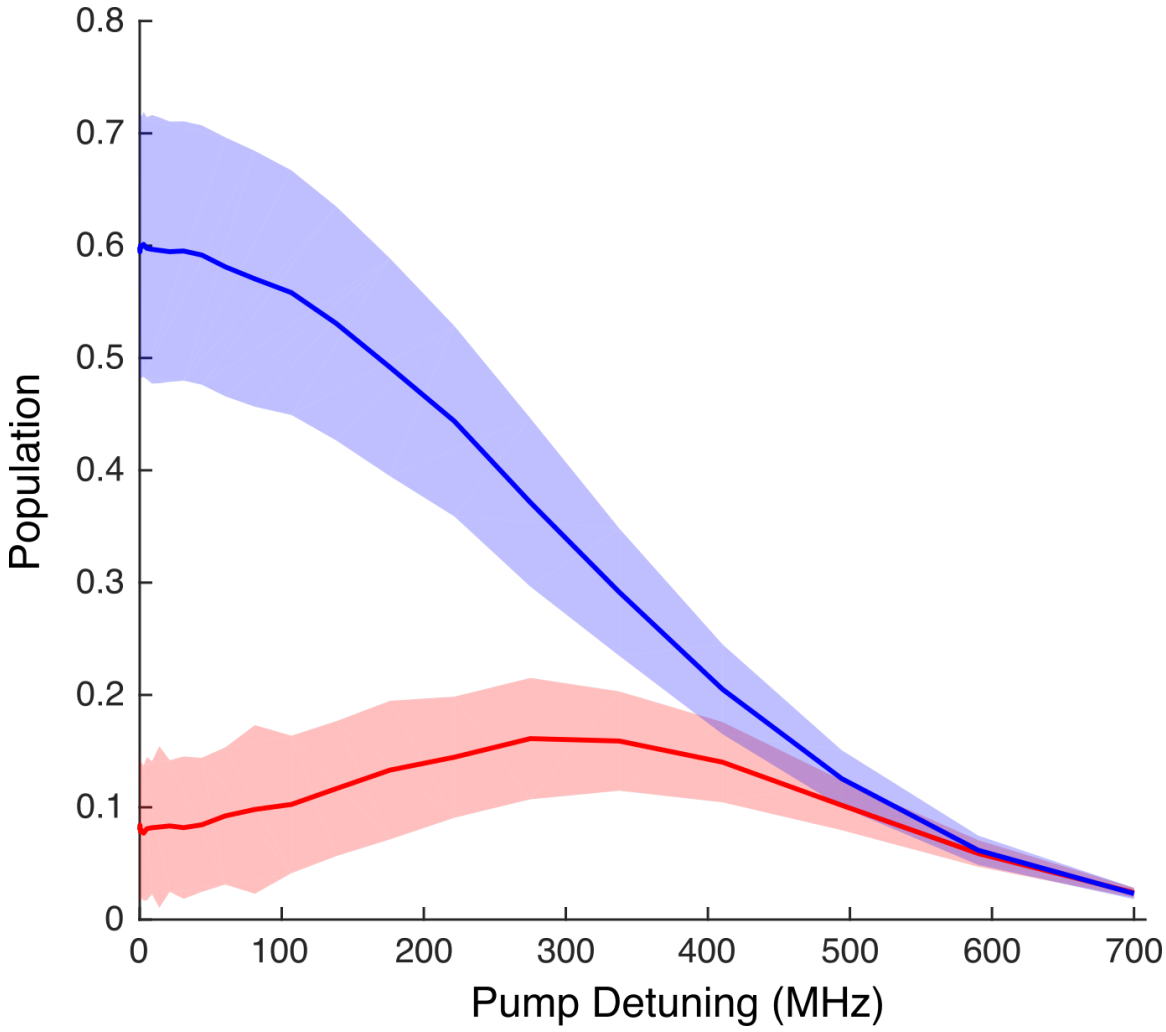

Figure 3-17: Simulated population transfer to the intermediate (red) and final (blue) state at the STIRAP timing as a function of the Pump laser detuning. This represents the effect of Doppler broadening on the total population transfer. For reference, the Pump transition was measured to have a HWHM of 155 MHz.

3.6 Conclusion

We have demonstrated, for the first time, population of high-ℓ Rydberg states by optical-mmW STIRAP. Population transfer occurs from a low-lying excited state of Ca atoms to an nf Rydberg state via an optically accessible lower-ℓ Rydberg state and involves coherent coupling of a laser and a mmW photon, differing by three orders of magnitude in frequency. This technique represents a new and widely applicable method for efficient population transfer into high-ℓ Rydberg states of atoms and molecules. In molecular systems, in which optically accessible low-ℓ Rydberg states often suffer from fast non-radiative decay, our method offers significant advantages over sequential excitation schemes. High-resolution spectroscopy of the Rydberg states of many molecules will be made possible by optical-mmW STIRAP.

Chapter 4

Spectroscopy of NO

4.1 Introduction

Since the early days of molecular spectroscopy, the nitric oxide molecule (NO) has occupied a special position for both theorists and experimentalists. It is, uniquely, a free radical in a bottle, making it a convenient system for high-resolution spectroscopic studies of Rydberg and valence states and their perturbations. Miescher performed much of the foundational spectroscopic analysis of NO, including the first detailed study of a high-ℓ Rydberg state of any molecule.[79] Intense study of NO has continued to the present day and touched on such diverse areas as combustion analysis,[90] collision dynamics,[82,172] atmospheric pollution,[31] and even biology.[1] In 1992, NO was declared "Molecule of the Year."[86]

In spite of this exalted position, there remain unexplored facets of NO. In particular, the high-ℓ Rydberg states of NO represent a vast state space that has eluded detailed investigation. The nf states, of course, have been studied by many authors,[4,15,27,39,49–51,58,79,107,117,118,165] and while the energy level structure is generally believed to follow the pattern of a core-nonpenetrating Rydberg state, the intramolecular dynamics (predissociation and autoionization) of nf states involve multi-state interactions and unusually rapid non-radiative decay. Some progress toward understanding the strangeness in the dynamics of the nf states is presented in Chapter 5. Rydberg states with $\ell > 3$ have been examined in just a handful of studies. Most

of these have examined the $5g$-$4f$ transition, which occurs in the infrared region, by emission[3,35] or absorption[97] spectroscopy. However, to expand the boundaries of the current level of understanding for these high-ℓ states, a data set covering a wide range of quantum numbers at high resolution is necessary. This motivated our approach, in the investigation of high-ℓ Rydberg-Rydberg transitions, to use CPmmW spectroscopy, which allows for high resolution data collection in an efficient multiplexed scheme with accurate relative transition intensities.

In this chapter, we begin by describing the basic theoretical framework for understanding high-ℓ Rydberg state energy level structure. Following a brief summary of some experimental details, each electronic state and transition in our excitation scheme is described. Finally, we discuss details of CPmmW spectroscopy experiments on NO, including unique assignment methods, surprising electric field effects, linewidth analysis, and a preliminary fit of the long-range electrostatic model.

4.2 Theory of molecular Rydberg states

A number of theoretical models exist for the description of molecular Rydberg states. These include approaches based on effective Hamiltonians,[75] multichannel quantum defect theory,[28] and, as will be used extensively in this work, long-range electrostatic interactions.[41] This final approach is particularly well suited for the description of high-ℓ, core-nonpenetrating Rydberg states of molecules, because the basic energy level structure is that of a hydrogen atom. Deviations from hydrogenicity are due to the fact that the ion at the center of the Rydberg state is not a point charge, but a collection of electron and nuclear charges. As its name implies, the long-range electrostatic model attempts to account for these non-hydrogenic interactions between the Rydberg electron and core using the long-range forces of classical electrostatics. Unlike other theoretical approaches for studying molecular Rydberg states, this means the model inputs are *physically meaningful*, rather than *effective* parameters. As will be discussed, this also requires careful application of the model only to states that satisfy the assumption of weak of core-penetration if the fit param-

eters are to be interpreted as "measurements" of the ion-core properties. A basic goal of our spectroscopy on NO is an improved understanding of the electrostatic model, generally, and of the electric structure of the NO^+ ion, specifically. In addition to the basic long-range electrostatic model, in this section we will also discuss the influence of magnetic interactions, specifically nuclear spin, on Rydberg states. Although hyperfine structure is not resolved in our experimental data, it can lead to broadening of the observed lines and so this discussion is included for completeness.

4.2.1 Long-range electrostatic model

The key to the long-range model of Rydberg states is the recognition of explicit physical mechanisms that perturb the Rydberg energy level structure from a purely hydrogenic form. This model was first considered by Jungen and Miescher,[79] and rigorously derived by Lundeen and co-workers.[142] However, we will generally follow the method of Eyler and Pipkin[41] using modern angular momentum algebra. The operations are most conveniently performed in a case (d) basis and we will begin by slightly augmenting the space-fixed case (d) wavefunction of Equation 1.59 by adding the vibrational and principal quantum numbers. The case (d) wavefunction now has the form:

$$|nvR\ell NM\rangle = \sum_{M_\ell, M_R} (-1)^{\ell - R + M} [2N+1]^{1/2} \begin{pmatrix} \ell & R & N \\ M_\ell & M_R & -M \end{pmatrix} |vR0M_R\rangle \, |n\ell M_\ell\rangle \tag{4.1}$$

We can explicitly write the electronic wavefunction for a hydrogenic Rydberg electron as

$$|n\ell M_\ell\rangle = |\ell M_\ell\rangle \, |n\ell\rangle = Y^\ell_{M_\ell}(\theta, \phi) R_{n,\ell}(r) \tag{4.2}$$

where $Y^\ell_{M_\ell}$ is a spherical harmonic with angles referenced to the space-fixed axis, and $R_{n,\ell}$ is a radial hydrogenic wavefunction. We will also invoke a separation of the rotational and vibrational degrees of freedom to write the nuclear wavefunction as

$$|vR0M_R\rangle = |RM_R\rangle \, |vR\rangle = Y^R_{M_R}(\theta_z, \phi_z) \, |vR\rangle \tag{4.3}$$

where the rotational wavefunction of a linear molecule is simply the spherical harmonic, $Y^R_{M_R}$, and the vibrational wavefunction, $|vR\rangle$, will depend on the rotational quantum number due to the R-dependent centrifugal barrier on the potential energy curve. The subscript z designates the angles that describe the internuclear axis in the space-fixed frame. Having carefully laid out the basis states to be used, we can now turn to consideration of the Hamiltonian:

$$H_{tot} = \frac{e^2}{r_{\rm Ryd}} + \sum_a \frac{e^2}{r_{{\rm Ryd},a}} - \sum_A \frac{q_A e^2}{r_{{\rm Ryd},A}} \tag{4.4}$$

where the subscript "Ryd" refers to the Rydberg electron, a refers to all other electrons in the ion-core, A refers to all nuclei, and q_A is the integer (positive) charge of the $A^{\rm th}$ nucleus. The first term is simply the hydrogenic potential, which will determine the zeroth-order energies. The second term describes interactions between the Rydberg electron and all other electrons, and the third term accounts for the finite internuclear separation. The zeroth-order Hamiltonian is equivalent to assuming that the second and third terms will perfectly cancel each other, or that the core electrons and nuclei occupy a negligible volume at the center of mass. We will handle these complicated many-body interactions by considering the two largest effects. First, the potential experienced by the Rydberg electron is modified by the non-sphericity of the ion-core, or in other words, the ion-core will generally possess an electric dipole, quadrupole, etc. Second, the field of the Rydberg electron can mix the ion-core states as a second-order effect. This will be handled by considering the simplest second-order electrostatic property of the ion-core, namely the dipole polarizability. The first-order electrostatic interactions are given by a multipole expansion:

$$H_{el} = \sum_{\rm core} \frac{e_{\rm Ryd} e_{\rm core}}{|r - r_{\rm core}|} \tag{4.5}$$

$$= \sum_{{\rm core},k} e_{\rm Ryd} e_{\rm core} \frac{r^k_{\rm core}}{r^{k+1}_{\rm Ryd}} P_k(\cos\omega_{\rm Ryd,core}) \tag{4.6}$$

where $\omega_{\rm Ryd,core}$ is the angle between the Rydberg electron and each of the core particles. Throughout this derivation, the subscript "core" refers to any core electron

or nucleus. We will re-write this expression using the spherical harmonic addition theorem, which takes several common forms:

$$P_k(\cos\theta_{ij}) = \frac{4\pi}{2k+1}\sum_q Y_{kq}(\theta_i,\phi_i)Y^*_{kq}(\theta_j,\phi_j) \tag{4.7}$$

$$= \sum_q (-1)^q C_{kq}(\theta_i,\phi_i)C_{k,-q}(\theta_j,\phi_j) \tag{4.8}$$

$$= C^k(\theta_i,\phi_i)\cdot C^k(\theta_j,\phi_j) \tag{4.9}$$

where C_{kq} are the modified spherical harmonics, or, equivalently, the q components of the spherical tensor operator C^k. This allows us to write an expression for the k^{th} multipole moment operator as

$$H_k = \sum_{\text{core},q} (-1)^q e_{\text{Ryd}} e_{\text{core}} \frac{r^k_{\text{core}}}{r^{k+1}_{\text{Ryd}}} \times C_{kq}(\omega_{\text{Ryd}},\nu_{\text{Ryd}})C_{k-q}(\omega_{\text{core}},\nu_{\text{core}}) \tag{4.10}$$

When averaged over the motion of the core electrons, the charge distribution of the core has cylindrical symmetry about the molecular axis, thus only the $q = 0$ term contributes. This yields the body-frame result:

$$H_k = \sum_{\text{core}} e_{\text{Ryd}} e_{\text{core}} \frac{r^k_{\text{core}}}{r^{k+1}_{\text{Ryd}}} C_{k0}(\omega_{\text{Ryd}},\nu_{\text{Ryd}})C_{k0}(\omega_{\text{core}},\nu_{\text{core}}) \tag{4.11}$$

$$= \frac{e_{\text{Ryd}}}{r^{k+1}_{\text{Ryd}}} C_{k0}(\omega_{\text{Ryd}},\nu_{\text{Ryd}})Q_k \tag{4.12}$$

where we have defined the k^{th} multipole moment by

$$Q_k = \sum_{\text{core}} e_{\text{core}} r^k_{\text{core}} C_{k0}(\omega_{\text{core}},\nu_{\text{core}}) \tag{4.13}$$

As the final step in deriving the multipole operator, we need to transform from the molecular frame to the laboratory frame in order to evaluate matrix elements. This is accomplished by recognizing that the (0,0) direction in the body frame refers to the

internuclear axis, and using the spherical harmonic addition theorem one more time.

$$H_k = \frac{e_{\mathrm{Ryd}}}{r_{\mathrm{Ryd}}^{k+1}} Q_k C_{k0}(\omega_{\mathrm{Ryd}}, \nu_{\mathrm{Ryd}}) \tag{4.14}$$

$$= \frac{e_{\mathrm{Ryd}}}{r_{\mathrm{Ryd}}^{k+1}} Q_k C_{k0}(\omega_{\mathrm{Ryd}}, \nu_{\mathrm{Ryd}}) C_{k0}(0,0) \tag{4.15}$$

$$= \frac{e_{\mathrm{Ryd}}}{r_{\mathrm{Ryd}}^{k+1}} Q_k P_k(\cos\Theta) \tag{4.16}$$

$$= -\frac{e}{r^{k+1}} Q_k C^k(\theta,\phi) \cdot C^k(\theta_z, \phi_z) \tag{4.17}$$

In the last step, e is no longer a signed quantity, and the explicit Rydberg subscript has been dropped. Now, we would like to evaluate the matrix element of the multipole moment operator H_k in the case (d) basis. Using Equations 4.1 and 4.17, we find:

$$\begin{aligned}
&\langle n'v'R'\ell'N'M'|H_k|nvR\ell NM\rangle \\
&\quad = -e\,\langle v'R'|Q_k|vR\rangle \left\langle n'\ell'|r^{-k}|n\ell\right\rangle \\
&\qquad \times \sum_{M_\ell, M_R, M'_\ell, M'_R} (-1)^{\ell'+\ell-R'-R+M'+M} \left[(2N'+1)(2N+1)\right]^{1/2} \\
&\qquad \times \begin{pmatrix} \ell' & R' & N' \\ M'_\ell & M'_R & -M' \end{pmatrix} \begin{pmatrix} \ell & R & N \\ M_\ell & M_R & -M \end{pmatrix} \\
&\qquad \times \left\langle \ell' M'_\ell | C^{(k)}(\theta,\phi) | \ell M_\ell \right\rangle \left\langle R' M'_R | C^{(k)}(\theta_z,\phi_z) | R M_R \right\rangle \qquad (4.18) \\
&\quad = -e\,\langle v'R'|Q_k|vR\rangle \left\langle n'\ell'|r^{-k}|n\ell\right\rangle \\
&\qquad \times \sum_{M_\ell, M_R, M'_\ell, M'_R} (-1)^{\ell'+\ell-R'-R+M'+M} \left[(2N'+1)(2N+1)\right]^{1/2} \\
&\qquad \times \begin{pmatrix} \ell' & R' & N' \\ M'_\ell & M'_R & -M' \end{pmatrix} \begin{pmatrix} \ell & R & N \\ M_\ell & M_R & -M \end{pmatrix} \\
&\qquad \times (-1)^{\ell'-M'_\ell} \begin{pmatrix} \ell' & k & \ell \\ -M'_\ell & 0 & M_\ell \end{pmatrix} \left\langle \ell' || C^{(k)}(\theta,\phi) || \ell \right\rangle \\
&\qquad \times (-1)^{R'-M'_R} \begin{pmatrix} R' & k & R \\ -M'_R & 0 & M_R \end{pmatrix} \left\langle R' || C^{(k)}(\theta_z,\phi_z) | R \right\rangle \qquad (4.19) \\
&\quad = -e\,\langle v'R'|Q_k|vR\rangle \left\langle n'\ell'|r^{-k}|n\ell\right\rangle
\end{aligned}$$

$$\times \delta_{N',N}\delta_{M',M}(-1)^{\ell-R'+N}\begin{Bmatrix}\ell' & R' & N\\ R & \ell & k\end{Bmatrix}$$

$$\times \left\langle \ell' || C^k(\theta,\phi) || \ell \right\rangle \left\langle R' || C^k(\theta_z,\phi_z) || R \right\rangle \tag{4.20}$$

$$= -e \left\langle v'R' | Q_k | vR \right\rangle \left\langle n'\ell' | r^{-k} | n\ell \right\rangle$$

$$\times \delta_{N',N}\delta_{M',M}(-1)^{\ell-R'+N}\begin{Bmatrix}N & R' & \ell'\\ k & \ell & R\end{Bmatrix}$$

$$\times (-1)^{\ell'}\left[(2\ell'+1)(2\ell+1)\right]^{1/2}\begin{pmatrix}\ell' & k & \ell\\ 0 & 0 & 0\end{pmatrix}$$

$$\times (-1)^{R'}\left[(2R'+1)(2R+1)\right]^{1/2}\begin{pmatrix}R' & k & R\\ 0 & 0 & 0\end{pmatrix} \tag{4.21}$$

$$= -e \left\langle v'R' | Q_k | vR \right\rangle \left\langle n'\ell' | r^{-k} | n\ell \right\rangle \delta_{N',N}\delta_{M',M}(-1)^{\ell+\ell'+N}$$

$$\times \left[(2\ell'+1)(2\ell+1)(2R'+1)(2R+1)\right]^{1/2}$$

$$\times \begin{Bmatrix}N & R' & \ell'\\ k & \ell & R\end{Bmatrix}\begin{pmatrix}\ell' & k & \ell\\ 0 & 0 & 0\end{pmatrix}\begin{pmatrix}R' & k & R\\ 0 & 0 & 0\end{pmatrix} \tag{4.22}$$

In the first step, we separated the angular components of the case (d) wavefunction from the vibrational and radial electronic components. The second step requires recalling that only the $q = 0$ component of the spherical tensor $C^{(k)}$ is non-zero and application of the Wigner-Eckart theorem. Condensing the sum of 3j symbols into the 6j symbol of Equation 4.20 necessitates conservation of the total angular momentum and its space-fixed projection. Finally, the Wigner-Eckart theorem is applied again and the result simplified to obtain Equation 4.22. This result could have also been derived with the use of a coupled case (d) wavefunction and the application of Formula 5.71 of Zare[163] for the matrix element of the product of spherical tensor operators, although that perhaps obscures the origin of this important result. The selection rules for this type of perturbation are given immediately by the Kronecker deltas and the form of the 3j symbols:

$$\Delta N = 0$$

$$\Delta M = 0$$

$$\Delta \ell = \pm k, \pm(k-2), \ldots, \pm k \bmod 2$$

$$\Delta R = \pm k, \pm(k-2), \ldots, \pm k \bmod 2$$

Our discussion of the polarizability operator will be less detailed, since much of the same machinery is used. The dipole polarizability of the ground electronic state is obtained from second-order perturbation theory of the dipole term as:

$$\alpha_{ij} = 2 \sum_{n \neq 0} \frac{\langle 0|\mu_i|n\rangle \langle n|\mu_j|0\rangle}{W_n - W_0} \tag{4.23}$$

where W_n is the energy of the n^{th} excited electronic state and W_0 is the ground state energy. The dipole polarizability generally has 9 components, but for a linear molecule it is simplified dramatically to a form with just two unique contributions.

$$\alpha_{ij} = \begin{pmatrix} \alpha_\perp & 0 & 0 \\ 0 & \alpha_\perp & 0 \\ 0 & 0 & \alpha_\parallel \end{pmatrix} \tag{4.24}$$

We re-write these molecule-fixed polarizabilities into the isotropic (mean), α, and anisotropic, γ, components of the polarizability:

$$\alpha = \frac{1}{3}\left(2\alpha_\perp + \alpha_\parallel\right) \tag{4.25}$$

$$\gamma = \alpha_\parallel - \alpha_\perp \tag{4.26}$$

Buckingham first showed that the contribution of the polarizability to the energy can be written in a simple form using the isotropic and anisotropic terms,[23] and we choose to write that result in the angular momentum terminology used throughout this work:

$$H_{pol} = -\frac{1}{2}\alpha E^2 - \frac{1}{3}\gamma E^2 P_2(\cos\Theta) \tag{4.27}$$

$$= -\frac{1}{2}\alpha\frac{e^2}{r^4} - \frac{1}{3}\gamma\frac{e^2}{r^4}C^{(2)}(\theta,\phi)\cdot C^{(2)}(\theta_z,\phi_z) \tag{4.28}$$

where in the second step we have substituted an explicit expression for the electric field due to the Rydberg electron, and used the spherical harmonic addition theorem in exactly the same way as in the multipole derivation. Since the dipole polarizability is a sum of products of dipole operators, which are each rank 1 tensors, the polarizability must transform under rotation as a rank 2 tensor. This is the origin of the angular dependence of the anisotropic polarizability, which looks identical to that of the quadrupole moment. As a result, no additional work is required to evaluate the matrix elements of this operator:

$$\begin{aligned}
&\langle n'v'R'\ell'N'M'|H_k|nvR\ell NM\rangle \\
&\quad = -e^2\left\langle n'\ell'|r^{-4}|n\ell\right\rangle\left[\frac{1}{2}\left\langle v'R'|\alpha|vR\right\rangle\delta_{\ell',\ell}\delta_{R',R}\right. \\
&\qquad + \frac{1}{3}\left\langle v'R'|\gamma|vR\right\rangle(-1)^{\ell+\ell'+N}\delta_{N',N}\delta_{M',M} \\
&\qquad \times\left[(2\ell'+1)(2\ell+1)(2R'+1)(2R+1)\right]^{1/2} \\
&\qquad \left.\times\begin{Bmatrix} N & R' & \ell' \\ 2 & \ell & R\end{Bmatrix}\begin{pmatrix}\ell' & 2 & \ell\\ 0 & 0 & 0\end{pmatrix}\begin{pmatrix}R' & 2 & R\\ 0 & 0 & 0\end{pmatrix}\right]
\end{aligned} \tag{4.29}$$

4.2.2 Hyperfine structure

The electrostatic model presented in the previous section correctly treats the electric fine structure splittings present in a Rydberg complex. In addition, magnetic fine structure resulting from interactions of the electron and nuclear spin may cause additional shifts and splittings of levels. This discussion follows the method outlined by Lundeen and co-workers,[6] which assumes an *ad hoc* Hamiltonian of the form:

$$H_{MFS} = H_{HFS} + H_{MS} + (-1)^S V_x \tag{4.30}$$

where the third term represents an exchange energy between the Rydberg electron and a core electron, and the second term represents the magnetic interaction between the

core and the Rydberg electron. Both of these effects involve an interaction between the Rydberg electron and the core, thus they decrease rapidly as n and ℓ increase. For the high-n, high-ℓ Rydberg states studied in this work, we can safely neglect these terms, as done in previous studies.[6] This leaves the hyperfine structure of the ion-core, H_{HFS}, as the only significant magnetic fine structure effect that must be considered. First, we will slightly revise our case (d) angular momentum coupling model to consider nuclear spin. The basis states from the long-range model appear on the left in Figure 4-1, and are formed by coupling the Rydberg electron orbital angular momentum with the ion-core rotation to form the spinless total angular momentum, $\boldsymbol{N} = \boldsymbol{R}+\boldsymbol{\ell}$. Next, we couple the nuclear spin, $\boldsymbol{I}$, to form the total angular momentum, $\boldsymbol{F} = \boldsymbol{N}+\boldsymbol{I}$, illustrated in the center panel of Figure 4-1. In fact, the *true* total angular momentum requires a final coupling of the Rydberg electron spin $\boldsymbol{s}$ to form $\boldsymbol{J} = \boldsymbol{F}+\boldsymbol{s}$. This splitting due to the Rydberg electron spin is extremely small, and is identical to zero if we ignore the terms H_{MS} and V_x in our total Hamiltonian.

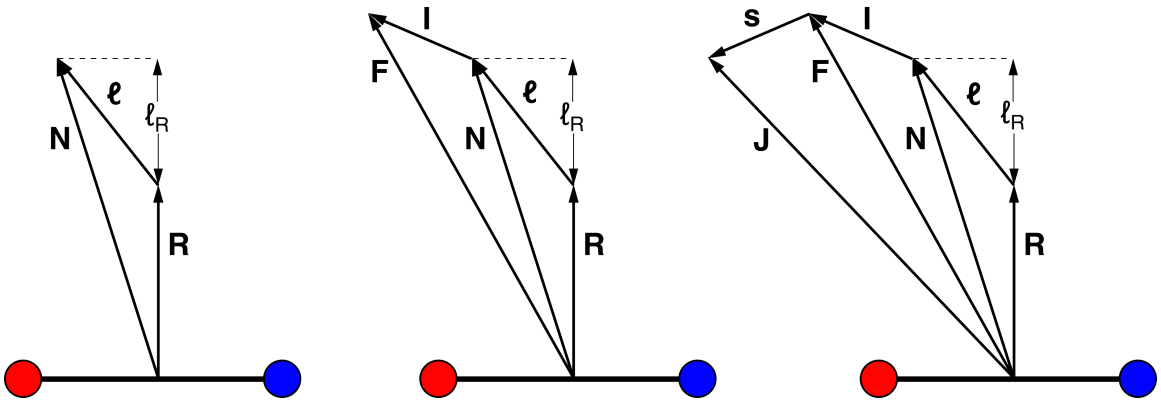

Figure 4-1: Angular momentum coupling in the presence of nuclear spin. Left: The Rydberg electron orbital angular momentum couples to the ion-core rotation to form $\boldsymbol{N}$. These energies are determined by the long-range model and form the zeroth-order basis states for consideration of nuclear spin effects. Center: The nuclear spin, $\boldsymbol{I}$, is coupled to $\boldsymbol{N}$, to form what we will call the total angular momentum $\boldsymbol{F}$. This results in a splitting of the zeroth-order energy levels into three sub-levels for a nucleus with $I = 1$. Right: In reality, the total angular momentum is given by the coupling of $\boldsymbol{F}$ with the Rydberg electron spin, $\boldsymbol{s}$, to form $\boldsymbol{J}$. This would split every hyperfine level into a pair of spin doublets. We will neglect this energy level splitting entirely.

The hyperfine structure of NO^+ results from the $I = 1$ nitrogen nucleus, and can

be described by the Hamiltonian:

$$H_{HFS} = H_Q + c\,(\boldsymbol{I} \cdot \boldsymbol{N}) \tag{4.31}$$

The second term in this expression describes the nuclear spin-rotation coupling. For closed shell species, this is typically a small effect ($c \lesssim 100$ kHz),[21,46] and this constant has not been measured for the NO^+ ion. In contrast, the electric quadrupole interaction, H_Q, is always an important term to consider in high-resolution spectroscopy of nitrogen-containing species. The electric quadrupole Hamiltonian describes the interaction between the electric quadrupole moment of the nitrogen nucleus and the electric field gradient due to all particles at the location of the quadrupolar nucleus. It can simply be written as the product of two rank 2 tensors:

$$H_Q = \boldsymbol{V}^{(2)} \cdot \boldsymbol{Q}^{(2)} = \sum_{q=-2}^{2} (-1)^q V_q^{(2)} Q_{-q}^{(2)} \tag{4.32}$$

where $V_q^{(2)}$ are the components of the electric field gradient tensor and $Q_q^{(2)}$ are the nuclear quadrupole tensor components. Using angular momentum machinery, we can arrive at an expression for the first order perturbation theory estimate of the nuclear quadrupole interaction energy:

$$\Delta E = \frac{1}{2} eqQ \left[\frac{(3/4)C(C+1) - I(I+1)N(N+1)}{I(2I-1)N(2N-1)} \right] \tag{4.33}$$

where $C = F(F+1) - N(N+1) - I(I+1)$ and eqQ is the quadrupole coupling constant. This constant has been measured for NO^+ to be -6.76 MHz.[17] In general, the perturbation theory result is an excellent approximation to the true energy. When increasing to very high n values or at extremely high resolution, it will become necessary to perform a full matrix diagonalization in which the off-diagonal elements couple levels with the same value of F and differences in N of $\Delta N = \pm 2$. The reason for this change in approach again arises from the ubiquitious Rydberg scaling rules. While the electric fine structure splitting of a Rydberg complex decreases approximately as

n^{-3}, there is no such reduction in hyperfine splitting since the radial wavefunction of the Rydberg electron is not involved. Thus, for sufficiently high n (or ℓ), the electric fine structure splitting will approach the scale of the hyperfine splitting and all levels with $\Delta F = 0$ and $\Delta N = 0, \pm 2$ will strongly interact.

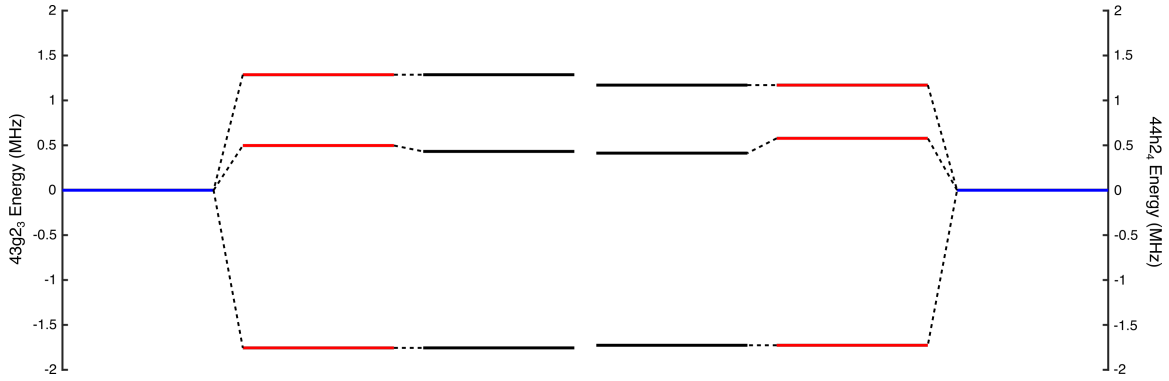

Figure 4-2: Energy level splitting due to electric quadrupole hyperfine interaction. The zeroth-order energies of the $43g2_3$ and $44h2_4$ Rydberg states are shown in blue on the left- and right-hand side of the plot, respectively. The first order perturbation theory result appears in red and the full matrix diagonalization result appears in black.

An example of the hyperfine splitting in NO Rydberg states appears in Figure 4-2. The zeroth-order energies of the $43g2_3$ and $44h2_4$ levels, obtained from the long-range model, appear in blue at 0 MHz on the left- and right-hand side of the plots, respectively. Since $I = 1$, the electric quadrupole interaction splits the single level into three hyperfine states. The first order perturbation theory result appears in red, and the full matrix diagonalization result appears in black. The correction due to inclusion of off-diagonal elements is clearly quite small. Only one of the three hyperfine levels exhibits a shift large enough to be seen on this scale. Comparing the two Rydberg states, the $44h2_4$ state exhibits a smaller hyperfine splitting because the interaction energy decreases with increasing N. The correction to the shifted level in the matrix diagonalization result is larger, though, because the electric fine structure splitting in the h state is smaller than the g state so the off-diagonal interaction in the h state is stronger. In general, the two states exhibit very similar hyperfine structure, which, combined with the fact that the strongest transitions in the spectrum satisfy the propensity rule $\Delta F = \Delta N$, means the expected hyperfine splitting in the Rydberg-

Rydberg spectra will be generally very small. Indeed, an explicit simulation of this transition, which appears in Figure 4-3, shows that there are three strong transitions within 150 kHz of each other that form a central peak, while satellite transitions several MHz away are almost two orders of magnitude weaker. Satellite lines have never been observed in our spectra, so the hyperfine splitting only influences the experimental spectra by adding some additional line broadening. In Figure 4-3, for example, each line is assumed to have a width of 600 kHz, and the central feature is broadened to nearly 700 kHz by the slight frequency offsets of the three intense $\Delta F = \Delta N$ lines.

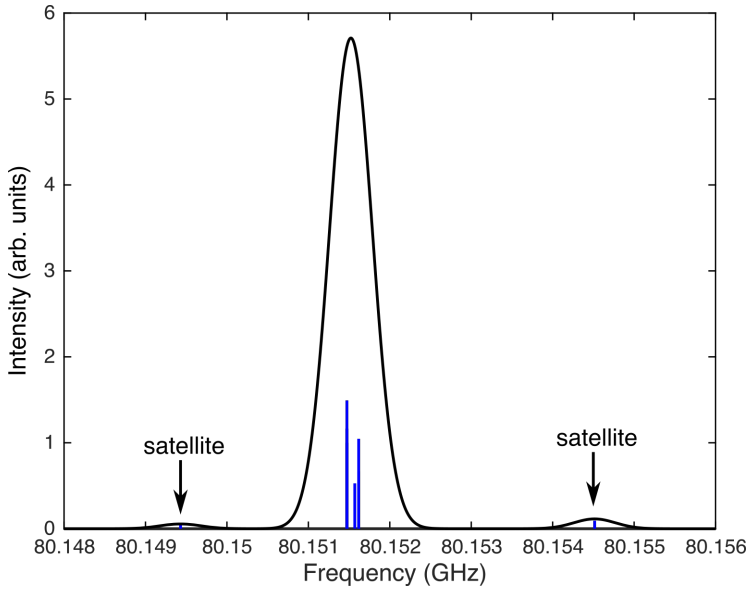

Figure 4-3: Simulation of the $44h2_4 \leftarrow 43g2_3$ transition including hyperfine splitting. The spectral intensity is concentrated in the closely spaced $\Delta F = \Delta N$ lines that form the central peak. Very weak satellite lines (labeled) are from transitions with $\Delta F \neq \Delta N$ and occur at spacings similar to the actual hyperfine splitting.

4.3 Experimental

The experiments described in this chapter employ a three-color triple-resonance laser excitation scheme to access ng Rydberg states of NO, which is shown schematically in Figure 4-4. The first laser is a frequency-doubled dye laser (Sirah, Cobra-Stretch) pumped by the third harmonic of a Nd:YAG laser (Spectra Physics, GCR-

270) and operating either at 452 nm with Coumarin 450 dye, or at 430 nm with Stilbene 420 dye. Following frequency doubling in a BBO crystal, the former (452 nm) provides access to the (0,0) band of the A-X transition at 226 nm and the latter (430 nm) to the (1,0) band at 215 nm. This initial step, following the $\Delta v = 0$ propensity rule for Rydberg-Rydberg transitions, selects the vibrational quantum number for all further electronic states in the excitation scheme. A second dye laser (Lambda Physik, Scanmate 2E) pumped by 355 nm light from the same Nd:YAG laser is operated at 423 nm with Stilbene 420 laser dye. This laser is tuned to be resonant with transitions in either the (0,0) or (1,1) band of the $4f$-A transition.

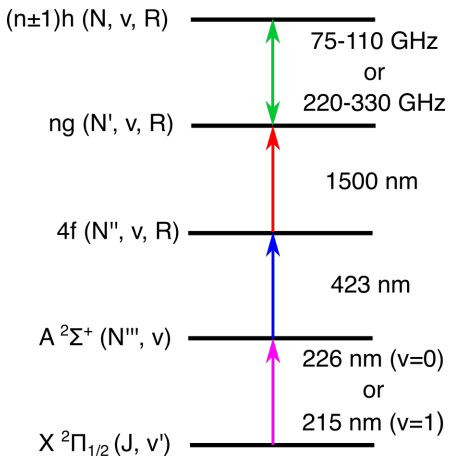

Figure 4-4: Energy level scheme for NO spectroscopy experiments. The A-X and $4f$-A transitions are probed by 1+1 and 1+1'+1' REMPI schemes, respectively. Transitions to ng states are probed by pulsed field ionization for $v = 0$ states and by autoionization for $v = 1$ states. The final mmW transitions can be probed by selective field ionization or by CPmmW spectroscopy.

The final laser photon, which transfers population from the $4f$ state to an ng level, vertical in vibrational quantum number, has been generated by two different setups. Initial laser spectroscopy on ng-$4f$ transitions was performed using the pulsed dye amplification system. In this setup, a CW Ti:Sapphire laser (MSquared, Solstis) operating near 830 nm seeds the dye amplifier chain (Lioptec, custom) pumped by the second harmonic of a Nd:YAG laser (Spectra Physics, LAB-170) at 10 Hz. This pulsed output is then mixed with residual 532 nm light from the same Nd:YAG in a BBO crystal, to produce the difference frequency near 1500 nm. We obtain approximately

7 ns, 2 mJ pulses of infrared light with an estimated bandwidth of 100 MHz.

For mmW experiments on high-n Rydberg states, even the narrow bandwidth of the pulsed amplification laser cannot resolve electric fine structure components. Therefore, we switched to a technically simpler setup using a pulsed dye laser. In this setup, a pulsed dye laser (Continuum, ND6000) is pumped by the second harmonic of a Nd:YAG laser (Spectra Physics, PRO-290) and operates near 630 nm with DCM laser dye. The dye laser output is then mixed with residual fundamental (1064 nm) from the Nd:YAG in a Li:NbO_4 crystal to produce the difference frequency radiation around 1500 nm. Although the bandwidth of this laser is substantially larger (~ 0.1 cm^{-1}), this system has some technical advantages. The Nd:YAG laser in this setup runs at 20 Hz, matching the repetition rate of the other lasers, and doubling the data collection rate. We can routinely obtain several 10s of mJ of pulsed radiation due to the higher efficiency of the DCM dye and the lithium niobate crystal. Finally, the alignment of a pulsed dye laser is significantly simpler, and minimal realignment is required from day to day.

Laser spectroscopy experiments were all performed using the ion-detection mode of our supersonic jet apparatus, shown schematically in Figure 4-5. In this experiment, NO seeded at 0.5% by volume in Ar is expanded through a pulsed nozzle (Parker Hannafin, General Valve Series 9) and passes through a 1 mm conical skimmer to enter a differentially pumped detection chamber. The beam passes through a second larger diameter skimmer before entering a gold shroud that houses the electrode stack. Laser excitation occurs at this point transverse to the beam propagation direction. For spectroscopy of the A state and $4f$ state, we employ a 1+1 or 1+1'+1' REMPI scheme, where the final photon non-resonantly ionizes the NO molecules out of an excited state level. A pulsed electric field extracts these ions in the orthogonal direction, and these ions are focused by the electrode stack onto an MCP detector. The ng Rydberg states are either detected in an analogous way, following spontaneous autoionization of states with $v = 1$, or by pulsed field ionization (PFI) for bound $v = 0$ Rydberg states. The maximum pulsed electric field voltage of about 450 V/cm limits the Rydberg states that can be detected by PFI to $n \gtrsim 33$. The ion detection chamber is additionally

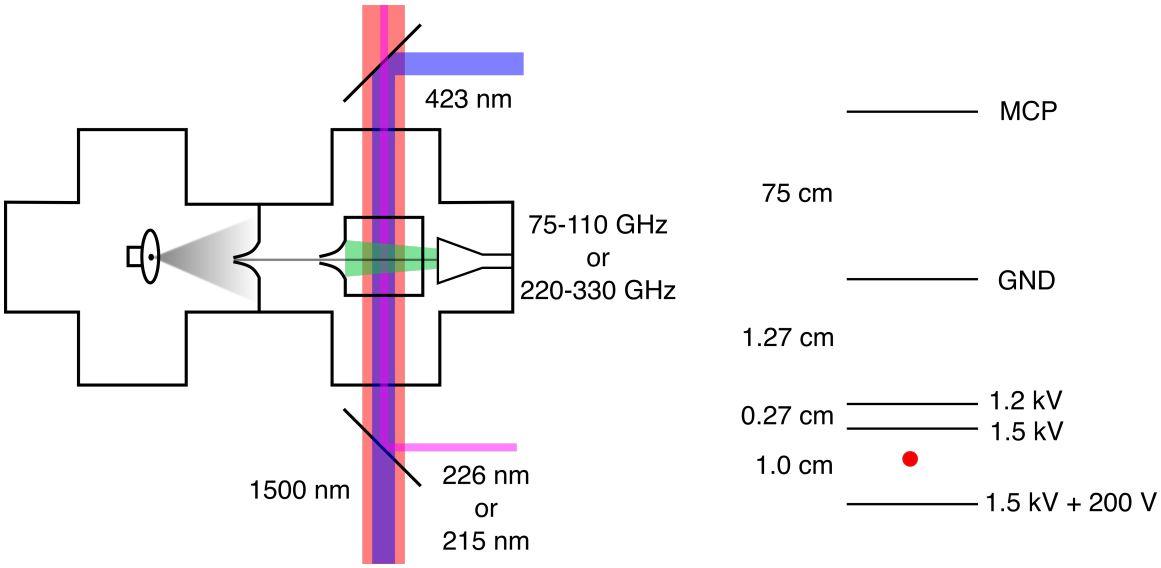

Figure 4-5: Left: Schematic of the experimental setup for ion-detected experiments in the supersonic jet apparatus. A supersonic jet is skimmed twice before entering the probe region of the differentially pumped detection chamber. Laser excitation occurs transverse to the direction of the molecular beam propagation. If used, mmW radiation is introduced counter-propagating along the molecular beam axis via a waveguide feedthrough in the chamber. The time-of-flight axis for the mass spectrometer points out of the plane. Right: Simplified schematic of the TOF electrode stack. Excitation occurs under nearly field-free conditions. A pulsed field is then applied to the bottom plate to simultaneously ionize high-n Rydberg states and extract ions for detection.

equipped with a waveguide feedthrough and standard gain horn, which allows us to broadcast mmW radiation along the propagation direction of the molecular beam. Although this system is useful for some preliminary mmW spectroscopy experiments, it suffers from the limited ability to control stray electric fields, as discussed in the following sections.

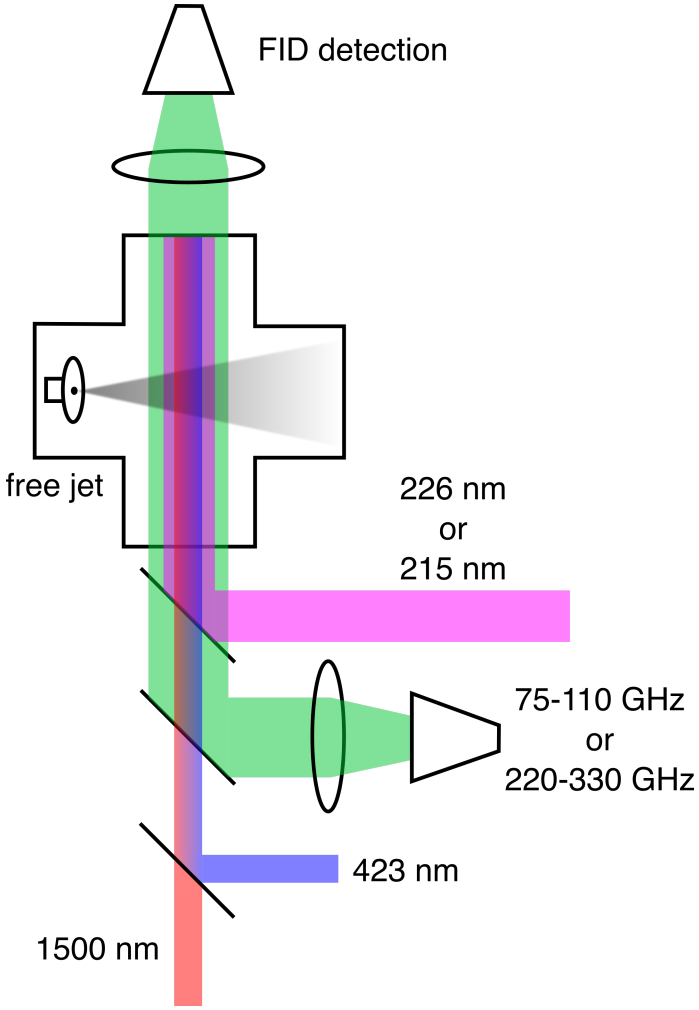

Figure 4-6: Schematic of the experimental setup for CPmmW experiments in the supersonic jet apparatus. An unskimmed free jet expansion is probed transversely by the co-propagating laser and mmW fields. FID from the polarized Rydberg-Rydberg transitions is detected at a second horn on the opposite side of the chamber.

The experimental setup for CPmmW spectroscopy experiments is shown schematically in Figure 4-6. The experiment occurs entirely in the first chamber of the supersonic jet apparatus. An *unskimmed* free jet expansion of the 0.5% NO in Ar mixture

is probed transversely by the laser and mmW fields approximately 30 cm downstream from the nozzle exit. As previously described, the radiation fields are first collimated and then overlapped at several dichroic optics, including an ITO-coated glass plate that reflects the mmW radiation. The mmW radiation in this experiment is generated by either the W band spectrometer or the high-frequency configuration of this spectrometer as described in Chapter 2. At the opposite end of the chamber, the FID from Rydberg-Rydberg transitions is collected, down-converted, and digitized on a high-speed oscilloscope. The guiding principle of this setup was discussed in our initial demonstration of CPmmW spectroscopy on Rydberg-Rydberg transitions.[126] We require a large interaction volume, produced by expanding the laser beam diameters and probing far downstream of the nozzle, in order to maximize the number of Rydberg emitters, while minimizing the number density. The minimum number of emitters is determined by the sensitivity of our detection system to typically $\gtrsim 10^5$,[30] while the maximum number density of $\lesssim 10^7$ cm^{-3} is determined by the onset of superradiant dynamics[61] that interfere with the spectroscopic experiment. This latter issue is addressed in a later section.

For the CPmmW experiments, we found it necessary to change the vacuum system on this apparatus from its initial configuration. Specifically, the chamber was initially equipped with a 1000 L/s turbomechanical pump (Varian, Turbo-V1000HT). While operating the CPmmW experiment with this pump, we observed mmW signals that persisted long after the nominal duration of the gas pulse. In some cases, these signals were even larger than those observed when the mmW probe overlapped with the gas pulse timing. This suggested to us that a significant amount of background gas remained in the chamber and likely affected the pulsed jet dynamics in the low density region of the expansion that we interrogated. To overcome this issue, we switched the vacuum system to a 3600 L/s diffusion pump (Varian, VHS-10). The increased pumping speed immediately produced more sensible observations. The mmW signal reached maximum intensity when the excitation pulses overlapped with the gas pulse and quickly decreased as the delay time was increased. Yan Zhou performed a quantitative analysis of these two systems and found that the residence

time for gas in the chamber with this diffusion pump was approximately 15 ms, as opposed to 50 ms with the slower turbo pump.[168] Since our experiment operates at 20 Hz, the 50 ms residence time indicates a significant amount of gas remains in the chamber from one experimental cycle to the next. By increasing the pumping speed of our vacuum system, we have removed the complicated and confusing influence of background gas on the experiment.

4.4 The A $^2\Sigma^+ \leftarrow$ X $^2\Pi_{1/2}$ transition

4.4.1 Energy level structure of the X $^2\Pi_{1/2}$ state

The ground state of NO is a $^2\Pi_\Omega$ state where the case (a) basis states have the quantum numbers: $\Lambda = \pm 1$, $\Sigma = \pm\frac{1}{2}$, and $\Omega = \pm\frac{1}{2}, \pm\frac{3}{2}$. It is necessary to first symmetrize the basis state wavefunctions to obtain solutions with well-defined parity.

$$|^2\Pi_{1/2} JMp^{\pm}\rangle = \frac{1}{\sqrt{2}}\left[|\Lambda = 1\rangle\,|S = \frac{1}{2}, \Sigma = -\frac{1}{2}\rangle\,|J, \Omega = \frac{1}{2}M\rangle \right. \\ \left. \pm\,|\Lambda = -1\rangle\,|S = \frac{1}{2}, \Sigma = \frac{1}{2}\rangle\,|J, \Omega = -\frac{1}{2}M\rangle\right] \tag{4.34}$$

$$|^2\Pi_{3/2} JMp^{\pm}\rangle = \frac{1}{\sqrt{2}}\left[|\Lambda = 1\rangle\,|S = \frac{1}{2}, \Sigma = \frac{1}{2}\rangle\,|J, \Omega = \frac{3}{2}M\rangle \right. \\ \left. \pm\,|\Lambda = -1\rangle\,|S = \frac{1}{2}, \Sigma = -\frac{1}{2}\rangle\,|J, \Omega = -\frac{3}{2}M\rangle\right] \tag{4.35}$$

The upper sign corresponds with + parity states and the lower sign with − parity states. These parity doublets occur in both spin-orbit manifolds for all $J > 1/2$. To distinguish between them, we assign a label for the spin state: F_1 for $\Omega = 1/2$ and F_2 for $\Omega = 3/2$. These parity doublets are degenerate except for perturbations by distant Σ symmetry electronic states, which, unlike states with $\Lambda \geq 1$, lack parity doublets for every value of N. This interaction lifts the degeneracy by so-called Λ-doubling. The rotational Hamiltonian appears in Equation 1.17. In addition, the spin-orbit

operator lifts the degeneracy of the $\Omega = \frac{1}{2}$ and $\Omega = \frac{3}{2}$ states:

$$\boldsymbol{H}_{so} = A\boldsymbol{L} \cdot \boldsymbol{S} \tag{4.36}$$

$$= AL_z S_z \tag{4.37}$$

where we have neglected $\Delta\Lambda = \pm 1$ terms connecting the X $^2\Pi_{1/2}$ state to other electronic states. The two Ω manifolds will be split by the spin-orbit operator by an amount approximately equal to A, which for the $v = 0$ level of the X state is $A_0 = 123.14$ cm^{-1}.[71] At 15 K, an upper limit on the temperatures relevant to this work, the upper $^2\Pi_{3/2}$ state has a Boltzmann weight of order 10^{-6} and is insignificantly populated. Solution of the 2×2 secular determinant for the total Hamiltonian, $\boldsymbol{H} = \boldsymbol{H}_{rot} + \boldsymbol{H}_{so}$, yields the energies of the $^2\Pi_\Omega$ state:

$$E = B_0 \left[\left(J - \frac{1}{2} \right) \left(J + \frac{3}{2} \right) \pm \frac{1}{2} X \right] \tag{4.38}$$

where the plus (minus) sign applies to the the $\Omega = 3/2$ ($\Omega = 1/2$) component, and

$$X = \sqrt{\frac{A}{B}\left(\frac{A}{B} - 4\right) + 4\left(J + \frac{1}{2}\right)^2} \tag{4.39}$$

The rotational constant of the X $^2\Pi_{1/2}(v = 0)$ state is given by:[71]

$$B_v = B_e - \alpha_e(v + 1/2) + \gamma_e(v + 1/2)^2 + \ldots \tag{4.40}$$

$$B_0 = 1.6961\,\text{cm}^{-1} \tag{4.41}$$

where the rotational constant is parametrized in the vibrational quantum number with coefficients α, γ, ..., and the e subscript refers to the value at the equilibrium bond length. Since we will generally work at low rotation, we can safely neglect the effect of centrifugal distortion, which for $v = 0$ of X $^2\Pi_{1/2}$ is characterized by the constant $D_0 = 5.34 \times 10^{-6}$ cm^{-1}.[71] A schematic of the X state energy levels is shown in the transition diagram of Figure 4-7.

Lastly, we can comment on the applicability of Hund's case (a) to the description

of the ground state. In reality, all rotational levels besides $J = 1/2$ exist in a coupling case between case (a) and case (b). The transition between these two limiting behaviors is given approximately by the relative energy scales of the rotational and spin-orbit operators: $2BJ \approx A$. For the ground state of NO, this case (a) $\rightarrow$ case (b) transition occurs at approximately $J \approx 35.5$, which is far above the rotational states considered in this work. Thus Hund's case (a) will be a good approximation for treating the $X^2\Pi_{1/2}$ state.

4.4.2 Energy level structure of the A $^2\Sigma^+$ state

The A $^2\Sigma^+$ state is the lowest-lying Rydberg state, and corresponds to excitation of an electron from the anti-bonding π^* electron from the ground state configuration into the non-bonding $3s\sigma$ Rydberg orbital. As a result, the equilibrium bond length of the A state is actually shorter than that of the ground state, an unusual reversal of the typical bond length change upon electronic excitation. On the other hand, most excited valence states of NO involve excitation of one of the bonding orbital π electrons to an anti-bonding π^* orbital, resulting in a longer bond length than in the ground state. This fact gives rise to a pattern in which the Rydberg states of NO have rotational constants of approximately 2 cm^{-1}, and excited valence states of NO have rotational constants of about 1 cm^{-1}.

For a Σ state, the rotational Hamiltonian is simplified by $\Lambda = 0$ and reads:

$$\boldsymbol{H}_{rot} = B\boldsymbol{R}^2 \tag{4.42}$$

$$= B\left(\boldsymbol{J} - \boldsymbol{S}\right)^2 \tag{4.43}$$

$$= B\left[\boldsymbol{J}^2 - 2J_zS_z + \boldsymbol{S}^2\right] - B\left[J_+S_- + J_-S_+\right] \tag{4.44}$$

In addition, we will consider a phenomenological spin-rotation operator, which lifts the degeneracy of the different spin states, which have the same value of N and different values of J:

$$\boldsymbol{H}_{sr} = \gamma\boldsymbol{R}\cdot\boldsymbol{S} \tag{4.45}$$

$$= \gamma \left(\boldsymbol{J} - \boldsymbol{S} \right) \cdot \boldsymbol{S} \tag{4.46}$$

$$= \gamma \left[J_z S_z - \boldsymbol{S}^2 \right] + \frac{\gamma}{2} \left[J_+ S_- + J_- S_+ \right] \tag{4.47}$$

The two different spin states will again be labeled F_1 and F_2, and are distinguished by their relations between J and N, the total angular momentum neglecting spin:

$$F_1 : J = N + \frac{1}{2} \tag{4.48}$$

$$F_2 : J = N - \frac{1}{2} \tag{4.49}$$

The correctly symmetrized basis states for F_1 and F_2 can be written as linear combinations of the case (a) basis functions:

$$\begin{aligned} |F_1\rangle = \frac{1}{\sqrt{2}} \Bigg[& |\Lambda = 0\rangle \left| S = \frac{1}{2}, \Sigma = \frac{1}{2} \right\rangle \left| J, \Omega = \frac{1}{2}, M \right\rangle \\ & + |\Lambda = 0\rangle \left| S = \frac{1}{2}, \Sigma = -\frac{1}{2} \right\rangle \left| J, \Omega = -\frac{1}{2}, M \right\rangle \Bigg] \end{aligned} \tag{4.50}$$

$$\begin{aligned} |F_2\rangle = \frac{1}{\sqrt{2}} \Bigg[& |\Lambda = 0\rangle \left| S = \frac{1}{2}, \Sigma = \frac{1}{2} \right\rangle \left| J, \Omega = \frac{1}{2}, M \right\rangle \\ & - |\Lambda = 0\rangle \left| S = \frac{1}{2}, \Sigma = -\frac{1}{2} \right\rangle \left| J, \Omega = -\frac{1}{2}, M \right\rangle \Bigg] \end{aligned} \tag{4.51}$$

Now we can solve the total Hamiltonian $\boldsymbol{H} = \boldsymbol{H}_{rot} + \boldsymbol{H}_{sr}$ for the energy levels of the $^2\Sigma^+$ state without the use of a secular determinant:

$$E_{F_1} = B \left(J + \frac{1}{2} \right) \left(J - \frac{1}{2} \right) + \frac{\gamma}{2} \left(J - \frac{1}{2} \right) \tag{4.52}$$

$$= BN(N+1) + \frac{\gamma}{2} N \tag{4.53}$$

$$E_{F_2} = B \left(J + \frac{1}{2} \right) \left(J + \frac{3}{2} \right) - \frac{\gamma}{2} \left(J + \frac{3}{2} \right) \tag{4.54}$$

$$= BN(N+1) - \frac{\gamma}{2} (N+1) \tag{4.55}$$

In the second line of each expression, we have replaced J with N and it becomes

apparent that the symmetrized case (a) basis states are equivalent to the case (b) basis states, and N rather than J is the pattern-forming quantum number. The energy expression, with the exception of the spin-rotation splitting, is the same as obtained from the case (b) Hamiltonian in Equation 1.31. The two spin states with the same value of N are split by the amount, $\gamma(N + 1/2)$, by the spin-rotation interaction. Both the $v = 0$ and $v = 1$ levels of the $A^2\Sigma^+$ state will be relevant to the work presented here; the relevant constants are:[71]

$$\tilde{\nu}_{00} = 44080 \text{ cm}^{-1} \tag{4.56}$$

$$\tilde{\nu}_{10} = 46541 \text{ cm}^{-1} \tag{4.57}$$

$$B_0 = 1.986 \text{ cm}^{-1} \tag{4.58}$$

$$B_1 = 1.967 \text{ cm}^{-1} \tag{4.59}$$

$$\gamma_0 = -2.691 \times 10^{-3} \text{ cm}^{-1} \tag{4.60}$$

$$\gamma_1 = -2.765 \times 10^{-3} \text{ cm}^{-1} \tag{4.61}$$

$$D_0 = 5.643 \times 10^{-6} \tag{4.62}$$

$$D_1 = 5.661 \times 10^{-6} \tag{4.63}$$

where $\tilde{\nu}_{v0}$ is the band origin for the specified vibrational level of the A $^2\Sigma^+(v) \leftarrow$ X $^2\Pi_{1/2}(v = 0)$ transition. Again, we can neglect centrifugal distortion in the low rotational states of interest, although the reported constants are included above for completeness. The energy level pattern for the A state appears schematically in Figure 4-7.

4.4.3 Transition Intensity

Allowed transitions between the A and X states, obey the standard selection rules for parity and total angular momentum:

$$\pm \leftrightarrow \mp \tag{4.64}$$

$$\Delta J = 0, \pm 1 \tag{4.65}$$

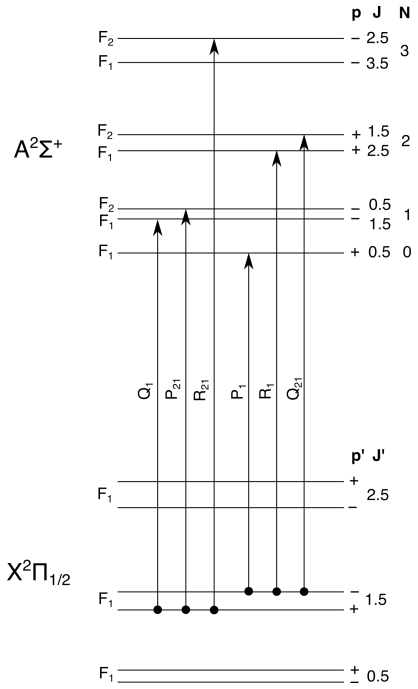

Figure 4-7: Level diagram for the A $^2\Sigma^+ \leftarrow$ X $^2\Pi_{1/2}$ transition. Transition labels appear next to each arrow. Number subscripts indicate the transition is between the specified spin states, F_1 or F_2. The energy level assignments are shown on the right side of each level.

Since N is not a good quantum number for the ground state, transitions to states with any N that satisfy the above selection rules are allowed. The rotational line intensities for the A $^2\Sigma^+ \leftarrow$ X $^2\Pi_{1/2}$ transition are calculated using two factors. First, since the initial state is the ground electronic state, multiple rotational states will be populated at the temperatures relevant to the experiments in this work, ca. 10 K. At this temperature, there will be no population in electronic excited states. The relative population in the rotational state $|JM\rangle$ is given by the Boltzmann factor:

$$P_M(J) = \frac{(2J+1)e^{-BJ(J+1)\frac{hc}{kT}}}{\sum_{J=1/2}^{\infty}(2J+1)e^{-BJ(J+1)\frac{hc}{kT}}} \tag{4.66}$$

The second factor is the intrinsic rotational line intensity, which was introduced in the introduction. Equation 1.75 will be used without modification, where we will choose $r = 0$ because our experiment uses linearly polarized light, and $q = -1$ for a $\Sigma \leftarrow \Pi$ transition. The only additional consideration is that we will transform

the A state from case (a) to case (b) using Equation 1.55 and summing over Σ and Ω. This is not strictly necessary, since we could use properly symmetrized case (a) wavefunctions for the A state and arrive at the same result. However, this is the strategy we will pursue for the other transition intensities that will be calculated in this work.

4.4.4 Results

A typical REMPI spectrum of the A $^2\Sigma^+ \leftarrow$ X $^2\Pi_{1/2}$ (1,0) transition appears in Figure 4-8. The experiment appears on top and a simulation appears below it, with the intensity normalized to the strongest line in each spectrum. Transitions to the F_1 and F_2 spin components of the upper state appear as blue and red lines, respectively. The simulation is for a rotational temperature of 3.5 K, which accurately reproduces the relative intensities of the observed lines. Several weak lines appear in the experimental spectrum that are absent in the simulation. These are due to warm background NO gas in the apparatus, which is not completely removed from the chamber before the next experimental cycle. These weak signals are consistent with a much higher rotational temperature than occurs in the molecular beam and are observed at laser timings that do not overlap with the gas pulse. Moreover, these signals are easily distinguished from the molecular beam signals on the time-of-flight axis of the mass spectrometer. The latter result in tightly bunched ion packets because all of the neutral molecules are initially concentrated in a beam, while the former produce ion packets that are much broader in time since the molecular density is similar everywhere in space. We have no reason to believe that these signals interfere with ion detection experiments, though, as mentioned in a previous section, we found it necessary to increase the pumping speed in our CPmmW experiments in order to reduce this background pressure.

The temperatures achievable with our supersonic jet source are highly dependent on the adjustment of the nozzle tension. In fact, we often adjust the nozzle tension slightly away from optimal in order to produce higher temperature beams because this give us access to higher rotational states for spectroscopic investigation.

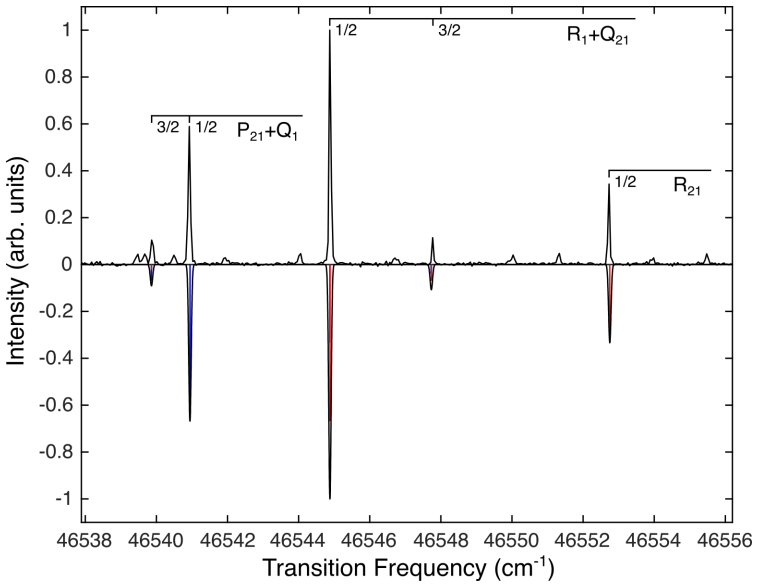

Figure 4-8: Top: Spectrum of the A-X transition measured by 1+1 REMPI in the supersonic jet apparatus. Bottom: Simulation of the same transition with a rotational temperature of 3.5 K. Red and blue lines are transitions to the F_1 and F_2 spin components of the upper state, respectively.

4.5 The $4f \leftarrow$ A $^2\Sigma^+$ transition

4.5.1 Energy level structure of the $4f$ state

The energy level pattern of the $4f$ state are characteristic of Hund's case (d). The rotational Hamiltonian in this case is trivial:

$$\boldsymbol{H}_{rot} = B\boldsymbol{R}^2 = BR(R+1) \tag{4.67}$$

where R is the rotational quantum number of the molecular framework or ion-core. This R-dependence is the largest splitting observed in the $4f$ complex; in essence, there is a $4f$ complex converging to the ionization potential associated with each rovibrational state of the ion-core. In an effective Hamiltonian treatment, each value of $|\ell_R|$ would be assigned its own term value containing contributions from the electronic energy of the core and the weakly bound Rydberg electron. The splitting of

ℓ_R terms is approximately given by[79]

$$T_{|\ell_R|} - T_0 = -\frac{3}{2}k\ell_R^2 \tag{4.68}$$

where k is a constant that characterizes the non-Coulombic interactions between the ion-core and the Rydberg electron. This is exactly the physics we consider in the long-range electrostatic model, so we will abandon the traditional effective Hamiltonian approach at this point and calculate the $4f$ state (and all Rydberg state) energy level structure using this model.

The parity of a case (d) state is given by $R + \ell$, so for a given $n\ell$ Rydberg state, all levels with the same R have the same parity and the parity alternates with the value of R. A schematic of the $4f$ energy levels is shown in Figure 4-9, in which the electric fine structure components, specified by N or ℓ_R, are displayed in an arbitrary order. The spin doublets for each N level are shown explicitly, though the splitting is expected to be far smaller than the resolution in this experiment. The degeneracy of the spin doublets is lifted by the spin-orbit operator, which is an effect due to core electrons, which are localized close to the molecular framework. As a result, increases in ℓ and n will rapidly reduce the magnitude of the effective spin-orbit constant, and, specifically, the spin-orbit splittings will scale as n^{-3} due to the $n^{-3/2}$ scaling of the amplitude of the inner lobe of the Rydberg wavefunction.

4.5.2 Transition Intensity

Calculation of the rotational line intensities for the $4f \leftarrow \mathrm{A}\ ^2\Sigma^+$ transition is more complicated. The initial state is well described by Hund's case (b), while the final state is best described in Hund's case (d). Thus, we will need to transform Equation 1.75 from two case (a) states to two case (b) states. Then, a second transformation for the final state to case (d) will be performed. This first step was performed in the work of Petrović and Field,[122] where the authors were able to eliminate the multiple

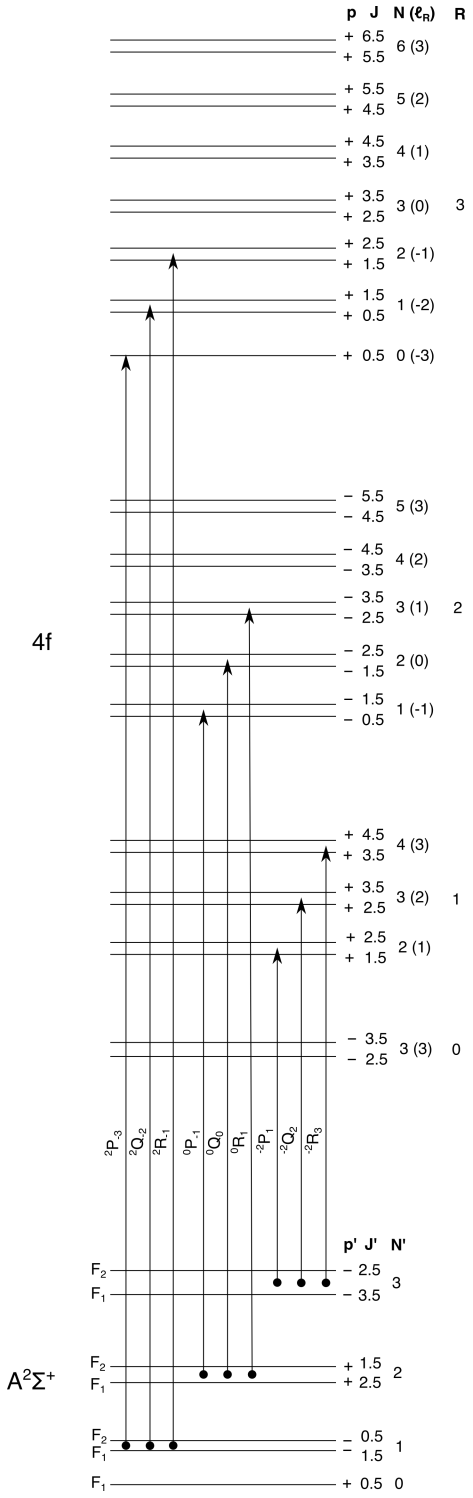

Figure 4-9: Level diagram for the $4f \leftarrow$ A $^2\Sigma^+$ transition. The transition labels next to each arrow indicate the numerical value of $N' - R$ in the left superscript, ℓ_R in the right subscript, and $\Delta N = -1, 0, 1$ by P, Q, and R as usual. The energy level assignments are shown on the right side of each level.

summations and find a simplified form for the transition dipole matrix element:

$$\begin{aligned}
&\langle JMN\Lambda Sp\,|\mu(1,r)|\,J'M'N'\Lambda'Sp'\rangle \\
&\quad = (-1)^{J'+J+S+1-\Lambda+M}\frac{1+(-1)^{p+p'+1}}{2(1+\delta_{\Lambda,0}+\delta_{\Lambda',0}-2\delta_{\Lambda',0}\delta_{\Lambda,0})^{1/2}} \\
&\qquad \times\left[(2N+1)(2N'+1)(2J+1)(2J'+1)\right]^{1/2} \\
&\qquad \times\begin{pmatrix} J' & 1 & J \\ -M' & -r & M\end{pmatrix}\begin{pmatrix} 1 & N' & N \\ -q & -\Lambda' & \Lambda\end{pmatrix}\begin{Bmatrix} 1 & N' & N \\ S & J & J'\end{Bmatrix} \\
&\qquad \times\langle\Lambda|\mu(1,q)|\Lambda'\rangle
\end{aligned} \tag{4.69}$$

Note that, relative to Equation 5 of Petrović and Field,[122] we have switched the primed and unprimed labels to reflect a primed lower state and unprimed upper state. In addition, we have corrected a sign error in the second 3j coefficient, which does not satisfy the triangle condition[163] ($m_1+m_2=-m_3$) as originally written.[122] Just as in the case of the A $^2\Sigma^+ \leftarrow$ X $^2\Pi_{1/2}$ transition, we can then perform the case (b) to case (d) transformation for the $4f$ state using Equation 1.68 and summing over all values of Λ. The last issue we must address is the electronic matrix element shown as the last factor in Equation 4.69. We can explicitly write the electronic components of the $4f$ state as $|4f\lambda\rangle$ which represents the product of a radial hydrogenic wavefunction and a spherical harmonic with projection λ on the internuclear axis. Similarly, the A state is also a Rydberg state with the dominant character $|3s\sigma\rangle$. However, atomic selection rules clearly establish that there is no oscillator strength connecting an s state and an f state. In NO, the s and d Rydberg series are profoundly mixed, which can be partly explained by the presence of a large quadrupole moment of the ion-core that mixes states with $\Delta\ell=\pm2$.[78] Although the A state, the $3s\sigma$ Rydberg state, is energetically distant from the $3d\sigma$ state, it appears that a small admixture of d character is indeed the primary source of oscillator strength for transitions from the A $^2\Sigma^+$ state to the nf Rydberg states.[27] Now, we can re-write the transition dipole

matrix element for the electronic part of the wavefunction as:

$$\langle 4f\lambda|\mu(1,q)|3d\sigma\rangle = (-1)^{3-\lambda}\begin{pmatrix} 3 & 1 & 2 \\ -\lambda & \lambda & 0 \end{pmatrix}\langle 4f||\mu^{(1)}||3d\rangle \tag{4.70}$$

where we have used the Wigner-Eckart theorem to extract the angular dependence on Λ, and recognized that only the $q = \lambda$ component is non-zero. The reduced matrix element in Equation 4.70 is a constant factor applied to all rotational lines so we will neglect it here. This yields, for the final transition dipole matrix element:

$$\begin{aligned}
&\left\langle 4f; JMNS = \frac{1}{2}R\ell \middle| \mu(1,r) \middle| \mathrm{A}^2\Sigma^+; J'M'N'\Lambda' = 0S' = \frac{1}{2}p' \right\rangle \\
&= \sum_{\Lambda}(-1)^{J'+J+S+N-\Lambda+M}\frac{1+(-1)^{p'+R+\ell+1}}{2} \\
&\quad \times [(2N+1)(2N'+1)(2J+1)(2J'+1)(2R+1)]^{1/2} \\
&\quad \times \begin{pmatrix} R & \ell & N \\ 0 & \Lambda & -\Lambda \end{pmatrix}\begin{pmatrix} 3 & 1 & 2 \\ -\Lambda & \Lambda & 0 \end{pmatrix}\begin{pmatrix} J' & 1 & J \\ -M' & -r & M \end{pmatrix} \\
&\quad \times \begin{pmatrix} 1 & N' & N \\ -\Lambda & 0 & \Lambda \end{pmatrix}\begin{Bmatrix} 1 & N' & N \\ \frac{1}{2} & J & J' \end{Bmatrix}
\end{aligned} \tag{4.71}$$

The square of this matrix element is taken and all transition probabilities through unresolved spin doublets and M sub-levels are summed to obtain the total line intensity.

The lines in the $4f \leftarrow$ A $^2\Sigma^+$ transition are labeled by the symbol ${}^{N'-R}\Delta N_{\ell_R}$, where P, Q, and R branches denote $\Delta N = -1$, 0, and 1, as normal, ℓ_R is the electric fine structure component of the $4f$ state, and $N' - R$ is the difference between the A state rotational quantum number and the $4f$ state ion-core rotational quantum number. Since each N' level of the A state has only one parity and the case (d) state parity is given by $R + \ell$, $N' - R$ is restricted to even values only. In practice, we will deal with just three branches: $N' - R = -2$, 0, 2. The only two additional parity allowed transitions, ${}^{-4}P_3$ and ${}^{4}R_{-3}$, have much weaker predicted intensities, which approach zero in the limit of high rotation.

4.5.3 Results

Spectra of the $4f$ ($v = 0$) state were collected by 1+1'+1' REMPI where the laser resonant with the $4f$-A transition also served to ionize NO molecules for detection. In general, a strong, blended R_1 + Q_{21} line of the A-X transition was pumped to select one rotational level (one pair of spin doublets) in the A state. The second dye laser pumps lines belonging to one of the three ($N' - R$) transitions. Figure 4-10 shows two typical spectra obtained by populating the $N' = 2$ (top) and $N' = 1$ (bottom) levels of the A state. The calculated spectrum, shown in red, uses previously determined A state term values[3] and the long-range model with parameters determined by Martin et al.[97] to determine the $4f$ level energies. Transition intensities are calculated assuming pure case (d) states for the $4f$ levels and the formulas in Equations 4.71 and 1.75. The predicted line positions and intensities are in modest agreement with the experimentally observed spectrum, with the noticeable exception of the $^2P_{-3}$ line, which does not appear in the lower spectrum and is more than an order of magnitude weaker in the upper spectrum. In fact, this line is also absent in the spectra collected from the $N' = 3$ and 4 states as well. This observation is curious, particularly since the $^2P_{-3}$ transition is the most intense line of the branch in the high rotation limit. Moreover, the study of the $4f$-A (1,1) band by Cheung et al. observed the $^2P_{-3}$ line for all N' levels with the expected intensity.[27] The unexpected transition intensity may be due to interference between transition intensity to different spin doublet components, or due to unconsidered admixture of another electronic state in the A $^2\Sigma^+$ ($v = 0$) state. We have no further evidence to resolve this question.

Table 4.1 summarizes the observed line positions in the (0,0) band of the $4f \leftarrow$ A $^2\Sigma^+$ transition. The $\cdots$ symbol indicates that the line does not exist and the $\circ$ symbol indicates that the line is predicted to have transition intensity, but was not observed in our spectra. With the exception of the $^2P_{-3}$ lines, previously discussed, all unobserved lines are predicted to have weak intensities.

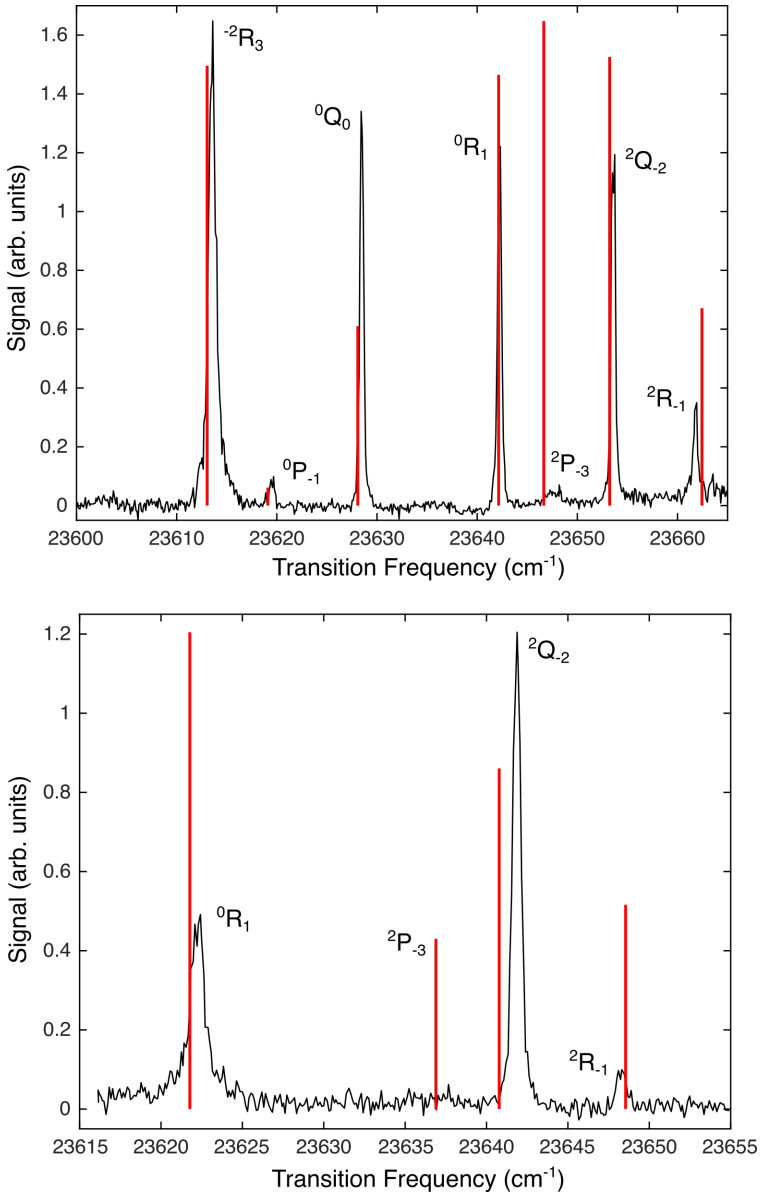

Figure 4-10: REMPI spectra of the $4f$-A (0,0) band. The experimental measurements are the black curve and theoretical predictions for each transition frequency and intensity appear as a red line spectrum. The top and bottom spectra correspond to $N' = 2$ and 1, respectively, in the A state.

Table 4.1: Observed line positions (cm^{-1}) for the $4f \leftarrow$ A $^2\Sigma^+$ (0,0) transition. The symbol $\cdots$ indicates that a transition is forbidden and the symbol $\circ$ indicates that a transition was not observed.

N'	$^{-2}R_3$	$^{-2}Q_2$	$^{-2}P_1$	$^{0}P_{-1}$	$^{0}Q_0$	$^{0}R_1$	$^{2}P_{-3}$	$^{2}Q_{-2}$	$^{2}R_{-1}$
0	$\cdots$	$\cdots$	$\cdots$	$\cdots$	$\cdots$	$\cdots$	$\cdots$	$\cdots$	$\circ$
1	$\cdots$	$\cdots$	$\cdots$	$\cdots$	23622.4	$\cdots$	$\circ$	23641.8	23648.5
2	23613.7	$\cdots$	$\cdots$	23619.5	23641.5	23628.4	23647.5	23653.8	23661.9
3	23605.4	23617.5	$\circ$	23628.6	23639.7	23639.7	$\circ$	23663.92	23670.9
4	23596.6	23608.1	23613.5	$\circ$	23639.9	23639.9	$\circ$	23672.94	23679.55

4.5.4 Long-range fit of the $4f$ $(v = 1)$ state

Surprisingly, a fit of the long-range model to the $4f$ $(v = 1)$ complex does not appear in the literature, in spite of the extensive data set for the $4f \leftarrow$ A $^2\Sigma^+$ (1,1) transition reported by Cheung et al.[27] Our fit of this data set provides some insight into the long-range model and its limitations in describing low-n, low-ℓ Rydberg states.

Term values for the $4f$ $(v = 1)$ states were calculated as the sum of the $4f$-A transition energies measured by Cheung et al.[27] and the A state term values determined by Amiot and Verges.[3] In fact, the A state term values were taken to be the mean of the F_1 and F_2 term values of each N reported in that study because this small splitting was not resolved in the $4f$-A transition. Our fit procedure adopts the usual assumptions made by previous authors: i) the $4f$ $(v = 1)$ state is isolated and does not interact with other Rydberg states differing in n, ℓ, or v; ii) only the isotropic polarizability, α, and quadrupole moment, Q, of the NO^+ core contribute; iii) the values of α and Q are assumed to be independent of the core rotation, R. In addition, we have fixed the $v = 1$ ioniziation potential at 77065.47 cm^{-1}.[15] We include a phenomenological term to describe the effects of core penetration on the Σ components of the complex. In case (d), this correction factor has the form:[39]

$$H_{ij}^{\rm pen} = d_\Sigma \sqrt{(2R_i+1)(2R_j+1)} \begin{pmatrix} \ell & N & R_i \\ 0 & 0 & 0 \end{pmatrix} \begin{pmatrix} \ell & N & R_j \\ 0 & 0 & 0 \end{pmatrix} \tag{4.72}$$

The resulting parameters determined from this fit appear in the second column of Table 4.2. A fixed value of the centrifugal distortion constant was included,[97] though this had little impact on the quality of the fit. In addition, the anisotropic polarizability, γ, was arbitrarily fixed to the value, $\alpha/3$, as in previous work. The reason for this assumption is that the quadrupole moment and anisotropic polarizability operators have identical angular dependence. As a result, the two parameters cannot be well determined, independently of each other. If we allow the value of γ to vary in the fit, we obtain a fit of similar quality and nearly identical parameter values. However,

the standard deviations of Q and γ increase by orders of magnitude and we find a pairwise correlation coefficient of almost exactly -1.

This inability to distinguish the quadrupole moment and the anisotropic polarizability is one of the most significant limitations to all previous long-range fits of nf Rydberg states. Although the angular factors are identical, the two parameters can be distinguished in other ways. First, the radial dependences of Q and γ differ by one order of magnitude so the scaling of these factors with n can reveal their separate effects. Second, and more subtly, the anisotropic polarizability can mix states with $\Delta n = 0$ and $\Delta\ell = 0, \pm 2$. This is different from the quadrupole operator, which can only mix states of the same ℓ for a given n since its radial matrix element vanishes for $\Delta\ell \neq 0$. Thus, a Rydberg state, $n\ell$, lying close in energy to $n(\ell \pm 2)$ states may be particularly sensitive to this polarizability-induced mixing. Both of these factors suggest that high-ℓ Rydberg states, which all lie close in energy, investigated over a wide range of principal quantum numbers, should provide a data set capable of distinguishing these two physical parameters.

Figure 4-11 shows the calculated and observed $4f$ energy levels as a function of R on a reduced term value plot. The rms deviation of this fit is 0.268 cm^{-1}, which is consistent with the reported ± 0.2 cm^{-1} precision of the measurements. The agreement is excellent up to about $R = 12$. Indeed, most of the error in the fit arises from these large-R states, and a fit to the data only up to $R = 12$ achieves a decreased rms deviation of 0.168 cm^{-1}, while the fit parameters are unchanged within 1σ. It is possible that the neglected R-dependence of the fit parameters leads to the discrepancy at large R.

Lastly, we can compare our fit to previous results for the nf states of NO, which appear in the remaining columns of Table 4.2. In this table, the asterisk indicates the parameter was fixed in the fit, the symbol $\cdots$ indicates that a particular parameter was neglected, and the symbol $\circ$ indicates that the value was not reported. An interesting trend emerges from this aggregated set of data. The fits to $4f$ data, especially in the first three columns, yield smaller values of Q and α than the higher n states reported in the last three columns of the table. In particular, note the very good

Table 4.2: Long-range fit parameters for the $4f$ $(v = 1)$ complex, and several other nf states. An asterisk next to the value means it is fixed in the fit procedure, the symbol $\cdots$ indicates the parameter was fixed as zero, and the symbol $\circ$ indicates the parameter was not reported. Values in parentheses give the standard deviation (σ) in the last significant digit, unless otherwise indicated. The source for each data set appears in the final row.

	$4f$ $(v = 1)$	$4f, 5f$ $(v = 0)^a$	$5g \leftarrow 4f$ $(v = 0)^b$	$4f$ $(v = 3)$	$7f, 12f, 15f$ $(v = 1)^c$	nf $(v = 1)^d$	nf $(v = 2)^e$
Q (ea_0^2)	0.6170 (35)	0.59 (4)	0.628 (3)	0.6894 (8)	0.74 (2)	0.80 (21)	0.83(23)
α (a_0^2)	7.755 (14)	7.6 (4)	7.768 (7)	8.182 (4)	8.17 (4)	8.1 (1.1)	9.0 (1.3)
γ (a_0^2)	$\alpha/3$*	$\alpha/3$*	$\alpha/3$*	$\alpha/3$*	$\alpha/3$*	$\alpha/3$*	$\alpha/3$*
d_Σ (cm^{-1})	-1.75 (22)	$\cdots$	-0.87 (17)	-2.54 (4)	-0.92 (2)	$\cdots$	$\cdots$
					-0.30 (2)		
					-0.14 (2)		
B (cm^{-1})	1.96562 (46)	1.886*	1.98794634*	1.9296 (7)	1.968 (2)	1.9680 (5)	1.9492 (8)
D (cm^{-1})	5.7×10^{-6}*	$\cdots$	5.704×10^{-6}*	$\cdots$	$\cdots$	$\circ$	$\circ$
Source	This work,[27]	79	97	39	15	165	165

[a] Emission spectroscopy on the rare isotope $N^{14}O^{18}$.

[b] Fitting is performed on the transition energies, rather than term values.

[c] Reported error is an estimate from the variation of the parameters among the three fits. From top to bottom, the reported d_Σ values are for $n = 7, 12, 15$.

[d] Values of n range from 9 to 20. Reported error is the 90% confidence interval.

[e] See footnote *d*

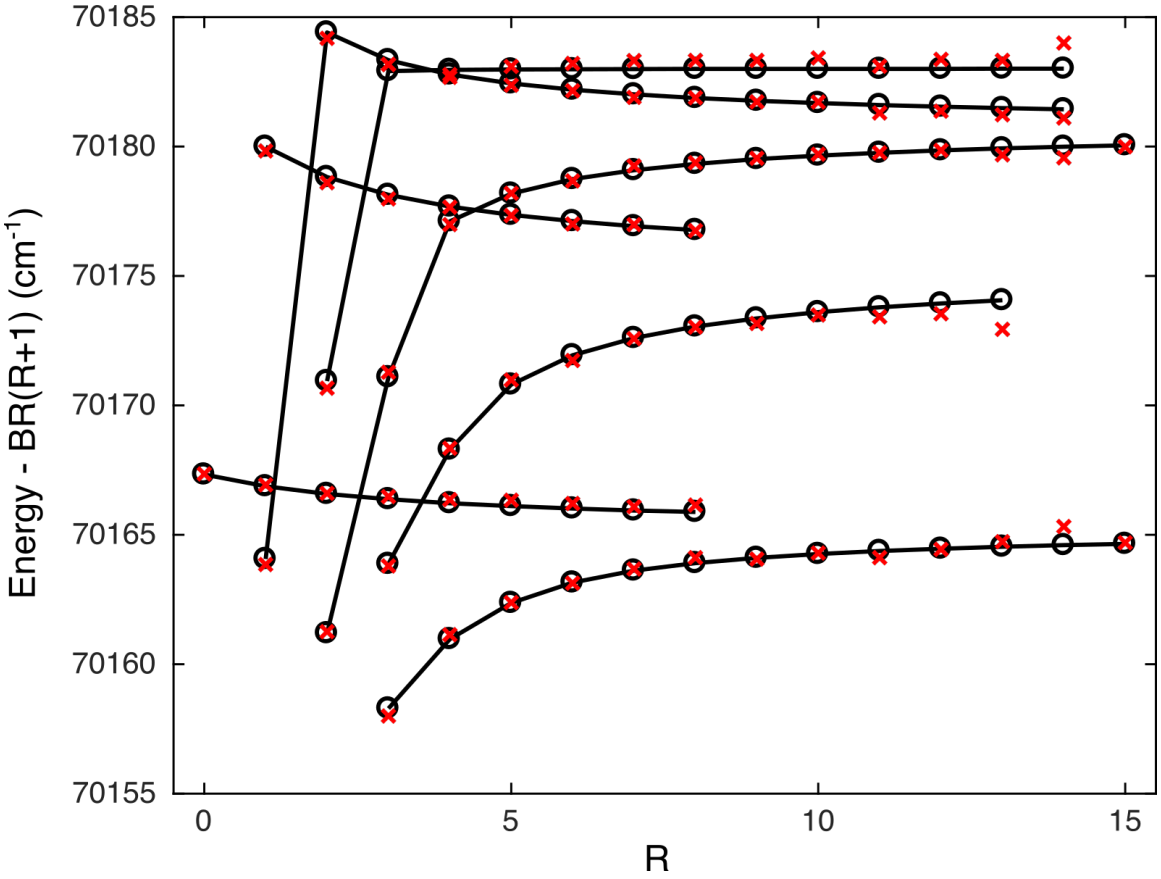

Figure 4-11: Reduced term value plot of observed (red crosses) and calculated (black circles) energy levels of the $4f$ ($v = 1$) Rydberg complex. The solid black lines connect states with the same ℓ_R value.

agreement of the Q and α values between our fit and the fit to the $5g \leftarrow 4f$ $(v = 0)$ transition by Martin et al. in the third column, as compared to the poor agreement with the results of Biernacki et al. on the $7f$, $12f$, and $15f$ $(v = 1)$ states in the fifth column. One might reasonably expect that the values obtained from different nf states with the same vibrational quantum number should agree better than those from different vibrational levels. The polarizabilities and multipole moments of the molecule vary with internuclear distance, therefore their vibrationally averaged values will be different for each vibrational level of the ion. This upending of expectations suggests to us that the treatment of the $4f$ level employing a long-range model does not capture the intended physics and the determined parameters are *effective* values of the polarizability and quadrupole moment rather than those of the free ion. This interpretation is further supported by the large magnitude of the core penetration factor, which is essential in fitting the $4f$ data, but quickly becomes only a minor correction at higher n. Indeed, beyond the well-known correlation of the anisotropic polarizability and quadrupole moment that was addressed previously, we find large pairwise correlation coefficients of 0.59 between Q and d_Σ, and 0.57 between α and d_Σ. Since d_Σ always has a negative value, this means that the magnitudes of Q and α are strongly anti-correlated with the magnitude of d_Σ. Thus, a large core-penetration factor reduces the values of Q and α in the $4f$ states relative to higher nf states. Moreover, this strong correlation of parameters limits our ability to interpret the parameters in a physically meaningful way. The core penetration of the $4f$ level, irrespective of vibrational state, perturbs the energy level structure sufficiently to reduce the appropriateness of the long-range model. In order to obtain realistic measurements of the free ion electrostatic parameters, truly core-nonpenetrating Rydberg states, such as the ng states, must be studied.

4.6 The $ng \leftarrow 4f$ transition

While spectroscopic studies of most electronic states of NO are prolific, there exists a surprising dearth of work on $ng \leftarrow nf$ transitions. The $5g \leftarrow 4f$ transition was

studied more than ten years ago by several teams.[35,97,150] Higher ng states have only been investigated in detail by Fujii and Morita, who first employed the three-color triple-resonance excitation scheme described here.[52] Their work established that, unlike the nf states, ng states do not rapidly predissociate, and moreover, the ng ($v = 1$) states decay predominantly by autoionization. This relative immunity to predissociative decay makes access to ng states essential to any experiment involving high-resolution mmW spectroscopy.

4.6.1 Transition Intensity

The transition intensity to consider here is between case (d) Rydberg states. This intensity formula is thus applicable not only to the laser excitation from the $4f$ state to the manifold of ng Rydberg states, but also for the microwave spectroscopy experiments, which involve transitions of $(n \pm 1)h \leftarrow ng$. The strategy for computing this transition moment matrix element is the same as for the previous electronic transitions. The transition intensity is initially written in case (a), then transformed to case (b) for both states, and finally to case (d) for both states. As was the case for a case (b) to case (b) transition, we have derived a 6j contraction that eliminates the multiple summations over Λ, Σ, and Ω:

$$\begin{aligned}\langle R\ell SNJM|\mu|R\ell' SN'J'M'\rangle = (-1)^{J+J'+S+N+N'+\ell+\ell'+R+M+1}(2R+1) \\ \times [(2J+1)(2J'+1)(2N+1)(2N'+1)(2\ell+1)(2\ell'+1)]^{1/2} \\ \times \begin{pmatrix} J' & 1 & J \\ -M' & -r & M \end{pmatrix} \begin{pmatrix} \ell & 1 & \ell' \\ 0 & 0 & 0 \end{pmatrix} \\ \times \begin{Bmatrix} 1 & N' & N \\ S & J & J' \end{Bmatrix} \begin{Bmatrix} \ell & N & R \\ N' & \ell' & 1 \end{Bmatrix}\end{aligned} \tag{4.73}$$

We have eliminated the radial electronic matrix element from this expression, but it should be considered explicitly in comparisons of transition intensities with different values of n and ℓ. The vibrational overlap integral is also not included. For Rydberg-Rydberg transitions, however, the Franck-Condon factor is extremely diagonal since

the potential energy curve of every Rydberg state converging to a given electronic state of the ion-core closely resembles the potential energy curve of that ion-core state. As a result, the $\Delta v = 0$ propensity rule is very strong. In addition, in the case (d) limit, $\Delta\ell = \pm 1$ and $\Delta R = 0$ are strict transition selection rules. Figure 4-12 is a schematic of the ng-$4f$ transition. The strict selection rules for case (d)-case (d) transitions result in just a single P, Q, and R line in a spectrum originating from a single $4f$ rotational level. As case (d) structure is relaxed, the $\Delta N = 0, \pm 1$ selection rule becomes less strict and weaker $\Delta J \neq \Delta N$ satellites may appear. If case (d) is a sufficiently bad approximation, as for some core-penetrating Rydberg states, $\Delta R \neq 0$ transitions turn on, though this is not expected for the ng Rydberg states of NO studied here.

4.6.2 Results

A spectrum of the $12g2_N \leftarrow 4f2_5$ (1,1) transition, detected by autoionization of the $12g$ level, appears in Figure 4-13. The narrowband pulsed dye amplification laser resolves some of the electric fine structure in this low n Rydberg state, representing the first time this internal structure has been resolved, aside from work on the very lowest $5g$ state.[97,150] The red spectrum is simulated by calculating the $4f$ term values using the A ($v = 1$) state term values of Biernacki et al.[15] and the $4f$-A (1,1) transition energies of Cheung et al.[27] and calculating the $12g$ term values by the long-range model using the parameters determined by Biernacki et al.[15] Note that the intensities of the overlapped P and Q transitions are multiplied by 10 in both the experiment and theory for ease of comparison. The calculated and measured transition frequencies show obvious disagreement. We have not exhaustively collected laser spectra of ng states because the goal of this work focuses on CPmmW spectrocopy. However, it seems likely that laser spectroscopy will be an additional path toward gaining new insight into the Rydberg energy level structure. Unlike CPmmW spectroscopy, careful calibration of the laser frequency is required. In addition, a narrowband laser system, like the one used here, should be employed in order to yield the most insight over the widest range of principal quantum numbers.

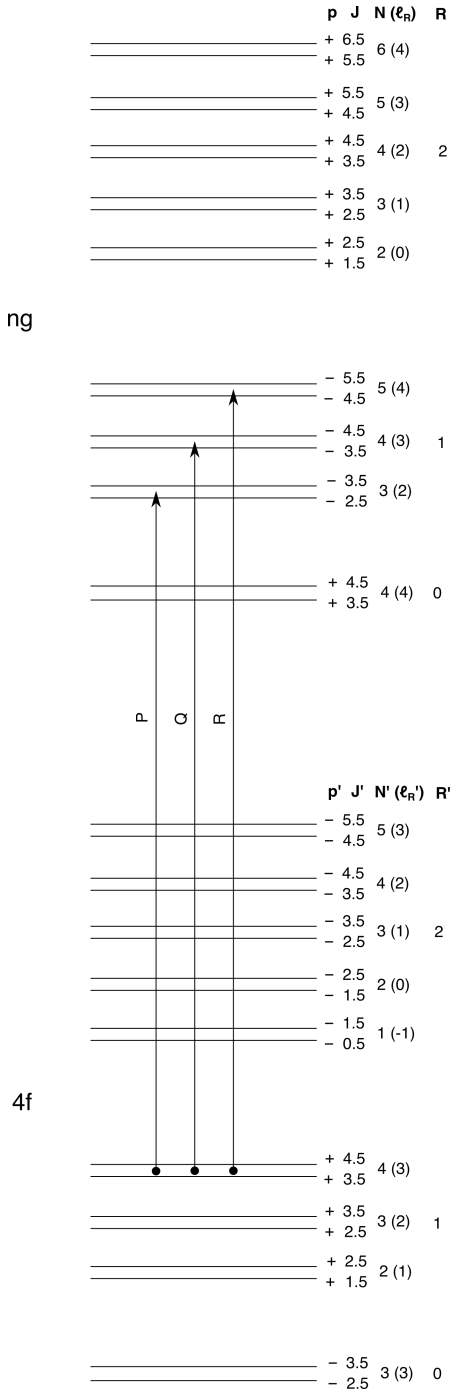

Figure 4-12: Level diagram for the $ng \leftarrow 4f$ transition. The energy level diagram for all Rydberg-Rydberg transitions, such as the $(n \pm 1)h \leftarrow ng$ transitions probed by microwave spectroscopy, will have a similar appearance. The selection rules for transitions between case (d) states dramatically restrict the number of lines in these spectra. The energy level assignments are shown on the right side of each level.

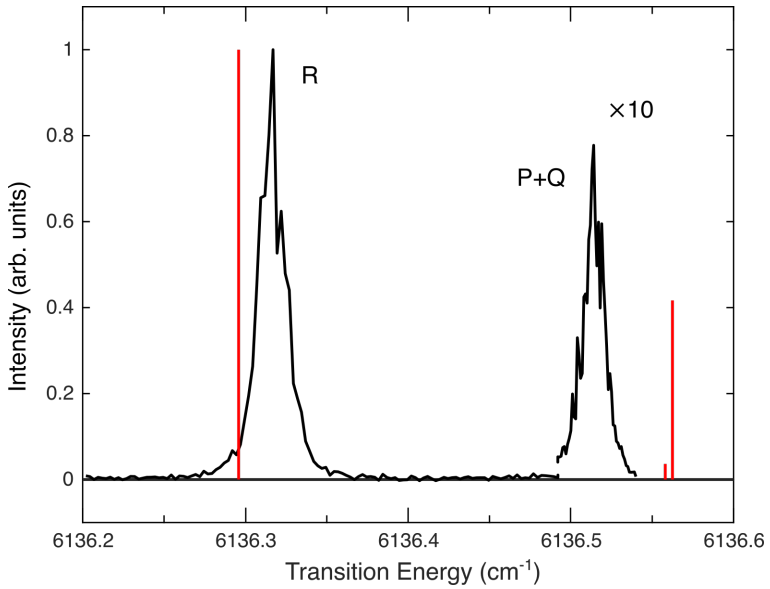

Figure 4-13: Laser spectrum of the $12g2_N \leftarrow 4f2_5$ (1,1) transition. The simulated spectrum appears as a red line spectrum. Note that the intensities of the overlapped P and Q transitions at high frequency have been multiplied by 10 in both the experiment and theory.

4.7 Millimeter-wave transitions

4.7.1 Ionization detected spectra

Rydberg-Rydberg transitions in the millimeter-wave region have previously been investigated using ionization detection. Ionization-detected mmW spectra of the rare gas atoms,[101,133] H_2 and its isotopologues,[63,113] and even benzene,[112] have been studied by the Merkt group. This technique typically uses selective field ionization to produce a mmW frequency-dependent ion signal. Following electronic excitation to some initial Rydberg state, $n\ell$, the mmW radiation drives transitions to final Rydberg states, $(n+m)(\ell \pm 1)$, where m is some positive integer. By applying an electric field with a carefully chosen magnitude, the higher energy final Rydberg state can be ionized and detected without also ionizing the lower Rydberg state. This is possible due to the dramatic scaling of the required ionization field with principal quantum number:[53]

$$F = \frac{1}{16n^4} \qquad \text{adiabatic} \tag{4.74}$$

$$F = \frac{1}{9n^4} \qquad \text{diabatic} \tag{4.75}$$

where the different proportionality factors arise for the different mechanisms of ionization. Critically, the laser excitation and mmW interrogation of the Rydberg states must occur under field-free conditions due to the extreme electric field sensitivity of the typically high-n states investigated. The Merkt group employs specially designed electrode stacks to achieve this goal.[102]

Ionization-detected Rydberg-Rydberg transitions in NO have been investigated by our group and others,[98,107] though, lacking the exquisite control over stray electric fields achieved in the Merkt group experiments, these spectra are severely broadened by the Stark effect. Figure 4-14 displays a typical example of a selective field ionization-detected spectrum from the initial $43g2_N$ state of NO for $N = 2$ and 3. The experimental data in black show two partially overlapping features with linewidths of several hundred MHz. At lower frequency are the transitions to $44f$ states and at higher frequency are the transitions to $44h$ states. The predicted line positions and intensities for the many close-lying transitions appear as a red stick spectrum. At this resolution, little information can be gleaned from the mmW spectrum. In particular, the electric fine structure of the transitions, which reports on the non-Coulombic interactions between the ion-core and Rydberg electron, is completely unresolved.

4.7.2 CPmmW spectra

The principles of CPmmW spectroscopy are described in Chapter 2. The present section describes some aspects of assigning Rydberg-Rydberg transitions in CPmmW spectra, the dramatic and unexpected effects of stray electric fields on the spectra, and progress toward a long-range electrostatic model to describe the Rydberg spectrum.

Assignment techniques

Beyond the predictions from the long-range electrostatic model, two important experimental methods allow us to unambiguously assign Rydberg-Rydberg transi-

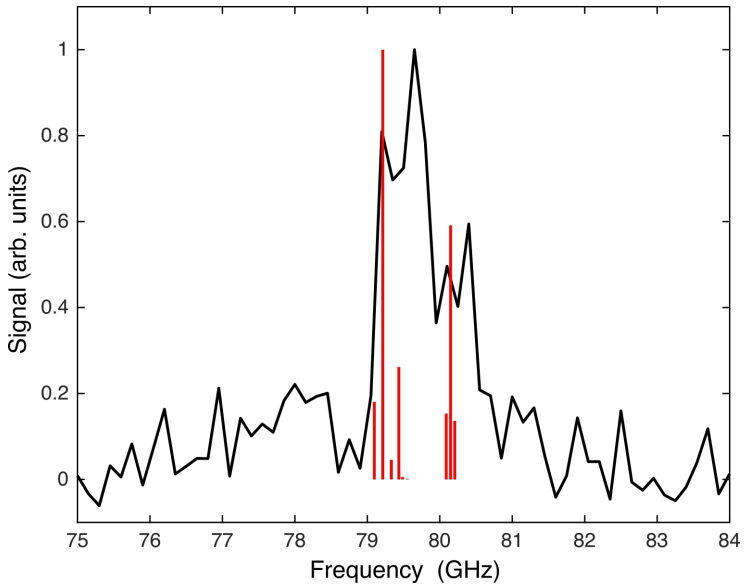

Figure 4-14: Selective field ionization-detected spectrum of the $44\ell \leftarrow 43g$ transitions. The experimental spectrum appears in black and a simulated spectrum, using the long-range parameters of Martin et al.,[97] appears as a red stick spectrum.

tions observed by CPmmW spectroscopy: combination differences and polarization diagnostics.

Combination differences, of course, are the gold standard for making and confirming assignments in more common vibrational and electronic spectroscopies. In those cases, *rotational* combination differences are established by locating pairs of transitions that either originate from the same initial level or terminate on the same final level. Those transitions are characteristically separated by an energy difference proportional to the ground or excited state rotational constant. In particular, plotting all differences between R-branch and P-branch transition energies against $J + 1/2$ results in many points lying along either the line $4B_0$ or $4B_1$ where B_0 and B_1 are the ground and excited state rotational constants, respectively. This method quickly organizes all observed transitions and confirms assignments that may initially be based on predicted line positions or the qualitative line pattern.

In Rydberg-Rydberg transitions, *electronic* combination differences of states with different n, ℓ, or N can be found in the spectra. As an example, Figure 4-15 shows some of the combination differences possible in the case of laser excitation of the $ng2_3$ and $ng2_2$ states, indicated by bold font. In the left-hand case, the sum of the

frequencies of the Q transitions (blue) upward and downward in n from one level is equal to the sum of the frequencies of the R transitions (red) upward and downward in n from a different laser-prepared level. Alternatively, as shown on the right-hand side of Figure 4-15, the energy difference between two sets of laser-prepared Rydberg states can be obtained to mmW accuracy by establishing a combination difference with final levels having a common value of n. These more complicated combination differences of sums is required because the energy splitting of two transitions with either a common initial or final state is not known *a priori*. This splitting represents the splitting of electric fine structure levels in either the initial or final state, and this is not a constant or a value that simply scales with N.

The flexibility of the AWG at the heart of the CPmmW spectrometer makes it easy to add additional mmW photons to an experiment. This makes multi-pulse experiments possible and a network of precisely connected Rydberg levels can be built up from laser excitation of a small number of initial states. In Figure 4-16, this idea is illustrated. Transitions from the initial ng states to neighboring $(n+1)h$ and $(n-1)h$ levels transfer population into these initially empty levels. A second mmW pulse then polarizes transitions from those h states to other ng Rydberg states that were not initially laser-populated. These secondary transitions establish combination differences, with sub-MHz accuracy, not only among themselves, but also with the primary transitions, and provide additional confirmation of assignments.

The second important technique for establishing unambiguous assignments for observed mmW transitions is polarization diagnostics. As one can see from the form of every transition intensity formula presented in this chapter, there is a spatial component that depends on M, the magnetic quantum number, and r, a constant determined by the polarization of the light that induces each transition. By collecting a spectrum with all laser and mmW fields in one polarization arrangement, and then collecting a second spectrum with a different polarization arrangement, transitions between levels with different total angular momentum, J, will show characteristic changes in the relative intensity pattern. This idea was explored in double resonance experiments on Rydberg states in previous work by the Field group.[122] We have found that when the

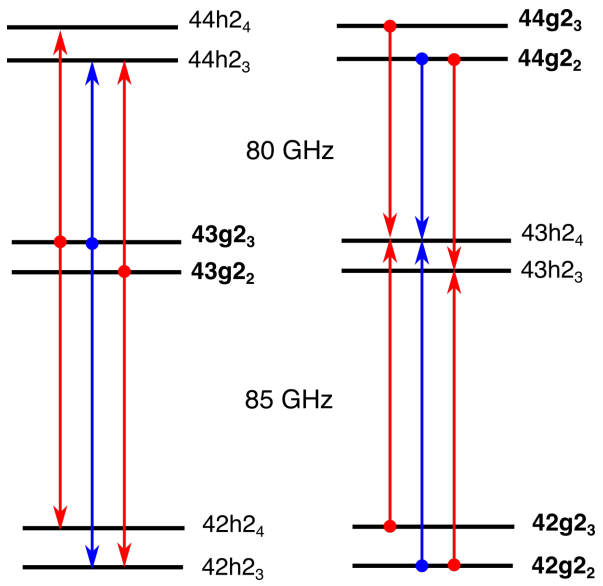

Figure 4-15: Schematic of typical Rydberg-Rydberg transitions probed by CPmmW spectroscopy. Laser excitation populates multiple initial electric fine structure components of the desired Rydberg state. Left: By probing transitions upward and downward in n, combination differences can be identified to confirm assignments. Right: Combination differences also link laser-populated levels to the accuracy of mmW transition frequencies.

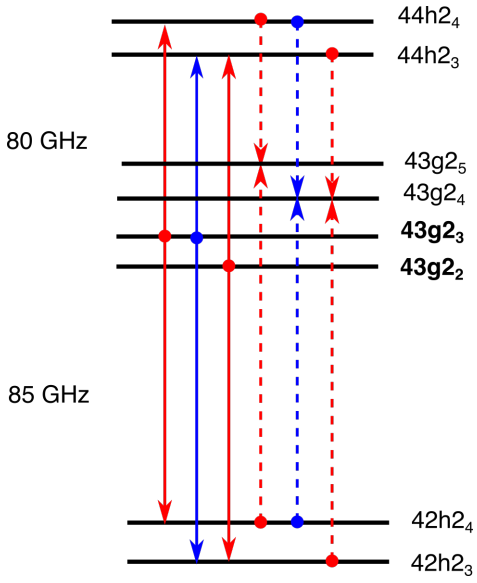

Figure 4-16: Schematic of Rydberg-Rydberg transitions probed by CPmmW spectrosopy. Similar to Figure 4-15, combination differences can be established from transitions upward and downward in n. In addition, after transferring population from the laser-populated state to another Rydberg state, transitions back to states with the initial value of n allow construction of a network of transitions.

angular momentum coupling case changes in the transition between two levels, this has the effect of reducing the contrast observed between two different polarization arrangements. In the optical-optical-optical-mmW excitation used for chirped-pulse experiments, the final three states — $4f$, ng, and $(n \pm 1)h$ — are all well described by Hund's case (d). Thus, we anticipated variations of the polarization arrangement of the IR and mmW photons would produce the most dramatic polarization effects. Since the mmW photon polarization cannot be changed without exchanging components and disrupting alignment, we rotate the linear polarization of the IR photon to produce either an arrangement of all linear, all parallel polarizations or a linear polarization arrangement with relative angles of $0° - 0° - 90° - 0°$. A typical spectrum is shown in Figure 4-17 for three exemplary two-step transition sequences, $44h2_3 \leftarrow 43g2_3 \leftarrow 4f2_2$, $44h2_4 \leftarrow 43g2_3 \leftarrow 4f2_2$, and $44h2_3 \leftarrow 43g2_2 \leftarrow 4f2_2$, in order from lowest to highest transition frequency. The arrangement with all parallel polarizations is shifted by 10 MHz for clarity. Beside each transition is listed the observed and calculated intensity ratio for perpendicular:parallel arrangements. Excellent qualitative agreement is observed between the calculation and the experiment, allowing us to confidently assign each transition.

It is worth briefly commenting on intensity measurements in CPmmW spectroscopy. Compared to sequential scanning techniques, the multiplexed broadband nature of chirped-pulse spectroscopy makes relative intensity measurements much more feasible and diagnostically reliable. Fluctuations in the molecular source or the laser intensities will affect all transitions in the same way, reducing the relative intensity noise. Reproducible relative intensities at the level of 15-30% are often cited.[115] However, care must still be taken if *quantitative* relative intensities are desired. The power output and detection sensitivity of the CPmmW spectrometer is frequency dependent so transitions at different frequencies, especially if they are widely separated, will be polarized by different amounts and detected with different efficiencies. By measuring the instrument response in the absence of the sample, the frequency dependent intensity can be corrected to improve relative intensity measurements, although the performance of this method has not been quantitatively investigated.[168]

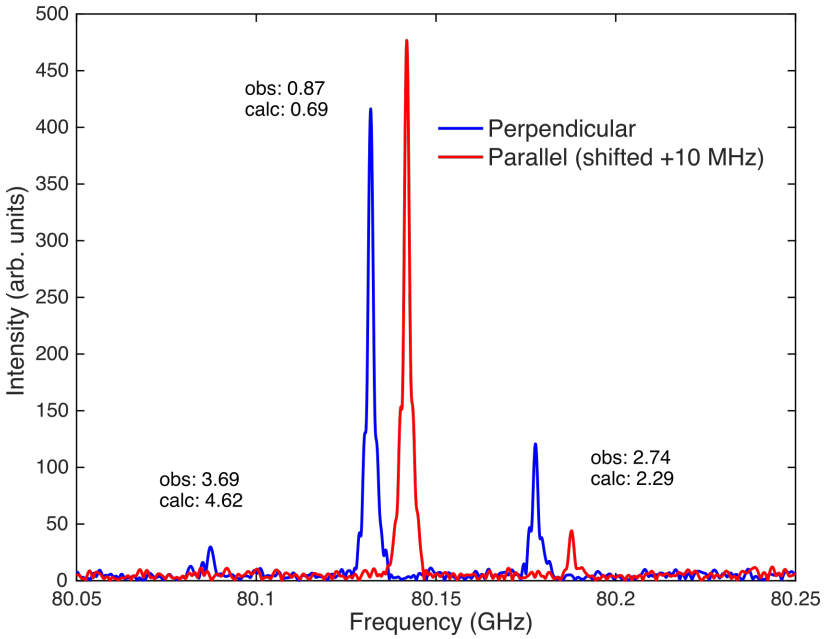

Figure 4-17: Polarization diagnostics can help to confirm transition assignments. In this case, altering the polarization arrangement of the IR and mmW photons (perpendicular vs. parallel) leads to significant, and predictable, increases or decreases in transition intensity.

Furthermore, the details of the chirped polarizing pulse can profoundly affect the relative intensities. Since many transitions share common initial or final levels, a change in polarization of one transition can impact the polarization of another. This is especially significant for Rydberg-Rydberg transitions with very large dipole moments, where population transfer at low mmW powers is possible. Switching the frequency chirp direction of the excitation pulse will also result in observation of different relative intensities and even a different number of transitions[169] Although this can complicate relative intensity measurements, it assists in experimental determination of the level connectivity.

Electric field effects

In contrast to the ion-detection apparatus, chirped-pulse spectra can be collected in an apparatus free of the large electric fields required in the former technique. However, as will be discussed at length in this section, the exquisite sensitivity of high-n, high-ℓ Rydberg states to electric fields means that small fields due to electrical equip-

ment outside the apparatus or patch charging on dielectric windows can noticeably perturb CPmmW spectra. Although our apparatus is very similar to the setup in which CPmmW spectroscopy of Rydberg states was initially demonstrated,[126] the high-ℓ states, with very small quantum defects, investigated in this work have substantially greater electric field sensitivity, revealing previously unobserved and unexpected stray fields in and around the apparatus.

A typical spectrum for our initial experimental setup is shown in Figure 4-18. The laser excitation populates both $41g2_3$ and $41g2_2$ Rydberg states. There are three allowed transitions from these two initial states to the electric fine structure components of the $40h$ state, all of which occur below 99 GHz in this spectrum. Two instrumental artifacts are indicated by asterisks. The intense line around 99.07 GHz is not predicted by our long-range electrostatic model and displays several characteristics that distinguish it from the anticipated transitions. This extra peak is not only more intense than the expected transitions, but it is also noticeably narrower. The extra transition typically has a linewidth of around 1 MHz, while the expected transitions are significantly broader, often around 5 MHz FWHM. The intensity of this extra transition was of typically similar or larger intensity than the assigned transitions. Moreover, when the density of the sample was increased, this transition displayed *superradiance*.

Superradiance is a phenomenon that has appeared frequently in our CPmmW spectroscopy experiments on Rydberg states,[30,126,169] and was recently investigated in detail by us in an atomic system.[61] Essentially, superradiance is a *collective* effective, related to FID emission, in which the presence of neighboring radiators (Rydberg atoms/molecules) modifies the radiation-matter interaction. Unlike FID, superradiant emission results in a large change in excited state population, accompanied by a "burst" of emitted radiation. The rate of superradiant decay, γ_{SR}, is given by:[95]

$$\gamma_{SR} = \frac{1}{\tau_{SR}} = \frac{A_{21} OD}{8\pi} = \frac{\pi \rho \mu^2}{3\epsilon_0 \hbar} \frac{L}{\lambda} \tag{4.76}$$

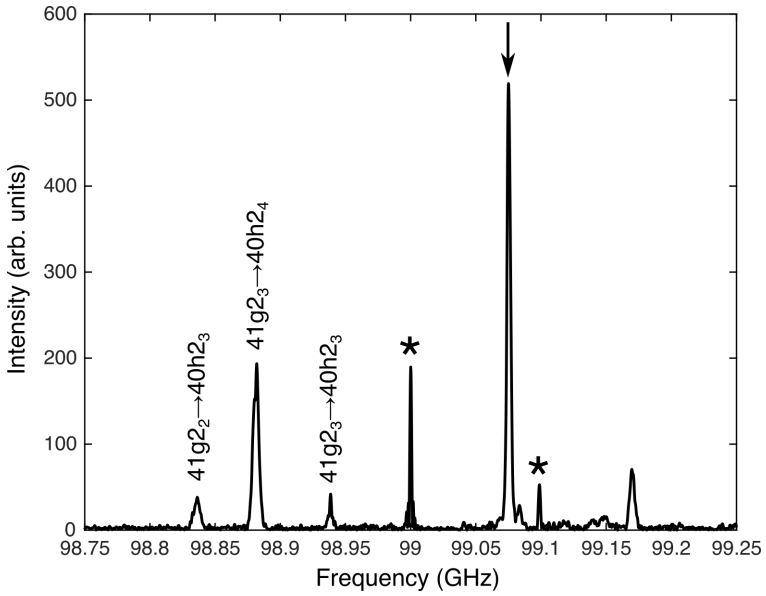

Figure 4-18: CPmmW spectrum from the $41g2_3$ and $41g2_2$ initial states. Instrumental artifacts are indicated by asterisks. The broader peaks below 99 GHz correspond to expected $41g$-$40h$ transitions. The intense, narrow line at 99.07 GHz, which displays superradiant emission at high densities, is assigned to an electric-field-induced $41g$-$40g$ transition.

where the optical depth (OD) and Einstein A coefficient (A_{21}) are defined as

$$OD = \rho\lambda^2 L \tag{4.77}$$

$$A_{21} = \frac{8\pi^2\mu^2}{3\epsilon_0\hbar\lambda^3} \tag{4.78}$$

In these equations, ρ is the number density, λ is the emission wavelength, L is the sample length, and μ is the transition dipole moment. Superradiant decay increases with three factors: the density, the transition dipole moment, and the sample length relative to the emission wavelength. The combination of huge Rydberg-Rydberg transition dipole moments and samples of length much larger than the wavelength of the radiation (3 mm at 100 GHz) explains the presence of superradiant decay in our experiments. The superradiant burst occurs with a characteristic time delay, τ_D, which according to the semiclassical model, is linearly related to the superradiant decay time, τ_{SR}:[62]

$$\tau_D = 2\tau_{SR}\log(\theta^i/2) \tag{4.79}$$

where θ^i is defined in the Bloch vector model as the initial tipping angle induced by the "trigger" pulse. The radiation that triggers superradiant decay can be applied by the experimentalist, as done in our previous experiments,[61] but can also come from the blackbody radiation of the 300 K chamber. This blackbody-triggered superradiance is what we have observed. At high Rydberg densities, superradiant emission follows laser excitation, even without application of any mmW fields. A typical single-shot observation of superradiant emission is shown in Figure 4-19. The three traces of superradiant emission are obtained by Fourier transforming the time domain signal to frequency space, applying a narrowband filter, and inverse Fourier transforming to reconstruct the isolated superradiant emission traces. The y-axis is the emitted power, $|E|^2$, at each frequency. Note that the laser excitation to a $43g$ state occurs at approximately zero on the time axis and the initial superradiance in the lower trace (red) occurs after a 100 ns delay.

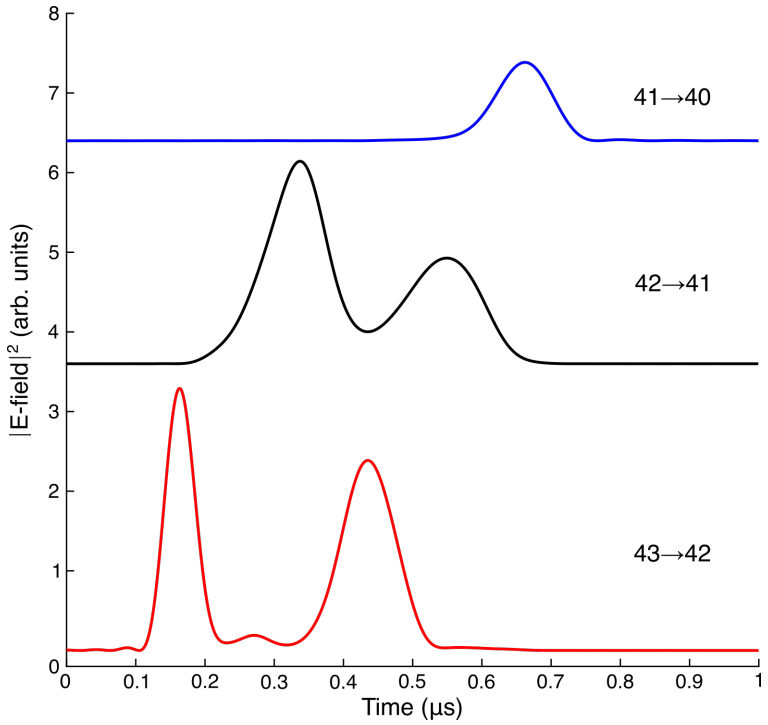

Figure 4-19: Cascading superradiant emission from a high density sample of NO Rydberg states, initially prepared in a $43g2_N$ state. The principal quantum numbers, n, of the transitions are indicated.

Superradiant decay is an obstacle to spectroscopy experiments not only because

it adds an additional decay mechanism that can lead to line broadening, but also because it can substantially modify the observed number of lines. In the presence of a weak and a strong transition, numerical simulations have shown that superradiant decay funnels population into the strong transition.[167] This energy steering is a result of the self amplification process in superradiance, where an initially small difference in transition intensities can grow by orders of magnitude. In the presence of strong superradiant emission, we observe no lines other than the superradiant one in the spectrum.

Another multi-level effect that occurs in superradiant emission is cascading transitions. In a ladder system, if population from an initially populated level superradiantly decays to a lower level, a new population inversion can be established between the second level and a third even lower energy level. If the sample density remains high enough, superradiant emission can again occur, leading to population transfer into the third level. This process will continue as long as the emission remains coherent within the dephasing time of the experiment and the optical density remains sufficiently high. This cascading superradiance is "triggered" only once on the initial transition and each subsequent superradiant event is dependent on the initial conditions of the first event. We clearly observe cascading superradiance in our experiment. In Figure 4-19, a $43g$ state is initially populated by the laser excitation. Emission between principal quantum numbers $43 \rightarrow 42$ (red) is first observed, and is then followed by superradiant bursts at widely separated frequencies corresponding to principal quantum numbers $42 \rightarrow 41$ (black), and $41 \rightarrow 40$ (blue). The intensity of each successive superradiant event decreases in amplitude. The detection bandwidth of the CPmmW spectrometer limits our ability to track the downward population cascade to $n > 39$.

Finally, in an extended sample, it is possible for the radiation emitted by an early part of the sample to be absorbed and eventually re-emitted by a later part. This results in multiple bursts of radiation escaping from the sample, which occur on the same transition and are initiated by the same superradiant event. This is dramatically displayed in our experiment. The first two superradiant transitions in the cascade

shown in Figure 4-19 display beating emission due to this type of propagation effect.

All of these observations place the superradiance observed in these experiments in a regime of high optical depth not previously attained in our Rydberg experiments.[61] This is likely due to the simple explanation that even at high dilutions, using a permanent gas like NO results in much higher density samples than are produced from ablation-loaded beam sources. By probing the free jet expansion far downstream of the nozzle exit, the sample density becomes low enough to avoid superradiance. This is the experimental configuration used for spectroscopy experiments. We find the superradiant emission useful, at least, for initial alignment of the lasers and the molecular beam, since this signal is strong enough to observe in a single-shot ("real time feedback"), and a sign that all lasers are on resonance and well-overlapped. Further study of this system may be fruitful in gaining new insights into superradiant physics, but that is beyond the scope of this thesis.

This discussion of superradiance demonstrates that this unexpected transition is not a minor extra line, but is so strong as to completely control the physics of our experiment under certain conditions. The last peculiarity of this line led us directly to consider stray electric fields. In Figure 4-20, the upward pointing spectrum shows transitions from a laser populated $42g$ state to levels with principal quantum number $n = 43$. The downward pointing spectrum shows transitions from a laser populated $43g$ state to levels with $n = 42$. The symmetry in the two spectra is striking. The anticipated g-h transitions occur at the low frequency and high frequency ends of the lower and upper spectra, respectively. In the middle of the spectra, the strong, unexpected line (and a second weaker one) occurs at the *same* frequency in both spectra. This indicates to us that the intense line is a transition between two ng states that are capable of being laser-populated, which should not be possible because they have the same parity. We observe the same set of lines for every pair of ng states within the spectrometer bandwidth.

At first glance, this assignment seems bizarre. This "forbidden" transition does not just gain intensity due to a small stray electric field. It becomes the dominant feature in the spectrum. To understand this behavior we must consider the Stark

effect in more detail.

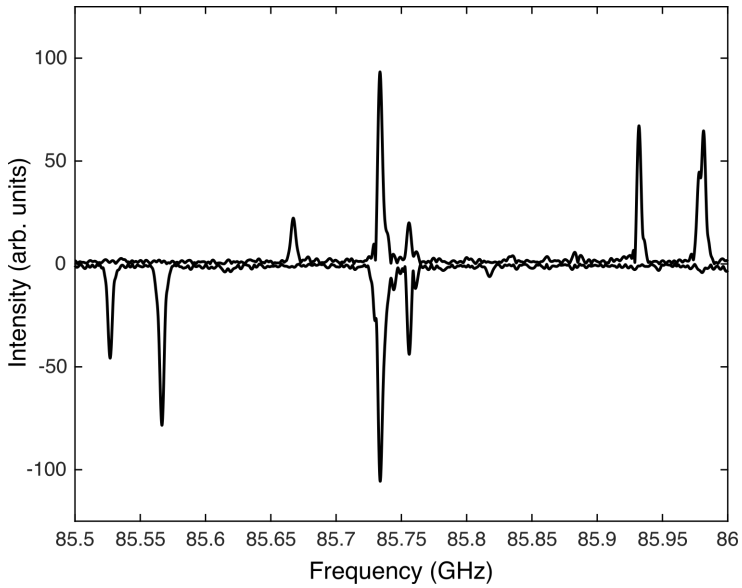

Figure 4-20: CPmmW spectrum from the $42g2_3$ and $42g2_2$ initial states (upward) and the $43g2_3$ and $43g2_2$ initial state (downward). Expected g-h transitions occur below 85.6 GHz and above 85.9 GHz in the two spectra. The two strong features in the center of the spectrum occur at the same frequency in both spectra, indicating the transitions occur between laser-populated levels, in violation of parity restrictions.

We start by examining a simple model to answer two questions regarding this so-called g-g transition: Why is it so intense? Why is it narrower than the expected transitions? To begin, Figure 4-21 shows the calculated Stark states for a single n-manifold of Rydberg states in NO. The methodology for calculating the Stark effect in NO is a matrix diagonalization procedure described by multiple authors, which we will not repeat here.[58,156] Highlighted in blue is a single ng state and highlighted in red is the nh state with which it interacts most strongly. Of course, the Stark effect involves field-induced interactions among many of the levels shown in the figure, but for the purposes of our model system we will only consider these two states in one Stark manifold and the same two states in a neighboring-n Stark manifold. Now, we can write the wavefunction for the nominal ng and nh states in the presence of a field as a linear combination of the two field-free basis states. For clarity, the basis states are indicated as $|nG\rangle$ and $|nH\rangle$, where n is a good quantum number in both the electric field and field-free cases because we will not consider electric fields large

enough to induce significant n mixing.

$$|ng\rangle = \cos\theta\,|nG\rangle + \sin\theta\,|nH\rangle \tag{4.80}$$

$$|nh\rangle = -\sin\theta\,|nG\rangle + \cos\theta\,|nH\rangle \tag{4.81}$$

Here, θ is a mixing angle to describe the effect of the electric field; under field-free conditions, $\theta = 0$ and the real states are identical to the basis states; in the presence of a large field, $\theta \approx \pi/4$ and the two states are completely mixed. Now consider the transition dipole moment between the laser-populated $|ng\rangle$ state and the states $|(n-1)h\rangle$ and $|(n-1)g\rangle$:

$$\langle (n-1)h\,|\mu|\,ng\rangle$$

$$= [-\sin\theta\,\langle (n-1)G| + \cos\theta\,\langle (n-1)H|]\,\mu\,[\cos\theta\,|nG\rangle + \sin\theta\,|nH\rangle] \tag{4.82}$$

$$= -\sin^2\theta\,\langle (n-1)G\,|\mu|\,nH\rangle + \cos^2\theta\,\langle (n-1)H\,|\mu|\,nG\rangle \tag{4.83}$$

$$= \mu_0\left(\cos^2\theta - \sin^2\theta\right) \tag{4.84}$$

$$\langle (n-1)g\,|\mu|\,ng\rangle$$

$$= [\cos\theta\,\langle (n-1)G| + \sin\theta\,\langle (n-1)H|]\,\mu\,[\cos\theta\,|nG\rangle + \sin\theta\,|nH\rangle] \tag{4.85}$$

$$= \sin\theta\cos\theta\,\langle (n-1)H\,|\mu|\,nG\rangle + \cos\theta\sin\theta\,\langle (n-1)G\,|\mu|\,nH\rangle \tag{4.86}$$

$$= 2\mu_0 \sin\theta\cos\theta \tag{4.87}$$

In Equations 4.84 and 4.87, we have made the well-justified assumption:

$$\langle (n-1)H\,|\mu|\,nG\rangle \approx \langle (n-1)G\,|\mu|\,nH\rangle = \mu_0 \tag{4.88}$$

In this simple model, destructive interference in the transition dipole moment of the "allowed" transition leads to a rapid decrease of intensity. All of this intensity ends up in the transition dipole moment of the "forbidden" transition, which gains its intensity through constructive interference between the contributing dipole moments. This suggests that a transfer of intensity from the g-h transition to the g-g transition at small electric field values may be physically reasonable.

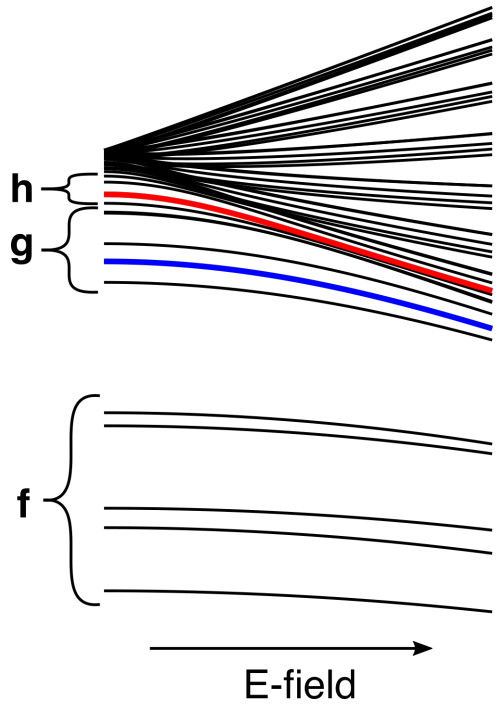

Figure 4-21: Full manifold of Stark states in NO. An ng state is highlighted in blue and shows a quadratic Stark shift. An nh state is highlighted in red and quickly approaches the regime of linear Stark effect due to the nearby high-ℓ manifold of states. The nf states occur far away from the ng and nh states on this energy scale and limited mixing occurs at the field values considered here.

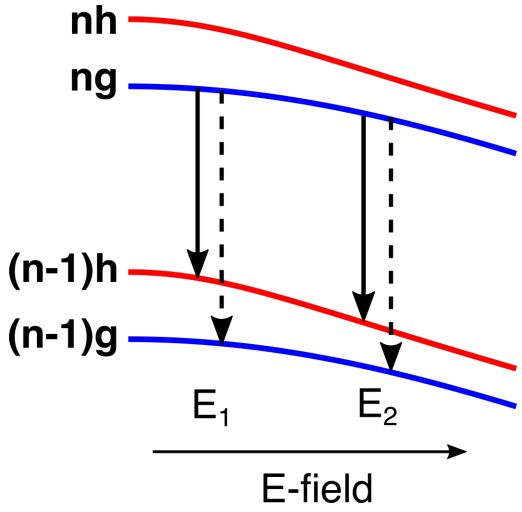

Figure 4-22: Simplified Stark tuning diagram indicating transitions from an initial ng state to either the $(n-1)h$ or $(n-1)g$ state as a function of electric field. The difference in $ng \rightarrow (n-1)h$ transition frequencies (solid arrows) at two electric field values is much larger than the difference in $ng \rightarrow (n-1)g$ transition frequencies (dashed arrows).

The second effect to consider is the difference in observed linewidths between the expected and unexpected transitions. To understand this effect, we have to consider not just an applied field, but an inhomogeneous field. This means that different parts of the Rydberg sample will experience electric fields of different magnitudes. Consider the simplified diagram in Figure 4-22. The Stark shift of the g states in blue is quadratic and substantially smaller than the approximately linear Stark shift of the h states in red. As a result, the frequency of the g-h transition at field value E_1 will be significantly different from the transition frequency at some larger field value E_2. If a distribution of electric fields exists in the apparatus, this will be manifest as a broadening of the linewidth. In contrast, the ng and $(n-1)g$ states have nearly identical Stark shifts at high n. Thus, the frequency of the g-g transition at two field values E_1 and E_2 will be very similar. In the presence of an inhomogeneous electric field, this transition will be minimally broadened. Moreover, in effect, the narrow g-g transition extracts superradiant emission from a larger fraction of the initially populated volume than the broad g-h transitions.

While this simple model has allowed us to develop some intuition regarding g-h and g-g transitions in the presence of an electric field, it has obviously required several simplifying assumptions. To more carefully investigate these field effects, we can consider the same physics using the Stark effect calculation presented in Figure 4-21. In this extended model, we consider all basis states in the initial laser-populated level with coefficients greater than 0.005, and calculate the transition dipole moment to all allowed components of the possible final states. To simplify the calculation, we assume that the transition dipole moments of all allowed transitions are the same and the M levels of the initial state, $|M| = 0$, 1, and 2, are initially equally populated. The accuracy of the simulation could certainly be improved by treating these two aspects more carefully.

In Figure 4-23, a simulated line spectrum for transitions out of the $41g2_3$ (blue) and $41g2_2$ (red) levels for several electric field values is presented. Note that the intensity axis is different for each plot. Under field-free conditions, only the three expected transitions have intensity. At field values as low as 30 mV/cm, the g-g

transitions near 99.1 GHz have intensity comparable to the g-h transitions, and by 60 mV/cm, these g-g transitions completely dominate the spectrum. As the field is increased further, the g-g transition begins to lose intensity as more basis states are mixed in and reduce the brightness of this transition.

To gain some sense of the effect of an inhomogeneous electric field, Figure 4-24 shows a simulated spectrum in the presence of a Gaussian electric field distribution centered at 30 mV/cm with a 10 mV/cm FWHM. The different Stark shifts of the ng and nh states result in dramatic broadening of the three g-h transitions between 96.8 and 99 GHz. Meanwhile, the nearly identical Stark shifts of the ng and $(n-1)g$ states results in all intensity piling up at the same frequency. This result demonstrates that an inhomogeneous field can produce the two different levels of broadening observed. In addition, it shows that field inhomogeneity will further decrease the intensity of the g-h transition relative to the g-g transition, so that the g-g transition can be the most intense feature in the spectrum at even lower fields than suggested by Figure 4-23.

The most obvious difference between this simulated spectrum and the experimental result is the presence of so much intensity in transitions to the high-ℓ manifold at frequencies below 98.8 GHz. It is possible that the emission from these many overlapping transitions will result in substantial destructive interference, which reduces the observed intensities below those of our naive calculation. Again, the explanation of many qualitative features in our observed spectra draws us to the conclusion that small, inhomogeneous electric fields, such as those due to charging of the chamber windows, could be responsible for the observed effects.

Obviously, elimination or compensation of the stray electric field in the apparatus is of paramount importance for accurate measurement of Rydberg-Rydberg transition frequencies. This is ongoing work. Several designs for electric field plates have been tested, which could compensate for the stray fields in the apparatus. Even with the addition of a single set of electric field plates along one axis, we observe dramatically reduced linewidths and a loss of intensity in the g-g transition, as shown in Figure 4-26. The challenge in direct compensation of stray fields is the required geometry of

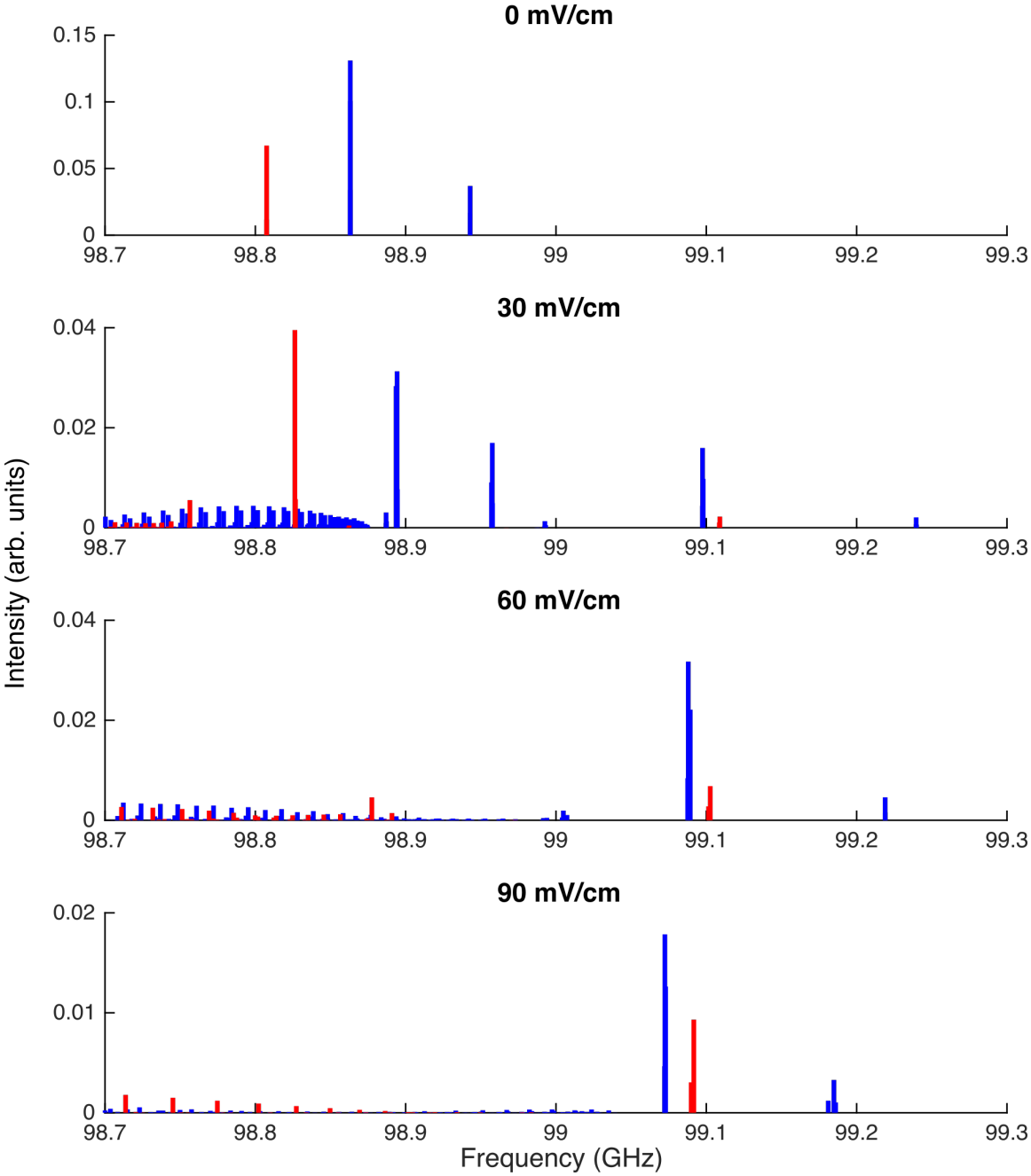

Figure 4-23: Simulation of the mmW spectrum from the initial $41g2_3$ (blue) and $41g2_2$ (red) states as a function of applied electric field. Note the intensity axis changes for each plot. As the electric field increases the intensity of the "allowed" transitions, shown unperturbed in the top plot, decreases rapidly. The g-g transitions near 99.1 GHz rapidly gain intensity before eventually weakening at high field values.

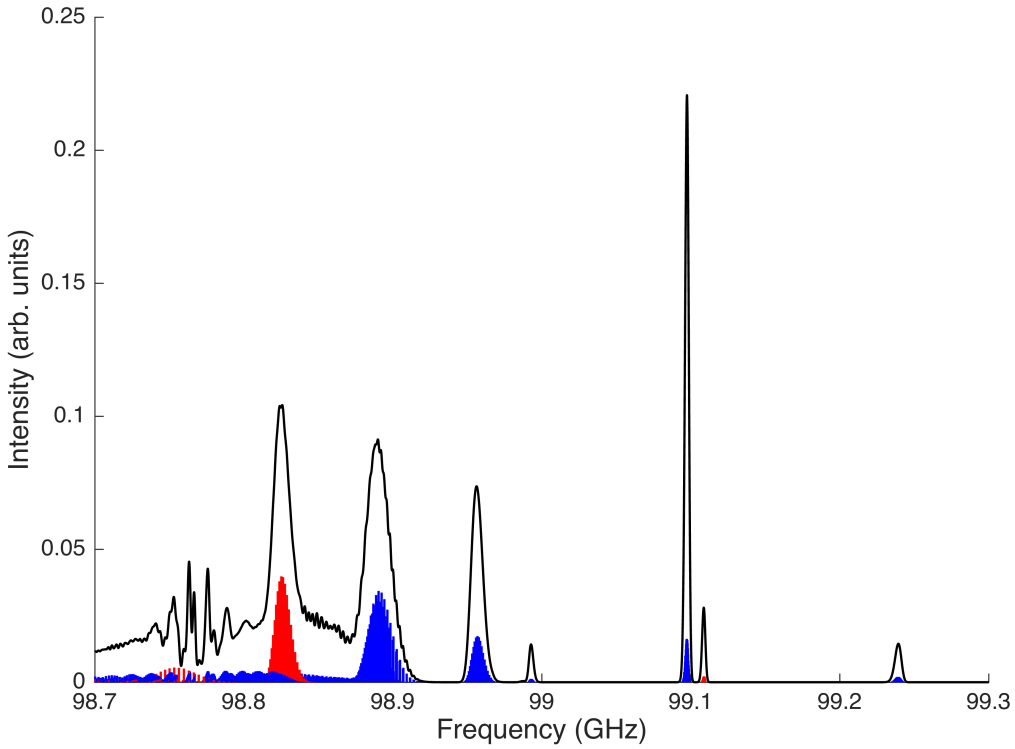

Figure 4-24: Simulation of the mmW spectrum from the initial $41g2_3$ (blue) and $41g2_2$ (red) states with a Gaussian distribution of applied electric field centered at 30 mV/cm with a FWHM of 10 mV/cm. The three "allowed" transitions experience dramatic electric field broadening, which further reduces their intensity. In contrast, the g-g transitions near 99.1 GHz are minimally broadened, leading to a pile up of transition intensity. The simulated intensity transferred into the high-ℓ manifold at frequencies below 98.9 GHz is much larger than observed experimentally.

the experiment. A free jet expansion propagates in one direction, while all laser and mmW fields are expanded to large diameters and intersect the molecular beam transversely. This means that any field plates introduced along these two axes must have large access ports, which will ruin the homogeneity of the applied field. Moreover, the very large sample volume makes the application of a homogeneous field, or equivalently, compensation of an inhomogeneous field, extremely challenging. In general, ion-detected Rydberg experiments use very small active areas in order to reduce the inhomogeneity of the field experienced by the sample. A small sample size is incompatible with the requirements of low number density needed to avoid superradiance, and high emitter number needed to detect FID. We are currently pursuing several new strategies, including the use of ITO or gold-coated glass electrodes to reduce the effects of patch charging on the field plates,[127] and irradiation of the chamber windows with UV light to "clean" charged materials from the surface, an approach used empirically by some atomic physics groups and investigated quantitatively by the LIGO research team.[130, 143, 148]

Linewidths in CPmmW spectra

Beyond the electric field broadening discussed here, what is the next largest broadening mechanism? From rotational spectroscopy experiments in this apparatus, we anticipate the Doppler broadening to be approximately 500 kHz in the W band, and 1.5 MHz in the 220-330 GHz high frequency band. In addition, lifetime broadening should be considered. Although ng states do not suffer from the extremely fast predissociation rates of nf states, predissociation will still be operative. The predissociation rate of ng states of NO has been estimated crudely by Fujii and Morita, who report a lifetime of 1 μs at $n = 55$.[52] Assuming n^{-3} scaling, this gives a lifetime of approximately 480 ns and a linewidth of 330 kHz for $n = 43$, and a 160 ns lifetime and 980 kHz linewidth for $n = 30$. In order to obtain an approximate measure of the predissociation rate, we have performed a lifetime measurement by varying the delay time between the excitation laser pulses that prepare the initial Rydberg state and the mmW chirped pulse that probes the state. Results for the $30g2_3$ state are shown

in Figure 4-25, which gives a lifetime of 204 ns. This is in excellent agreement with Fujii and Morita's value and predicts a natural linewidth of 780 kHz. Extrapolating to $n = 43$, we estimate a lifetime of 600 ns and linewidth of 265 kHz. Either from our measurement or the estimate of Fujii and Morita, the natural linewidth of ng states is comparable to the expected Doppler width and so the total linewidth includes both the Doppler and natural linewidth contributions. We find expected linewidths of 565-600 kHz for $n = 43$ and 1.7-1.8 MHz for $n = 30$.

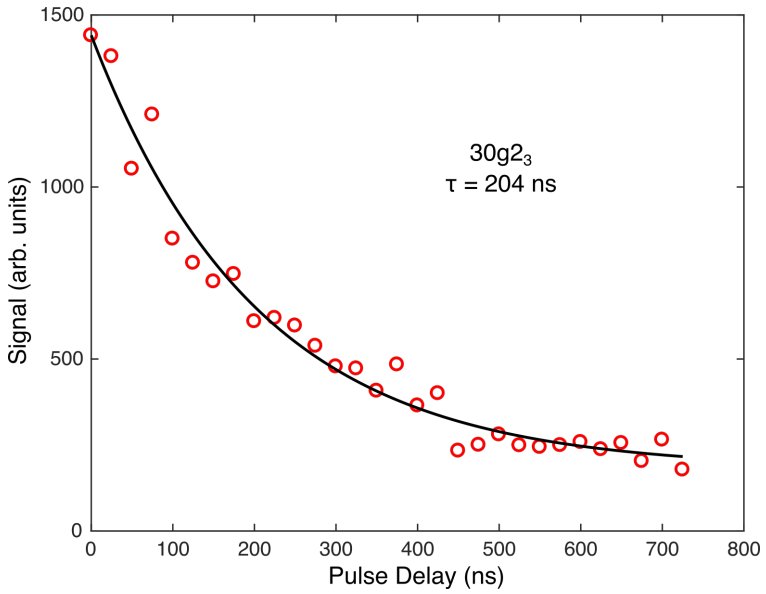

Figure 4-25: Lifetime measurement of the $30g2_3$ state. Since the linewidth is corrupted by electric field broadening, the lifetime is measured by monitoring the mmW signal as a function of delay between the excitation laser that populates the Rydberg state and the mmW pulse that probes the $30g2_3 \rightarrow 29h2_4$ transition. This population decay time demonstrates that the natural linewidth (∼780 kHz) is much narrower than the observed linewidth (∼5 MHz), confirming that the observed transitions are broadened by external effects rather than by the intrinsic lifetime.

While our attempts at stray field compensation have not yet achieved reproducible zero field conditions, we have observed significant narrowing of the linewidths relative to the absence of field compensation. Figure 4-26 shows a spectrum of $44h \leftarrow 43g$ transitions with the narrowest linewidths we have observed. A fit to the $44h2_4 \leftarrow 43g2_3$ transition appears on the right side of Figure 4-26. The additional lobes on each side of the center peak are likely due to uncompensated magnetic fields in the chamber. By fitting only the central peak, we find a linewidth of approximately 800 kHz. This is

quite close to our expectation and additional broadening may be due to the magnetic field effects just mentioned or due to unresolved hyperfine splitting of the transition, as discussed earlier in this chapter. Regarding the former, we previously compensated for magnetic fields using Helmholtz coils, a technique that requires observing the splitting present in Figure 4-26 in order to reduce it. The hyperfine splitting is, of course, intrinsic to the molecule, but would result in characteristically broader lines for lower N transitions, where the splitting is largest. In summary, this result suggests stray field compensation is possible, though a reproducible method requires further development.

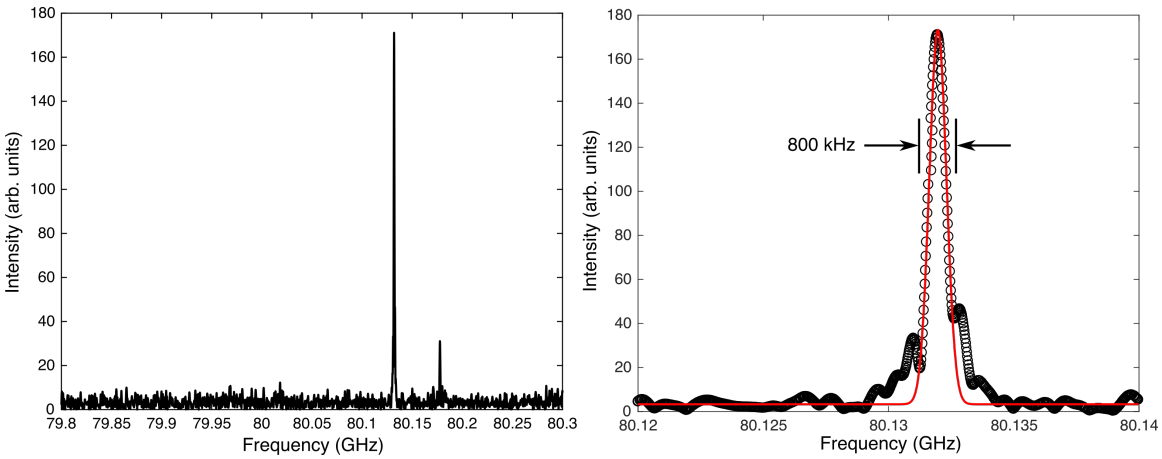

Figure 4-26: CPmmW spectrum from the $43g2_3$ and $43g2_2$ initial states. With field plates inserted into the apparatus the stray field magnitude and inhomogeneity is decreased, leading to no intensity in the g-g transitions and to narrow g-h transitions. In the right panel, a fit to the $44h2_4 \leftarrow 43g2_3$ transitions is shown with a linewidth of less than 1 MHz FWHM. The side lobes are likely due to uncompensated magnetic field in the apparatus and only the central peak is fit.

Long-range fit to mmW data

We perform a *preliminary* fit to the high-resolution CPmmW data in order to demonstrate some of the advantages of this type of data in obtaining meaningful long-range electrostatic values for the NO^+ ion. All of the observed lines exhibit broadening beyond the expected Doppler and natural linewidths, and typically have linewidths of $\sim$5 MHz. In addition to broadening, shifts of the line centers from the field-free values are also possible. Both of these factors reduce the accuracy of

the input data and impact the quality of the fit. All of the observed line positions and their assignments appear in Table 4.3. These data represent just a fraction of the state space that we can sample by CPmmW spectroscopy. In particular, only two values of the rotational quantum number are present, $R = 1$ and 2, and the full range of ℓ_R values is not sampled. In spite of these deficiencies, we perform two different long-range fits to the data. In both, the rotational and centrifugal distortion constants are fixed at the values determined by rotational spectroscopy, $B = 1.98794634$ cm^{-1} and $D = 5.704 \times 10^{-6}$ cm^{-1}.[17] This is necessary because the data set is made up of Rydberg-Rydberg transitions, rather than term values, so the rotational energy does not explicitly appear. Rather, the rotational constant more subtly affects the magnitude of the $\Delta R = \pm 2$ interactions in the model. Fitting this parameter accurately requires a more extensive data set.

In the first fit, we allow the quadrupole moment, isotropic polarizability, and anisotropic polarizability to vary. Different from the fit procedure described for the $4f$ ($v = 1$) state, we consider the polarizability-induced mixing of states with $\Delta n = 0$ and $\Delta \ell = \pm 2$ in the model. These off-diagonal radial matrix elements are calculated by integration of numerically-generated hydrogenic wavefunctions. This fit produces the parameters listed in the first column of Table 4.4, and a rms deviation of 4.59 MHz. The value of the fit error is similar to the observed Stark-broadened linewidths. In contrast to our experience with the $4f$ ($v = 1$) state, the pairwise correlation coefficient of Q and γ is reduced to just -0.53 from near unity. We interpret this significant reduction in the parameter correlation to mean that our data set contains the physics necessary to distinguish these parameters. As mentioned in the previous discussion of the $4f$ level, Q and γ are distinguishable by the n-scaling and by the impact of $\Delta n = 0$, $\Delta \ell = \pm 2$ perturbations. By containing a wide range of principal quantum numbers and transitions between states of high-ℓ, which are close in energy to $n(\ell \pm 2)$ Rydberg states, our data set is sensitive to both of these effects. The residuals from this fit appear in the third column of Table 4.3 in units of MHz. We can assign each transition unambiguously from this long-range fit because the differences between transition frequencies are an order of magnitude larger than our

Table 4.3: Observed line positions for g-h ($v = 0$) transitions by CPmmW spectroscopy. The reported residual is from the fit with a floated γ value.

Assignment	ν_{obs} (GHz)	$\nu_{\mathrm{obs-calc}}$ (MHz)	Assignment	ν_{obs} (GHz)	$\nu_{\mathrm{obs-calc}}$ (MHz)
$44h2_3 \leftarrow 43g2_3$	80.0858	1.9	$41g2_3 \rightarrow 40h2_3$	98.9383	5.2
$44h2_4 \leftarrow 43g2_3$	80.1308	4.7	$44h1_5 \leftarrow 43g1_4$	80.0698	4.5
$44h2_3 \leftarrow 43g2_2$	80.1769	5.8	$43g1_4 \rightarrow 42h1_5$	85.6236	-5.6
$43g2_2 \rightarrow 42h2_3$	85.8270	-3.1	$43h1_5 \leftarrow 42g1_4$	85.8581	3.8
$43g2_3 \rightarrow 42h2_4$	85.5666	-2.6	$43h1_4 \leftarrow 42g1_3$	85.9602	-0.3
$43g2_3 \rightarrow 42h2_3$	85.6164	2.5	$42g1_3 \rightarrow 41h1_4$	91.8758	-1.3
$43h2_4 \leftarrow 42h2_3$	85.9316	-4.0	$42g1_4 \rightarrow 41h1_5$	91.9651	-6.1
$43h2_3 \leftarrow 42g2_2$	85.9811	-2.7	$42h1_5 \leftarrow 41g1_4$	92.2181	2.9
$42g2_2 \rightarrow 41h2_3$	91.8577	0.6	$41g1_4 \rightarrow 40h1_5$	98.9469	-4.9
$42g2_3 \rightarrow 41h2_4$	91.8996	1.6	$41h1_5 \leftarrow 40g1_4$	99.2186	5.2
$42g2_3 \rightarrow 41h2_3$	91.9522	8.0	$30g2_2 \rightarrow 29h2_3$	255.8408	-5.6
$42h2_3 \leftarrow 41g2_3$	92.2402	-3.4	$30g2_3 \rightarrow 29h2_4$	255.9525	-4.6
$42h2_4 \leftarrow 41g2_3$	92.2915	0.2	$30h2_4 \leftarrow 29g2_3$	257.0434	-10.2
$42h2_3 \leftarrow 41g2_2$	92.3443	2.0	$29g2_3 \rightarrow 28h2_4$	283.8591	1.0
$41g2_2 \rightarrow 40h2_3$	98.8364	-2.4	$29h2_4 \leftarrow 28g2_3$	285.0700	-6.6
$41g2_3 \rightarrow 40h2_4$	98.8818	-1.8			

Table 4.4: Ion-core electric parameters from long-range model fits to $ng \leftrightarrow nh$ transitions observed by CPmmW spectroscopy, with either a varied (Fit 1) or fixed (Fit 2) value of γ. Values of the free ion, calculated by quantum chemical methods, are reported in the third column.

	Fit 1	Fit 2	Calculated
Q (ea_0^2)	0.489 (11)	0.5001 (90)	0.3715
α (a_0^2)	7.297 (25)	7.303 (23)	6.696
γ (a_0^2)	2.81 (16)	$\alpha/3$	2.811
σ_{rms} (MHz)	4.59	4.60	$\cdots$

fit residuals.

In the second fit, we arbitrarily fixed $\gamma = \alpha/3$ as done in most previous analyses. The parameters, which appear in the second column of Table 4.4, do not change significantly, and are within 1σ of those determined by the first fit. A future larger data set will tighten the uncertainty of these fit parameters and improve our evaluation of the goodness of each fit. The rms error for the two fits is very similar as well. This result gives us some confidence that the fit with a varied γ has not converged to an unrealistic solution.

Lastly, we calculated some of the electrostatic properties of the NO^+ ion by quantum chemistry to serve as a comparison for the experimentally determined values. The details of the calculation are given in Chapter 5. In the third column of Table 4.4, we report the vibrationally averaged values of Q, α, and γ for the $v = 0$, $R = 0$ level of ground-state NO^+. These values do not change significantly for different values of R at low rotation, so the values for $R = 1$ and $R = 2$ are not reported. Significantly, Fit 1, with a varied γ value produces numbers in better agreement with the quantum chemistry calculation. In addition, the γ/α ratio from quantum chemistry is approximately 2.4, and the ratio from our Fit 1 is 2.6. Both of these ratios are substantially different from the factor of 3 typically assumed in long-range analyses. Despite the imperfections of our initial data set, this preliminary analysis suggests CPmmW spectroscopy produces the quality and quantity of data that can expand the boundaries of our understanding of NO Rydberg states.

4.8 Conclusion

After decades, study of NO continues to generate new insights, both fundamental and idiosyncratic. Beyond our initial goal of improving the long-range electrostatic model for Rydberg states, the spectroscopy detailed in this chapter opens up several important avenues for further investigation. Multichannel quantum defect theory (MQDT) is *the* model to completely describe the spectroscopy and dynamics of molecular Rydberg states. Although the parameters of MQDT are less transparent to interpretation than those of the long-range model, the level of detail offered by MQDT predictions can spur new insights.[77] The MQDT description of NO is, at the moment, surprisingly unsophisticated for two seemingly contradictory reasons. First, the gross energy level structure is very simple, so only very high-resolution techniques like mmW spectroscopy are capable of probing the subtle inter-series interactions.[58] Second, the dynamics of the low-ℓ states are very complicated and involve weak interactions with multiple valence states, which are difficult to probe by both experiment and theory.[124] Our high-resolution spectroscopy of core-nonpenetrating Rydberg states that are minimally perturbed by the complex valence state interactions may offer a path through these two issues. In addition to new molecular insights, the high optical density and strong superradiant dynamics of our experimental setup are ripe for further study. Understanding of the Stark-induced transitions that produce the cascading superradiance is required to develop a realistic model of the system, and may offer a unique handle with which to manipulate superradiant decay. Further work in this area will be of foundational importance.

Chapter 5

Autoionization of high-ℓ Rydberg states of NO

5.1 Introduction

For every rovibrational level of the ion-core, a series of Rydberg states exists that converges to that limit. If a Rydberg state has energy greater than the lowest ionization potential, due to rotational or vibrational excitation of the ion-core, it can non-radiatively decay by *autoionization*. In this process, energy is exchanged between the rovibrationally excited ion-core and the Rydberg electron resulting in ejection of the electron and relaxation of the ion-core to a lower energy rovibrational state. We will focus primarily on vibrational autoionization of molecular Rydberg states, but autoionization can also occur due to electronic or spin-orbit excitation in both molecules and atoms.

How does this exchange of energy occur? Since the electronic state of the ion-core does not change in the vibrational autoionization process, the vibrational motion of the core must be entirely responsible. From our discussion of the long-range electrostatic model of Rydberg states in Chapter 4, we know that the Rydberg electron and ion-core interact via the multipole moments of the ion-core at long range. Since these multipole moments are, in general, dependent on the internuclear distance, vibrational motion will mediate the interaction between the quasi-bound Rydberg state

and particular ionization continua, defined by the rovibrational state of the bare ion and the partial wave of the ejected electron. Thus, autoionization is nothing more than a special type of perturbation within the long-range model and the rate can be obtained from Fermi's golden rule:

$$\Gamma = \frac{2\pi}{n^3} \left| \langle \Phi_f \left| H' \right| \Psi_i \rangle \right|^2 \tag{5.1}$$

where H' is the Hamiltonian containing all long-range interactions, Φ_f is the final continuum state, and Ψ_i is the initial Rydberg state. Both states are normalized per unit energy, which results in the additional factor of $1/n^3$. The matrix elements of the long-range Hamiltonian look exactly like those in Chapter 4, except that the bound perturber state is replaced by a continuum state specified by quantum numbers that describe the bare ion, as well as the energy, ϵ, and orbital angular momentum, ℓ, of the electron. For example, the dipole interaction has the form:

$$\begin{aligned}
&\langle v' R' \epsilon \ell' N' M' | H_{\text{dipole}} | v R n \ell N M \rangle \\
&\quad = -e \left\langle v' R' \right| \mu(z) \left| v R \right\rangle \left\langle \epsilon \ell' \right| r^{-2} \left| n \ell \right\rangle \delta_{N',N} \delta_{M',M} (-1)^{\ell+\ell'+N} \\
&\qquad \times \left[(2\ell'+1)(2\ell+1)(2R'+1)(2R+1) \right]^{1/2} \\
&\qquad \times \begin{Bmatrix} N & R' & \ell' \\ 1 & \ell & R \end{Bmatrix} \begin{pmatrix} \ell' & 1 & \ell \\ 0 & 0 & 0 \end{pmatrix} \begin{pmatrix} R' & 1 & R \\ 0 & 0 & 0 \end{pmatrix}
\end{aligned} \tag{5.2}$$

To gain some intuition into the effect of the multipole moments on the autoionization rate, we can examine in more detail the relevant term in this Hamiltonian. Let's assume some generic multipole moment, Q, as a function of internuclear distance, z, and expand this term as a Taylor series about the equilibrium distance of the ion-core, z_e.

$$Q(z) = Q(z_e) + \frac{\mathrm{d}Q}{\mathrm{d}z}(z_e)(z - z_e) + \frac{1}{2}\frac{\mathrm{d}^2 Q}{\mathrm{d}z^2}(z_e)(z - z_e)^2 + \ldots \tag{5.3}$$

Going forward, we will cut the expansion off at the quadratic term for the sake of brevity. Now, we will evaluate the matrix element $\langle v' R' | Q(z) | v R \rangle$ for a rovibrational state of the free ion indicated by primed quantum numbers and a rovibrational state

of the ion-core indicated by unprimed quantum numbers:

$$\begin{aligned}\langle v'R'|Q(z)|vR\rangle &= \langle v'R'|Q(z_e)|vR\rangle + \left\langle v'R' \left| \frac{\mathrm{d}Q}{\mathrm{d}z}(z_e)(z-z_e) \right| vR \right\rangle \\ &\quad + \left\langle v'R' \left| \frac{1}{2}\frac{\mathrm{d}^2Q}{\mathrm{d}z^2}(z_e)(z-z_e)^2 \right| vR \right\rangle \qquad (5.4) \\ &= Q(z_e)\langle v'R'|vR\rangle + \frac{\mathrm{d}Q}{\mathrm{d}z}(z_e)\langle v'R'|(z-z_e)|vR\rangle \\ &\quad + \frac{1}{2}\frac{\mathrm{d}^2Q}{\mathrm{d}z^2}(z_e)\left\langle v'R' \left|(z-z_e)^2\right| vR\right\rangle \qquad (5.5)\end{aligned}$$

By Fermi's golden rule, the autoionization rate is proportional to the square of this matrix element. We examine Equation 5.5 to understand some general properties of long-range autoionization behavior. First, consider rotational autoionization, in which only the rotational state changes ($v' = v$, $R' < R$), versus vibrational autoionization ($v' < v$). Within the harmonic approximation, the first term of this expansion contributes to rotational autoionization, but not to vibrational autoionization. Thus, we might expect, in general, that rotational autoionization is faster than vibrational autoionization. This is rarely observed experimentally because for most molecules with small rotational constants, vibrational autoionization occurs at much lower n than rotational autoionization, and autoionization lifetimes scale as n^3.

We can also use Equation 5.5 to justify the commonly invoked $\Delta v = -1$ propensity rule in vibrational autoionization. Within the harmonic approximation, the second term has the selection rule $\Delta v = \pm 1$, while the third term has the selection rule $\Delta v = \pm 2$, and so on.[a] This means that the leading term for the $\Delta v = v' - v = -1$ process is larger than the leading term for the $\Delta v = v' - v = -2$. A similar argument will show that even larger changes in v will have even higher order derivatives as the leading term and will usually be negligible. While this argument is generally

[a]This is easiest to see using raising/lowering operators:

$$\begin{aligned}\langle v|z|v+q\rangle &= \langle v|(a_+ + a_-)|v+q\rangle \\ &= \langle v|a_+|v+q\rangle + \langle v|a_-|v+q\rangle \\ &= \sqrt{v+q+1}\,\langle v|v+q+1\rangle + \sqrt{v+q}\,\langle v|v+q-1\rangle \\ &\neq 0 \qquad \text{iff} \quad q = \pm 1\end{aligned}$$

correct, it should be pointed out that even for a Morse oscillator there will be some contribution from lower order derivatives to $|\Delta v| > 1$ autoionization channels, which will make these rates larger than the minuscule values expected from the harmonic approximation. In addition, the harmonic approximation tells us that the $\Delta v = -1$ rate will increase linearly with v since $\langle v|z|v+1\rangle = \sqrt{v+1}$.

5.2 Multipole moments and polarizabilities of the NO^+ ion

One of the two required inputs to the long-range model of autoionization is the multipole moments and polarizabilities of the ion-core as a function of internuclear distance. Unlike the simplified treatment in Chapter 4, which only considered the polarizability and quadrupole moment, we will consider all multipole moments up to the hexadecapole moment, Q_4=Φ. These values can be calculated *ab initio* by a number of quantum chemistry packages and methods. In this work, most of the results presented have been obtained using the ORCA program suite;[108,109] the Psi4 package[119] was also used for the calculation of the octupole and hexadecapole moments.

The computational method chosen for this work is a Complete Active Space self consistent field (CASSCF) method.[76] CASSCF is a multiconfigurational wavefunction method in which the electrons and orbitals of the molecule are divided into three subspaces. In the first and third subspace, called the *inactive* and *virtual* space, all orbitals are doubly occupied or doubly unoccupied, respectively. In the second subspace, the *active* space, we allow possible configurations and perform a full-CI calculation. The electrons and orbitals included in the active space should be those that contribute most to the multiconfigurational nature of the wavefunction. By partitioning the space of electrons and orbitals correctly, one can obtain qualitatively correct wavefunctions for regions of state space where the electronic configuration is changing rapidly, as in bond dissociation. This method appropriately treats the effects of static electron correlation, which arises from the near-degenerate energies

of determinants encountered in bond dissociation. However, CASSCF does not accurately capture dynamical correlation, the correlated movement of electrons in the system. To improve the absolute energy determination, we use the N-valence electron perturbation theory (NEVPT2) method[5] following the initial CASSCF calculation. This dramatically improves the accuracy of the potential energy curve (PEC) used for calculation of vibrational wavefunctions. However, throughout this work, the calculation of electric properties is performed on the CASSCF wavefunction. As a test of the importance of dynamical correlation in the calculation of electrostatic properties, we used the Psi4 package to calculate electric properties at select internuclear distances using a multireference configuration interaction (MRCI) wavefunction . However, as found by Fehér and Martin,[44] this more expensive method had little effect on the values of the electric properties, despite large effects on the total energy.

All calculations used Dunning's correlation consistent polarized quadruple zeta basis set, augmented with diffuse functions (aug-cc-pVQZ).[36] Test calculations with a 5Z basis set resulted in nearly identical energies and properties. The inclusion of diffuse functions was critical to obtaining accurate polarizability values.

Throughout this section, figures will show calculated values as markers. The smooth lines that appear in each plot are cubic spline interpolations of the calculated points. These interpolations are shown because smoothly varying functions are required for the calculation of the vibrational wavefunctions and the vibrationally integrated multipole moments.

The calculated potential energy curve of the NO^+ ground state appears in red in Figures 5-1 and 5-2. In blue are the results of a CCSDT calculation performed by Joshua Baraban.[9] Coupled cluster methods are often considered the gold standard for inclusion of dynamical correlation. Our result yields energies comparable to the CCSDT curve, suggesting that our perturbative approach has correctly handled correlation, at least in the bonding region of the potential energy curve. Our PEC approaches a dissociation limit at approximately 10.6 eV, in agreement with the literature value.[145] The CASSCF calculation of Fehér and Martin appears in black.[44] While the shape of the PEC is similar in the bonding region, the absence of dynamical

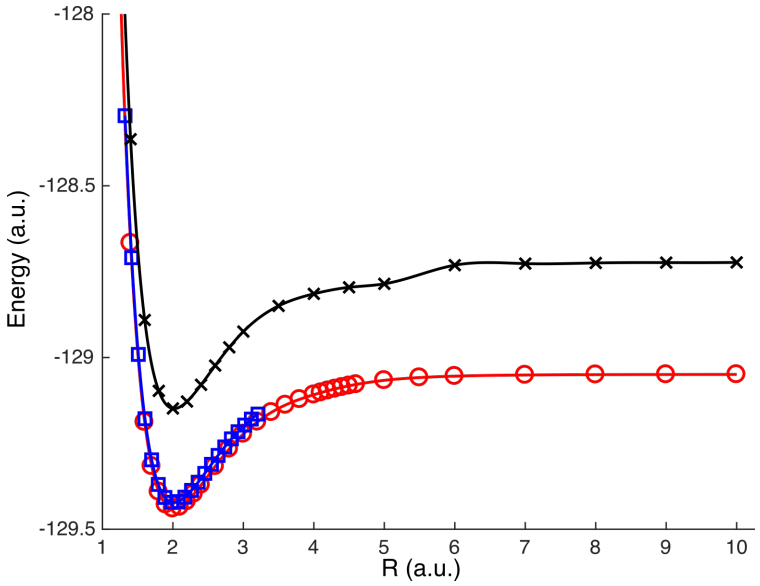

Figure 5-1: Red: NEVPT2 potential energy curve. Blue: CCSDT potential energy curve calculated by Joshua Baraban.[9] Black: CASSCF potential energy curve calculated by Fehér and Martin.[44] The inclusion of dynamic correlation by NEVPT2 significantly lowers the energy of the CASSCF result and yields a result comparable to sophisticated coupled cluster methods. The discontinuity in the CASSCF curve between 5 and 6 a.u. is likely a result of the calculation converging to the wrong dissociation limit, as discussed in the text.

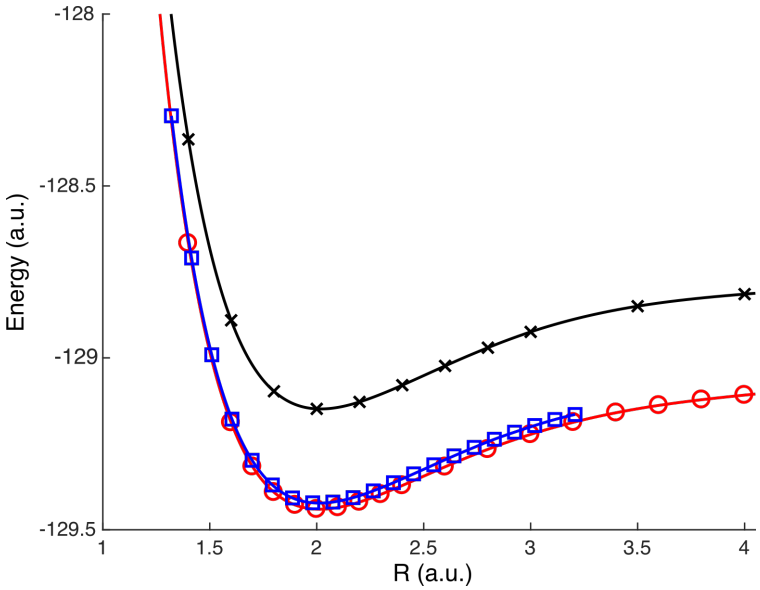

Figure 5-2: The same potential energy curves as Figure 5-1, zoomed into the bonding region of NO^+. Red: NEVPT2 potential energy curve. Blue: CCSDT potential energy curve calculated by Joshua Baraban.[9] Black: CASSCF potential energy curve calculated by Fehér and Martin.[44]

correlation clearly raises the energy for all internuclear distances. In addition, a discontinuity is obvious between 5 and 6 a.u. This, along with some odd behavior in the multipole moment curves presented below, raised our suspicions that this calculation may have converged to the wrong solution at some values of the internuclear distance. Indeed, we found that our own CASSCF calculation would frequently converge to an incorrect configuration depending on the initial guess for the wavefunction. This was particularly a problem using the Psi4 program suite. To better understand this challenge it is useful to examine the electronic configuration of the $[N, O]^+$ system in the bonding region and at the dissociation limit.

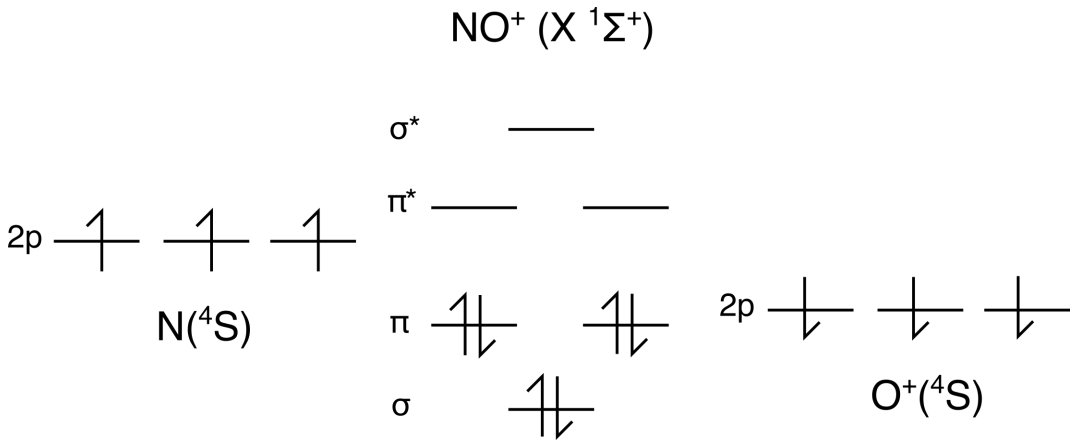

Figure 5-3: Molecular orbital diagram for NO^+ showing the dominant electron configuration in the bonding region of the ground state and the atomic configuration (^{4}S) of the N atom and O^+ ion in the correct dissociation limit.

In the bonding region, the NO^+ ground state is $^1\Sigma^+$, and has a closed shell electronic configuration as shown in Figure 5-3. The ground state dissociates to N and O^+, which are isoelectronic, as shown in Figure 5-3, and have ^{4}S ground states. The same six p orbitals in the atomic dissociation limit form the valence molecular orbitals of relevance in the bonding region. Thus, in the absence of state mixing, the electronic configuration should smoothly change from three doubly occupied and three unoccupied orbitals to six singly occupied orbitals along a singlet surface. This analysis suggests that a (6,6) CASSCF calculation[b] should accurately capture the configurations involved in bond dissociation along the ground state. The calculated occupancy

[b]The notation (n,m) CASSCF specifies that n electrons in m orbitals make up the active space.

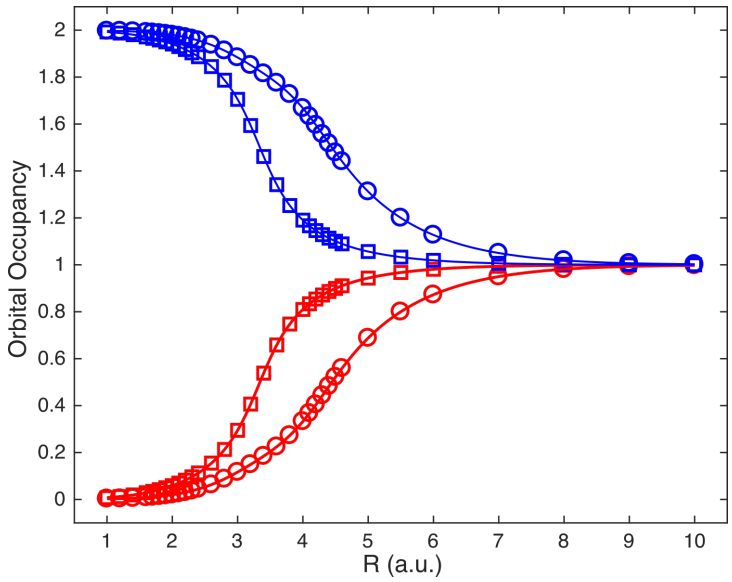

Figure 5-4: Orbital occupancy of NO^+ as a function of internuclear distance. The circle markers are the molecular pσ orbitals, and the square markers are the molecular pπ orbitals. The pπ orbitals are doubly degenerate at all internuclear spacings. As the bond length is increased, the initially doubly occupied orbitals (blue) lose electron density and the initally unoccupied orbitals (red) become filled. At the separated atom limit every p orbital is singly occupied as required for two ^{4}S atoms.

of these six orbitals as a function of internuclear distance is shown in Figure 5-4. The configuration changes rapidly, first between 3 and 4 a.u. as the electrons redistribute in the molecular π orbitals, and then more slowly between 3.5 and 5.5 a.u. as the molecular σ orbitals become involved. As a result of the configuration change, this large span of internuclear distance is challenging to compute and likely explains all discrepancies between our calculation and that of Fehér and Martin.[44] The dissociation limit of their calculation is approximately 11.6 eV, which corresponds better to the dissociation limit of $N^+(^3P) + O(^3P)$ than the correct limit described above.[145]

We now turn to a qualitative description of the electric properties of the NO^+ ground state. The dipole, quadrupole, octupole, and hexadecapole moments from our calculation (red circles) and that of Fehér and Martin (black triangles) are shown in Figures 5-5, 5-6, 5-7, and 5-8. All values are computed in the center of mass frame. The dipole moment presents the most interesting and intuitively appealing variation. In the chosen frame of reference, a positive dipole moment refers to a dipole pointing from O to N, that is positive charge on N and negative charge on O.

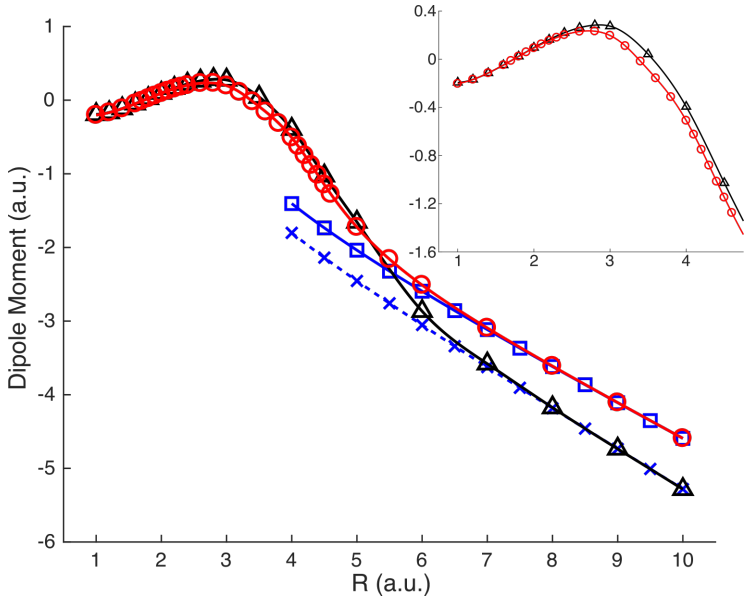

Figure 5-5: Dipole moment, calculated in the center of mass frame, as a function of internuclear distance, R. Red: CASSCF, this work. Black: CASSCF, Fehér and Martin.[44] Blue: Separated atom calculation as described in text. Square data points are for the $N(^4S) + O^+(^4S)$ limit. Cross data points with the dashed line are the *negative* of the result for the dipole moment in the $N^+(^3P) + O(^3P)$ limit. It is unclear how the sign error occurred in the previous result.[44] See text for discussion.

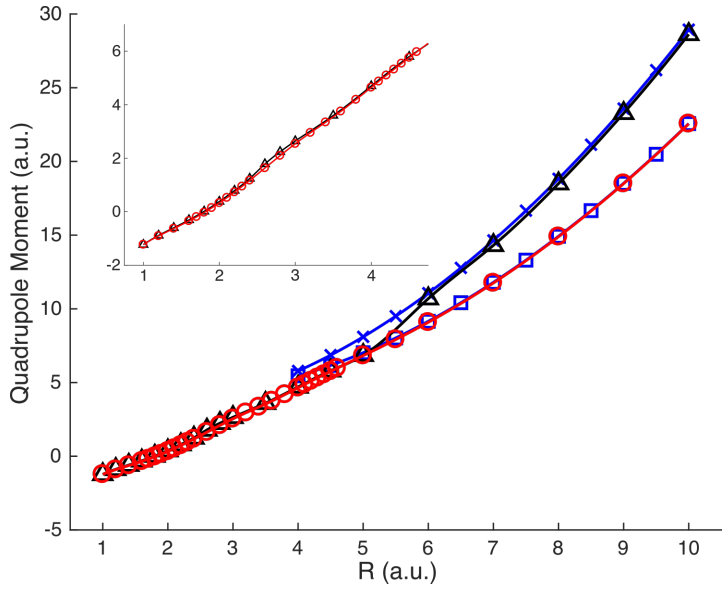

Figure 5-6: Quadrupole moment as a function of internuclear distance, R. Red: CASSCF, this work. Black: CASSCF, Fehér and Martin.[44] Blue: Separated atom calculation as described in text. Square data points are for the $N(^4S) + O^+(^4S)$ limit, and the cross data points are for the $N^+(^3P) + O(^3P)$ limit.

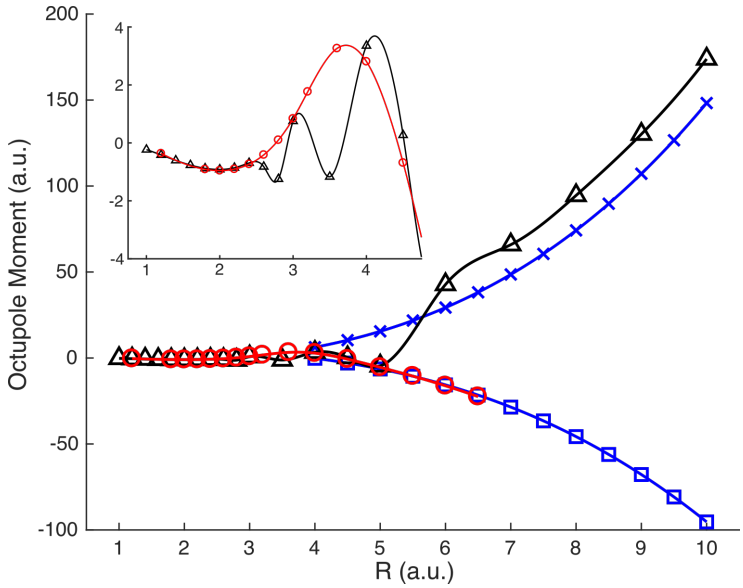

Figure 5-7: Octupole moment as a function of internuclear distance, R. Red: CASSCF, this work. Black: CASSCF, Fehér and Martin.[44] Blue: Separated atom calculation as described in text. Square data points are for the $N(^4S) + O^+(^4S)$ limit, and cross data points are for the $N^+(^3P) + O(^3P)$ limit.

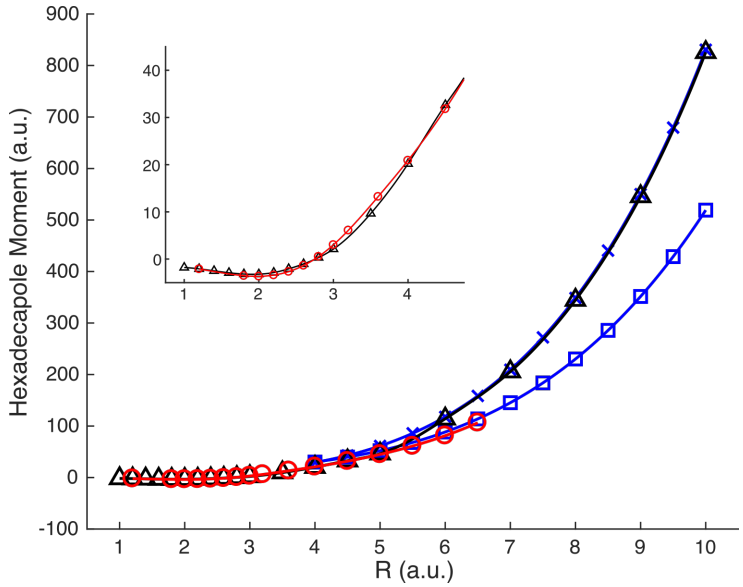

Figure 5-8: Hexadecapole moment as a function of internuclear distance, R. Red: CASSCF, this work. Black: CASSCF, Fehér and Martin.[44] Blue: Separated atom calculation as described in text. Square data points are for the $N(^4S) + O^+(^4S)$ limit, and cross data points are for the $N^+(^3P) + O(^3P)$ limit.

In the bonding region, around 2 a.u., the dipole moment is positive and very small. This agrees with our intuition since the electronegativities of the two neutral atoms should be very similar, but oxygen is slightly more electronegative than nitrogen.[70] As the atoms are pushed together, the π orbitals will be stabilized with respect to the σ orbitals, eventually leading to a reversal of the energy ordering. This shifts electron density along the bond axis from oxygen toward nitrogen and results in an increasingly negative, though still small, dipole moment at R<2 a.u. As the atoms are pulled apart, the dipole moment first becomes increasingly positive as expected. Around 3 a.u., the dipole moment turns around. This is exactly the point when the electronic configuration begins to change as shown in Figure 5-4, and electron density moves into N-weighted orbitals. The slope of the dipole moment function changes substantially until approximately 6 a.u. where it begins to increase in magnitude linearly with increasing R. As mentioned above, the dissociation limit corresponds with $N(^4S) + O^+(^4S)$, resulting in a negative dipole moment at large internuclear distance. Again, our calculation begins to disagree with the literature result in the configuration-changing region. However, if the previous result actually converges to the $N^+(^3P) + O(^3P)$ limit, the dipole moment from that work should have the opposite sign of our result.

The even multipole moments (quadrupole, hexadecapole), show only slight disagreement with the previous calculation for R<6 a.u. Beyond that point they increase monotonically with internuclear distance and have significantly different values from the previous result. The other odd moment, the octupole, shows more complex variation. Reminiscent of the dipole, the octupole changes substantially in the configuration-changing region, and exhibits both a minimum and maximum. Our calculated moment varies smoothly with internuclear distance in contrast with the discontinuities found by Fehér and Martin.[44] Unlike for the dipole, the sign of our octupole moment at large R disagrees with the Fehér and Martin calculation.

To address these discrepancies and gain confidence in our own calculation, we examine the values of the multipole moments using a simple model for the separated atom limit. We begin by placing the origin of the coordinate system on the charged

atom, which is O^+ for the lowest dissociation limit, and N^+ for the next higher dissociation limit. This places the neutral atom N (O) at some distance, z, from the ion along the positive (negative) z-axis. The presence of the ion induces a dipole on the neutral atom, which points away from the origin and is considered positive (negative) for the $[N, O^+]$ ($[N^+, O]$) limit. For simplicity, we assume that the induced dipole is simply a point dipole at the location of the neutral atom. The functional form for this ion-induced dipole is directly related to the atomic dipole polarizability:

$$\mu_{\text{ind}}(R) = \frac{\alpha \times q}{z^2} \tag{5.6}$$

where α is the dipole polarizability of the atom of interest, and q is the charge of the atomic ion, which is 1 in all cases considered here. We would like to evaluate all of the multipole moments in the center of mass frame in order to compare with the quantum chemical calculations. This is accomplished using the general formula for displacement of the multipole moments along an axis of cylindrical symmetry:[140]

$$Q_L(z-b) = \sum_{j=0}^{L} (-b)^{L-j} \binom{L}{j} Q_j(z) \tag{5.7}$$

where $Q_L(z)$ is the L^{th} multipole moment evaluated at z, $+b\hat{z}$ is the displacement of the origin at which the multipole moment is evaluated, and the binomial coefficient is defined as:

$$\binom{L}{j} = \frac{L!}{j!(L-j)!} \tag{5.8}$$

This formula also allows us to express the initial higher-order multipole moments, which are created by the presence of a point dipole at a distance, z, from the origin. In terms of the induced dipole, $\mu_{\text{ind}}(z)$, the next three multipole moments are written as:

$$\Theta = -2z \times \mu_{\text{ind}}(z) = \frac{-2\alpha}{z} \tag{5.9}$$

$$\Omega = 3z^2 \times \mu_{\text{ind}}(z) = z\alpha \tag{5.10}$$

$$\Phi = -4z^3 \times \mu_{\text{ind}}(z) = -4z\alpha \tag{5.11}$$

The symbols Θ, Ω, and Φ refer here to the quadrupole, octupole, and hexadecapole moments. After applying Equation 5.7 to the first five multipole moments to shift the origin to the center of mass we find:

$$q = 1 \tag{5.12}$$

$$\mu = \frac{\alpha}{z^2} - z_{CM} \tag{5.13}$$

$$\Theta = z_{CM}^2 - \frac{2\alpha(z + z_{CM})}{z^2} \tag{5.14}$$

$$\Omega = -z_{CM}^3 + \frac{3\alpha(z + z_{CM})^2}{z^2} \tag{5.15}$$

$$\Phi = z_{CM}^4 - \frac{4\alpha(z + z_{CM})^3}{z^2} \tag{5.16}$$

where z_{CM} is the center of mass position defined by

$$z_{CM} = \frac{\sum_i m_i z_i}{\sum_i m_i} \tag{5.17}$$

where m_i and z_i are the masses and positions of the two nuclei. An alternative, but ultimately equivalent formulation of this problem is to set the initial origin at the neutral atom position. This puts the charged atom at some distance from the origin, which will produce an initial additional dipole contribution beyond the induced dipole, as well as higher order moments. This approach is perhaps the more intuitive method since the moments resulting from the ion have the simple forms $-qz$, qz^2, $-qz^3$, ..., as expected.

The result of this separated atom calculation for the $N(^4S) + O^+(^4S)$ limit is shown as blue squares in Figures 5-5, 5-6, 5-7, 5-8. The agreement between this simple model and the quantum chemical calculation is excellent at large internuclear distance. This result also confirms that our calculation approaches the correct dissociation limit as the bond length increases.

We perform the same separated atom calculation for the higher energy $N^+(^3P)$ +

$O(^3P)$ dissociation limit and these results appear as blue crosses in the above figures. It is immediately clear that the previous quantum chemical calculation by Fehér and Martin is indeed converging to this higher limit. However, two discrepancies must be addressed. First, the dashed blue line with crosses in Figure 5-5 is actually the *negative* of the result obtained by our separated atom calculation. In accord with our intuition, our calculation confirms that the $[N^+, O]$ dipole has the opposite sign of the $[N, O^+]$ dipole. Some data processing error must have occurred in the earlier work.[44] Second, unlike the other moments, there remains a significant difference between the Fehér and Martin octupole result and the separated atom calculation. We do not have a satisfactory explanation for this difference, although it may be related to whatever error produced the opposite sign for the dipole moment in that work.

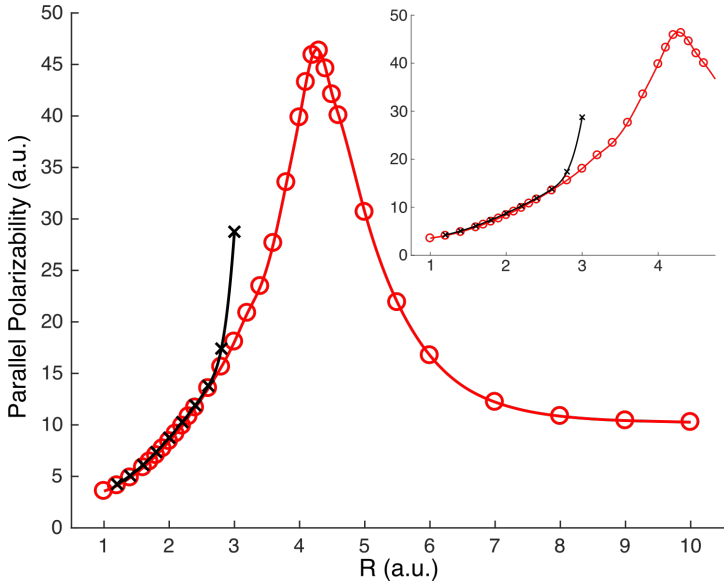

Figure 5-9: Parallel polarizability (α_{zz}) as a function of internuclear distance, R. Red: CASSCF, this work. Black: MP2, Fehér and Martin.[44]

The functions for the NO^+ polarizability, parallel and perpendicular to the internuclear axis, appear in Figures 5-9 and 5-10, respectively. We expect that both of these values should approach the sum of the polarizabilities of the constituent atoms, N and O^+, in the separated atom limit. The two values do indeed approach the same value $\alpha \sim 10$ a.u., which is quite similar to the sum of atomic polarizability values of α_N=7.36(7.17) and α_{O^+}=2.67(2.63). These were calculated using the same

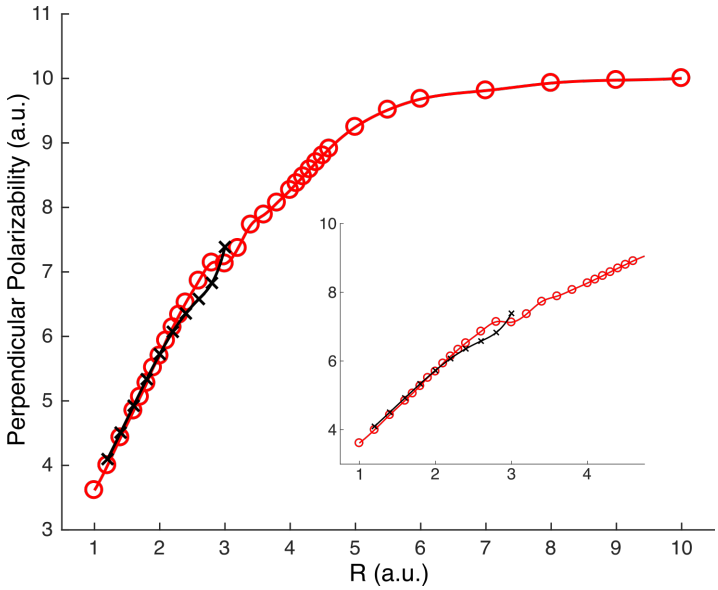

Figure 5-10: Perpendicular polarizability (α_{xx}) as a function of internuclear distance, R. Red: CASSCF, this work. Black: MP2, Fehér and Martin.[44]

aug-cc-pVQZ basis set and a NEVPT2(MP2) method. The multireference method requires numerical calculation of the polarizability using the computed dipole moment at various applied electric fields, while the MP2 method allows for an analytical determination of the polarizability. The similar results from the two approaches suggest that our calculations throughout have converged sufficiently tightly to give accurate polarizability values. The peak in the parallel polarizability around 4 a.u. is a result of the expansion of the molecular wavefunction along the internuclear axis as the two atoms approach each other, but are not yet tightly bound. This feature has been observed repeatedly in both *ab initio* and semiempirical calculations of the polarizabilities of diatomic molecules, including the isoelectronic molecules N_2 and CO, as well as neutral NO.[45,93,96,106,149] As the two atoms approach each other more closely, the polarizability along the bond axis decreases along with the spatial extent of the wavefunction. In contrast, except for ∼3 a.u. where the π orbital configuration starts to change, the perpendicular polarizability decreases monotonically as the atoms are brought together because the electronic wavefunction significantly contracts in the perpendicular direction as the bond is formed.

As the internuclear distance approaches zero, the molecule approaches the united

atom limit. For N and O^+ along a singlet surface this corresponds to $P^+(^1D)$. The polarizability of P^+ in this electronic configuration was calculated using an MP2 method and the same aug-cc-pVQZ basis set to be 15.1 a.u.,[c] which implies that the polarizability must increase again as z is further reduced toward the united atom limit. There is some ambiguity in the literature on this point. Several semiempirical models suggest that the polarizability should begin increasing toward small z within the range investigated in this work.[144,149] However, this increase is not consistently observed by *ab initio* methods, perhaps due to the challenge of obtaining converged calculations at very small values of the internuclear distance.[45,93,149] We were able to obtain some converged NEVPT2 calculations at shorter than 1 a.u. internuclear distance. However, the orbital occupancy changed abruptly, in contrast to the smooth changes observed throughout the rest of the range of internuclear distance investigated. This inconsistency prompted us to abandon any interpretation of those calculation results. Further investigation of this phenomenon seems warranted, though it is beyond the scope of this work.

We can again compare our results with the earlier work of Fehér and Martin.[44] Unlike the multipole moments, those authors were only able to obtain values of the polarizability using the MP2 method. Since this perturbative method is not valid in regions of internuclear distance where the electronic configuration changes rapidly, their results only extend to an internuclear distance of 3 a.u. Our results using a CASSCF wavefunction are in good agreement with their MP2 values over this range of internuclear distance.

5.3 Numerical inputs

One advantage of the long-range electrostatic model is that it is entirely *ab initio*, requiring as inputs the multipole moment and polarizability values and the radial hydrogenic matrix elements. In Section 5.2, we discussed the quantum chemical cal-

[c]For $P^+(^1D)$, unlike the first row elements, we were unable to obtain a CASSCF wavefunction that converged sufficiently tightly to be able to numerically compute the polarizability.

culations performed to obtain an accurate potential energy curve and electric properties of the NO^+ ion-core. The required model input is in fact the matrix element, $\langle v'R'|Q_k(z)|vR\rangle$, where there is an explicit internuclear distance dependence, z, to the multipole moment or polarizability of interest. For bound Rydberg states, this is simply the expectation value of the Q_k multipole moment for the desired rovibrational state. For autoionizing Rydberg states, this is a matrix element off-diagonal in v and/or R. In either case, the vibrational wavefunctions are obtained numerically by a simple 1D discrete variable representation (DVR) calculation, following Colbert and Miller.[29] For an interval $(0, \infty)$, as in the diatomic internuclear distance, we choose the limits to be $a = 0$ and $b \to \infty$. For a large number of data points, $N \to \infty$, the grid spacing is $\Delta z = (b - a)/N$. Then we can write the kinetic energy operator as:

$$T_{i,i'} = -\frac{\hbar^2}{2\mu\Delta z^2}(-1)^{i-i'} \left\{ \begin{array}{ll} \pi^2/3 - 1/2i^2, & i = i' \\ \dfrac{2}{(i-i')^2} - \dfrac{2}{(i+i')^2}, & i \neq i' \end{array} \right\} \tag{5.18}$$

where $z_i = i\Delta z$, $i = 1, \ldots,$ and μ is the reduced mass of the system. The potential energy, which is diagonal in i, is written as the sum of the calculated potential energy curve and a centrifugal potential term, which produces a small dependence of the wavefunctions on the rotational quantum number:

$$U(z_i) = U_{\text{calc}}(z_i) + \frac{R(R+1)}{2\mu z_i^2} \tag{5.19}$$

The total Hamiltonian, $H = T + U$, is diagonalized to obtain the vibrational wavefunctions. The built-in trapezoidal numerical integration procedure of MATLAB, *trapz*, is then used with the calculated electric properties to obtain the desired matrix elements.

The hydrogenic electronic wavefunctions are obtained by numerical integration of the Schrödinger equation for a Coulombic potential by the Numerov method.[171] In order to obtain an approximately constant number of points for each cycle of the wavefunction, a square root scaling of the radial dimension is used.[40] These wavefunctions can be normalized in the typical way, $\langle n\ell|n\ell\rangle = 1$. Energy normalization simply

requires multiplication of the space-normalized wavefunction by $n^{1.5}$. For both the bound and continuum wavefunctions needed for autoionization calculations, we found it superior for integration to proceed from small to very large r, particularly since the inner lobes of the continuum wavefunctions contribute most to the calculated matrix elements. For the bound wavefunctions, it is necessary to cut off the integration when the solution begins to diverge at large r. It is well known that the continuum wavefunctions, with energy ϵ, should obey energy- rather than space-normalization. Rather than attempt a numerical normalization procedure, we compute the analytical value of the hydrogenic continuum wavefunction at the position of the first maximum[14] and scale the numerical wavefunction accordingly. This approach took advantage of the relatively efficient computation of hypergeometric functions built in to the MATLAB software package. Again, built-in trapezoidal numerical integration was used to calculate the final radial electronic matrix elements.

As a measure of the numerical error in our calculations, we compare in Figure 5-11 the fractional error of several numerically computed expectation values of radial functions for the $25f$ state relative to the analytical results. The solid (hatched) bars indicate the error is less than (greater than) the analytical value, and the red (blue) bars indicate the result from inward (outward) Numerov integration of the hydrogenic wavefunction. For positive k values of the r^k matrix elements, the inward integration procedure produces very accurate results because the matrix elements are weighted heavily at very large r. For negative k values, the matrix elements of interest to this work, the situation is reversed. The outward integration procedure produces accurate wavefunctions at short r where these matrix elements are heavily weighted. Moreover, the error is essentially constant at just under 1% for all k. The wavefunctions produced by inward integration require a cutoff at short r where the integration begins to diverge; this arbitrary cut-off at short r results in an increasingly worse approximation for larger negative k values. Indeed, the amplitude of the wavefunction in the first lobe controls the relative accuracy. The fractional error of the r^{-k} expectation values determined from the outward integration procedure generally decreases for larger ℓ, and for smaller n.

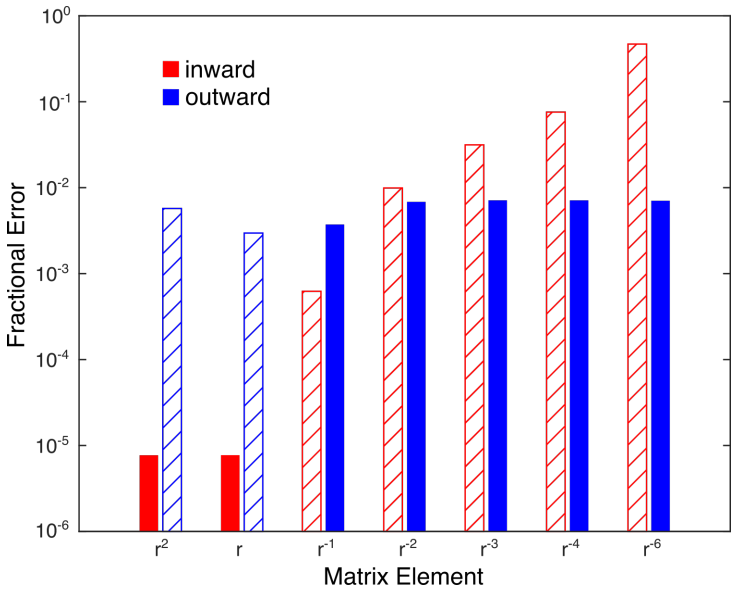

Figure 5-11: Fractional error in r^k expectation values for a $25f$ wavefunction calculated by inward (red) or outward (blue) Numerov integrations. Solid (hatched) bars indicate the direction of the error is negative (positive). Outward integration for both bound and continuum wavefunctions is used in this work because it produces more accurate r^{-k} matrix elements.

5.4 Experimental

In order to gain some confidence in our model for long-range autoionization, we measure lifetimes of ng ($v = 1$) Rydberg states for a range of values of n, R, and ℓ_R. The experimental design is similar to the ionization detected spectroscopy experiments described in Chapter 4. A supersonic expansion of ~0.5% NO by volume in Ar passes through a 1 mm conical skimmer into a differentially pumped detection chamber that contains a Wiley-McLaren type time-of-flight mass spectrometer (TOF-MS). At this point, the lasers employed in the triple resonance excitation scheme previously described intersect the molecular beam transversely. The three lasers were delayed with respect to each other by approximately 10 ns and loosely focused into the chamber. Upon excitation to the autoionizing Rydberg state, production of free electrons and NO^+ ions begins immediately. In order to detect ions, a field is pulsed on the bottom of the electrode stack and ions are accelerated through a ~75 cm field-free region and impinge on a multichannel plate (MCP) detector. By varying the delay between the final excitation laser and the pulsed extraction field, the measured ion

yield correlates with the lifetime of the chosen Rydberg state. The approximately 10 ns "turn-on" time of the extraction field limits the fastest autoionization rates that can be measured by this method. While the extraction field is present, the Rydberg states continue to autoionize and this appears as a tail of ions following the prompt extracted ion signal. This signal is corrupted by the very large extraction field, which mixes the initially laser-prepared state with the bath of higher-ℓ states, making any interpretation challenging. Therefore, we only integrate over the prompt signal, which results from ions already present when the extraction field turns on. In other words, those Rydberg states had already autoionized. To improve the statistics of the lifetime fitting and control for any slow drift of laser intensity and/or frequency, we randomize the order of data collection and collect twelve measurements for each delay time. An error-weighted exponential function was fit to the averaged data, starting several nanoseconds after the initial appearance of ion signal to avoid the influence of the extraction field "turn-on." In the next two subsections, we discuss two major sources of error that contribute to these measurements.

5.4.1 State Selectivity

The bandwidth of the pulsed dye laser (~ 0.05 cm^{-1}) used in these experiments is larger than the typical separation between two ℓ_R components of the investigated ng states. As a result it is possible to excite more than one component by P, Q, and R transitions out of the intermediate $4f$ level. In order to obtain measurements of selected ngR_N states we take advantage of the intrinsic line intensity differences. Since the final transition in this step involves a change of $\Delta\ell = +1$ between the two Rydberg states, there is a strong $\Delta N = +1$ propensity rule. By choosing excitation schemes that result in an R branch transition in the last step, we enhance the selectivity of our excitation scheme for particular ℓ_R states. In addition, we choose either P_1 or R_{21} lines of the A $^2\Sigma^+ \leftarrow$ X $^2\Pi_{1/2}$ transition in order to select a single J level in the A state. This choice generally enhances the selectivity, although only in a few cases do we prepare a single J of the final ngR_N state: specifically, when an R branch of the $4f \leftarrow$ A $^2\Sigma^+$ transition is used. The complete preparation schemes for all investigated

Table 5.1: Excitation scheme and selectivity for preparation of the indicated Rydberg state. In all cases, a final R transition is the most intense line, and nearly all contamination is due to a Q transition to the $N-1$ component.

State	A←X	$4f$ ←A	Selectivity
$ng0_4$	$R_{21}(0.5)$	${}^{-2}R_3(2)$	1.0
$ng1_3$	$P_1(2.5)$	${}^{0}R_1(1)$	1.0
$ng1_4$	$R_{21}(1.5)$	${}^{-2}Q_2(3)$	0.976
$ng1_5$	$R_{21}(1.5)$	${}^{-2}R_3(3)$	0.988
$ng2_2$	$P_1(1.5)$	${}^{2}R_{-1}(0)$	1.0
$ng2_3$	$R_{21}(0.5)$	${}^{0}Q_0(2)$	0.959
$ng2_4$	$R_{21}(0.5)$	${}^{0}R_1(2)$	0.965
$ng2_5$	$R_{21}(2.5)$	${}^{-2}Q_2(4)$	0.920
$ng2_6$	$R_{21}(2.5)$	${}^{-2}R_3(4)$	0.972
$ng3_1$	$P_1(2.5)$	${}^{2}P_{-3}(1)$	1.0
$ng3_2$	$P_1(2.5)$	${}^{2}Q_{-3}(1)$	0.626
$ng3_3$	$R_{21}(1.5)$	${}^{0}P_{-1}(3)$	0.614
$ng3_5$	$R_{21}(3.5)$	${}^{-2}P_1(5)$	0.724
$ng3_6$	$R_{21}(3.5)$	${}^{-2}Q_2(5)$	0.872
$ng3_7$	$R_{21}(3.5)$	${}^{-2}R_3(5)$	0.955

states are listed in Table 5.1, along with the state selectivity of the excitation scheme, which is calculated using the transition intensity formulas presented in Chapter 4.

While for the majority of states, very high purity of the desired state is obtained, the selectivities for $ng3_2$, $ng3_3$, and $ng3_5$ states are only 0.63, 0.61, and 0.72, respectively. The majority of the contamination in this preparation scheme is from the Q branch, which excites the $N-1$ component. In spite of this, it is evident from the results presented in Figures 5-16, 5-17, and 5-18 that these less perfectly selected states do not exhibit greater discrepancy with the calculation than the other data. This may simply be a result of the modest variation expected among the different ℓ_R states, so that contamination of the desired state preparation by a neighboring state will not dramatically alter the measured rate.

In all of these experiments, the polarization of all three lasers is linear and par-

allel. It is possible that a different polarization arrangement could further enhance the selectivity of the preparation scheme. This is certainly observed in the work of Petrović and Field where double resonance experiments using circular polarization of the same and opposite helicities produced dramatic differences in the P and R branch transition intensities.[122] It is important to note that those experiments involved transitions between three states well described by Hund's case (b). Our calculations have shown that this type of polarization discrimination is reduced when the involved states belong to different angular momentum coupling cases. In our experiment, the four involved states belong to three different Hund's cases and, as a result, we expect any enhancement due to a special polarization arrangement to be modest.

5.4.2 State Purity

As discussed at length in Chapter 4, Rydberg states exhibit extreme sensitivity to electric fields. Several studies have noted that the lifetimes of low-ℓ, rapidly predissociating states can be lengthened in the presence of electric fields.[107,157] In particular, experiments by Vrakking and Lee[158] demonstrated that, in the presence of a small dc electric field estimated to be 25-40 mV/cm, the $nf2_1$ and $np0_1$ states exhibited an order of magnitude enhancement in lifetime as the principal quantum number was increased beyond the critical values of $n = 65$ and 115, respectively. Later, Vrakking performed an explicit calculation of the lifetime enhancement due to the Stark effect,[156] incorporating estimated predissociation lifetimes for all states, which weighted the decay rate by the bright state character of each Stark state. This theoretical model gave excellent agreement with the experimentally determined lifetimes. A simpler estimate based on Rydberg scaling rules can also predict these critical values of n. The energy of an $n\ell$ Rydberg state in zero field is approximately

given by:[d]

$$E = -\frac{1}{2n^2} - \frac{\delta_\ell}{n^3} \tag{5.20}$$

where δ_ℓ is a generic quantum defect for the ℓ Rydberg series. When placed in an electric field, F, the extreme red (blue) $m = 0$ Stark states have the energy:

$$E = -\frac{1}{2n^2} \mp \frac{3n^2F}{2} \tag{5.21}$$

From these two formulae, we find that an extreme Stark state with principal quantum number, n, meets the nearest member of a low-ℓ Rydberg series when the electric field is

$$F = \frac{2|\Delta_\ell|}{3n^5} \tag{5.22}$$

where $\Delta_\ell = \delta_\ell - q$ and q is the nearest integer. Calculations are most easily performed in atomic units. For reference, the atomic unit of electric field is approximately 5.14×10^9 V/cm. Equation 5.22 resembles the formula for the more familiar Inglis-Teller limit, $F_{\text{Inglis-Teller}} = 1/3n^5$, which gives the electric field at which the extreme red and blue Stark states of adjacent principal quantum numbers intersect.[53] Both depend on the energy shifts of the extreme Stark states, so the critical field given by Equation 5.22 could be considered an intra-n version of the Inglis-Teller limit. This field is significant because we naively expect the lifetime of a nominal $n\ell$ Rydberg state to change significantly when that state begins to interact with the bath of high-

[d] This convenient approximate formula is obtained from the normal Rydberg formula and assumes that the quantum defect, δ_ℓ, is much smaller than the principal quantum number.

$$\begin{aligned}
E &= -\frac{1}{2(n+\delta_\ell)^2} \\
&= -\frac{(n+\delta_\ell)^2}{2(n+\delta_\ell)^4} \\
&= -\frac{n^2 + 2\delta_\ell n + \delta_\ell^2}{2(n+\delta_\ell)^4} \\
&\approx -\frac{n^2}{2(n+\delta_\ell)^4} - \frac{2\delta_\ell n}{2(n+\delta_\ell)^4} \\
&\approx -\frac{1}{2n^2} - \frac{\delta_\ell}{n^3}
\end{aligned}$$

ℓ states, which have intrinsically long lifetimes. Using the quantum defects, $\delta_f = 0.0101$ and $\delta_p = 0.7$, we find $F = 30$ and 51 mV/cm for $65f$ and $115p$, respectively. These values are consistent with both the experimental observations[158] and the more sophisticated model by Vrakking.[156]

In our supersonic jet apparatus, we assume that the inhomogeneity of the stray field is small in order to estimate the magnitude of the stray field from the width of our ion-detected mmW spectra. As demonstrated in Chapter 4, electric field inhomogeneity significantly broadens all Rydberg-Rydberg transitions. However, the small excitation volume and symmetry of the electrode stack make neglect of field inhomogeneity a reasonable approximation. If the inhomogeneity is significant and additional line broadening occurs, our estimate may be regarded as an upper bound on the magnitude of the electric field. The mmW spectra in the ion-detection apparatus are substantially broadened by stray field, so we assume that the observed linewidths are approximately given by the width of the entire n Stark manifold, which is simply the energy difference between the extreme red and blue Stark states:

$$\Delta E = 3n^2F \tag{5.23}$$

From the ion-detected $44f, 44h \leftarrow 43g$ spectrum presented in Figure 4-14, we measure a linewidth of approximately 680 MHz, which corresponds to an electric field of approximately 90 mV/cm. This is a representative value, though we have observed linewidths corresponding to fields as small as 40 mV/cm in this apparatus. Therefore, we take 100 mV/cm as an estimate for the stray field in the apparatus in order to investigate the influence of an electric field on our autoionization lifetime measurements.

First, we compare this stray field with the critical electric field given by Equation 5.22. For a $28g$ state, with the approximate quantum defect, $\delta_g \approx 0.003$, we find $F \approx 600$ mV/cm. This field is many times larger than our estimate for the stray field in the apparatus. It is unlikely that a dramatic change in lifetime comparable to that observed by Vrakking and Lee[158] occurs in our experiment.

We perform a calculation of the Stark effect for NO Rydberg states to obtain a more quantitative estimate of the state mixing caused by this small electric field. The state purity for all $28g$ states investigated in this work remains high at a field of 100 mV/cm. For most states, the leading basis state character is > 0.98. The state with the smallest fractional character of 0.9695 is $28g1_5$. In general, for a given R, the higher N states are more mixed. These very high state purities suggest that our lifetime measurements are minimally perturbed by the presence of stray electric fields. Moreover, we observe no systematic discrepancies that point to the influence of stray field. The measurements generally do not show better agreement with the calculations at lower N or lower n where we anticipate the effects of electric field-induced state-mixing to be smaller.

Looking at the $28g0_4$ state more closely, we perform a simplified three state version of Vrakking's Stark-induced lifetime calculation.[156] In addition to the g state of interest, we consider the two states with which it interacts most strongly, the $28f0_3$ and $28h0_5$ states. These field-free states contribute about 0.1% and 1%, respectively, of the basis state character to the Stark state at 100 mV/cm. Using our long-range model, we can calculate the expected autoionization rate of the $28h0_5$ state to be $\Gamma_h = 7.4 \times 10^6$ s^{-1}, and the $28g0_4$ rate to be $\Gamma_g = 1.23 \times 10^7$ s^{-1}. The nf state decays predominantly by predissociation. The formula for predissociation decay rates of nf states given by Bixon and Jortner[16] predicts the $28f0_3$ decay to be approximately one order of magnitude faster than the $28g0_4$ autoionization rate, $\Gamma_f = 3.6 \times 10^8$ s^{-1}. To determine the total measured decay rate we calculate the Stark state decay rate as the sum of the decay rates of the basis states weighted by their fractional character.

$$\Gamma_{i,\mathrm{Stark}} = |A_{i,f}|^2\Gamma_f + |A_{i,g}|^2\Gamma_g + |A_{i,h}|^2\Gamma_h \tag{5.24}$$

Next, the laser excitation does not fully resolve the three Stark states that correspond to the field-free f, g, and h states, so the measured rate is the sum of the Stark state

decay rates weighted by their bright state g character.

$$\Gamma_{obs} = \sum_i |A_{i,g}|^2 \Gamma_{i,\text{Stark}} \tag{5.25}$$

Performing this simplified three state calculation gives a total observed decay rate, $\Gamma_{obs} = 1.27 \times 10^7$ s^{-1}. The mixing of f state character into the nominal g state results in faster decay than in the absence of an electric field.

Finally, we perform a full calculation of the Stark-induced decay rates, following the model of Vrakking,[156] in order to gain some further insight. We assume that all components of the f complex have the same predissociation lifetime, $\Gamma_f = 3.6 \times 10^8$ s^{-1}. For every state with $\ell \geq 4$, we calculate the autoionization rate with our long-range model. The calculation proceeds as in the simplified model where the Stark state decay rate is a weighted sum of the basis state decay rates, and the total observed decay rate is the sum of all Stark state decay rates weighted by the bright state character. In addition, we explicitly account for the laser linewidth of 0.05 cm^{-1}. The result for all ℓ_R components of the $28g3_N$ complex is shown in Figure 5-12. The decay rates of all components of this state increase as the electric field increases. For field values up to 100 mV/cm, the decay rates change by less than 3% relative to the field-free values. At 500 mV/cm, some decay rates have changed by more than 50%. In addition, the decay rates of each component do not increase with electric field at the same rate. For example, Figure 5-12 shows that the $\ell_R = 3$ component has the second smallest decay rate at zero field, but has the fourth largest decay rate at 500 mV/cm. This ℓ_R-specific change in the decay rates could serve as a diagnostic for the magnitude of the stray field in the chamber.

It is informative to compare the change in decay rates of the f and g states. Figure 5-13 shows the decay rates of the $28f3_N$ (left) and $28g3_N$ (right) complexes as a function of electric field, up to 6 V/cm. The decay rates of the f states decrease by a full order of magnitude from $\sim 3.6 \times 10^8$ s^{-1} to $\sim 2 \times 10^7$ s^{-1}. The rate of change is fastest around 2.5 V/cm, which is similar to the critical field value $F = 2.01$ V/cm predicted by Equation 5.22. As expected, when the f states begin to interact with

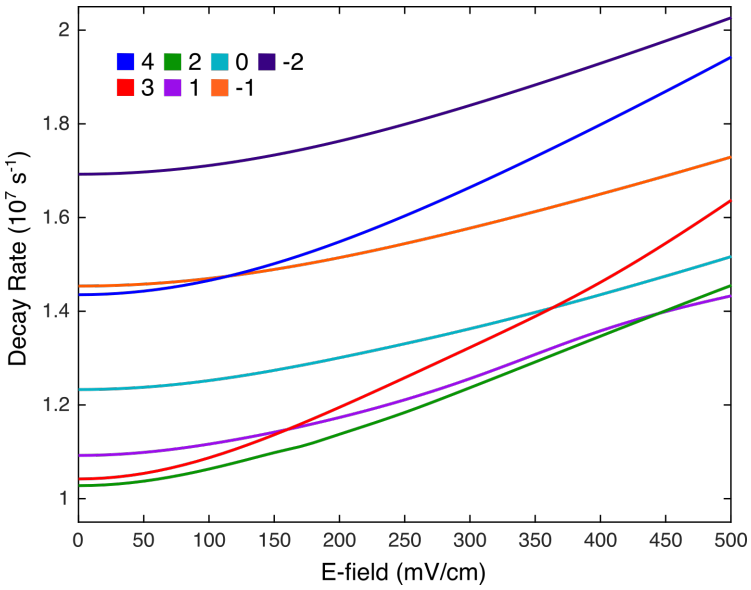

Figure 5-12: Stark-induced decay rates of the members of the $28g3_N$ complex. The colors correspond to the nominal ℓ_R value of each Stark state as indicated in the legend. The details of the calculation are given in the text.

the extreme red Stark state, the decay rates change dramatically.

Interestingly, this critical field value is also significant for the g state decay rates, which generally reach a maximum around 2.5 V/cm, before decreasing toward the same final value as the f state decay rates, $\sim 2\times10^7$ s^{-1}. Significantly, the g state decay rate changes by less than an order of magnitude over the entire range of electric field values, in contrast to the huge change observed here in the f state decay rate, and the large lifetime enhancement in nf and np states observed by Vrakking and Lee.[158] On the basis of Figure 5-13, the dynamics of the g and f states are intimately related. The decrease in f state decay rate comes almost entirely from its interaction with the g state until the point at which this nominal g Stark state meets the high-ℓ manifold and all states converge to some "fully-mixed" average decay rate. In further support of this picture, the decay rate of the h states, not shown, first decreases as the field increases due to interaction with the high-ℓ manifold, before eventually increasing to the value of the average decay rate. The g state acts as an effective barrier between the rapidly predissociating f state and the slowly autoionizing high-ℓ states.

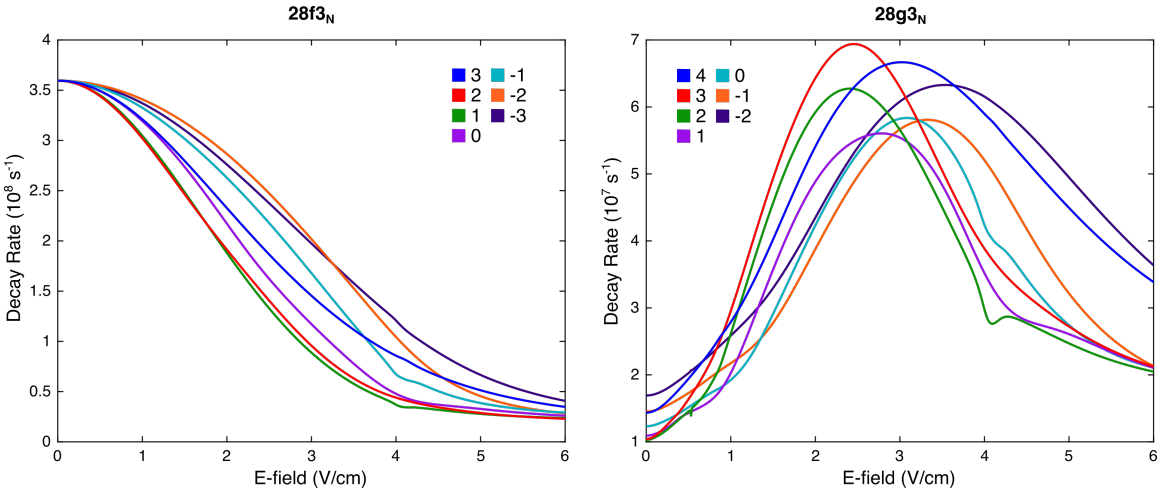

Figure 5-13: Stark-induced decay rates of the members of the $28f3_N$ (left) and $28g3_N$ (right) states as a function of electric field. Note the difference in decay rate scale for the two plots. The colors correspond to the nominal ℓ_R value of each Stark state as indicated in the legend. The details of the calculation are given in the text.

5.5 Autoionization rates

We begin by examining some general results of the long-range autoionization model in order to better interpret the experimental results and compare them with the specific model predictions. The rates of autoionization for the components of the $25g$ complex are plotted in Figure 5-14. For the range of rotational quantum numbers considered, no rotational autoionization channels are open, so vibrational autoionization ($\Delta v = -1$) is the only operative decay mechanism. The ℓ_R labels appear in red (positive Kronig symmetry) and blue (negative Kronig symmetry) and states with the same value of ℓ_R are connected by solid lines. As the high rotation limit is approached, each pair of states with the same $|\ell_R|$ value approach the same rate because, in this limit, ℓ_R is a good quantum number for the projection of ℓ on the rotation axis, and effectively characterizes the interaction of the Rydberg electron with the ion-core. As R increases further, the rates do not approach an R-independent constant value due to two effects. First, more decay channels become energetically allowed at higher R, particularly decay by rotational autoionization, which can be similar to or greater than the vibrational autoionization rate. Second, the multipole moments are R-dependent because the internuclear distance increases as R increases.

This will cause a gradual change in the autoionization rate with R.

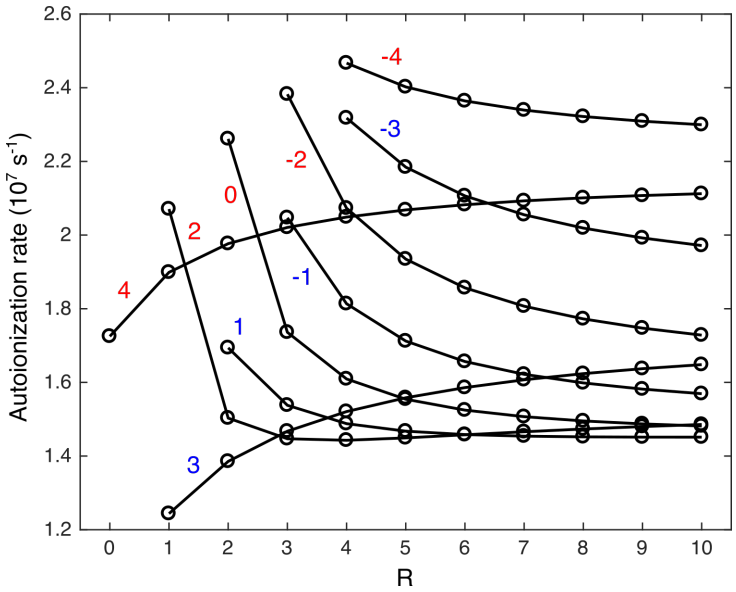

Figure 5-14: Total autoionization rates as a function of R for the $25gR_N$ complex. The rate for the ℓ_R components are labeled on the plot in red (positive Kronig symmetry) and blue (negative Kronig symmetry) numbers and connected by solid lines. The variation with ℓ_R and R is rapid at low R. In the limit of high rotation, the two states with the same value of $|\ell_R|$ approach the same autoionization rate.

It is particularly informative to examine the autoionization rate as a function of ℓ. The rates, summed over all ℓ_R, for each particular electrostatic mechanism of the $25\ell 10_N$ complex are plotted in Figure 5-15. Note that for any given decay channel it is necessary to sum the *amplitudes* of each mechanism's contribution before squaring to find the rate, as dictated by Fermi's golden rule in Equation 5.1. The results plotted in this figure amount to assuming that only one electrostatic mechanism exists for the molecule, and thus they cannot represent a *real* molecule. Nevertheless, this plot allows for insight into the relative strengths of different mechanisms for the low-ℓ and high-ℓ Rydberg states of NO. This is the key insight that explains both the NO results presented here and how our results may be translated to other molecular systems.

At low ℓ, the relative rates vary with the magnitude of the electrostatic parameter part of the full matrix element in Equation 5.2. In other words, the polarizability matrix element, $\langle v=0|\alpha(z)|v=1\rangle$, is larger than the quadrupole matrix element, $\langle v=0|Q(z)|v=1\rangle$, which is larger than that of the dipole, etc., and the autoioniza-

tion rates follow this same order. The dip in all rates for $\ell = 0$ is likely due to both a real effect, the smaller number of allowed decay channels, and a numerical artifact, the generally poorer quality of the numerically generated s hydrogenic wavefunctions. To frame this result more generally, the contribution of each mechanism to the autoionization rate is dictated by the *specific* electric properties of the molecule under investigation.

At high ℓ, the relative rates are ordered by the radial electronic part of the full matrix element, which is the interaction between the continuum and bound electron wavefunctions. In other words, the dipole matrix element has a radial contribution that varies as r^{-2}, the quadrupole matrix element has a r^{-3} radial contribution, the polarizability matrix element has a r^{-4} radial contribution, etc., and the autoionization rates follow this order. As ℓ becomes larger, the dipole dominates the autoionization dynamics because the dipole is the longest range mechanism. In the limit of high-ℓ, the contribution of each mechanism to the autoionization rate is dictated by the *universal* scaling of the radial hydrogenic matrix elements.

At first, this might seem to be a surprising result. The dipole moment of NO^+ is extremely small for a heteronuclear diatomic molecule, and, in all previous treatments of the Rydberg energy level structure of NO, its effect has been entirely neglected without detriment. The key lies in *how* the dipole contributes to the autoionization rate relative to the perturbation of bound states.

First, we consider how perturbations due to the dipole moment will affect a bound Rydberg energy level. As a reminder, this matrix element has the form:

$$\begin{aligned}
&\langle v'R'n'\ell'N'M'|H_{\text{dipole}}|vRn\ell NM\rangle \\
&\quad = -e\,\langle v'R'|\mu(z)|vR\rangle\,\left\langle n'\ell'|r^{-2}|n\ell\right\rangle\,\delta_{N',N}\delta_{M',M}(-1)^{\ell+\ell'+N} \\
&\qquad \times\left[(2\ell'+1)(2\ell+1)(2R'+1)(2R+1)\right]^{1/2} \\
&\qquad \times\begin{Bmatrix} N & R' & \ell' \\ 1 & \ell & R \end{Bmatrix}\begin{pmatrix} \ell' & 1 & \ell \\ 0 & 0 & 0 \end{pmatrix}\begin{pmatrix} R' & 1 & R \\ 0 & 0 & 0 \end{pmatrix}
\end{aligned} \tag{5.26}$$

By examining Equation 5.26, we see that only matrix elements off-diagonal in ℓ are

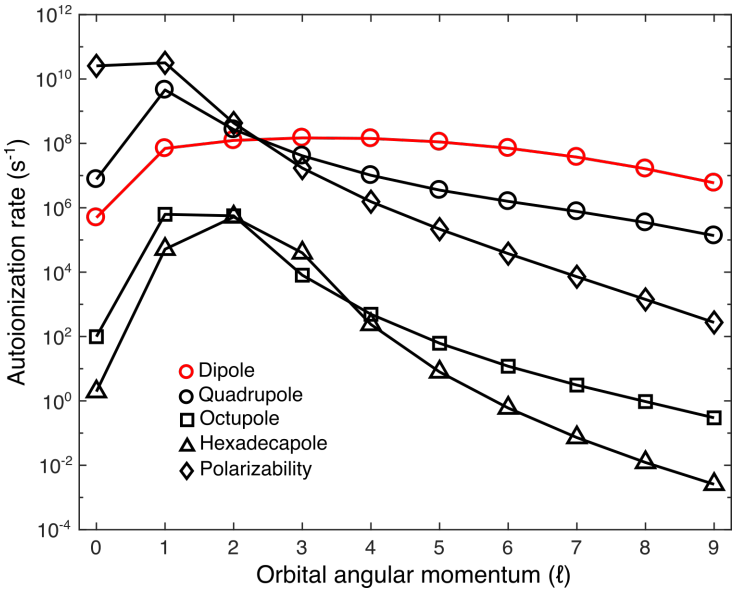

Figure 5-15: Autoionization rates of particular electrostatic mechanisms as a function of ℓ for the $25\ell10_N$ complex. The rates are summed over all ℓ_R components to give a single rate for the complex of states. Note that when more than one mechanism is operative for one decay channel, as is generally the case, the *amplitudes* of each mechanism must be summed. This means that the sum of the rates in this plot will not give the correct total autoionization rate. The relative contributions at low-ℓ vary significantly with ℓ, as the innermost lobe of the wavefunction shifts further away from the ion-core. For states with $\ell \geq 4$ the relative rates are ordered by the power of the involved radial electronic matrix element (r^{-2} for the dipole, r^{-3} for the quadrupole, r^{-4} for the polarizability, etc.). The dipole mechanism is dominant at high-ℓ because it is the longest-range mechanism.

non-zero because of the selection rules imposed by the angular dependence. In addition, the radial matrix element of r^{-2} vanishes for perturbations with $\Delta n = 0$, $\Delta\ell = \pm 1$.[e] Thus, in perturbation theory, the first-order contribution vanishes. Watson showed that, in second-order perturbation theory, the dipole moment contribution is non-zero and has the same quantum number dependence as the quadrupole moment in first order.[159] Within a perturbation theory treatment, then, it is not possible to distinguish between effects due to the quadrupole moment, Q, and the square of the dipole moment, μ^2. In addition, the quadrupole moment of NO^+ is much larger than the dipole moment, so any energy shift caused by the dipole interaction is completely obscured.

In contrast, the autoionization rate is directly related to the perturbation matrix element in Equation 5.2 by Fermi's Golden Rule. This matrix element has the same angular dependence as the bound state matrix element in Equation 5.26, but the radial part is always non-zero. Thus, the dipole moment plays an essential role in the autoionization of all $n\ell$ Rydberg states of NO. The autoionization of high-ℓ Rydberg states is a useful way to observe and, perhaps quantify, the effect of the NO^+ dipole moment.

Figures 5-16, 5-17, and 5-18 show the measured decay rates for several states along with the autoionization rates calculated with our long-range model. The data for the $ng3_4$ state is missing for each value of n because there is no excitation scheme available to excite only this state due to the overlap of the $^0R_1(3)$ and $^0Q_0(3)$ lines in the $4f \leftarrow$ A $^2\Sigma^+$ (1,1) band. The uncertainties in these plots represent the 95% confidence intervals obtained from a fit to the raw data. These experimental and calculated values also appear in Table 5.3. We can make several observations about these data sets. First, the order of magnitude of the *total* decay rate for all measured states agrees with the model predictions for the *autoionization* rates. This strongly distinguishes the ng Rydberg states from the nf states previously studied. With the

[e] A general property of radial hydrogenic functions, $R_{n,\ell}$, is:[131]

$$\left\langle R_{n,\ell'} \left| \frac{1}{r^{\ell+1}} \right| R_{n,\ell+\ell'} \right\rangle = 0$$

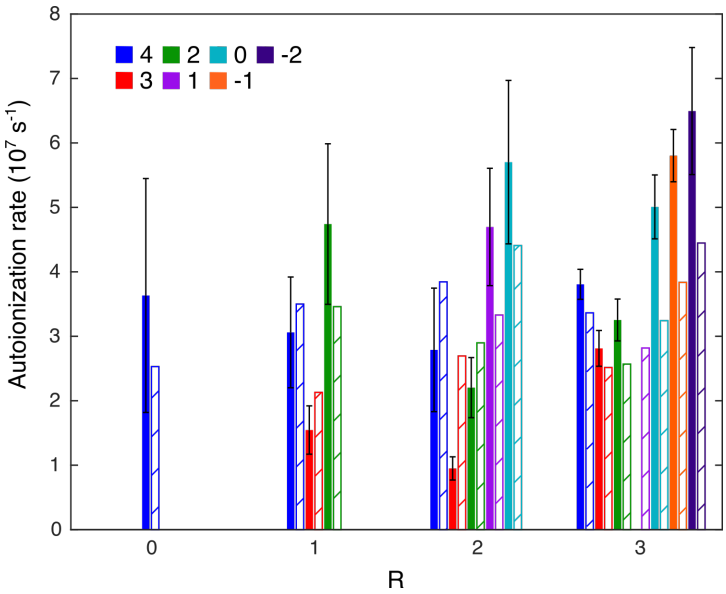

Figure 5-16: Measured (solid) and calculated (hatched) autoionization rates for several $22gR_N$ complexes. Experimental uncertainties are 95% confidence intervals from a fit to the raw data. A dip in the autoionization rate at the center of each complex of states is observed in the experimental and calculated data.

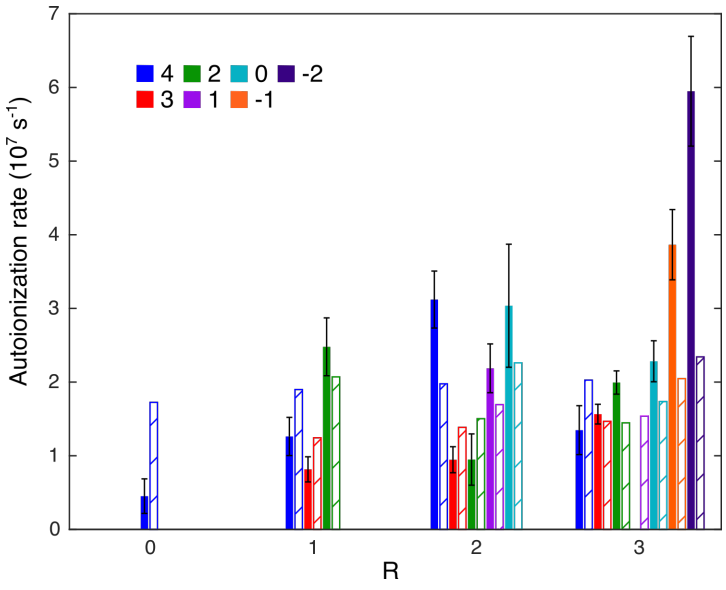

Figure 5-17: Measured (solid) and calculated (hatched) autoionization rates for several $25gR_N$ complexes. Experimental uncertainties are 95% confidence intervals from a fit to the raw data. With the exception of $R = 3$, a dip in the autoionization rate at the center of each complex of states is observed in the experimental and calculated data.

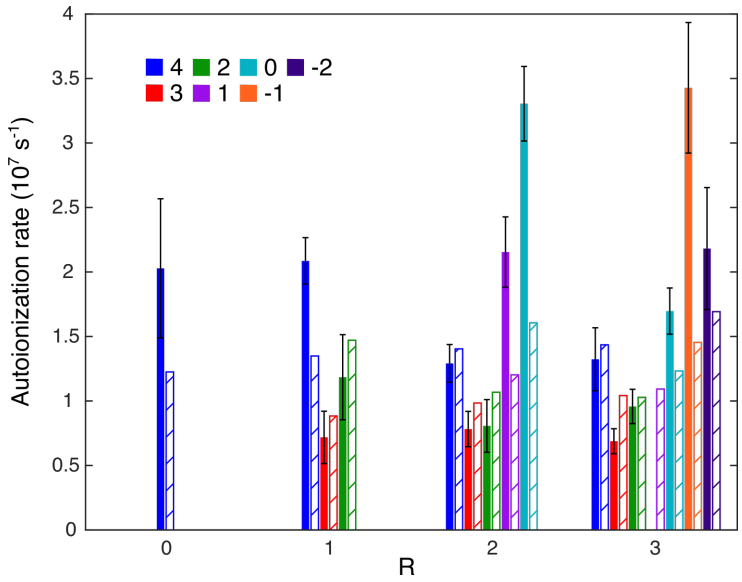

Figure 5-18: Measured (solid) and calculated (hatched) autoionization rates for several $28gR_N$ complexes. Experimental uncertainties are 95% confidence intervals from a fit to the raw data. A dip in the autoionization rate at the center of each complex of states is observed in the experimental and calculated data.

exception of only a few measurements for negative Kronig symmetry states, the total decay rate of nf states is orders of magnitude faster than the long-range model predictions.[15,50] Table 5.2 summarizes the calculated autoionization rates and previously measured decay rates[15] for several nf states. This distinction between the nf and ng decay rates strongly suggests that the ng states are the first Rydberg series in NO in which autoionization, rather than predissociation, is the dominant non-radiative decay mechanism. This agrees with the conclusions of Fujii and Morita,[52] who noted a significant difference between the yields of the predissociation and autoionization decay channels.

Looking at the variation of rates with ℓ_R for each value of R, a trend emerges from the experimental measurements, which qualitatively agrees with the calculation. At the center of the cluster of ℓ_R states, the rate is slower relative to the rates for states with the largest and smallest ℓ_R values. For $R = 1$, the autoionization rate of the $\ell_R = 3$ state is always slower than that of either $\ell_R = 4$ or $\ell_R = 2$. For $R = 2$, the autoionization rates of $\ell_R = 3$ and $\ell_R = 2$ are always slower than that of $\ell_R = 0$, 1, and 4. This trend is only broken in the case of $25g3_N$, shown in Figure 5-17, where

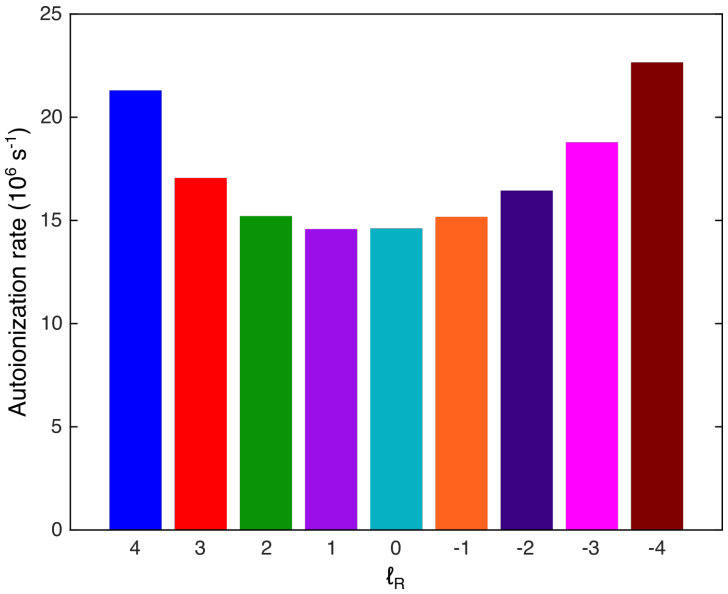

Figure 5-19: Autoionization rates for all ℓ_R components of the $25g25_N$ Rydberg complex. The $|\ell_R| = 4$ states autoionize fastest, and the rate reaches a minimum around $\ell_R = 0$.

the measured $\ell_R = 4$ rate is slower (though with large error bars) than the measured rates of the two lower ℓ_R states.

It is informative to look at the relative rates of a large-R state, for which all ℓ_R components and all possible decay pathways are available. Figure 5-19 shows the calculated rates for $25g25_N$ states, and one recognizes the same, though a more symmetric, pattern of rates. The states with large $|\ell_R|$ values have the fastest autoionization rates, while the rate for the $\ell_R = 0$ state is slowest.

This pattern has a simple and detailed physical interpretation. As exemplified by Figure 5-15, the autoionization of ng states is predominantly determined by the magnitude of the dipole term. In addition, the radial matrix element, $\langle \epsilon\ell | r^{-2} | ng \rangle$, is heavily weighted at small r so we can examine the contributions from the wavefunctions of interest over a small range of r close to zero. The ng bound state wavefunction and the relevant continuum wavefunctions, ϵf and ϵh, are plotted in Figure 5-20. For typical vibrational autoionization energies, $\epsilon \sim 0.01$, the phase shift of the ϵf outgoing waves results in almost perfect destructive interference between the first two lobes of the ϵf wavefunction and the innermost lobe of the ng wavefunction. In con-

trast, the phase shift of the ϵh waves results in near perfect constructive interference between the inner lobes of the ϵh and ng wavefunctions. This fortuitous cancellation for $\epsilon f \sim 25g$ means that we can restrict our attention to the $\Delta\ell = +1$ decay channel. This means that there are only two decay paths with substantial rates: $\Delta R = \pm 1$, $\Delta\ell = +1$ for each ℓ_R value.

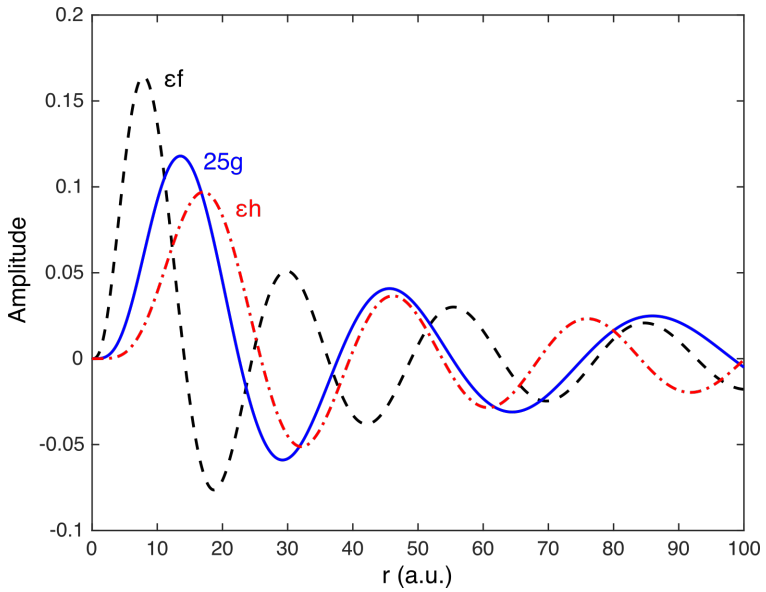

Figure 5-20: Numerical radial hydrogenic wavefunctions for the $25g$ (red, solid) bound state and the ϵf (black, dashed) and ϵh (red, dot-dashed) continuum states, with $\epsilon = 0.01$, representative of the energy for vibrational autoionization.

Within the dipole matrix element of Equation 5.2, the angular dependence of interest is given by the 6j symbol:

$$\begin{Bmatrix} N & R' & \ell' \\ 1 & \ell & R \end{Bmatrix}$$

By plugging relevant values of the quantum numbers into this expression, we find that the value of the 6j symbol is maximum for the $R' = R - 1$ decay channel when $N = R - \ell$ ($\ell_R = -\ell$) and minimum when $N = R + \ell$ ($\ell_R = +\ell$). Similarly, it is maximum for the $R' = R+1$ decay channel when $N = R+\ell$ ($\ell_R = +\ell$) and minimum when $N = R-\ell$ ($\ell_R = -\ell$). Thus, the states with extreme values of ℓ_R have very large autoionization rates in either the $R' = R - 1$ or $R + 1$ channel. These contributions

produce larger total autoionization rates for the $\ell_R = \pm 4$ states, than the sum of the modest rates in both channels for the $\ell_R = 0$ state. Thus, the autoionization rate is smallest for $\ell_R = 0$ and largest for $\ell_R = \pm 4$. At low R, this pattern is quantitatively different due to the presence of fewer states, but the qualitative pattern persists.

Greater insight into the origin of the angular dependence requires a deeper examination of the meaning of the 6j symbol. The angular momentum problem described by a 6j symbol is the coupling of three angular momenta. In the case of these electrostatic perturbation matrix elements, the angular momenta involved are the core rotation, the Rydberg orbital angular momentum, and k, the order of the tensor that describes the electrostatic moment ($k = 1$ for the dipole moment, 2 for the quadrupole moment, etc.). There is ambiguity in this statement, however, because there are two possible ways to couple three angular momenta. Both $\boldsymbol{N} = \boldsymbol{R} + \boldsymbol{\ell}$ and $\boldsymbol{N} = \boldsymbol{R'} + \boldsymbol{\ell'}$ are valid coupling schemes, where $\boldsymbol{R'} = \boldsymbol{R} + \boldsymbol{k}$ and $\boldsymbol{\ell'} = \boldsymbol{\ell} + \boldsymbol{k}$. Since these two coupling schemes must be equivalent, their eigenfunctions, $|R'\ell'N\rangle$ and $|R\ell N\rangle$, must be connected by a unitary transformation:

$$|R'\ell'N'M'\rangle = \sum_R \langle R\ell N|R'\ell'N'\rangle \, |R\ell NM\rangle \, \delta_{N'N}\delta_{M'M} \tag{5.27}$$

where the expansion coefficient, called a *recoupling coefficient*, is the scalar product of the eigenfunctions association with the two angular momentum coupling schemes, and might be thought of as a three angular momenta analog of the Clebsch-Gordan coefficient. Thus, the probability that a system in a state with the coupling scheme $\boldsymbol{N} = \boldsymbol{R} + \boldsymbol{\ell}$ will be found in a state with the coupling scheme $\boldsymbol{N} = \boldsymbol{R'} + \boldsymbol{\ell'}$ is simply the square of the recoupling coeffecient:

$$P = \langle R\ell N|R'\ell'N\rangle^2 = (2R+1)(2\ell'+1) \begin{Bmatrix} R' & k & R \\ \ell & N & \ell' \end{Bmatrix}^2 \tag{5.28}$$

In Equation 5.28, we have made a connection to the 6j symbol, which is written in a modified form, but is equivalent to the one that appears in Equation 5.2. A geometric interpretation of this quantity is possible by considering the vector model

of angular momenta, which is presented in Figure 5-21. The six angular momenta, $\boldsymbol{N}$, $\boldsymbol{R}$, $\boldsymbol{\ell}$, $\boldsymbol{R'}$, $\boldsymbol{\ell'}$, and $\boldsymbol{k}$ form the sides of an irregular tetrahedron with volume:[163]

$$V = \frac{1}{3}\left[\frac{1}{2}(R \times N) \cdot R'\right] \tag{5.29}$$

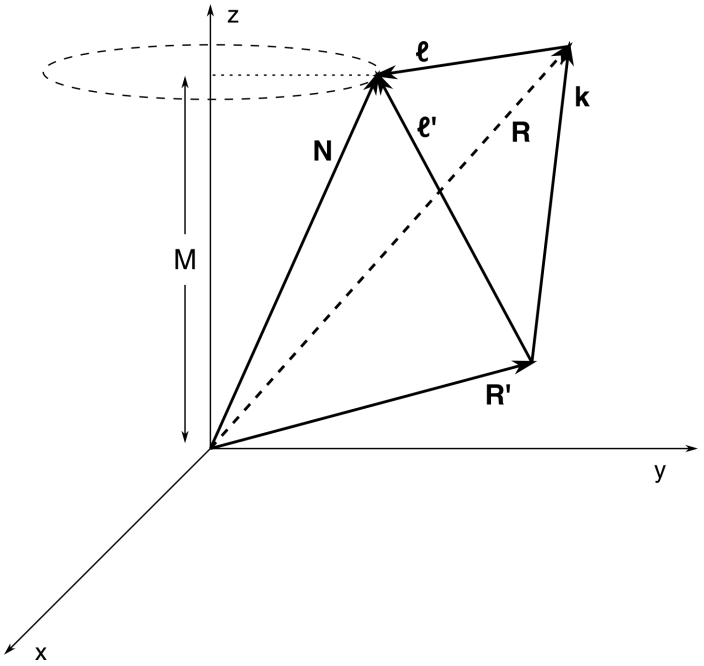

Figure 5-21: Vector model of the 6j symbol that describes the coupling of angular momenta in the bound Rydberg state and free electron-ion state.

We will not walk through the details, but it can be shown that this volume is directly related to the square of the 6j symbol in the (classical) limit of large angular momenta by:[163]

$$\begin{Bmatrix} R' & k & R \\ \ell & N & \ell' \end{Bmatrix}^2 = \frac{1}{24\pi V} \tag{5.30}$$

In the vector model of angular momentum, the trend in the autoionization rates we found above states that the value of the 6j symbol is maximum when the core rotation and Rydberg orbital angular momentum are parallel or anti-parallel to each other in both the initial (R,ℓ) and the final (R',ℓ') state. Our geometric interpretation bears out this fact. In the *classical* limit, this situation describes a tetrahedron with zero volume and a singular value for Equation 5.30. *Quantum mechanically*, the value of

the 6j symbol in this case is finite, but very large. Alternatively, we could state that, because the angular momenta in the inital (R,ℓ) and final (R',ℓ') state all lie along the same axis, the initial state makes the maximum possible projection onto the final state and hence the probability for autoionization into this channel is very large.

Returning to the autoionization data set, we can now focus on where discrepancies with the calculated rates appear. In general, the calculated values appear to underestimate the experimentally determined rates. This becomes clear when looking at the aggregated data plotted in Figure 5-22. The solid line in that figure is a fit to the data and the 95% confidence interval is indicated by the gray shaded area. For reference, the dashed line has a slope that corresponds to perfect agreement between the measurements and calculations. The fitted trend line indicates the measured rates are generally larger than the calculated rates. The slope of this line appears to be strongly affected by the states with the fastest autoionization rates. In particular, the ℓ_R states on the right-hand side of the $R = 2$ and 3 complex of states in Figures 5-16, 5-17, and 5-18 show some of the largest differences between the calculation and experiment. The rates for the states $\ell_R = -1, 0$ for $R = 2$ and $\ell_R = 0, 1, 2$ for $R = 3$ are all underestimated by the calculation. Assuming that the experimental values are accurate, it is challenging to speculate on the source of error in the calculation.

One factor that has already been mentioned is that the phase shift of the outgoing radial wavefunction with respect to the bound Rydberg wavefunction can have a profound effect on the relative rates in each channel. For low-ℓ continuum wavefunctions, there will be a phase shift due to core-penetration, which is entirely ignored in this calculation. This phase shift could lead to either larger or smaller rates in certain channels. In the case of the autoionizing ng Rydberg states, the ϵf continuum wavefunctions will be most important since they are involved in the dipole mechanism. While we would not expect core-penetration to be very significant for $\ell = 3$, an explicit core-penetration term has frequently been used in the literature (and in our fit in Chapter 4) to correctly fit the energies of the nf Rydberg states with significant σ character.[15,39] Thus, core-penetration of the continuum ϵf wavefunctions may not be negligible.

Core-penetration is an explicit physical phenomenon that we have so far neglected. We should also discuss any errors in the quantum chemical calculations of the multipole moments. In particular, the dependence of the dipole moment on internuclear distance has an explicit impact on the relative rates for the $R' = R \pm 1$ decay channels, where the $R' = R + 1$ channel is generally faster than $R' = R - 1$. This difference becomes larger for larger R. This is an important consequence of the specific shape of the dipole moment function and any errors in $\mu(z)$ would affect autoionization in a state-specific manner.

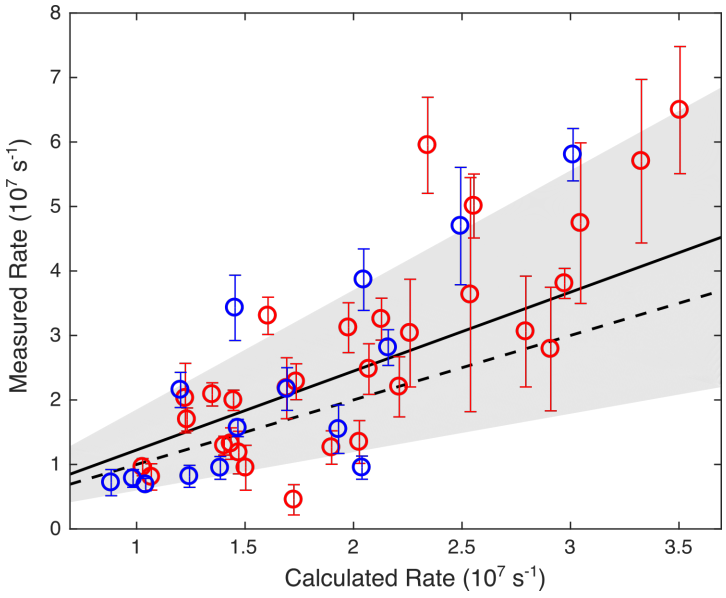

Figure 5-22: All measured ng decay rates plotted against the calculated rates. The dashed line has a slope of 1 and would represent perfect agreement between the measurements and the calculation. The solid line is a proportional fit to the data with fit uncertainty represented by the shaded gray area. As suggested by the plot of individual n states, the calculation generally underestimates the measured rates. Although the calculated rates from our model explain a large fraction of the variance in the data set, there is not quantitative agreement.

In order to further contrast our data for ng states with the observations for nf Rydberg states, it is worthwhile to investigate how the autoionization rate depends on the σ character of the Rydberg state. These high-n, high-ℓ Rydberg states are very well described in a Hund's case (d) basis set. As demonstrated in Chapter 1, the case (d) state can be written in a case (b) basis, where the square of the expansion coefficients are the fractional character of each case (b) basis state. For example, the

case (d) state $ng4_0$ has 100% σ character since no other Λ state can contribute to a state with $N = 0$. Another important distinction between case (d) states is between those with positive and negative Kronig symmetry. For a case (d) Rydberg state, Kronig symmetry is determined entirely by the even-/odd-ness of ℓ and ℓ_R. For ng states, ℓ is even so all even ℓ_R components have positive Kronig symmetry, and all odd components have negative Kronig symmetry. As a result, only even ℓ_R components of an ng state can have any σ character. Similarly, only odd ℓ_R components of an nf state have any σ character.

This type of analysis, based on fractional σ character, was performed by Fujii and Morita[50] on the $7f(v = 1)$ lifetime data collected by Biernacki, Colson, and Eyler.[15] A similar analysis is presented in Figure 5-23. In this data set, the negative Kronig symmetry states (even ℓ_R states) exhibit much slower decay rates than the positive Kronig symmetry states (odd ℓ_R states). The lifetimes of the positive Kronig symmetry states correlate perfectly with the fractional σ character of the Rydberg state. Since predissociation is caused by electronic states with wavefunction amplitude localized near the core, and σ states are the most core-penetrating states, this leads to the conclusion that predissociation is the dominant decay mechanism for nf Rydberg states of NO. The decay rates observed by Biernacki et al.[15] along with our calculated autoionization rates, appear in Table 5.2.

Regarding the decay of ng states, we have already argued that autoionization is the dominant non-radiative decay mechanism. Figure 5-24 shows our measured rates, scaled by n^3 to remove the expected scaling of lifetime with principal quantum number, and plotted against the fractional σ character. We obtain a similar level of agreement as with our long-range calculations, but only for the positive Kronig symmetry states. In contrast to the nf states, the negative Kronig symmetry states have rates which span the same range of rates as the positive Kronig symmetry states.

Table 5.2: Decay rates (experimental and calculated), Kronig symmetry, and fractional σ character of several levels of the $7f$, $12f$, and $15f$ ($v = 1$) complexes. All experimental rates (uncertainties) are reported by Biernacki et al.[15] Some states have been measured by observation of more than one spectroscopic line and are reported one after the other. Calculated rates are from the long-range autoionization model described in the text. The reported σ character is for a pure case (d) basis state. The parenthetical values in that column are from a fit obtained by Anezaki et al.[4] and used in the analysis by Fujii and Morita.[50]

State	Kronig	Expt. Rate (10^9 s^{-1})	Calc. Rate (10^9 s^{-1})	σ character (%)
$7f0_3$	+	33.55 (4.21)	1.49	14.3 (20.5)
$7f1_2$	+	47.06 (3.90)	1.85	25.7 (28.5)
$7f2_1$	+	69.30 (8.80)	2.15	42.9 (44.1)
		83.57 (11.69)		
$7f2_2$	−	5.40 (0.75)	1.40	0.0 (0.0)
$7f2_3$	+	24.06 (1.88)	1.39	19.1 (15.3)
$7f3_0$	+	148.09 (19.92)	2.37	100.0 (100.0)
$7f3_1$	−	4.08 (0.57)	1.98	0.0 (0.0)
$7f3_2$	+	36.25 (5.09)	1.54	26.7 (25.1)
$7f4_1$	+	66.29 (7.60)	2.20	57.1 (55.9)
$7f4_2$	−	7.79 (0.82)	1.75	0.0 (0.0)
$7f4_3$	+	43.17 (2.51)	1.43	23.4 (22.0)
		35.06 (2.07)		
$7f4_4$	−	5.78 (0.63)	1.32	0.0 (0.0)
$7f4_5$	+	29.59 (4.46)	1.29	18.0 (17.1)
$12f0_3$	+	7.41 (1.57)	0.28	14.3
$12f1_2$	+	1.51 (1.89)	0.35	25.7
		1.38 (0.44)		
$12f1_3$	−	0.21 (1.89)	0.19	0.0
$12f1_4$	+	7.29 (2.39)	0.31	19.1
$12f2_1$	+	10.43 (1.89)	0.42	42.9
$12f2_2$	−	0.16 (1.26)	0.26	0.0

Continued on next page

Table 5.2 – continued from previous page

State	Kronig	Expt. Rate (10^9 s^{-1})	Calc. Rate (10^9 s^{-1})	σ character (%)
$12f2_3$	+	7.04 (1.57)	0.27	19.1
$12f3_0$	+	13.63 (1.38)	0.46	100.0
$12f3_2$	+	3.58 (1.95)	0.29	26.7
		3.71 (0.57)		
$12f3_3$	−	0.31 (1.95)	0.25	0.0
$12f3_4$	+	9.24 (1.89)	0.25	18.2
$12f4_1$	+	8.92 (1.26)	0.43	57.1
$12f4_3$	+	4.78 (1.26)	0.27	23.4
$12f5_2$	+	6.47 (2.20)	0.41	47.6
$12f5_3$	−	0.23 (2.51)	0.31	0.0
$12f5_4$	+	6.09 (2.01)	0.26	22.0
$15f0_3$	+	3.27 (1.26)	0.14	14.3
$15f1_2$	+	5.34 (0.69)	0.18	25.7
$15f1_3$	−	0.69 (1.88)	0.10	0.0
$15f1_4$	+	6.16 (2.07)	0.16	19.1
$15f2_1$	+	18.66 (1.45)	0.21	42.9
$15f2_3$	+	3.64 (1.32)	0.14	19.1
$15f3_1$	−	2.20 (0.44)	0.19	0.0
$15f3_2$	+	4.27 (2.01)	0.15	26.7
$15f3_3$	−	0.69 (1.88)	0.13	0.0
$15f3_4$	+	3.14 (1.95)	0.13	18.2
$15f4_1$	+	7.67(1.38)	0.22	57.1
$15f4_3$	+	4.08 (1.38)	0.14	23.4
$15f5_2$	+	10.30 (2.70)	0.21	47.6
$15f5_3$	−	1.45 (2.01)	0.16	0.0
$15f5_4$	+	5.09 (2.07)	0.13	22.0

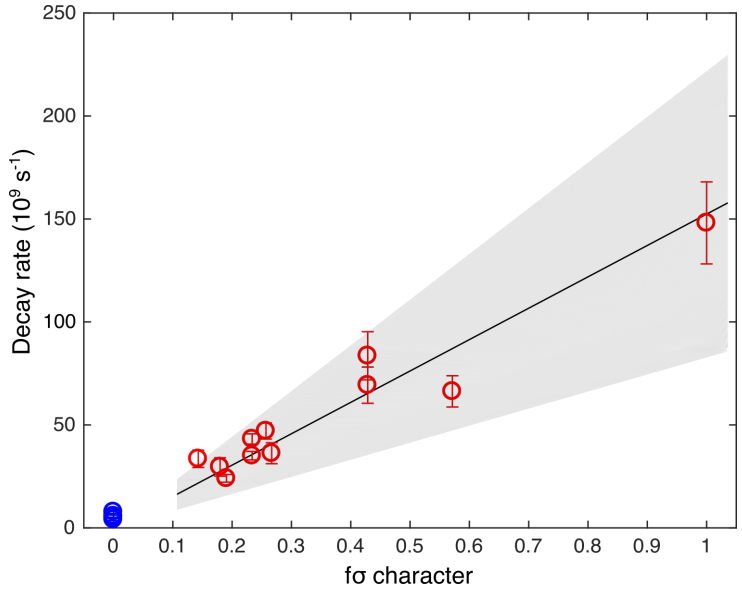

Figure 5-23: Total decay rates of the $7f(v = 1)$ complex measured by Biernacki et al.[15] plotted against the fractional σ character for a case (d) basis state. The negative Kronig symmetry states (blue) are all longer-lived than the positive Kronig symmetry states (red), whose decay rates are directly proportional to the fractional $f\sigma$ character of the state. The solid line is a fit to the positive Kronig symmetry states only, and the gray shaded area represents the fit error.

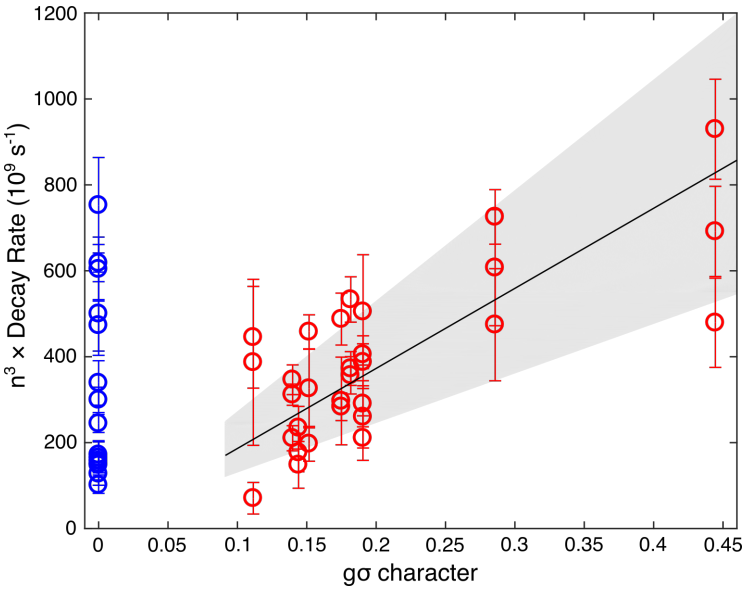

Figure 5-24: Measured decay rates of ng Rydberg states scaled by n^3 versus the fractional σ character of each state.The blue data points are negative Kronig symmetry states, which all have zero σ character by symmetry. The variation of positive Kronig symmetry state decay rates varies with σ character because, within the long-range model, this value is correlated with the angular dependence of the autoionization rates.

If the variation with σ character is not indicative of a decay mechanism, why does this positive correlation exist? If we examine the variation of fractional case (b) character with increasing rotation, we note that, in the limit of high rotation, the $|\ell_R| = 4$ states have maximum σ character, while the $\ell_R = 0$ states have maximum γ ($\Lambda = 4$) character. This is a geometric effect in the classical limit. At high rotation, ℓ_R is a good quantum number that indicates the projection of ℓ on the rotation axis. Thus, $|\ell_R| = 4$ states have $\boldsymbol{\ell}$ aligned along the rotation axis, which means that the projection of $\boldsymbol{\ell}$ on the internuclear axis, Λ, is zero. Similarly, for $\ell_R = 0$, the $\boldsymbol{\ell}$ vector has zero projection on the rotation axis. This means that $\boldsymbol{\ell}$ lies perpendicular to the rotation axis and parallel to the internuclear axis, making the maximum projection, $\Lambda = 4$. At low rotation, we cannot rely on this geometric picture. Instead, we find the low-Λ character to be concentrated in the low N states, since it is necessary that $N \geq \Lambda$. The lowest values of N appear within a complex for the most negative values of ℓ_R. These are exactly the states that we calculate and observe to have the fastest autoionization rates.

Considering this discussion, we speculated that the data will show a positive correlation not only with the fractional σ character, but also with the fractional π character, if the σ character result is simply an artifact of working at low rotation. The same type of plot as Figure 5-24 appears in the four panels of Figure 5-25 for the π, δ, ϕ, and γ characters of the measured states. The measured rates are positively correlated with π character as speculated, and, unlike the σ character, this includes the negative Kronig symmetry states as well. As Λ increases, the correlation gradually gets worse, and fewer of the measured states have non-zero contributions. For ng states we conclude that correlation of the decay rates with Λ is accidental, or more accurately, peculiar to the low rotational states investigated in this work.

For the nf ($v = 1$) data reported in Table 5.2, we examined similar plots of the decay rates as a function of the higher Λ character. There is no obvious correlation with the data, even for the fractional π character. In the case of nf states, the σ character itself has a definite mechanistic impact, as previously suggested. This analysis strongly suggests to us that the long-range autoionization model provides a

more consistent explanation of the ng state data than predissociative decay, and one that will continue to be valid at high rotation.

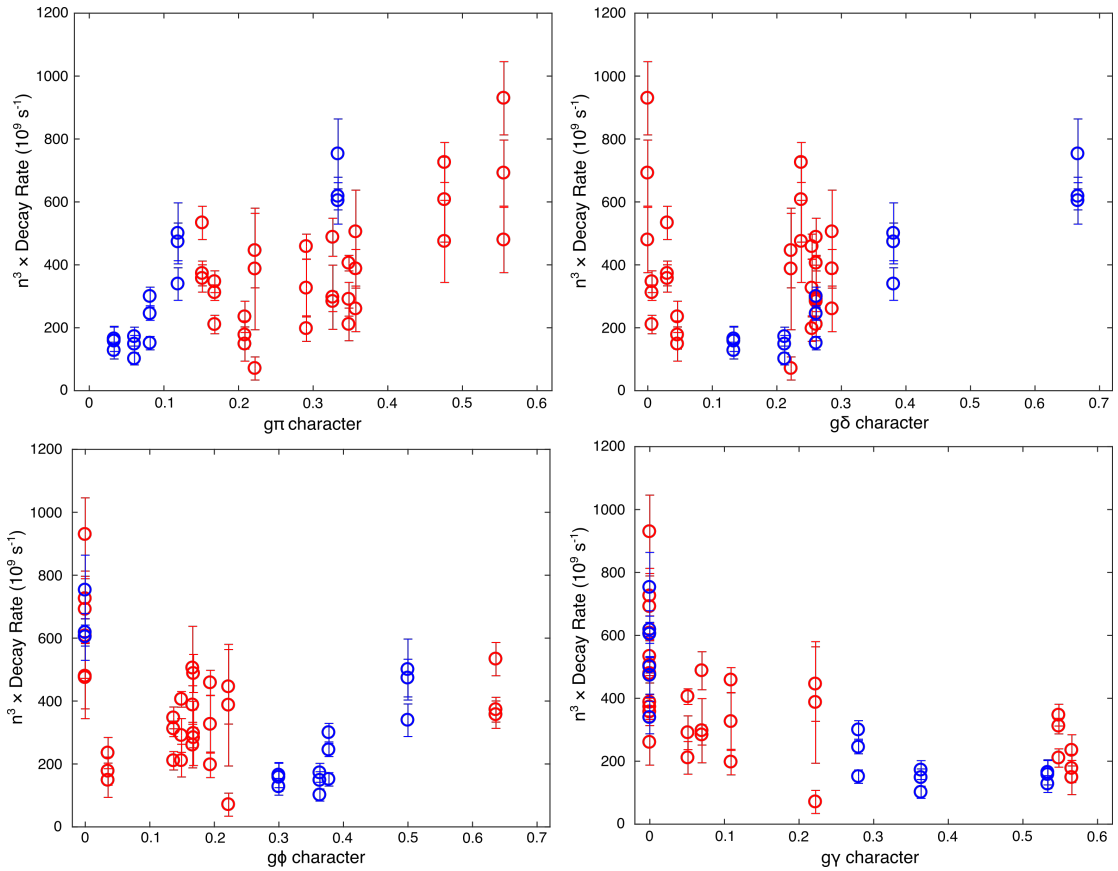

Figure 5-25: Plots of the total measured decay rates, scaled by n^3, against fractional π, δ, ϕ, and γ state character (from left to right, top to bottom). There is strong positive correlation with the data for the $g\pi$ character as for the $g\sigma$ character, but this correlation is gradually lost at higher Λ. This suggests that any correlation with Λ is accidental, or more accurately, peculiar to the low rotational states investigated in this work.

Table 5.3: Decay rates (experimental and calculated) of the $22g$, $25g$, and $28g$ ($v = 1$) states. Experimental errors (95% confidence intervals) are reported in parentheses.

State	Expt. Rate (10^7 s^{-1})	Calc. Rate (10^7 s^{-1})
$22g0_4$	3.63 (1.81)	2.54
$22g1_3$	4.74 (1.25)	3.05
$22g1_4$	1.55 (0.38)	1.83

Continued on next page

Table 5.3 – continued from previous page

State	Expt. Rate (10^7 s^{-1})	Calc. Rate (10^7 s^{-1})
$22g1_5$	3.06 (0.86)	2.79
$22g2_2$	5.70 (1.27)	3.33
$22g2_3$	4.70 (0.91)	2.49
$22g2_4$	2.20 (0.47)	2.21
$22g2_5$	0.95 (0.18)	2.04
$22g2_6$	2.79 (0.96)	2.91
$22g3_1$	6.50 (0.99)	3.51
$22g3_2$	5.80 (0.41)	3.01
$22g3_3$	5.01 (0.50)	2.56
$22g3_4$	···	2.26
$22g3_5$	3.25 (0.33)	2.13
$22g3_6$	2.81 (0.28)	2.16
$22g3_7$	3.81 (0.23)	2.97
$25g0_4$	0.45 (0.24)	1.73
$25g1_3$	2.48 (0.39)	2.07
$25g1_4$	0.82 (0.17)	1.24
$25g1_5$	1.26 (0.26)	1.90
$25g2_2$	3.04 (0.84)	2.26
$25g2_3$	2.19 (0.33)	1.69
$25g2_4$	0.95 (0.35)	1.50
$25g2_5$	0.95 (0.18)	1.39
$25g2_6$	3.12 (0.39)	1.98
$25g3_1$	5.95 (0.75)	2.34
$25g3_2$	3.87 (0.48)	2.05
$25g3_3$	2.28 (0.28)	1.74
$25g3_4$	···	1.54
$25g3_5$	1.99 (0.16)	1.45

Continued on next page

Table 5.3 – continued from previous page

State	Expt. Rate (10^7 s^{-1})	Calc. Rate (10^7 s^{-1})
$25g3_6$	1.57 (0.13)	1.47
$25g3_7$	1.35 (0.33)	2.03
$28g0_4$	2.03 (0.54)	1.23
$28g1_3$	1.18 (0.29)	1.47
$28g1_4$	0.72 (0.20)	0.88
$28g1_5$	2.09 (0.18)	1.35
$28g2_2$	3.30 (0.29)	1.61
$28g2_3$	2.16 (0.27)	1.20
$28g2_4$	0.81 (0.20)	1.07
$28g2_5$	0.78 (0.14)	0.98
$28g2_6$	1.29 (0.15)	1.40
$28g3_1$	2.18 (0.47)	1.69
$28g3_2$	3.43 (0.51)	1.45
$28g3_3$	1.70 (0.18)	1.23
$28g3_4$	···	1.09
$28g3_5$	0.96 (0.13)	1.03
$28g3_6$	0.69 (0.10)	1.04
$28g3_7$	1.32 (0.24)	1.44

5.6 Ion rotational state distributions

5.6.1 nf states

One significant source of motivation for this work on the autoionization dynamics of NO comes from an important set of experiments performed by Park and Zare.[117,118] Their experiment observed rotationally resolved photoelectron spectra resulting from

vibrational autoionization of ns, np, and nf Rydberg states of NO. Using two dye lasers, Rydberg states were populated by double resonance *via* a single rotational level of the A $^2\Sigma^+$ state. The selected Rydberg state decayed by vibrational autoionization in an electric and magnetic field-free region. The electrons produced by this process, which are ejected orthogonal to both the laser and molecular beam propagation directions, were detected after a 50 cm field-free flight, on an MCP. By using a heated nozzle, very high rotational quantum numbers ($17<R<21$) were accessed. This was essential in order to populate ion rotational states with an energy spacing larger than the energy resolution of the photoelectron spectrometer.

For nearly all states investigated, a wide range of final ion rotational states were observed, indicating extensive angular momentum exchange between the ion-core and the Rydberg electron in the vibrational autoionization process. In Figure 5-26, we reproduce several representative examples of the observed spectra for nf states. At the time of these experiments, this was an astounding result for several reasons. First, in all MQDT treatments of autoionization, the ejected electron was assumed to have the same ℓ value as the initial Rydberg state.[80,128,129] Second, the only other experiment of its kind was performed on singlet np states of H_2 and the observed ion rotational state distributions were entirely consistent with the production of *only* ϵp partial waves by autoionization.[125] Third, the appearance of both even and odd partial waves from the autoionization of ns, np, and nf states suggested a mixing of odd and even angular momenta that was not evident in any previous spectra of bound NO Rydberg states.[15,48] Indeed, it was firmly accepted that the dipole moment of NO^+ was too small to induce significant state mixing, and moreover many discussions of the electronic structure of NO relied on the preservation of pseudo-u/g symmetry in this "near homonuclear" molecule.[103] Finally, it seems to fly in the face of our classical intuition that sufficient angular momentum could be exchanged between a light electron and the much heavier nuclear framework to induce large changes in the rotational state of the NO^+ ion.

These upended expectations, in combination with the known strong predissociation of all NO Rydberg states with $\ell \leq 3$, suggested to the authors and others

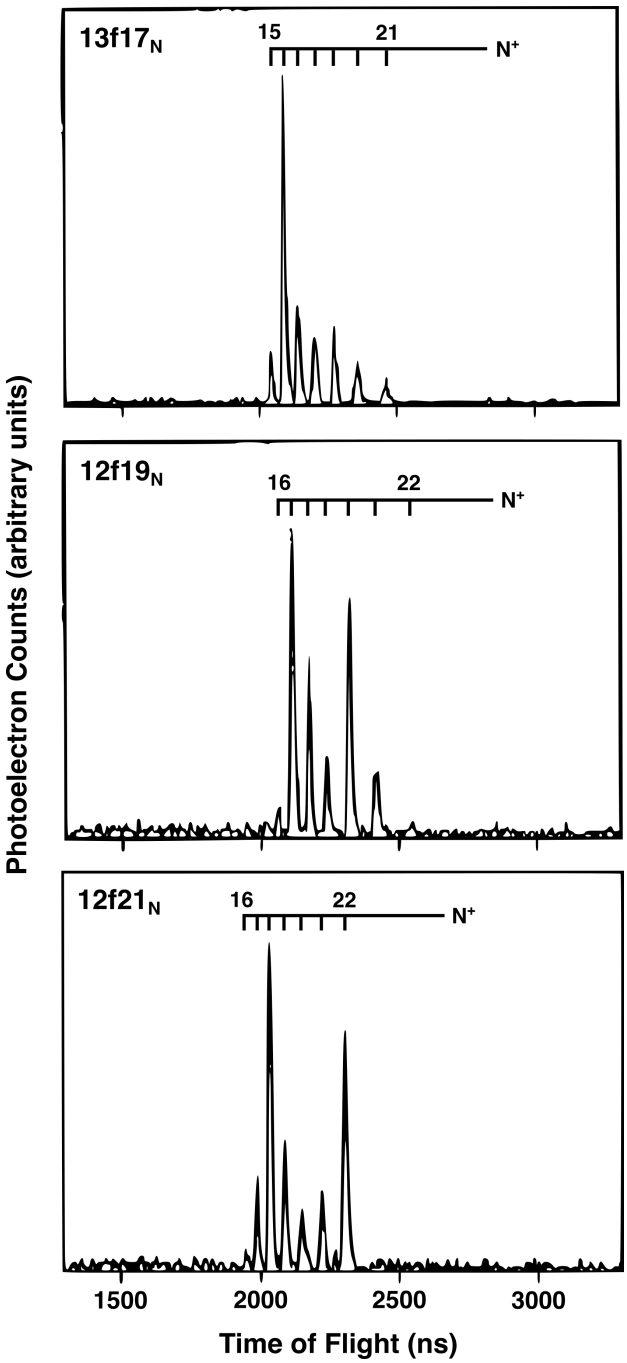

Figure 5-26: Angle- and energy-resolved photoelectron spectra measured by Park and Zare[117,118] following vibrational autoionization of the indicated nfR_N states, where the $N = 18$, 19, and 20 components are unresolved by the excitation laser. The time of flight axis is calibrated in order to associate a particular N^+ value of the resulting ion with each photoelectron peak, indicated by the comb at the top of each plot. Top, Center: Reprinted from H. Park and R. N. Zare, *J. Chem. Phys.*, **106**, 2239 (1997), with the permission of AIP Publishing. Bottom: Reprinted figure with permission from H. Park, D. J. Leahy, and R. N. Zare, *Phys. Rev. Lett.*, **76**, 1591-1594 (1996). Copyright 1996 by the American Physical Society.

that an indirect electronic interaction with predissociating states was an important mechanism in the autoionization process.[117,118,124] Two valence states known to be important in the predissociation of NO are the I $^2\Sigma^+$ and A$'$ $^2\Sigma^+$ states, which possess nearly pure gerade and ungerade symmetry, respectively.[103] However, these states are known to interact with each other in low-lying vibrational levels of the I state, and the observation of predissociation products indicates that both states are directly or indirectly involved in the predissociation of low-ℓ Rydberg states.[49] Thus, in the predissociation-mediated mechanism, the autoionizing Rydberg states first interact with the predissociation continua, where the required u/g mixing occurs. A second interaction with the ionization continua occus, which results in production of the free ion and an electron in many even and odd ℓ partial waves. While such a mechanism could explain the Park and Zare observations,[117,118] the complexity of such a proposed multi-state interaction has frustrated formulation of a thorough theoretical treatment.[124] In our work, while we have not attained a complete accounting of the results of Park and Zare,[117,118] we propose that long-range electrostatic autoionization plays an important role in the dynamics of nf states and does explain most of the decay channels observed by Park and Zare.[117,118]

Before examining the results of our long-range electrostatic autoionization model, we will examine in detail the experimental results. It is important to note that, in Park and Zare's experiments, the laser bandwidth made it impossible to resolve individual ℓ_R components of the nf states investigated, so all observed photoelectron spectra are the result of autoionization from three levels within a Rydberg complex. When exciting the $\ell_R = 1$, 2, and 3 components of a Rydberg complex, as in the top panel of Figure 5-26, there is an intense $N^+ = R-1$ peak and weaker peaks extending from $N^+ = R$ to $N^+ = R+4$. In addition, a weak $N^+ = R-2$ peak was also observed in this example. There is a roughly inverse pattern observed for the $\ell_R = -1$, -2, and -3 states in the bottom panel of Figure 5-26. An intense peak appears at $N^+ = R+1$ and peaks are observed all the way down to $N^+ = R-4$. The intensity pattern is different from the $\ell_R = 1$, 2, and 3 result, however, and the $N^+ = R-3$ peak appears as the most intense feature in the spectrum. A quite different pattern is observed for

the $\ell_R = -1$, 0, and 1 states in the middle panel of Figure 5-26. The strong peaks range from $N^+ = R - 2$ up to $N^+ = R + 2$. This more symmetric distribution of ion rotational states for the $\ell_R = -1$, 0, and 1 components suggests to us that the angular momentum is not completely scrambled in the autoionization process, as might be suggested by a predissociation-induced mechanism.

A few years later, the Zare group extended this work by measuring photoelectron spectra from autoionizing $v = 2$ Rydberg states.[164] In this second set of experiments, circular dichroism was used to verify the purity of states prepared by each excitation scheme. This allowed for measurement of nearly pure $\ell_R = -3$ and 3 states. Three representative photoelectron spectra from the thesis of Runchuan Zhao[164] are reproduced in Figure 5-27. The solid and dashed lines in every plot are the spectra collected at two different observation angles. We will not discuss the photoelectron angular distributions in any detail. The top and bottom spectra result from selective excitation of the $\ell_R = 3$ and $\ell_R = -3$ states, respectively. The resulting $v^+ = 1$ ion rotational state distributions ($\Delta v = -1$) show striking similarities to the earlier results in the top and bottom panels of Figure 5-26. For the top (bottom) spectrum, the $N^+ = R - 1$ ($N^+ = R + 1$) peak is very intense, followed by a strong $N^+ = R$ ($N^+ = R$) peak and then weaker peaks extending out to $N^+ = R + 4$ ($N^+ = R - 4$). Again, the intensity patterns in the two spectra are not exactly inverted, but there exists an even more obvious symmetry than in the Park and Zare data[117,118] of Figure 5-26. The center plot of Figure 5-27 is the result of exciting $N = 15$, 16, and 17 ($\ell_R = -1$, 0, and 1) components of the $13f16_N(v = 2)$ state and thus represents an almost identical experiment to that shown in the center plot of Figure 5-26. The symmetry of this distribution is also more striking than in the earlier work: a weak $N^+ = R$ peak appears surrounded by intense $N^+ = R - 2, R - 1, R + 1$, and $R + 2$ peaks.

$\Delta v = -1$ decay

The first insight that a long-range electrostatic mechanism alone can produce many partial waves and many ion rotational states for the nf Rydberg states comes

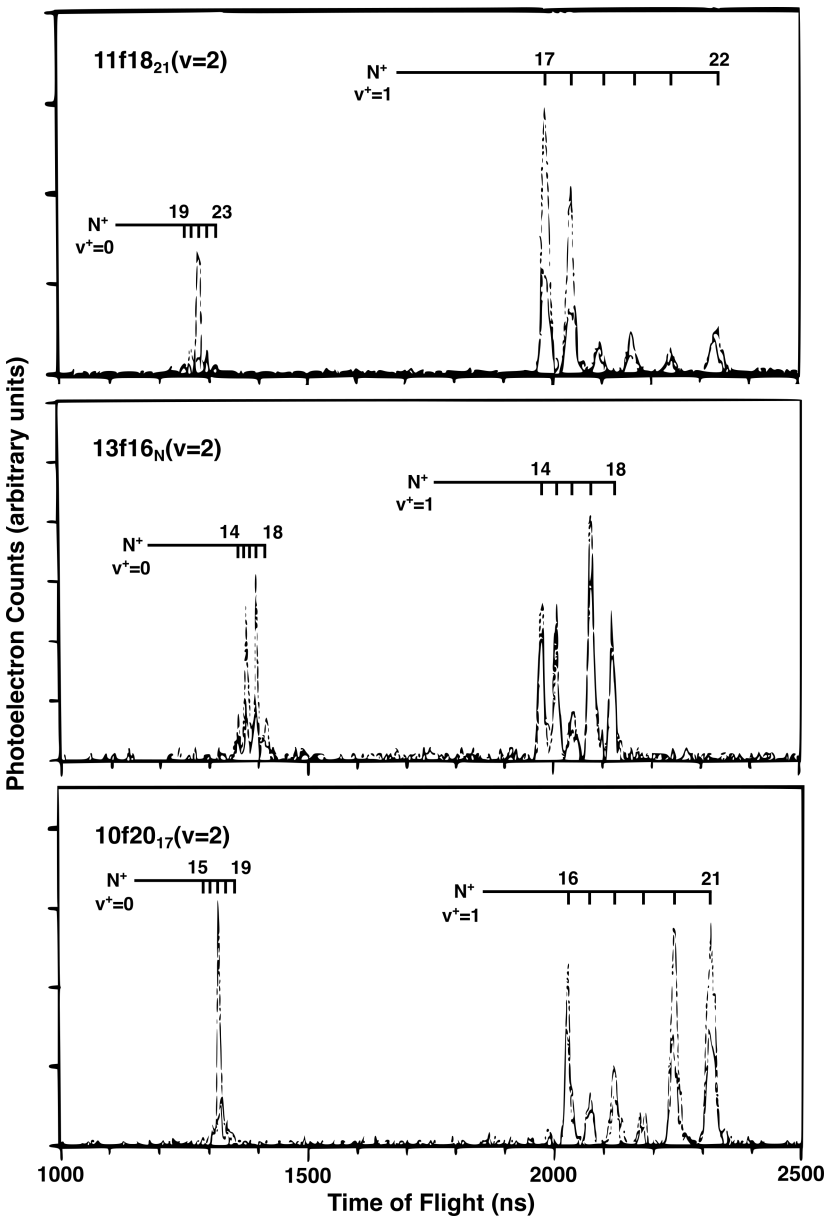

Figure 5-27: Angle- and energy-resolved photoelectron spectra measured by Zhao[164] following vibrational autoionization of the indicated nfR_N states. The time of flight axis is calibrated in order to associate a particular N^+ and v^+ value of the resulting ion with each photoelectron peak, indicated by the comb at the top of each plot. The dashed and solid line spectra in each plot are collected at two different angles. The top and bottom plots are the results for the single ℓ_R component that was selectively excited. In both of those plots, the intense peak at the center of the $v^+ = 1$ signal is an artifact and not a product of the nf state autoionization. The center plot shows the autoionization products following excitation of the $N = 15$, 16, and 17 components of the $13f16_N$ complex. Reproduced with permission from Zhao, R. *Vibrational autoionization from nf Rydberg states of nitric oxide*, PhD thesis, Stanford University, 2004. Copyright 2004 by Runchuan Zhao.

from Figure 5-15. At high-ℓ, the dipole mechanism dominates all other autoionization processes. At $\ell = 3$, however, the dipole, quadrupole, and dipole polarizability all make similar contributions to the total autoionization rate. Thus, we might expect that all even and odd changes of rotation, $R - N^+$, up to ± 2 should be of similar intensity.

In Figure 5-28, we have plotted the rotational state distribution calculated by our long-range model for the same states investigated by Park and Zare that appear in Figure 5-26. In Figure 5-29, we have plotted the calculated rotational state distributions for the states investigated by Zhao that are shown in Figure 5-27. When comparing the experimental data to the calculations it is important to note two things. First, the experimental results are angle-resolved, which means only the photoelectrons ejected at a specified angle relative to the laser polarization direction were detected. Since the photoelectron angular distribution can be different depending on the particular partial wave, these results are not the same as the angle-integrated photoelectron spectrum and do *not* represent the total rotational state distribution. Second, as mentioned previously, not every experiment was able to resolve the individual ℓ_R levels of the nf complexes investigated. While we could scale our calculated distributions by the relative intensities of the P, Q, and R branches in the excitation scheme, we chose to simply plot the results for an equal distribution of population in the three ℓ_R levels, since the exact intensity distributions cannot be directly compared.

We begin the discussion with the results for the $\ell_R = -1$, 0, and 1 states, which appear in the center plots of Figures 5-28 and 5-29. The relevant experimental results are in the center plots of Figures 5-26 and 5-27. The calculation predicts non-negligible intensity in all five rotational states, $N^+ = R - 2$ to $N^+ = R + 2$, observed in both sets of experiments. The agreement with Zhao's results are particularly striking. One curious feature in the calculated and experimentally observed distributions for these states is the weak intensity of the $N^+ = R$ peak relative to the intensities of the other significant peaks. This is a result of interference between the quadrupole and polarizability mechanisms in the autoionization. Both mechanisms have approximately equal magnitudes for all decay channels of the nf states. In general, the two mech-

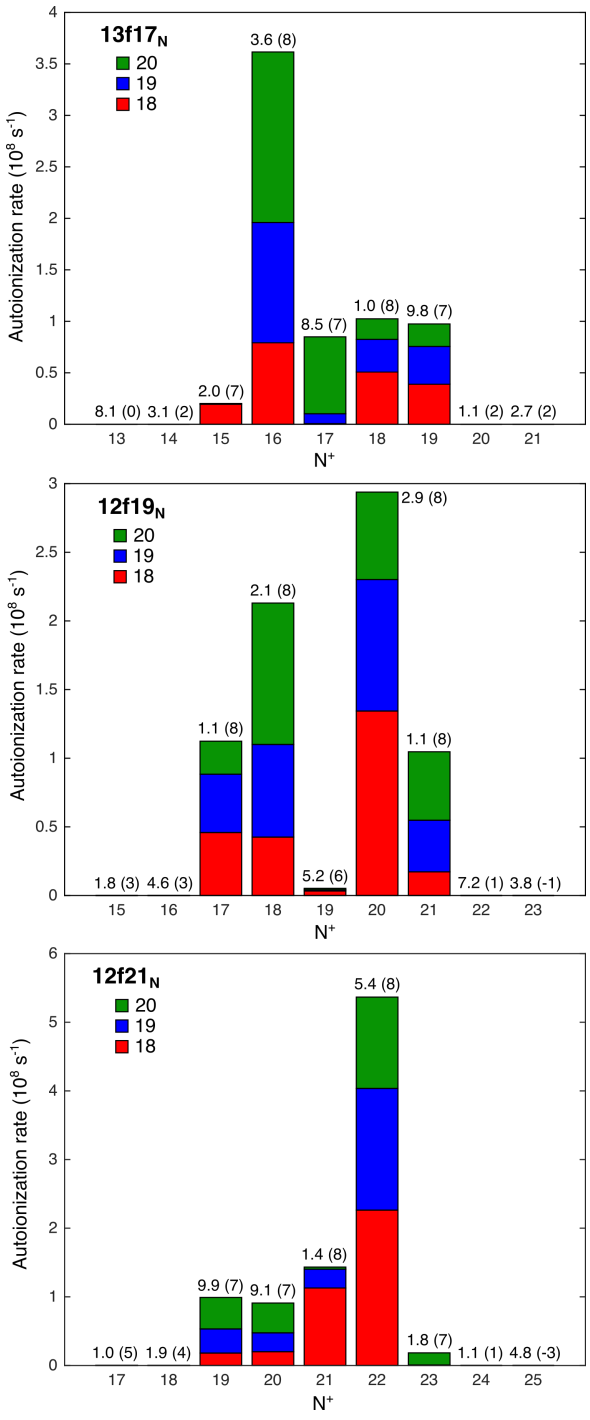

Figure 5-28: Total rotational N^+ distributions of the NO^+ ion following vibrational autoionization of the indicated nfR_N states. The rates for each autoionization N^+ channel are summed for the three contributing states, $N = 18$, 19, and 20. Above each bar is the total autoionization rate, where the number in parentheses indicates the order of magnitude.

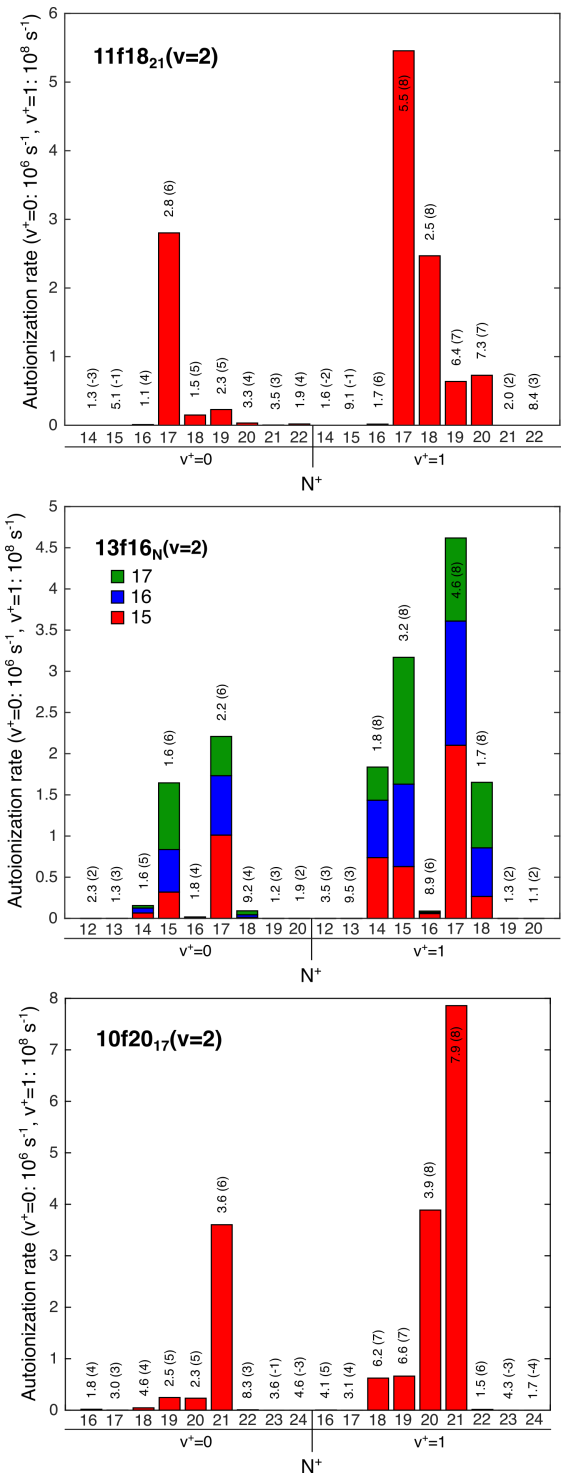

Figure 5-29: Total rotational N^+ distributions of the NO^+ ion produced following vibrational autoionization of the indicated nfR_N states into both $v^+ = 0$ and $v^+ = 1$ channels. Note that the scales of the two vibrational channels differ by two orders of magnitude. The top and bottom plots are for a single ℓ_R component, while the center plot is the sum of the three indicated states. Above each bar is the total autoionization rate, where the number in parentheses indicates the order of magnitude.

anisms constructively interfere because the polarizabilities and quadrupole moment have similar magnitudes and monotonically increase with internuclear distance in the region near the equilibrium internuclear distance, and because the quadrupole mechanism has the same angular dependence as the anisotropic polarizability. However, for the $\Delta R = 0$, $\Delta \ell = 0$ channel, the isotropic polarizability, which lacks any angular dependence, also contributes to the polarizability matrix element. This is the basis for how the polarizability and quadrupole terms can end up with opposite signs and destructively interfere. This destructive interference is most significant for the nf components with ℓ_R values close to zero.

Looking at the results for the $\ell_R = 1$, 2, and 3 states in the top panel of Figure 5-28, several features resemble the experimental results in the top panel of Figure 5-26. In both spectra, the $N^+ = R - 1$ peak is the dominant feature. This is followed by weaker peaks for $N^+ = R, R + 1$, and $R + 2$, all of similar intensity. In addition, there is a much weaker peak at $N^+ = R - 2$ in both the calculation and experiment. Obviously missing from the calculated distribution are peaks with significant intensity at $N^+ = R + 3$ and $N^+ = R + 4$. These two channels only have contributions from the octupole and hexadecapole moments, respectively, which, according to Figure 5-15, are substantially weaker than the polarizability, dipole, and quadrupole mechanisms. As a result, those channels have autoionization rates that are many orders of magnitude slower and hence will not result in a significant yield of ions in those rotational states.

The absence of the $N^+ = R + 3$ and $N^+ = R + 4$ peaks is not an indication that the long-range electrostatic model is fundamentally incapable of describing these ion state distributions. Although we have included high-order multipole moments in our model, we have completely neglected higher-order polarizabilities of the ion-core. The dipole-quadrupole polarizability, $A_{\gamma,\alpha\beta}$, could produce odd-valued changes in the rotational quantum number, while the quadrupole polarizability, $C_{\alpha\beta,\gamma\delta}$, could produce even-valued rotation changes. These are the next two terms that result from second order perturbation theory applied to the multipole expansion. The higher-order (non-linear) polarizabilities are obtained by third and fourth order perturbation the-

ory. Applied to the dipole moment, the first hyperpolarizability (dipole-dipole-dipole polarizability), $\beta_{\alpha\beta\gamma}$, produces odd rotational changes, and the second hyperpolarizability (dipole-dipole-dipole-dipole polarizability), $\gamma_{\alpha\beta\gamma\delta}$, produces even changes. All of these higher-order polarizabilities have shorter range radial matrix elements, but if the magnitude of the vibrationally averaged polarizability is sufficiently large, they may be responsible for a significant effect for $\ell \leq 3$ Rydberg states. For example, Figure 5-15 shows that, for low ℓ, the polarizability, which has a r^{-4} radial matrix element, has a larger contribution to the rate than the quadrupole moment, which has a r^{-3} radial matrix element. Consideration of these higher-order effects will be the next step in this work.

In addition to the possibility that other electrostatic properties produce peaks with large $N^+ - R$ changes, there is also the possibility that low-ℓ partial waves contribute more intensity than predicted by our model. The matrix elements that produce the largest changes in the core rotation can also produce the largest changes in orbital angular momentum. For example, the $N^+ = R - 3$, $\Delta\ell = -3$ channel produces a ϵs partial wave *via* autoionization of an initial nf state. There is reason to believe our calculation of the rates in these channels is inaccurate. The current model uses purely hydrogenic continuum wavefunctions, and completely neglects any phase shift due to the finite size of the ion-core or close-range interactions with the core. While this assumption is justified for high-ℓ states, low-ℓ states will be significantly impacted. Consideration of $\epsilon\ell$ phase shifts for low-ℓ partial waves is a second avenue for future work that may lead to more accurate predictions.

A final possibility is the presence of a predissociation-mediated mechanism, as suggested by several authors.[117,118,124] The agreement between the experiments and our calculation for the $\ell_R = -1$, 0, and 1 results suggest that these ℓ_R components decay mainly by long-range mechanisms. This means that the $N^+ = R + 3$ and $N^+ = R + 4$ peaks observed in the top panel of Figure 5-26 are produced by either the $\ell_R = 2$ or 3 components. The change in the relative intensities of the $N^+ = R+3$ and $N^+ = R + 4$ peaks between the top panel of Figure 5-26 ($\ell_R = 1$, 2, and 3) and the top panel of Figure 5-27 ($\ell_R = 3$) suggests that these peaks may be produced

mainly by the $\ell_R = 3$ component. In the high rotation limit, the $\ell_R = 3$ state has the largest fractional σ character. As a result, this state likely interacts most strongly with the valence states responsible for predissociation. Thus, the $\ell_R = 3$ component of an nf complex may report in a unique way on the influence of a predissociation-mediated autoionization mechanism. This state-specific hypothesis simplifies the number of Rydberg-valence state interactions that would need to be included in a more sophisticated multi-state model of predissociation. This additional autoionization mechanism should be considered in future work.

Examination of the $\ell_R = -1$, -2, and -3 states in the bottom panel of Figure 5-28 show that the calculation agrees with the experimental results in the bottom panel of Figure 5-26 in the same ways as for the $\ell_R = 1$, 2, and 3 states. An intense $N^+ = R + 1$ peak and weaker $N^+ = R$, $R - 1$, and $R - 2$ peaks appear in both the calculation and the experiment. As before, the peaks with large changes in rotation, $N^+ = R - 3$ and $N^+ = R - 4$, are not captured by the calculation. It may be worth noting that the rates for those channels in the calculation are orders of magnitude larger than those for the channels with opposite sign changes, $N^+ = R + 3$ and $N^+ = R+4$. This may suggest that the mechanism that produces these large changes in rotation obeys the same angular momentum coupling as the existing octupole and hexadecapole mechanisms. We interpret this as a further impetus for the need to consider higher-order extensions to our model in any future work.

The isolated $\ell_R = 3$ and $\ell_R = -3$ states investigated by Zhao[164] in the top and bottom panels of Figure 5-27 show distributions similar to the unresolved results of Park and Zare.[117,118] The absence of a $N^+ = R-1$ ($N^+ = R+1$) peak in the spectra from Zhao relative to the spectra from Park and Zare is an important difference, which is reproduced by our calculation in the top and bottom panels of Figure 5-29. This occurs because Zhao's experiment populated single $\ell_R = 3$ ($\ell_R = -3$) states, while the Park and Zare experiment also populated the $\ell_R = 1$ ($\ell_R = -1$) component. These states produce the $N^+ = R - 1$ ($N^+ = R + 1$) peaks, which are shown in red (green) in the top (bottom) panel of Figure 5-28. Zhao also observes large rotational changes, $N^+ - R = \pm 3$ and ± 4, which are orders of magnitude weaker in our calculation than

in the experiment. Once again, we note that the channels with the correct sign change in rotation are orders of magnitude faster than the channels with the opposite sign change.

$\Delta v = -2$ decay

In addition to $\Delta v = -1$, the $\Delta v = -2$ channel is also open for the $v = 2$ Rydberg states investigated by Zhao.[164] These ion states appear at earlier times (higher energies) in all three panels of Figure 5-27. They are slightly more challenging to interpret for a few reasons. First, the resolution of the time-of-flight photoelectron spectrometer is inversely related to the kinetic energy of the photoelectrons. Thus, the $v^+ = 0$ rotational peaks are incompletely resolved in this spectrum. Second, the very intense peak at the center of the $v^+ = 0$ distributions in the top and bottom panels was found by Zhao to be insensitive to laser detuning and so is unlikely to result from autoionization of the nf states.[164] This suggests that some type of additional perturbation may be at work in this decay channel, or additional states are unintentionally populated during the preparation of the desired nf states.

Nevertheless, we will summarize some of the observations for this ionization channel. As in the $v^+ = 1$ distribution, there appears to be interesting symmetry. For $\ell_R = 3$, the ion rotational states have roughly similar intensity for $N^+ = R+1$ through $N^+ = R + 5$, and, for $\ell_R = -3$, the distribution spans $N^+ = R - 1$ to $N^+ = R - 5$ with roughly equal intensities. For the center plot of Figure 5-27, it is clear that the $v^+ = 0$ rotational distribution is quite similar to the $v^+ = 1$ rotational distribution. There are very intense $N^+ = R + 1$ and $N^+ = R - 1$ peaks, weaker $N^+ = R + 2$ and $N^+ = R - 2$ peaks, and a very weak $N^+ = R$ peak.

For the $\ell_R = -1$, 0, and 1 result, our calculated distribution of ion rotational states in the center panel of Figure 5-29 agree with the observation in the center panel of Figure 5-27. As in the $\Delta v = -1$ channel, the $N^+ = R$ channel is weak due to an interference between the quadrupole moment and polarizability. One discrepancy between our calculation and the results of Zhao is the very intense $\Delta v = -2$ decay observed in the experiments. As discussed at the beginning of this chapter, the $\Delta v =$

-2 decay is generally expected to be much slower than the $\Delta v = -1$ decay. In our calculations, this expectation is borne out and the decay rates differ by approximately two orders of magnitude. The intensity of the $v^+ = 0$ peaks relative to the $v^+ = 1$ peaks suggest that there is at most a one order of magnitude $v^+ = 0$ vs. $v^+ = 1$ difference in the experiment. We have no explanation for this discrepancy.

We look next at the results of the $\Delta v = -2$ channel for the $\ell_R = 3$ and -3 states in the top and bottom panels of Figure 5-29, respectively. Unlike the $\ell_R = -1$, 0, and 1 experimental result of Zhao, the intensity of these $\Delta v = -2$ channels is about 1% of the $\Delta v = -1$ channels, in agreement with the calculation and our intuition. The $v^+ = 0$ channel distributions measured by Zhao are substantially different than any distribution described so far. A wide range of rotational states is populated with minimal variation in intensity. In contrast, our calculation suggests that the $v^+ = 0$ distribution should be very similar to the $v^+ = 1$ distribution. One difference is the relative strength of the channels for large rotational changes. In the upper (lower) panel of Figure 5-29, the $N^+ = R + 4$ ($N^+ = R - 4$) channel has the same order of magnitude as the $N^+ = R + 2$ ($N^+ = R - 2$) channel. This is never the case in our calculation for $\Delta v = -1$ decay. The other significant discrepancy is the appearance of $N^+ = R + 5$ and $N^+ = R - 5$ peaks in the experimental results. Our calculation cannot produce such large changes in rotation. Consideration of higher-order multipole moments and polarizabilities would be required to obtain any amplitude in this decay channel.

This entire discussion must be qualified by Zhao's observation of a very intense photoelectron peak in the same energy range that appears to originate from a state other than the nf Rydberg state. This unknown decay channel may have corrupted the rotational state distribution. In addition, previous work demonstrated the particular importance of the predissociation-mediated autoionization process in $\Delta v > 1$ vibrational autoionization.[57] These photoelectron spectra for the $\Delta v = -1$ channel may assist in disentangling the possible contributions of that mechanism versus the long-range mechanism in a more global model of vibrational autoionization.

5.6.2 ng states

Although we are unable to directly measure the rotational distributions following autoionization of ng Rydberg states, it is instructive to examine the predictions from our long-range model calculation. We will begin the discussion by examining Figure 5-30, where we have plotted the predictions for the $25g10_N$ state, which will serve as the model result for the high rotation limit. The most obvious result from this plot is the intense peaks for all ℓ_R components that occur in the $N^+ = R - 1$ and/or $N^+ = R + 1$ channels. This pattern is exactly the one we have previously described in discussing the total autoionization rates. The dipole dominates over the other electrostatic mechanisms due to the long range of the dipole interaction. The $\ell_R = -4$ state produces predominantly ions with $N^+ = R - 1$, while the $\ell_R = 4$ state produces predominantly ions with $N^+ = R + 1$. Again, this is exactly the pattern that we described for a majority $\Delta\ell = +1$ decay, which occurs due to the destructive interference between the ng wavefunction and the ϵf continuum wavefunction.

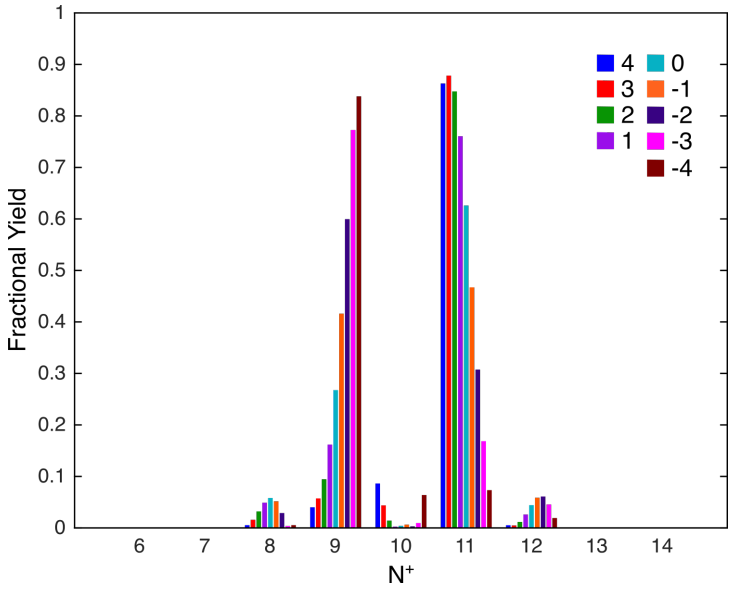

Figure 5-30: Rotational distributions of the NO^+ ion following vibrational autoionization of the $25g10_N$ state. The ℓ_R value is color coded as indicated in the legend. The dipole mechanism results in the most significant intensity in the $N^+ = R + 1$ and/or $N^+ = R - 1$ channels.

The $N^+ = R$ channel behaves similarly to the same decay channel for nf states as

previously described. The $\Delta R = 0$, $\Delta \ell = 0$ channel makes the largest contribution. For the $\ell_R = 0$ component, there is nearly perfect destructive interference between the quadrupole and polarizability mechanisms that results in very slow autoionization rates. For the extreme ℓ_R states, the interference becomes constructive and the autoionization rate increases.

The $N^+ = R \pm 2$ channels are also mostly controlled by the quadrupole and polarizability matrix elements. Since the isotropic polarizability plays no role in these decay channels, the quadrupole and polarizability mechanisms always constructively interfere. The $\Delta \ell = 0$ channel typically has the largest contribution, which results in the fastest decay for components with ℓ_R close to zero. The $\Delta \ell = \pm 2$ channels also have non-negligible amplitude, which is responsible for making the variation of autoionization rates with ℓ_R not symmetric about $\ell_R = 0$.

As expected, there is essentially no production of ion rotational states with $N^+ = R \pm 3$ or $N^+ = R \pm 4$ since the octupole and hexadecapole mechanisms are even weaker for the ng states than the nf states, as a result of the electronic wavefunction's inner turning point shifting to larger r.

Figure 5-31 shows the predicted ion rotational states that result from every component of the $25gR_N$ states for $R = 0$, 1, 2, and 3. These are the specific states investigated in our experiment. Many of the same trends occur in these plots as in the $25g10_N$ result just described. In particular, the dipole mechanism results in either one or two dominant rotational states for the resultant ion. Indeed, the low-R, high-ℓ_R states produce single rotational states of the ion with even higher purity than in the limit of high rotation. The $25g0_4$ state autoionizes to produce an NO^+ ion with $N^+ = 0$ in $\sim 92\%$ yield, while the $25g2_5$ state produces $N^+ = 3$ ions in $\sim 93\%$ yield. Thus, we suggest that high-ℓ Rydberg states of NO are useful "precursors" for the production of quantum state-selected molecular ions by vibrational autoionization. Our long-range autoionization model serves as the recipe book.

In addition to vibrational autoionization, rotational autoionization can play an important role in the non-radiative decay of Rydberg states. All states of NO considered up to this point, including the high rotation levels studied by the Zare group,

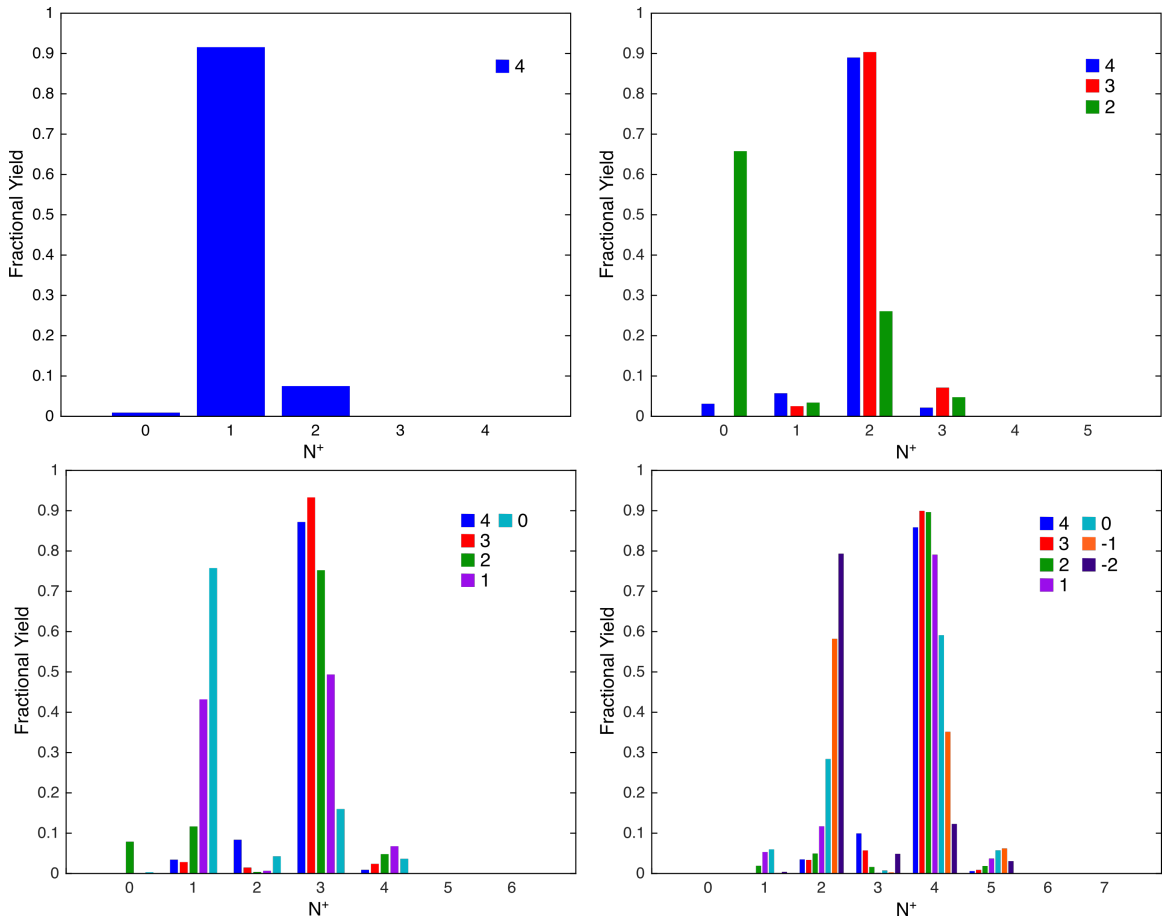

Figure 5-31: Rotational distributions of the NO^+ ion following vibrational autoionization of the $25gR_N$ states. From left to right, top to bottom, $R = 0$, 1, 2, and 3. The ℓ_R value is color coded as indicated in the legend of each plot. The dipole mechanism results in the most significant intensity in the $N^+ = R+1$ and/or $N^+ = R-1$ channel.

can only autoionize by a vibrational mechanism. Rotational autoionization channels, assuming a maximum change in the rotation of $N^+ - R = -4$, remain closed until quite high n or high R. This is governed simply by the magnitude of the ion-core rotational constant. For a very large rotational constant as for H_2^+ with $B \approx 10^{-4}$ a.u., rotational autoionization can occur at very low n and R; for example, O'Halloran and co-workers[111] studied the rotational autoionization of npR_N states of H_2 with quantum numbers $1 < R < 6$ and $20 < n < 40$. Although NO^+ is a first row diatomic molecule, the rotational constant, $B \approx 10^{-5}$ a.u., is substantially smaller. Nevertheless, the rotational autoionization dynamics are interesting to examine even if they exist in a state space that is experimentally challenging to access.

In Figure 5-32, we plot the ion rotational state distribution and total rotational autoionization rate for all components of the $35g25_N$ ($v = 0$) state. For this choice of n and R, all rotational channels are energetically allowed. The dipole mechanism still produces the fastest autoionization rates for all values of ℓ_R. However, the intensity in the remaining three channels is substantially larger than observed in vibrational autoionization. This occurs because rotational autoionization is controlled by the *magnitude* of the multipole moments and polarizability, while vibrational autoionization is approximately dictated by their *derivatives* with respect to the internuclear distance. The dipole moment is quite small at the equilibrium internuclear distance, but has a relatively steep derivative; the value of $\langle v = 0|\mu|v = 0\rangle$ is only about five times larger than the value of $\langle v = 1|\mu|v = 0\rangle$. In contrast, with the exception of the quadrupole, the other moments and polarizabilities have magnitudes at least an order of magnitude larger than their first derivatives. While this distinction does alter the rotational state distribution, it should be noted that the dipole mechanism is still the most important. For the $35g25_N$ complex, the $\ell_R = -4$ and $\ell_R = -3$ states have near unity yield in $N^+ = R - 1$, and also have the fastest total autoionization rates. The total decay rate decreases as ℓ_R increases and is minimum for the $\ell_R = 4$ component, which has the smallest amplitude in the $\Delta\ell = +1$, $\Delta R = -1$ channel as it does in vibrational autoionization.

The strategy to produce single rotational states of the ion by rotational autoioniza-

tion is straightforward. To prepare NO^+ in the N^+ rotational state, the experimenter should excite the ngR_{R-4} ($v = 0$) Rydberg state where $R = N^+ + 1$ and n is dictated by the energy scale:

$$\frac{1}{2n^2} < 2BR \tag{5.31}$$

where the left-hand side is the Rydberg energy and the right side is the energy difference between the initial and desired final rotational state. Unfortunately, this would require $n > 166$ for $N^+ = 0$, or $n > 117$ for $N^+ = 1$. An alternative strategy is to rely upon the slightly slower $\Delta R = -2$ process and excite a ngR_R Rydberg state where $R = N^+ + 2$ and the state lies within the energy interval:

$$2BR < \frac{1}{2n^2} < 2B(2R - 1) \tag{5.32}$$

For the choice $N^+ = 0$, $95 < n < 118$, and for $N^+ = 1$, $74 < n < 96$. One could continue this exercise all the way to $\Delta R = -4$, although the autoionization rate will decrease significantly. Without showing the explicit expression, accessing $N^+ = 0$ by this route requires $52 < n < 56$ and accessing $N^+ = 1$ requires $44 < n < 48$. These are still relatively high principal quantum numbers and only a few values of the principal quantum number will produce the desired ion rotational state. This latter fact makes the scheme more vulnerable to an unexpected perturbation, which could corrupt the dynamics, since few alternative initial Rydberg states are possible. All of these numbers have assumed the rotational constant for NO^+, which is smaller than for a typical diatomic hydride, but is quite large relative to most heavy atom diatomic molecules. A smaller rotational constant will exacerbate all of the issues in this rotational autionization scheme. This discussion highlights the experimental advantage of identifying a vibrational autoionization route to low N^+ states of the molecular ion.

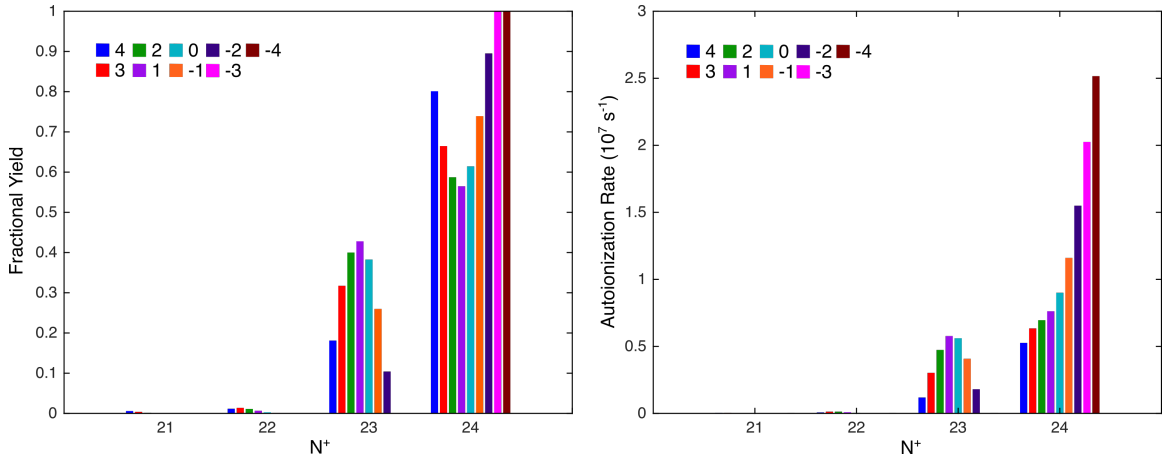

Figure 5-32: Left: Rotational distributions of the NO^+ ion following rotational autoionization of the $35g25_N(v = 0)$ states. The ℓ_R value is color coded as indicated in the legend. The dipole mechanism results in the most significant intensity in the $N^+ = R - 1$ channel. Unlike the vibrational case, observable intensity exists in the $N^+ = R - 3$ and $N^+ = R - 4$ channels. Right: Absolute autoionization rates for each channel. The $N^+ = R - 1$ channel has the fastest decay for all states, while the decay into $N^+ = R - 3$ and $N^+ = R - 4$ channels is at least two orders of magnitude slower.

5.7 Conclusion

Autoionization lifetimes of ng Rydberg states of NO have been directly measured for the first time. We find qualitative agreement with the predictions from a long-range electrostatic model of the autoionization process, though the calculated rates are generally slower than the observed rates. Significantly, the non-radiative decay of ng states is dominated by autoionization rather than predissociation as in all low-ℓ Rydberg states of NO. In addition, we find that this long-range model predicts NO^+ state distributions following the autoionization of nf levels that are largely consistent with the experimental observations from the Zare group.[117,118,164] The agreement is particularly striking for states with $|\ell_R| \leq 1$. The extreme ℓ_R components decay by $R - N^+ = \pm 3$, and ± 4 channels, which are not captured by our model. Extensions of the long-range model to include higher-order polarizabilities, or explicit phase shifts due to core-penetration, may shed light on these discrepancies. In addition, re-examination of a predissociation-mediated autoionization model is warranted. Finally, we propose that vibrational autoionization of selected ng Rydberg states is an efficient

means to produce molecular ions in few, or even a single selected quantum state. While our investigation focuses on NO, this experimental and theoretical methodology will be applicable to a variety of diatomic molecules because high-ℓ Rydberg states obey a universal scaling of the long-range autoionization mechanisms. Quantum-state selected ions are a useful tool for experiments in precision measurement,[56,92] ultracold chemistry,[134,146] and quantum computing.[135]

Chapter 6

Conclusions and Outlook

This thesis has explored new physics and scientific applications of the high-ℓ Rydberg states of atoms and molecules. When the Rydberg electron possesses sufficient orbital angular momentum, the centrifugal barrier prevents its close approach to the ion-core. This inability of the Rydberg electron to interact with the ion-core profoundly affects the properties of a molecular Rydberg state, because molecules suffer from rapid non-radiative decay by predissociation. The electronic valence states responsible for this non-radiative decay have large wavefunction amplitude in the region of the ion-core. For low-ℓ, *core-penetrating* Rydberg states, these predissociative wavefunctions interact strongly with the Rydberg electron wavefunction, which leads to fragmentation of the molecule. When the value of ℓ is sufficiently high, the probability of finding the Rydberg electron in the core-region becomes vanishingly small, and these *core-nonpenetrating* Rydberg states exhibit enhanced lifetimes characteristic of their atomic counterparts. Moreover, the physics of the Rydberg electron$\leftrightarrow$ion-core interaction is simplified because the complex, many-body interactions due to the ion-core are strongly attenuated. This fact allows us to treat the ion-core as a polarizable, multipole point source, which communicates with the Rydberg electron exclusively *via* long-range electrostatic forces. In this long-range theory, the spectroscopy and dynamics of the high-ℓ, core-nonpenetrating states are completely described in an *a priori*, mechanistically explicit way, granting predictive power that will guide the design of new Rydberg experiments.

While the experimental and theoretical advantages of high-ℓ states are transparent, a general method for their preparation is not. The low orbital angular momentum of the ground molecular state of most molecules is due to the s and p valence electrons involved in the bonding of the constituent atoms. Since each photon in an excitation scheme transmits no more than one unit of angular momentum to the molecule, several photons are required to raise the value of ℓ sufficiently to access core-nonpenetrating states. In addition, this pathway must typically traverse low-ℓ, core-penetrating Rydberg states, which decay rapidly by predissociation. To address this challenge, we develop the method of optical-millimeter-wave (mmW) stimulated Raman adiabatic passage (STIRAP). This technique for coherent population transfer in a three-level system has been shown to transfer population with near unity efficiency from an initial state to a final state without directly populating an intermediate, possibly lossy, state.[13] In our proposed application, the optical photon addresses the transition between a molecular valence state and low-ℓ, predissociated Rydberg state, while the mmW photon connects this low-ℓ Rydberg state to a neighboring, long-lived, core-nonpenetrating state. Our inital demonstration on a thermal beam of Ca atoms allows for complete experimental characterization of the intermediate and final state populations as a function of the optical-mmW timing and detuning, and subsequent numerical simulations to assist in interpretation. Several known experimental imperfections, including Doppler broadening, the temporal profile of the mmW pulse, and the transverse profile of the laser beam, are explicitly included in the simulations. The observed $\gtrsim$50% population transfer in the so-called "counter-intuitive" pulse timing, and robust population transfer on two-photon resonance for all one-photon detunings, are characteristic features of the STIRAP process that are reproduced by our numerical simulations. Simulation of a hypothetical system with a lossy intermediate state and otherwise identical parameters indicates the possibility that this method can populate high-ℓ Rydberg states of molecules as well as atoms.

In particular, nitric oxide could serve as an ideal test system for optical-mmW STIRAP in molecules. The nf states of NO are strongly predissociated, exhibiting lifetimes of $\tau \approx 10$ ns for $n \approx 40$. In contrast, the ng states are decidedly core-

nonpenetrating, and possess lifetimes more than an order of magnitude longer. An excitation scheme, which requires minimal modifications of the existing laser and mmW sources, would involve access to a $29f$ state through the H $^2\Sigma^+$, H' $^2\Pi$ ($3d\sigma$, $3d\pi$) complex, with our pulse amplified laser system operating around 840 nm. The mmW Stokes transition around 280 GHz connects the predissociated $29f$ level to the long-lived $28g$ level and this population transfer can be probed *via* the $29h \leftarrow 28g$ transition at approximately 285 GHz. Rabi frequencies similar to those in our proof-of-principle Ca experiment are attainable with this scheme. The fast predissociation of the intermediate state presents a stringent test of optical-mmW STIRAP, but the well-known level structure of NO, supplemented by our own observations of mmW transitions, makes this test experimentally feasible. Optical-mmW STIRAP is a general population transfer method that will enable access to the high-ℓ Rydberg states of a plethora of new molecules.

Having populated the high-ℓ Rydberg states of molecules, these long-lived states are amenable to investigation by high-resolution mmW spectroscopy. Of particular interest is refinement and extension of the long-range electrostatic model, which serves as a mechanistically explicit model for the energy level structure of high-ℓ states.[41] Significant work in this vein has until now been limited to high-resolution spectroscopy of H_2[6,141] and relatively low-resolution laser spectroscopy of a few other molecules, including NO.[15,97] By employing a three-color, triple-resonance laser excitation scheme, we directly populate ng states of NO, which possess predissociation-limited lifetimes approaching 1 μs at $n \approx 50$.[52] We probe Rydberg-Rydberg transitions using chirped-pulse millimeter-wave (CPmmW) spectroscopy, making NO only the second molecule investigated by this powerful, multiplexed technique. The obtained high-resolution data set of g-h transitions spans a wider range of state space than possible in previous work. In particular, the resolution of the electric fine structure in high-n Rydberg states reports directly on the "non-sphericity" of the ion-core, or in other words, the polarizability and multipole moments that perturb the Rydberg states from hydrogenicity. A preliminary fit of our data set suggests that previously inaccessible electric properties of the NO^+ ion can be determined by our spectroscopy.

Further work on the spectroscopy of NO first requires improved control over the stray electric fields in the apparatus, which shift and broaden the observed transitions. In addition to this technical improvement, a greater variety of transitions bear investigation in future work. These include: i) $\Delta n > 1$ transitions, which will extend the range of observed n to higher values, where Rydberg states exhibit greater sensitivity to some of the electrostatic perturbations of interest; ii) transitions in the $v = 1$ and $v = 2$ Rydberg manifolds, which will report in a direct way on the autoionization decay dynamics and the variation of electrostatic properties with internuclear distance; iii) transitions in regions of n where stroboscopic resonances additionally perturb the Rydberg level structure due to Rydberg-Rydberg transition energies similar to the NO^+ rotational transition energies. A wealth of spectroscopic information and physical insights remain unexplored in the Rydberg states of NO. An additional Ph.D. thesis (and more!) could be spent uncovering it all.

Beyond spectroscopy, autoionization dynamics of high-ℓ Rydberg states can be described by a long-range electrostatic model. Specifically, vibrational autoionization involves the exchange of energy between the vibrationally excited ion-core and the Rydberg electron *via* the internuclear distance-dependent electrostatic properties of the ion-core. By directly measuring autoionization rates of ng Rydberg states of NO, we demonstrate that the decay of these states is dominated by autoionization consistent with the predictions of this long-range model. This result is in striking contrast with the nf Rydberg states of NO, which decay rapidly by predissociation.[49,52] Surprisingly, we find that although the total decay rates of the nf states are incompatible with a long-range autoionization model, the rotational states of the product ions are generally consistent with our model. These NO^+ ion rotational state distributions, measured in pioneering experiments by the Zare group,[117,118,164] were surprising because they indicated extensive angular momentum exchange between the Rydberg electron and the ion-core. Our long-range model indicates that this angular momentum exchange is in large part due to the NO^+ electric dipole moment, a previously unappreciated mechanism. Using the long-range electrostatic model, we make predictions of the ion rotational state distributions following vibrational autoionization

of ng Rydberg states of NO. Due to the dominant influence of the dipole decay mechanism, very few rotational states are populated, and in some cases, more than a 90% yield in a single rotational state is possible.

This last theoretical result represents an area of exciting new applications that may be applied to many other molecules. In particular, all first row diatomic ions possess a significant electric quadrupole moment that causes mixing of s and d character in the low Rydberg states. Upon identification of the lowest $3s\sigma$ Rydberg state, an excitation scheme that accesses ng states *via* the $4f$ complex, in analogy to the excitation scheme used in our work, is applicable. Either by photoelectron spectroscopy or laser spectroscopy of the resultant ions, the rotational state distributions can be probed and directly compared to the predictions of our long-range model. Extensions of the current model to non-$^1\Sigma^+$ ion-core electronic states is required to address these new molecular systems. However, the strong influence of the dipole moment in autoionization decay of high-ℓ states will be a consistently dominant feature for all heteronuclear species. Vibrational autoionization of core-nonpenetrating Rydberg states represents a novel and efficient method for generation of molecular ions in a single quantum state. These will be useful systems in a wide range of modern physics experiments.

High-ℓ, core-nonpenetrating Rydberg states are a special class of unexplored and unexploited electronic states that merge the complexity of a molecule with the simplicity of a Rydberg atom. More mature atomic Rydberg-state-enabled technologies can be applied to these systems, further advancing the goal of raising molecules to the same level of control and insight as for atoms. Applications far beyond those described in this thesis, from electrostatic trapping[69] and many-body physics[61] to precision measurement[92] and ultracold chemistry,[2,146] will benefit from our enhanced understanding of these unique states.

Bibliography

[1] Nobel Media AB. Summary. NobelPrize.org, 2019. Online; accessed 8-November-2019.

[2] P. Allmendinger, J. Deiglmayr, O. Schullian, K. Höveler, J. A. Agner, H. Schmutz, and F. Merkt. New method to study ion-molecule reactions at low temperatures and application to the $H_2^+ + H_2 \rightarrow H_3^+ + H$ reaction. *ChemPhysChem*, 17:3596–3608, 2016.

[3] C. Amiot and J. Verges. Fourier transform spectrometry of the $D^2\Sigma^+$-$A^2\Sigma^+$, $E^2\Sigma^+$-$D^2\Sigma^+$, and $E^2\Sigma^+$-$A^2\Sigma^+$ systems of nitric oxide. *Physica Scripta*, 26:422–438, 1982.

[4] Y. Anezaki, T. Ebata, N. Mikami, and M. Ito. Two-color multiphoton ionization and fluorescence dip spectra of NO in a supersonic free jet. Highly excited ns, np, nf Rydberg states. *Chemical Physics*, 97:153–163, 1985.

[5] C. Angeli, R. Cimiraglia, S. Evangelisti, T. Leininger, and J.-P. Malrieu. Introduction of n-electron valence states for multireference perturbation theory. *The Journal of Chemical Physics*, 114:10252, 2001.

[6] P. W. Arcuni, E. A. Hessels, and S. R. Lundeen. Series mixing in high-L Rydberg states of H_2: An experimental test of polarization-model predictions. *Physical Review A*, 41:3648–3662, 1990.

[7] H. Ashkenas and F. S. Sherman. *Rarefied Gas Dynamics*, volume 2. Academic Press, New York, 1966.

[8] Y. S. Au, C. B. Connolly, W. Ketterle, and J. M. Doyle. Vibrational quenching of the electronic ground state in ThO in cold collisions with ^{3}He. *Physical Review A*, 90:032703, 2014.

[9] J. Baraban. Personal communication, June 2017.

[10] J. F. Barry, E. S. Shuman, and D. DeMille. A bright, slow cryogenic molecular beam source for free radicals. *Physical Chemistry Chemical Physics*, 13:18936–18947, 2011.

[11] T. Bauer, J. S. Kolb, T. Löffler, E. Mohler, H. G. Roskos, and U. C. Pernisz. Indium-tin-oxide-coated glass as a dichroic mirror for far-infrared electromagnetic radiation. *Journal of Applied Physics*, 92:2210, 2002.

[12] K. Bergmann, H. Theuer, and B. W. Shore. Coherent population transfer among quantum states of atoms and molecules. *Reviews of Modern Physics*, 70:1003–1025, 1998.

[13] K. Bergmann, N. V. Vitanov, and B. W. Shore. Perspective: Stimulated Raman adiabatic passage: The status after 25 years. *The Journal of Chemical Physics*, 142:170901, 2015.

[14] H. A. Bethe and E. E. Salpeter. *Quantum mechanics of one- and two-electron atoms*. Springer-Verlag Berlin Heidelberg, New York, 1957.

[15] D. T. Biernacki, S. D. Colson, and E. E. Eyler. High resolution laser spectroscopy of NO: The A, $v = 1$ state and a series of nf, $v = 1$ Rydberg states. *The Journal of Chemical Physics*, 89:2599, 1988.

[16] M. Bixon and J. Jortner. The dynamics of predissociating high Rydberg states of NO. *The Journal of Chemical Physics*, 105:1363, 1996.

[17] W. C. Bowman, E. Herbst, and F. C. De Lucia. Millimeter and submillimeter spectrum of NO^+. *The Journal of Chemical Physics*, 77:4261, 1982.

[18] T. Breeden and H. Metcalf. Stark acceleration of Rydberg atoms in inhomogeneous electric fields. *Physical Review Letters*, 47:1726–1729, 1981.

[19] G. G. Brown, B. C. Dian, K. O. Douglass, S. M. Geyer, and B. H. Pate. The rotational spectrum of epifluorohydrin measured by chirped-pulse fourier transform microwave spectroscopy. *Journal of Molecular Spectroscopy*, 238:200–212, 2006.

[20] G. G. Brown, B. C. Dian, K. O. Douglass, S. M. Geyer, S. T. Shipman, and B. H Pate. A broadband Fourier transform microwave spectrometer based on chirped pulse excitation. *Review of Scientific Instruments*, 79:053103, 2008.

[21] J. Brown and A. Carrington. *Rotational spectroscopy of diatomic molecules*. Cambridge University Press, Cambridge, UK, 2003.

[22] J. M. Brown and B. J. Howard. An approach to the anomalous commutation relations of rotational angular momenta in molecules. *Molecular Physics*, 31:1517–1525, 1976.

[23] A. D. Buckingham. Theory of long-range dispersion forces. *Discussions of the Faraday Society*, 40, 1965.

[24] N. E. Bulleid, S. M. Skoff, R. J. Hendricks, B. E. Sauer, E. A. Hinds, and M. R. Tarbutt. Characterization of a cryogenic beam source for atoms and molecules. *Physical Chemistry Chemical Physics*, 15:12299, 2013.

[25] W. C. Campbell and J. M. Doyle. Cooling, trap loading, and beam production using a cryogenic helium buffer gas. In Roman V. Krems, William C. Stwalley, and Bretislav Friedrich, editors, *Cold Molecules: Theory, Experiments, Applications*. CRC Press, Boca Raton, FL, 2009. Chapter 13.

[26] W. C. Campbell, G. C. Groenenboom, H.-I. Lu, E. Tsikata, and J. M. Doyle. Time-domain measurement of spontaneous vibrational decay of magnetically trapped NH. *Physical Review Letters*, 100(8):083003, 2008.

[27] W. Y. Cheung, W. A. Chupka, S. D. Colson, D. Gauyacq, P. Avouris, and J. J. Wynne. Rydberg-Rydberg transitions of NO using an optical-optical double resonance multiphoton ionization technique. *The Journal of Chemical Physics*, 78:3625, 1983.

[28] M. S. Child. *Theory of Molecular Rydberg States*. Cambridge University Press, 2011.

[29] D. T. Colbert and W. H. Miller. A novel discrete variable representation for quantum mechanical reactive scattering via the S-matrix Kohn method. *The Journal of Chemical Physics*, 96:1982, 1992.

[30] A. P. Colombo, Y. Zhou, K. Prozument, S. L. Coy, and R. W. Field. Chirped-pulse millimeter-wave spectroscopy: Spectrum, dynamics, and manipulation of Rydberg-Rydberg transitions. *The Journal of Chemical Physics*, 138:014301, 2013.

[31] P. J. Crutzen. Role of NO and NO_2 in the chemistry of the troposphere and stratosphere. *Annual Reviews of Earth and Planetary Science*, 7:443–472, 1979.

[32] T. Cubel, B. K. Teo, V. S. Malinovsky, J. R. Guest, A. Reinhard, B. Knuffman, P. R. Berman, and G. Raithel. Coherent population transfer of ground-state atoms into Rydberg states. *Physical Review A*, 72:023405, 2005.

[33] I. Dabrowski, D. W. Tokaryk, M. Vervloet, and J. K. G. Watson. New Rydberg-Rydberg transitions of the ArH and ArD molecules. I. Emission from *np* states of ArD. *The Journal of Chemical Physics*, 104:8245, 1996.

[34] M. J. S. Dewar and S. D. Worley. Photoelectron spectra of molecules. I. Ionization potentials of some organic molecules and their interpretation. *The Journal of Chemical Physics*, 50:654, 1969.

[35] K. Dressler, C. Jungen, and E. Miescher. Identification of the 5g-4f Rydberg-Rydberg transition of the NO molecule. *Journal of Physics B: Atomic and Molecular Physics*, 14:L701, 1981.

[36] T. H. Dunning. Gaussian basis sets for use in correlated molecular calculations. I. The atoms boron through neon and hydrogen. *The Journal of Chemical Physics*, 90:1007, 1989.

[37] K. S. E. Eikema, W. Ubachs, W. Vassen, and W. Hogervorst. Lamb shift measurement in the 1 ^1S ground state of helium. *Physical Review A*, 55:1866, 1997.

[38] U. Even, J. Jortner, D. Noy, N. Lavie, and C. Cossart-Magos. Cooling of large molecules below 1 K and He clusters formation. *The Journal of Chemical Physics*, 112:8068, 2000.

[39] E. Eyler and D. T. Biernack. Analysis of the $4f$, $v = 3$ state of NO. *The Journal of Chemical Physics*, 88:2850, 1988.

[40] E. E. Eyler. Autoionization of nonpenetrating Rydberg states in diatomic molecules. *Physical Review A*, 34:2881–2888, 1986.

[41] E. E. Eyler and F. M. Pipkin. Triplet $4d$ states of H_2: Experimental observation and comparison with an *ab initio* model for Rydberg-state energies. *Physical Review A*, 27:2462–2478, 1983.

[42] E. E. Eyler, A. Yiannopoulou, S. Gangopadhyay, and N. Melikechi. Chirp-free nanosecond laser amplifier for precision spectroscopy. *Optics Letters*, 22:49–51, 1997.

[43] M. S. Fee, K. Danzmann, and S. Chu. Optical heterodyne measurement of pulsed lasers: toward high-precision pulse spectroscopy. *Physical Review A*, 45:4911, 1992.

[44] M Fehér and P. A. Martin. Ab initio calculations of the properties of NO^+ in its ground electronic state X $^1\Sigma^+$. *Chemical Physics Letter*, 215:565–570, 1993.

[45] M. Fehér and P. A. Martin. *Ab initio* calculation of the electrical properties of the X $^2\Sigma_g^+$ ground and A $^2\Pi_u$ excited states of N_2^+. *Journal of the Chemical Society Faraday Transactions*, 91:1063–1066, 1995.

[46] W. H. Flygare. Magnetic interactions in molecules and an analysis of molecular electronic charge distribution from magnetic parameters. *Chemical Reviews*, 74:653–687, 1974.

[47] D. B. Fraser and H. D. Cook. Highly conductive, transparent films of sputtered $In_{2-x}Sn_xO_{3-y}$. *Journal of the Electrochemical Society*, 119:1368–1374, 1972.

[48] S. Fredin, D. Gauyacq, M. Horani, C. Jungen, G. Lefevre, and F. Masnou-Seeuws. s and d Rydberg series of NO probed by double resonance multiphoton ionization: multichannel quantum defect analysis. *Molecular Physics*, 60:825–866, 1987.

[49] A. Fujii and N. Morita. Detection of nitrogen atoms produced by predissociation of superexcited Rydberg states of NO. *Chemical Physics Letters*, 182:304–309, 1991.

[50] A. Fujii and N. Morita. Rotational state dependence of decay dynamics in the superexcited $7f$ Rydberg state ($v = 1$) of NO. *The Journal of Chemical Physics*, 97:327, 1992.

[51] A. Fujii and N. Morita. Laser investigation of the competition between rotational autoionization and predissociation in superexcited np Rydberg states of NO. *The Journal of Chemical Physics*, 98:4581, 1993.

[52] A. Fujii and N. Morita. Three-color triple resonance spectroscopy of highly excited ng Rydberg states of NO: Decay dynamics of high-ℓ Rydberg states. *The Journal of Chemical Physics*, 103:6029, 1995.

[53] T. F. Gallagher. *Rydberg Atoms*. Cambridge University Press, New York, 1994.

[54] S. Gangopadhyay, N. Melikechi, and E. E. Eyler. Optical phase perturbations in nanosecond pulsed amplification and second-harmonic generation. *Journal of the Optical Society of America B*, 11:231–241, 1994.

[55] U. Gaubatz, Rudecki P., S. Schiemann, and K. Bergmann. Population transfer between molecular vibrational levels by stimulated Raman scattering with partially overlapping laser fields. a new concept and experimental results. *The Journal of Chemical Physics*, 92:5363, 1990.

[56] M. Germann, X. Tong, and S. Willitsch. Observation of electric-dipole-forbidden infrared transitions in cold molecular ions. *Nature Physics*, 10:820–824, 2014.

[57] A. Giusti-Suzor and C. Jungen. Theoretical study of competing photoionization and photodissociation processes in the NO molecule. *The Journal of Chemical Physics*, 80:986, 1984.

[58] A. L. Goodgame, H. Dickinson, S. R. Mackenzie, and T. P. Softley. The Stark effect in the $v^+ = 1$ autoionizing Rydberg states of NO. *The Journal of Chemical Physics*, 116:4922, 2002.

[59] D. D. Grimes. *Millimeter-Wave Dynamics and Control of Rydberg-Rydberg Transitions*. PhD thesis, Massachusetts Institute of Technology, Cambridge, MA, 2017.

[60] D. D. Grimes, T. J. Barnum, Y. Zhou, A. P. Colombo, and R. W. Field. Coherent laser-millimeter-wave interactions en route to coherent population transfer. *The Journal of Chemical Physics*, 147:144201, 2017.

[61] D. D. Grimes, S. L. Coy, T. J. Barnum, Y. Zhou, S. F. Yelin, and R. W. Field. Direct single-shot observation of millimeter-wave superradiance in Rydberg-Rydberg transitions. *Physical Review A*, 95:043818, 2017.

[62] M. Gross and S. Haroche. Superradiance: An essay on the theory of collective spontaneous emission. *Physics Reports*, 93:301–396, 1982.

[63] C. Haase, M. Beyer, C. Jungen, and F. Merkt. The fundamental rotational interval of para-H_2^+ by MQDT-assisted Rydberg spectroscopy of H_2. *The Journal of Chemical Physics*, 142:064310, 2015.

[64] T. Halfmann and K. Bergmann. Coherent population transfer and dark resonances in SO_2. *The Journal of Chemical Physics*, 104:7068, 1996.

[65] B. Hemmerling, E. Chae, A. Ravi, L. Anderegg, G. K. Drayna, N. R. Hutzler, A. L. Collopy, J. Ye, W. Ketterle, and J. M. Doyle. Laser slowing of CaF molecules to near the capture velocity of a molecular MOT. *Journal of Physics B: Atomic, Molecular and Optical Physics*, 49:174001, 2016.

[66] H. Herburger. Demonstration of optical-millimeter-wave stimulated raman adiabatic passage in calcium. Master's thesis, ETH Zurich, Switzerland, 2017.

[67] HighFinesse GmbH. *Wavelength Meter Ångstrom WS/7 User Manual.*

[68] S. D. Hogan and F. Merkt. Demonstration of three-dimensional electrostatic trapping of state-selected Rydberg atoms. *Physical Review Letters*, 100:043001, 2008.

[69] S. D. Hogan, C. Seiler, and F. Merkt. Rydberg-state-enabled deceleration and trapping of cold molecules. *Physical Review Letters*, 103:123001, 2009.

[70] C. E. Housecroft and A. G. Sharpe. *Inorganic Chemistry, Third Edition.* Pearson Education Limited, Harlow, England, 2008.

[71] K. P. Huber and G. Gerzberg. *Molecular spectra and molecular spectra. Volume IV. Constants of diatomic molecules.* Van Nostrand Reinhold Company, New York, 1979.

[72] N. R. Hutzler, H.-I. Lu, and J. M. Doyle. The buffer gas beam: An intense, cold, and slow source for atoms and molecules. *Chemical Reviews*, 112:4803–4827, 2012.

[73] N. R. Hutzler, M. F. Parson, Y. V. Gurevich, P. W. Hess, E. Petriz, B. Spaun, A. C. Vutha, D. DeMille, G. Gabrielse, and J. M. Doyle. A cryogenic beam of refractory, chemically reactive molecules with expansion cooling. *Physical Chemistry Chemical Physics*, 13:18976–18985, 2011.

[74] P. L. Jacobson, D. S. Fisher, C. W. Fehrenbach, W. G. Sturrus, and S. R. Lundeen. Determination of the dipole polarizabilities of H_2^+ (0,0) and D_2^+ (0,0) by microwave spectroscopy of high-l Rydberg states of H_2 and D_2. *Physical Review A*, 56:R4361–4364, 1997.

[75] Z. J. Jakubek and R. W. Field. Core-penetrating Rydberg series of BaF: $s \sim p \sim d \sim f$ supercomplexes. *Physical Review Letters*, 27:2167–2170, 1994.

[76] F. Jensen. *Introduction to Computational Chemistry*. John Wiley & Sons, Inc., West Sussex, England, 2007.

[77] J. Jiang, Barnum T. J., S. L. Coy, and R. W. Field. Analysis of vibrational autoionization of CaF Rydberg stats. *The Journal of Chemical Physics*, 150:154305, 2019.

[78] C. Jungen. Rydberg series in the NO spectrum: an interpretation of quantum defects and intensities in the s and d series. *The Journal of Chemical Physics*, 53:4168, 1970.

[79] C. Jungen and E. Miescher. Absorption spectrum of the NO molecule. IX. The structure of the f complexes, the ionization potential of NO, and the quadrupole moment of NO^+. *Canadian Journal of Physics*, 47:1769–1787, 1969.

[80] C. Jungen, S. T. Pratt, and S. C. Ross. Multichannel quantum defect theory and double-resonance spectroscopy of autoionizing levels of molecular hydrogen. *The Journal of Physical Chemistry*, 99:1700–1710, 1995.

[81] L. A. Kaledin, M. C. Heaven, and R. W. Field. Thermochemical properties (D_0^0 and IP) of the lanthanide monohalides. *Journal of Molecular Spectroscopy*, 193:285–292, 1999.

[82] J. J. Kay, G. Paterson, M. L. Costen, K. E. Strecker, K. G. McKendrick, and D. W. Chandler. Communication: Direct angle-resolved measurements of collision dynamics with electronically excited molecules: $NO(A^2\Sigma^+)$+Ar. *The Journal of Chemical Physics*, 134:091101, 2011.

[83] J. Kim. *Buffer-gas Loading and Magnetic Trapping of Atomic Europium*. PhD thesis, Harvard University, Cambridge, MA, 1997.

[84] Z. Kis, A. Karpati, B. W. Shore, and N. V. Vitanov. Stimulated Raman adiabatic passage among degenerate-level manifolds. *Physical Review A*, 70:053405, 2004.

[85] C. Kittrell, E. Abramson, J. L. Kinsey, S. A. McDonald, D. E. Reisner, and R. W. Field. Selective vibrational excitation by stimulated emission pumping. *Journal of Chemical Physics*, 75:2056, 1981.

[86] D. E. Koshland Jr. The molecule of the year. *Science*, 258:1861, 1992.

[87] I. Kozyryev, L. Baum, K. Matsuda, P. Olson, B. Hemmerling, and J. M. Doyle. Collisional relaxation of vibrational states of SrOH with He at 2 K. *New Journal of Physics*, 17:045003, 2015.

[88] A. Kuhn, G. W. Coulston, G. Z. He, S. Schiemann, K. Bergmann, and W. S. Warren. Population transfer by stimulated raman scattering with delayed pulses using spectrally broad light. *The Journal of Chemical Physics*, 96:4215, 1992.

[89] A. Kuhn, S. Steuerwald, and K. Bergmann. Coherent population transfer in NO with pulsed lasers: the consequences of hyperfine structure, Doppler broadening and electromagnetically induced absorption. *The European Physical Journal D*, 1:57–70, 1998.

[90] M. P. Lee, B. K. McMillin, and R. K. Hanson. Temperature measurements in gases by use of planar laser-induced fluorescence imaging of NO. *Applied Optics*, 32:5379–5396, 1993.

[91] Hélène Lefebvre-Brion and Robert W. Field. *The spectra and dynamics of diatomic molecules*. Elsevier, New York, 2004.

[92] H. Loh, J. Wang, M. Grau, T. S. Yahn, R. W. Field, C. H. Greene, and E. A. Cornell. Laser-induced fluorescence studies of HfF^+ produced by autoionization. *The Journal of Chemical Physics*, 135:154308, 2011.

[93] B. I. Loukhovitski, A. S. Sharipov, and A. M. Starik. Influence of vibrations and rotations of diatomic molecules on their physical properties: I. Dipole moment and static dipole polarizability. *Journal of Physics B: Atomic, Molecular and Optical Physics*, 49:125102, 2016.

[94] M.-J. Lu and J. D. Weinstein. Cold TiO($X\ ^3\Delta$)-He collisions. *New Journal of Physics*, 11:055015, 2009.

[95] J. C. MacGillivray and M. S. Feld. Theory of superradiance in an extended, optically thick medium. *Physical Review A*, 14:1169–1189, 1976.

[96] P. A. Martin and M. Fehér. Casscf calculations of the multipole moments and dipole polarisability functions of the $X\ ^2\Sigma^+$ and $A\ ^2\Pi$ states of CO^+. *Chemical Physics Letters*, 232:491–496, 1995.

[97] P. A. Martin, R. J. Stickland, C. S. B. Martin, and P. B. Davies. Infrared diode laser spectroscopy of the 5g-4f Rydberg transition of nitric oxide. *Canadian Journal of Physics*, 72:979–988, 1994.

[98] F. B. V. Martins, J. S. Keller, and E. R. Grant. Control of molecular ultracold plasma relaxation dynamics by mm-wave Rydberg-Rydberg transitions. *Molecular Physics*, 117:3096–3107, 2019.

[99] S. E. Maxwell, N. Brahms, R. deCarvalho, D. R. Glenn, J. S. Helton, S. V. Nguyen, D. Patterson, J. Petricka, D. DeMille, and J. M. Doyle. High-flux beam source for cold, slow atoms or molecules. *Physical Review Letters*, 95:173201, 2005.

[100] T. G. McGurk, T. G. Schmalz, and W. H. Flygare. Fast passage in rotational spectroscopy: Theory and experiment. *The Journal of Chemical Physics*, 60:4181, 1974.

[101] F. Merkt, A. Osterwalder, R. Seiler, R. Signorell, H. Palm, H. Schmutz, and R. Gunzinger. High Rydberg states of argon: Stark effect and field-ionization properties. *Journal of Physics B: Atomic, Molecular, and Optical Physics*, 31:1705–1724, 1998.

[102] F. Merkt and H. Schmutz. Very high resolution spectroscopy of high Rydberg states of the argon atom. *The Journal of Chemical Physics*, 108:10033, 1998.

[103] E. Miescher and K. P. Huber. Electronic spectrum of the NO molecule. In A. D. Buckingham, editor, *International Review of Science, Physical Chemistry Series 2, Volume 3. Spectroscopy*. Butterworths, London, 1976.

[104] D. M. Mittleman. Perspective: Terahertz science and technology. *Journal of Applied Physics*, 122:230901, 2017.

[105] L. Moi, C. Fabre, P. Goy, M. Gross, S. Haroche, P. Encrenaz, G. Beaudin, and B. Lazareff. Heterodyne detection of Rydberg atom maser emission. *Optics Communications*, 33:47–50, 1980.

[106] W. Müller and W. Meyer. Static dipole polarizabilities of Li_2, Na_2, and K_2. *Journal of Chemical Physics*, 85:953–957, 1986.

[107] E. Murgu, J. D. D. Martin, and T. F. Gallagher. Stabilization of predissociating nitric oxide Rydberg molecules using microwave and radio-frequency fields. *The Journal of Chemicla Physics*, 115:7032, 2001.

[108] F. Neese. The ORCA program suite. *Wiley Interdisciplinary Reviews: Computational Molecular Science*, 2:73–78, 2012.

[109] F. Neese. Software update: the ORCA program suite, version 4.0. *Wiley Interdisciplinary Reviews: Computational Molecular Science*, 8:e1327, 2017.

[110] K.-K. Ni, S. Ospelkaus, M. H. G. de Miranda, A. Pe'er, B. Neyenhuis, J. J. Zirbel, S. Kotochigova, P. S. Julienne, D. S. Jin, and J. Ye. A high phase-space-density gas of polar molecules. *Science*, 322:231–235, 2008.

[111] M. A. O'Halloran, P. M. Dehmer, S. T. Pratt, J. L. Dehmer, and F. S. Tomkins. Double-resonance studies of rotational autoionization of H_2. *The Journal of Chemical Physics*, 90:930, 1989.

[112] A. Osterwalder, S. Willitsch, and F. Merkt. High-resolution pulsed field ionization study of high Rydberg states of benzene. *Journal of Molecular Structure*, 599:163–176, 2001.

[113] A. Osterwalder, A. Wüest, F. Merkt, and C. Jungen. High-resolution millimeter wave spectroscopy and multichannel quantum defect theory of the hyperfine structure in high Rydberg states of molecular hydrogen H_2. *The Journal of Chemical Physics*, 121:11810, 2004.

[114] C. D. Panda, B. R. O'Leary, A. D. West, J. Baron, P. W. Hess, C. Hoffman, E. Kirilov, C. B. Overstreet, E. P. West, D. DeMille, J. M. Doyle, and G. Gabrielse. Stimulated Raman adiabatic passage preparation of a coherent superposition of ThO $H^3\Delta_1$ states for an improved electron electric-dipole-moment measurement. *Physical Review A*, 93:052110, 2016.

[115] G. B. Park and R. W. Field. Perspective: The first ten years of broadband chirped pulse Fourier transform microwave spectroscopy. *The Journal of Chemical Physics*, 144:200901, 2016.

[116] G. B. Park, A. H. Steeves, K. Kuyanov-Prozument, J. L. Neill, and R. W. Field. Design and evaluation of a pulsed-jet chirped-pulse millimeter-wave spectrometer for the 70–102 GHz region. *The Journal of Chemical Physics*, 135:024202, 2011.

[117] H. Park, D. J. Leahy, and R. N. Zare. Extensive electron-nuclear angular momentum exchange in vibrational autoionization of np and nf Rydberg states of NO. *Physical Review Letters*, 76:1591–1594, 1996.

[118] H. Park and R. N. Zare. Roationally resolved photoelectron spectra from vibrational autoionization of NO Rydberg levels. *The Journal of Chemical Physics*, 106:2239, 1997.

[119] R. M. Parrish, L. A. Burns, D. G. A. Smith, A. C. Simmonett, A. E. DePrince III, E. G. Hohenstein, U. Bozkaya, A. U. Sokolov, R. Di Remigio, R. M. Richard, J. F. Gonthier, A. M. James, H. R. McAlexander, A. Kumar, M. Saitow, X. Wang, B. P. Pritchard, P. Verma, H. F. Schaefer III, K. Patkowski, R. A. King, E. F. Valeev, F. A. Evangelista, J. M. Turney, T. D. Crawford, and C. D. Sherrill. Psi4 1.1: An open-source electronic structure program emphasizing automation, advanced libraries, and interoperability. *Journal of Chemical Theory and Computation*, 13:3185–3197, 2017.

[120] D. Patterson and J. M. Doyle. Cooling molecules in a cell for FTMW spectroscopy. *Molecular Physics*, 110:1757–1766, 2012.

[121] H. Pauly. *Atom, Molecule, and Cluster Beams.* Springer-Verlag, Berlin, 2000. Vol. 1.

[122] V. S. Petrović and R. W. Field. Polarization dependence of transition intensities in double resonance experiments: Unresolved spin doublets. *The Journal of Chemical Physics*, 128:014301, 2008.

[123] J. H. Piskorski. *Cooling, Collisions and non-Sticking of Polyatomic Molecules in a Cryogenic Buffer Gas Cell.* PhD thesis, Harvard University, Cambridge, MA, 2014.

[124] S. T. Pratt. Vibrational autoionization and predissociation in high Rydberg states of nitric oxide. *The Journal of Chemical Physics*, 108:7131, 1998.

[125] S. T. Pratt, E. F. McCormack, J. L. Dehmer, and P. M. Dehmer. Rotational state distributions from vibrational autoionization of H_2 revisited. *The Journal of Chemical Physics*, 92:1831, 1990.

[126] K. Prozument, A. P. Colombo, Y. Zhou, G. B. Park, V. S. Petrović, S. L. Coy, and R. W. Field. Chirped-pulse millimeter-wave spectroscopy of Rydberg-Rydberg transitions. *Physical Review Letters*, 107:143001, 2011.

[127] I. M. Rabey, J. A. Devlin, E. A. Hinds, and B. E. Sauer. Low magnetic Johnson noise electric field plates for precision measurement. *Review of Scientific Instruments*, 87:115110, 2016.

[128] M. Raoult and C. Jungen. Calculation of vibrational preionization in H_2 by multichannel quantum defect theory: Total and partial cross sections and photoelectron angular distributions. *The Journal of Chemical Physics*, 74:3388, 1981.

[129] M. Raoult, C. Jungen, and D. Dill. Photoelectron angular distributions in H_2: Calculation of rotational-vibrational preionization by multichannel quantum defect theory. *Journal de Chimie Physique et de Physico-chimie biologique*, 77:599–604, 1980.

[130] S. Rowan, S. Twyford, R. Hutchins, and J Hough. Investigations into the effects of electrostatic charge on the Q factor of a prototype fused silica suspension for use in gravitational wave detectors. *Classical and Quantum Gravity*, 14:1537–1541, 1997.

[131] A. Russek, M. R. Patterson, and R. L. Becker. Auto-ionization in molecular systems. *Physical Review*, 167:17–25, 1968.

[132] J. R. Rydberg. On the structure of the line-spectra of the chemical elements. *Philosophical Magazine*, 29:331–337, 1890.

[133] M. Schäfer and F. Merkt. Millimeter-wave spectroscopy and multichannel quantum-defect-theory analysis of high Rydberg states of krypton: the hyperfine structure of $^{83}Kr^+$. *Physical Review A*, 74:062506, 2006.

[134] P. C. Schmid, M. I. Miller, J. Greenberg, T. L. Nguyen, J. F. Stanton, and H. J. Lewandowski. Quantum-state-specific reaction rate measurements for the photo-induced reaction $Ca^+ + O_2 \rightarrow CaO^+ + O$. *Molecular Physics*, 117:3036–3042, 2019.

[135] D. I. Schuster, L. S. Bishop, I. L. Chuang, D. DeMille, and R. J. Schoelkopf. Cavity QED in a molecular ion trap. *Physical Review A*, 83:012311, 2011.

[136] S. M. Skoff, R. J. Hendricks, C. D. J. Sinclair, J. J. Hudson, D. M. Segal, B. E. Sauer, E. A. Hinds, and M. R. Tarbutt. Diffusion, thermalization and optical pumping of YbF molecules in a cold buffer-gas cell. *Physical Review A*, 83:023418, 2011.

[137] D. Sprecher, C. Jungen, W. Ubachs, and F. Merkt. Towards measuring the ionisation and dissociation energies of molecular hydrogen with sub-MHz accuracy. *Faraday Discussions*, 150:51–70, 2011.

[138] A. L. Steber, B. J. Harris, J. L. Neill, and B. H. Pate. An arbitrary waveform generator based chirped pulse Fourier transform spectrometer operating from 260 to 295 GHz. *Journal of Molecular Spectroscopy*, 280:3–10, 2012.

[139] G. Stokes. On the effect of the internal friction of fluids on the motion of pendulums. *Transactions of the Cambridge Philosophical Society*, 9:8–106, 1851.

[140] A. J. Stone. *The Theory of Intermolecular Forces*. Oxford University Press, Oxford, second edition, 2013.

[141] W. G. Sturrus, E. A. Hessels, P. W. Arcuni, and S. R. Lundeen. Microwave spectroscopy of high-L H_2 Rydberg states: The (0,1) 10 G, H, I, and K states. *Physical Review Letters*, 61:2320–2323, 1988.

[142] W. G. Sturrus, E. A. Hessels, P. W. Arcuni, and Lundeen S. R. Laser spectroscopy of ($v = 0$, R=1)10F and ($v = 0$, R=1)10G states of H_2: A test of the polarization model. *Physical Review A*, 38:135–151, 1988.

[143] K.-X. Sun, B. Allard, S. Buchman, S. Williams, and R. L. Byer. LED deep UV source for charge management of gravitational reference sensors. *Classical and Quantum Gravity*, 23:S141–S150, 2006.

[144] A. Temkin. Internuclear dependence of the polarizability of N_2. *Physical Review A*, 17:1232–1235, 1978.

[145] T. O. Tiernan and R. E. Marcotte. Collision-induced dissociation of NO^+ and O_2^+ at low kinetic energies: Effects of internal ionic excitation. *The Journal of Chemical Physics*, 53:2107–2122, 1970.

[146] X. Tong, T. Nagy, J. Y. Reyes, M. Germann, M. Meuwly, and S. Willitsch. State-selected ion-molecule reactions with Coulomb-crystallized molecular ions in traps. *Chemical Physics Letters*, 547:1–8, 2012.

[147] D. Townsend, A. L. Goodgame, S. R. Procter, S. R. Mackenzie, and T. P. Softley. Deflection of krypton Rydberg atoms in the field of an electric dipole. *Journal of Physics B: Atomic, Molecular and Optical Physics*, 34:439–450, 2001.

[148] D. Ugolini, R. Amin, G. Harry, J. Hough, I. Martin, V. Mitrofanov, S. Reid, S. Rowan, and K.-X. Sun. Charging issues in LIGO. In R. Caballero, J. C. D'Olivo, G. Medina-Tanco, L. Nellen, F. A. Sánchez, and J. F. Valdés-Galicia, editors, *Proceedings of the 30th International Cosmic Ray Conference*, volume 3, pages 1283–1286, 2008.

[149] A. J. C. Varandas and Rodrigues S. P. J. Internuclear dependence of static dipole polarizability in diatomic molecules. *Chemical Physics Letters*, 245:66–74, 1995.

[150] M. Vervloet, A. L. Roche, and C. Jungen. Observation of high-ℓ Rydberg states of nitric oxide. *Physical Review A*, 38:5489–5493, 1988.

[151] Inc. Virginia Diodes. Virginia diodes custom transmitters. http://vadiodes.com/en/products/custom-transmitters. Accessed: 2019-10-16.

[152] N. V. Vitanov, A. A. Rangelov, B. W. Shore, and K. Bergmann. Stimulated Raman adiabatic passage in physics, chemistry, and beyond. *Reviews of Modern Physics*, 89:015006, 2017.

[153] N. V. Vitanov, B. W. Shore, L. Yatsenko, K. Böhmer, T. Halfmann, T. Rickes, and K. Bermann. Power broadening revisited: theory and experiment. *Optics Communications*, 199:117–126, 2001.

[154] E. Vliegen and F. Merkt. Normal-incidence electrostatic Rydberg atom mirror. *Physical Review Letters*, 97:033002, 2006.

[155] E. Vliegen, H. J. Wörner, T. P. Softley, and F. Merkt. Nonhydrogenic effects in the deceleration of Rydberg atoms in inhomogeneous electric fields. *Physical Review Letters*, 92:033005, 2004.

[156] M. J. J. Vrakking. Lifetimes of Rydberg states in ZEKE experiments. III. Calculations of the dc electric field dependence of predissociation lifetimes of NO. *The Journal of Chemical Physics*, 105:7336, 1996.

[157] M. J. J. Vrakking and Y. T. Lee. Enhancements in the lifetimes of NO Rydberg states in dc electric fields: Implications for zero-electron-kinetic-energy photoelectron spectroscopy experiments. *Physical Review A*, 51:894–897, 1995.

[158] M. J. J. Vrakking and Y. T. Lee. Lifetimes of Rydberg states in zero-electron-kinetic-energy experiments. I. Electric field induced and collisional enhancement of NO predissociation lifetimes. *The Journal of Chemical Physics*, 102:8818, 1995.

[159] J. K. G. Watson. Effects of a core electric dipole moment on rydberg states. *Molecular Physics*, 81:277–289, 1994.

[160] J. K. G. Watson. Rotation-electronic coupling in diatomic Rydberg states. In C. Sándorfy, editor, *The role of Rydberg states in spectroscopy and photochemistry*. Kluwer Academic Publishers, 1999.

[161] J. D. Weinstein. *Magnetic Trapping of Atomic Chromium and Molecular Calcium Monohydride*. PhD thesis, Harvard University, Cambridge, MA, 2001.

[162] W. H. Wing. Electrostatic trapping of neutral atomic particles. *Physical Review Letters*, 45:631–634, 1980.

[163] R. N. Zare. *Angular Momentum*. John Wiley & Sons, Inc., 1988.

[164] R. Zhao. *Vibrational autoionization from nf Rydberg states of nitric oxide*. PhD thesis, Stanford University, 2004.

[165] R. Zhao, I. M. Konen, and R. N. Zare. Optical-optical double resonance photoionization spectroscopy of nf Rydberg states of nitric oxide. *The Journal of Chemical Physics*, 121:9938, 2004.

[166] V. Zhelyazkova, M. Žeško, H. Schmutz, J. A. Agner, and F. Merkt. Fluorescence-lifetime-limited trapping of Rydberg helium atoms on a chip. *Molecular Physics*, 117:298–2989, 2019.

[167] Y. Zhou. Cooperative effects in a dense Rydberg gas. *Molecular Physics*, 110:1909–1915, 2012.

[168] Y. Zhou. *Direct observation of Rydberg-Rydberg transitions via CPmmW spectroscopy*. PhD thesis, Massachusetts Institute of Technology, Cambridge, MA, 2014.

[169] Y. Zhou, D. D. Grimes, T. J. Barnum, D. Patterson, S. L. Coy, E. Klein, J. S. Muenter, and R. W. Field. Direct detection of Rydberg-Rydberg millimeter-wave transitions in a buffer gas cooled molecular beam. *Chemical Physics Letters*, 640:124–136, 2015.

[170] Y. Zhou, K. B. Ng, L. Cheng, D. N. Gresh, R. W. Field, J. Ye, and E. A. Cornell. Visible and ultraviolet laser spectroscopy of ThF. *Journal of Molecular Spectroscopy*, 358:1–16, 2019.

[171] M. L. Zimmerman, M. G. Littman, M. M. Kash, and D. Kleppner. Stark structure of the Rydberg states of alkali-metal atoms. *Physical Review A*, 20:2251–2275, 1979.

[172] A. Zutz and D. J. Nesbitt. Angle-resolved molecular beam scattering of NO at the gas-liquid interface. *The Journal of Chemical Physics*, 147:054704, 2017.